NASA

ADVANCED ION THRUSTER AND ELECTROTHERMAL LAUNCHER RESEARCH

PREPARED FOR

LEWIS RESEARCH CENTER

NATIONAL AERONAUTICS AND SPACE ADMINISTRATION

GRANT NGR-06-002-112

Annual Report

January 1983

Paul J. Wilbur
Department of Mechanical Engineering
Colorado State University
Fort Collins, Colorado

NF01896

1 Report No NASA CR 168083	2 Government Accession No	3 Recipient's Catalog No
4 Title and Subtitle Advanced Ion Thruster and Electrothermal Launcher Research		5 Report Date Jan. 1983
		6 Performing Organization Code
7 Author(s) Paul J. Wilbur		8 Performing Organization Report No
		10 Work Unit No
9 Performing Organization Name and Address Department of Mechanical Engineering Colorado State University Fort Collins, Colorado 80523		
		11 Contract or Grant No NGR-06-002-112
		13 Type of Report and Period Covered Dec. 1, 1981 - Dec. 1, 1982
12 Sponsoring Agency Name and Address National Aeronautics and Space Administration Washington, D.C. 20546		
		14 Sponsoring Agency Code

15 Supplementary Notes

16 Abstract

The results of experimental and theoretical research on electron bombardment ion thruster phenomena are presented. This work includes 1) the development of a theoretical model of orificed hollow cathode operation that predicts experimentally observed cathode performance with reasonable accuracy, 2) extensive experimental results describing the deflection and divergence characteristics of ion beamlets emanating from a two grid optics system as a function of the relative offset of screen and accel grids hole axes, 3) basic experimental studies which show how the ion currents associated with discharge chamber operation can be controlled to improve ion thruster performance markedly, 4) experimental investigations into limitations imposed by basic physical laws on reductions in screen grid hole size and grid spacing for ion optics systems, 5) experimental studies showing the influence of stray magnetic fields in the vicinity of a neutralizer on the performance of that neutralizer and 6) a theoretical analysis showing the extent to which the ion current density extracted from a thruster can be enhanced by injecting electrons into the region between its ion accelerating grids.

A theoretical analysis of the electrothermal ramjet concept of launching space bound pay-loads at high acceleration levels is described. A simple system design which could be used to implement the concept is identified. The operation of this system is broken down into two phases. In the light gas gun phase the payload is accelerated to the velocity at which the second or ramjet phase can commence. Preliminary idealized models of operation are examined and shown to yield overall energy efficiences for a typical earth escape launch of 60 to 70%. When shock losses are incorporated these efficiences are still observed to remain at the relatively high values of 40 to 50%.

17 Key Words (Suggested by Author(s)) Electrostatic Thruster Hollow Cathode Electrothermal Ramjet	18 Distribution Statement Unclassified - Unlimited		
19 Security Classif (of this report) Unclassified	20 Security Classif (of this page) Unclassified	21 No of Pages 149	22 Price*

N-83-19809#

TABLE OF CONTENTS

Table of Contents (Continued)

LIST OF FIGURES

List of Figures (Continued)

MERCURY HOLLOW CATHODE RESEARCH

Dan Siegfried

An extensive experimental investigation of mercury hollow cathodes has been completed. A model describing the basic physical processes taking place within the cathode has been developed. It can be used to predict, to first order, important cathode operating parameters such as emission length and insert temperature. The analytical formulation of the model is based on the concept of an idealized "ion production region" which is defined as the volume circumscribed by the emitting portion of the insert. The energy exchange mean free path for primary electrons is used as a criterion for determining the length of this region. An ion production region aspect ratio (dia.-to-length) of two is suggested as a design criterion for minimizing keeper voltage. The model accounts for electrons produced in the ion production region both by surface emission and by volume ionization. Surface and volume energy balances are used to predict plasma density and plasma potential in this region. An empirical relation is presented which can be used to estimate cathode internal pressure (a necessary input to the model) using the mass flow rate, discharge current and cathode orifice diameter. Calculations based on the model are compared with experimental results.

This research is described in some detail in Reference 1, which was released recently, and it will therefore not be reproduced here. In addition a summary of this work is described in a recently completed paper[2] which is included in Appendix A of this report.

ION BEAMLET VECTORING

J. M. Homa

An experimental study of ion beamlets emerging from two-grid optical systems that were vectored by translating the screen/accelerator grid holes relative to each other was completed. A paper[3] describing this work is included in Appendix A of this report. A more detailed description of this research will also be presented in thesis form and present plans call for this work to be released as a NASA Contractor report. The results of this research can be used to design accelerating systems in which the direction and focus of emerging beamlets are important. Deflection and divergence angle data were collected for two-grid systems as a function of the relative displacement of these grids. At large displacements, accelerator grid impingement was observed to become a limiting factor and this defined the useful range of beamlet deflection. Beamlet deflection was found to vary linearly with grid offset angle over this range. Values of deflection-to-offset angle ratio and the useful range of beamlet deflection were determined as functions of grid hole geometries, perveance levels, and accelerating voltage levels. The divergence of the beamlets was found to be unaffected by deflection over the useful range of beamlet deflection.

CONTROLLING ION CURRENTS TO DISCHARGE CHAMBER SURFACES

J. R. Brophy

The study of mechanisms that enable a designer to control the loss rates of ions to various discharge chamber surfaces in an ion thruster continued to focus on the use of the flexible magnetic field ion source

during the past year. The resulting research has been described in a paper[4] included in Appendix A of this report.

The flexible magnetic field thruster is a unique research tool for studying the behavior of direct current electron-bombardment ion thrusters. It utilizes a long wire anode shielded by a circumferential magnetic field. The magnetic field around the anode, which is produced by passing a direct current of up to 150 amperes through the wire, restricts primary electron flow from the discharge plasma to the anode. Different magnetic field configurations can be created by routing the anode wire in various ways through the discharge chamber. Divergent, cusped and multipole magnetic field configurations have for example been created in this manner. The thruster is also designed so ion currents to various internal surfaces can be measured directly and these measurements facilitate calculation of the distribution of ion currents within the discharge chamber. Experiments indicate that the distribution of ion currents inside the discharge chamber is strongly dependent on the shape and strength of the magnetic field but independent of the discharge current, discharge voltage, and neutral flow rate. Through proper selection of the magnetic field shape and strength, the fraction of the ions produced in the discharge chamber that is directed toward the screen grid has been increased to over 50%. Measurements of the energy cost per plasma ion indicate that this cost decreases with increasing magnetic field strength due to increased anode shielding from the primary electrons. Energy costs per argon plasma ion as low as 50 eV were measured. The energy cost per beam ion was found to be a function of the energy cost per plasma ion, extracted ion fraction and discharge voltage. Part of the energy cost per beam ion goes into creating many ions in the plasma and then extracting only a fraction of them into the beam. The rest of the energy goes into accelerating the

remaining plasma ions into the walls of the discharge chamber. Measurement of ion fluxes across a virtual anode surface appear to indicate that ions cross this surface with velocities approaching their random thermal velocity rather than the Bohm velocity.

ION EXTRACTION USING CLOSELY SPACED GRIDS

Dean Rovang

Experimental work has shown that the ion current density that can be extracted through two grid systems can be enhanced if small diameter apertures in closely spaced grids are used. This work is described in a paper[5] contained in Appendix A. It has focused on accelerator systems with small screen hole diameters (≤ 2.0 mm) operating at net-accelerating voltages of 100, 300, and 500 V. The apparatus developed for this study is shown to be well suited for measuring the impingement-limited perveance, electron backstreaming, and electrical breakdown characteristics of two-grid ion accelerator systems. Results suggest that the impingement-limited perveance is not dramatically affected by reductions in screen hole diameter to 1.0 mm. Impingement-limited performance was found to be dependent on the grid separation distance, the discharge-to-total accelerating voltage ratio, and the net-to-total accelerating voltage ratio. Results obtained using closely spaced grids having small hole diameters and operating at fixed low values of net accelerating voltage show that the onset of high impingement current occurs at <u>progressively higher current density levels as the net-to-total accelerating voltage ratio is increased</u>. This unexpected result suggests a new philosophy of high current density grid operation at high net-to-total accelerating voltage ratios. When grids are operating at this condition

it appears the onset of electron backstreaming ultimately determines the extractable ion current density. Beam current densities as high as 25 mA/cm^2 were obtained using grids with 1.0 mm diameter holes operating at a net accelerating voltage of 500 V.

THE INFLUENCE OF STRAY MAGNETIC FIELDS ON THE ION BEAM NEUTRALIZATION

Feng Yu-Cai

Work has continued on the study of the influence of magnetic fields in the vicinity of the neutralizer on its capacity to couple to and neutralize an ion beam emerging from a thruster. This work is described in a paper[6] also included in Appendix A. This paper describes the experimental investigation in which a comparison of the ion beam neutralization characteristics of a local neutralizer (within ∿ 5 cm of the beam edge) with those associated with a distant one (∿ 1 meter away from thruster) was made. The influence of magnetic fields in the vicinity of the neutralizer cathode orifice which were either parallel with or normal to the neutralizer axis were studied. Plasma property profiles which reflected the influence of the magnetic fields were measured. The results indicated that magnetic fields at the region of a neutralizer cathode orifice influence its ability to couple to the ion beam. They show that there is a potential jump from the neutralizer cathode orifice to the plasma which exists close to the orifice. The magnitude of this potential jump increases as the axial component of magnetic flux density increases. A magnetic field perpendicular to the neutralizer axis induces a potential rise a few centimeters further downstream of the neutralizer cathode. Test results indicate the path length from the neutralizer to the beam along magnetic field lines

also has an effect on the beam-to-neutralizer plasma potential difference but this effect was typically smaller than the other two effects. The results suggest that in order to minimize the adverse effects of stray magnetic fields, a region as free of magnetic fields as possible should be selected for placement of the neutralizer.

ENHANCEMENT OF ION BEAM CURRENTS
THROUGH SPACE CHARGE COMPENSATION

Feng Yu-Cai

Introduction

Langmuir[7] has discussed the possibility of increasing the space charge
limited electron current between two electrodes by injecting positive ions
into the electron space charge and thereby partially neutralizating its
detrimental effect on electron extraction. In the following work the
neutralization of the positive ion space charge induced by injecting negative
changes into the region between the grids of a positively charged ion accel-
erator has been studied theoretically. If it is possible to do this the
ion current density of the extracted beam could be increased. This could
lead to an increased thrust density for electrostatic thrusters.

Several options for charged particle injection are considered and the
results suggest that the extracted ion beam density can be increased greatly
by negatively charged particle injection. The ratio of the extracted beam
current density to the conventional space charge limited value can be in-
creased through the use of charged particle injection by a factor 30 or
more, depending on the current density and velocity distribution of the
injected negatively charged particle beams. The ratio of injected particle
current density to the ion beam current density required to effect this
change is of the order of the square root of the ratio of the extracted ion
mass to the injected particle mass. In the following development the injected
negatively charge particles will be designated as electrons and the extracted
beam will be designated positive ions. The analysis is carried out in general
terms however and the injected particles could just as well be negative ions.

Further, the results are applicable to the case where positive ion injection is used to enhance the extracted current densities of negative ion beams.

Electron Injection Between the Acceleration Grids

Consider an infinite plane screen grid "A" at potential V_A and a parallel plane cathode (accelerator grid "C" at zero potential located at a distance a from "A" as shown in Fig. 1). Assume an infinite supply of ions without appreciable initial velocities is available at the screen grid. If these ions are extracted at the space charge limit, the potential gradient at the screen grid will be zero, and the current density is given by the Child-Langmuir equation[8]

$$j_{i_0} = \frac{4\varepsilon_0}{9} \left(\frac{2e}{m_i}\right)^{1/2} \frac{V_A^{3/2}}{a^2} \tag{1}$$

where e is the ion charge, ε_0 is the permittivity of free space and m_i is the mass of the ions.

Let us now consider the effect of introducing negative electrons without initial velocity, uniformly distributed over a plane "B" which is at a distance b from "A" as suggested in Fig. 2. Between "B" and "A" there is as a result of this injection an electron current per unit area j_e. Because of the partial neutralization of the ion space charge, the ion current per unit area from the screen grid will increase to a new value, j_i. We assume that the ions and electrons do not collide with gas molecules nor with each other and that no appreciable number of ions or electrons is lost by re-combination during the passage between the electrodes. Let $v_i(x)$ be the velocity of the ions at any point p, which is a distance x from the screen grid "A". The ion current density at p is then $\rho_i(x)$. The corresponding quantities for the electrons are denoted by the subscript e.

Then in region A-B one has

PLANE "A"
(POTENTIAL V_A)

PLANE "C"
(POTENTIAL $V_C=0$)

j_{i_0}

O a x
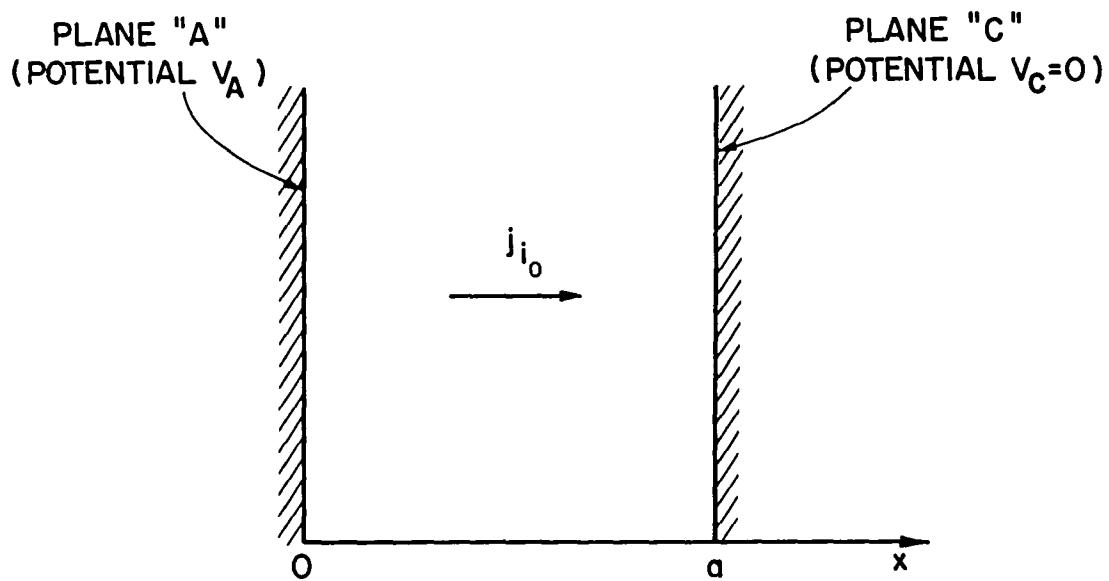
Fig. 1 Configuration without Electron Injection

ARBITRARY PLANE
(POTENTIAL V)

PLANE " B "
(POTENTIAL V_B)

PLANE "A"
(POTENTIAL V_A)

PLANE "C"
(POTENTIAL $V_C = 0$)

j_i j_i

j_e

O b a x
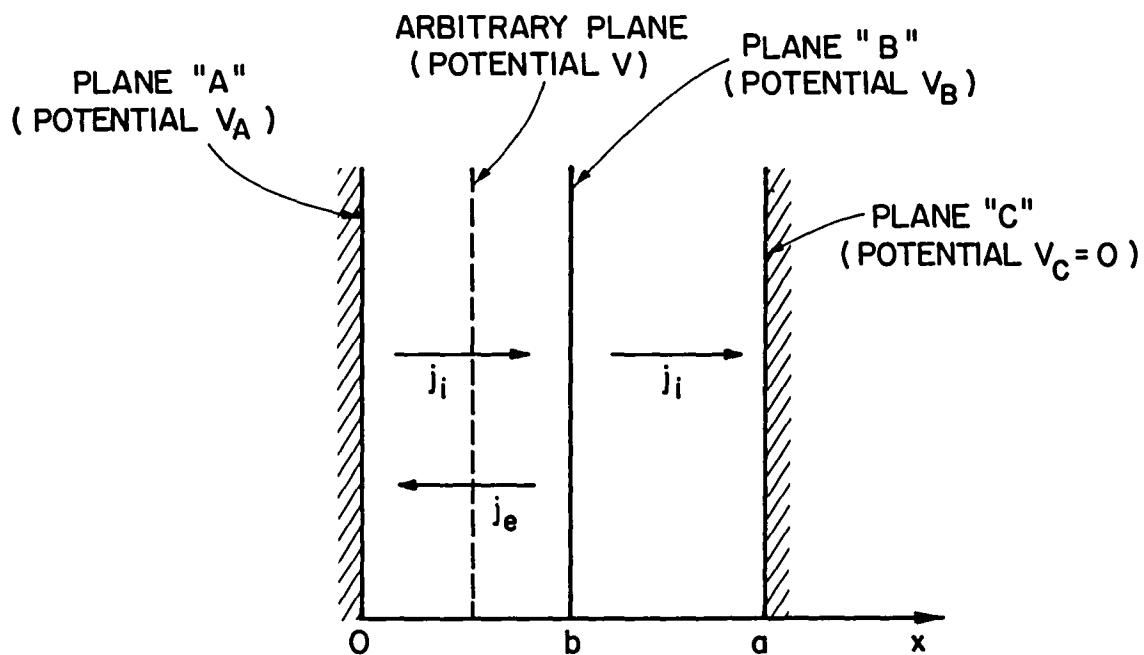
Fig. 2 Configuration with Intra-grid Electron Injection

$$\rho_i(x) = \frac{j_i}{v_i(x)} \tag{2}$$

where

$$v_i(x) = \sqrt{\frac{2(V_A-V)e}{m_i}} . \tag{3}$$

The electron charge density in this same region is given by

$$\rho_e(x) = \frac{j_e}{v_e(x)} \tag{4}$$

where

$$v_e(x) = \sqrt{\frac{2(V-V_B)e}{m_e}} , \tag{5}$$

V is the potential at a point p and V_B is the potential at plane "B".

Poisson's equation may be written in one dimension as

$$\frac{d^2V}{dx^2} = \frac{j_e}{\epsilon_0\sqrt{\frac{2(V-V_B)e}{m_e}}} - \frac{j_i}{\epsilon_0\sqrt{\frac{2(V_A-V)e}{m_i}}} . \tag{6}$$

Using the definitions,

$$\alpha \equiv \frac{j_e}{j_i}\sqrt{\frac{m_e}{m_i}} , \quad \phi \equiv V/V_A , \quad \lambda \equiv x/a \tag{7}$$

and combining Eqs. (1) and (6) one obtains

$$\frac{d^2\phi}{d\lambda^2} = \frac{4}{9}\frac{j_i}{j_{i_0}}\left[\alpha(\phi-\phi_B)^{-\frac{1}{2}} - (1-\phi)^{-\frac{1}{2}}\right] . \tag{8}$$

where $\phi_B \equiv V_B/V_A$ as suggested by the definition Eq. (7).

In the space charge limited case the boundary condition at the screen

grid is
$$\left(\frac{d\phi}{d\lambda}\right)_{\lambda=0} = 0 . \tag{9}$$

Applying this same zero gradient condition at plane "B" for the integration

of Eq. (8) gives

$$\frac{d\phi}{d\lambda} = -\frac{4}{3}\left(\frac{j_i}{j_{i_0}}\right)^{\frac{1}{2}}\left[\alpha(\phi-\phi_B)^{\frac{1}{2}} + (1-\phi)^{\frac{1}{2}} - \alpha(1-\phi_B)^{\frac{1}{2}}\right]^{\frac{1}{2}} . \tag{10}$$

The normalized position of plane "B" (λ_B) can be determined by integrating this expression to obtain:

$$\lambda_B = \frac{3}{4} \left[\frac{j_{i_0}}{j_i} \right]^{\frac{1}{2}} \int_{\phi_B}^{1} \left[\alpha(\phi-\phi_B)^{\frac{1}{2}} + (1-\phi)^{\frac{1}{2}} - \alpha(1-\phi_B)^{\frac{1}{2}} \right]^{-\frac{1}{2}} d\phi \qquad (11)$$

In the region B-C of Fig. 2 only ions are present and their charge density is given by

$$\rho_i(x) = \frac{j_i}{v_i(x)} \qquad (12)$$

where

$$v_i(x) = \sqrt{\frac{2e(V_A-V)}{m_i}} . \qquad (13)$$

Poisson's equation is given in this region by

$$\frac{d^2\phi}{d\lambda^2} = - \frac{4}{9} \frac{j_i}{j_{i_0}} (1-\phi)^{\frac{1}{2}} . \qquad (14)$$

Integrating this equation one obtains

$$\left(\frac{d\phi}{d\lambda} \right)^2 = \frac{16}{9} \frac{j_i}{j_{i_0}} (1-\phi)^{\frac{1}{2}} + C . \qquad (15)$$

The constant of integration for Eq. (15) is again selected so that $\frac{d\phi}{d\lambda} = 0$ at $\phi = \phi_B$ and the equation becomes

$$\frac{d\phi}{d\lambda} = - \frac{4}{3} \left[\frac{j_i}{j_{i_0}} \right]^{\frac{1}{2}} \left[(1-\phi)^{\frac{1}{2}} - \alpha(1-\phi_B)^{\frac{1}{2}} \right]^{\frac{1}{2}} . \qquad (16)$$

Integrating this equation from $\lambda = \lambda_B$ to 1 one has

$$1 - \lambda_B = \frac{3}{4} \left[\frac{j_{i_0}}{j_i} \right]^{\frac{1}{2}} \int_{0}^{\phi_B} \left[(1-\phi)^{\frac{1}{2}} - \alpha(1-\phi_B)^{\frac{1}{2}} \right]^{-\frac{1}{2}} d\phi . \qquad (17)$$

Adding Eqs. (11) and (17) we obtain the ratio of extracted beam current

density with injected electrons to the space charge limited ion current without electron injection. It is given by

$$\frac{j_i}{j_{i_0}} = \frac{9}{16} \left\{ \int_{\phi_B}^{1} \left[\alpha(\phi-\phi_B)^{\frac{1}{2}} + (1-\phi)^{\frac{1}{2}} - \alpha(1-\phi_B)^{\frac{1}{2}} \right]^{-\frac{1}{2}} d\phi \right. $$
$$ \left. + \int_{0}^{\phi_B} \left[(1-\phi)^{\frac{1}{2}} - \alpha(1-\phi_B)^{\frac{1}{2}} \right]^{-\frac{1}{2}} d\phi \right\}^2 . \tag{18}$$

In the space charge limited case the boundary condition at plane "B" is

$$\left(\frac{d\phi}{d\lambda} \right)_B = 0 \tag{19}$$

and from Eq. (16) we see this means

$$\alpha = 1 \quad \text{or} \quad j_e = \sqrt{\frac{m_i}{m_e}} \; j_i . \tag{20}$$

Eq. (18) can be integrated to give

$$\frac{j_i}{j_{i_0}} = \frac{9}{16} \left\{ \int_{\phi_B}^{1} \left[(\phi-\phi_B)^{\frac{1}{2}} + (1-\phi)^{\frac{1}{2}} - (1-\phi_B)^{\frac{1}{2}} \right]^{-\frac{1}{2}} d\phi + \frac{4}{3} (1-\sqrt{1-\phi_B})^{3/2} \right. $$
$$ \left. + 4(1-\phi_B)^{\frac{1}{2}} (1-\sqrt{1-\phi_B})^{\frac{1}{2}} \right\}^2 \tag{21}$$

For the case where $\phi_B = 1$, Eq. (21) gives

$$\frac{j_i}{j_{i_0}} = 1 . \tag{22}$$

This means that if plane "B", from which electron emission occurs, coincides with the screen grid, the extracted beam current density cannot be increased by electron injection. For the case where $\phi_B = 0$, i.e. locating the electron emission plane at the accelerator grid, Eq. (21) can be integrated numerically to obtain

$$\frac{j_i}{j_{i_o}} = 1.87 \ . \tag{23}$$

This is the same result obtained by Langmuir for the case where ions were injected into the electron space charge.[8] Differentiating Eq. (21) with respect to ϕ_B, and setting the result equal to zero one obtains the value of ϕ_B that results in the maximum ion current. This occurs when $\phi_B = 0.4$ at which potential Eq. (21) gives

$$\frac{j_i}{j_{i_o}} = 4.6. \tag{24}$$

Numerical integration of Eqs. (10) and (16) has been accomplished for this optimal case where $\phi_B = 0.4$ and $\alpha = 1$. This integration yields the profile of electrical potential which can be used in turn to obtain the potential gradient, and ion velocity profiles. Fig. 3 shows the normalized versions of these profiles. For this optimal case the electron emission plane is located at $b/a = 0.43$ as shown in the figure. Either increases or decreases in the optimal value of b/a cause the peak electric field to decrease from the value shown in the lower plot and this in turn causes the ion current density to decrease from its maximum value. It is noted that the electric field has been normalized using the ratio of the intra-grid potential difference to the grid separation distance. This is the electric field that would exist between the grids if the ion and electron densities between the grids were negligible. The electric field for the case of electron injection is observed to be over 50% above this reference electric field. Figure 4 shows how the maximum positive ion current that can be extracted through the grids varies with the electron injection current and the potential of the plane from which the electrons are emitted. The extracted ion and injected electron currents have been normalized using
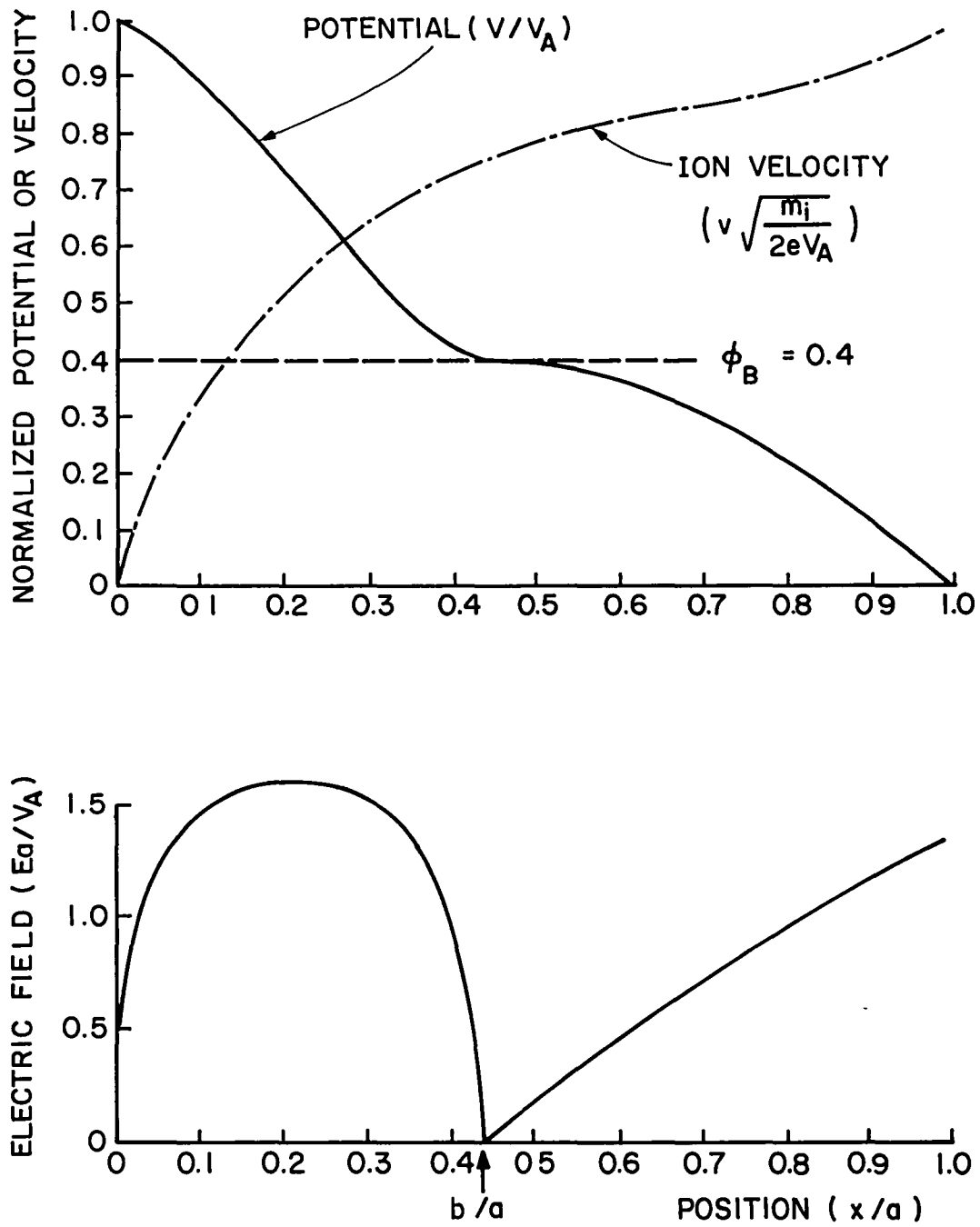
Fig. 3   Property Profiles for Optimal Intra-electrode
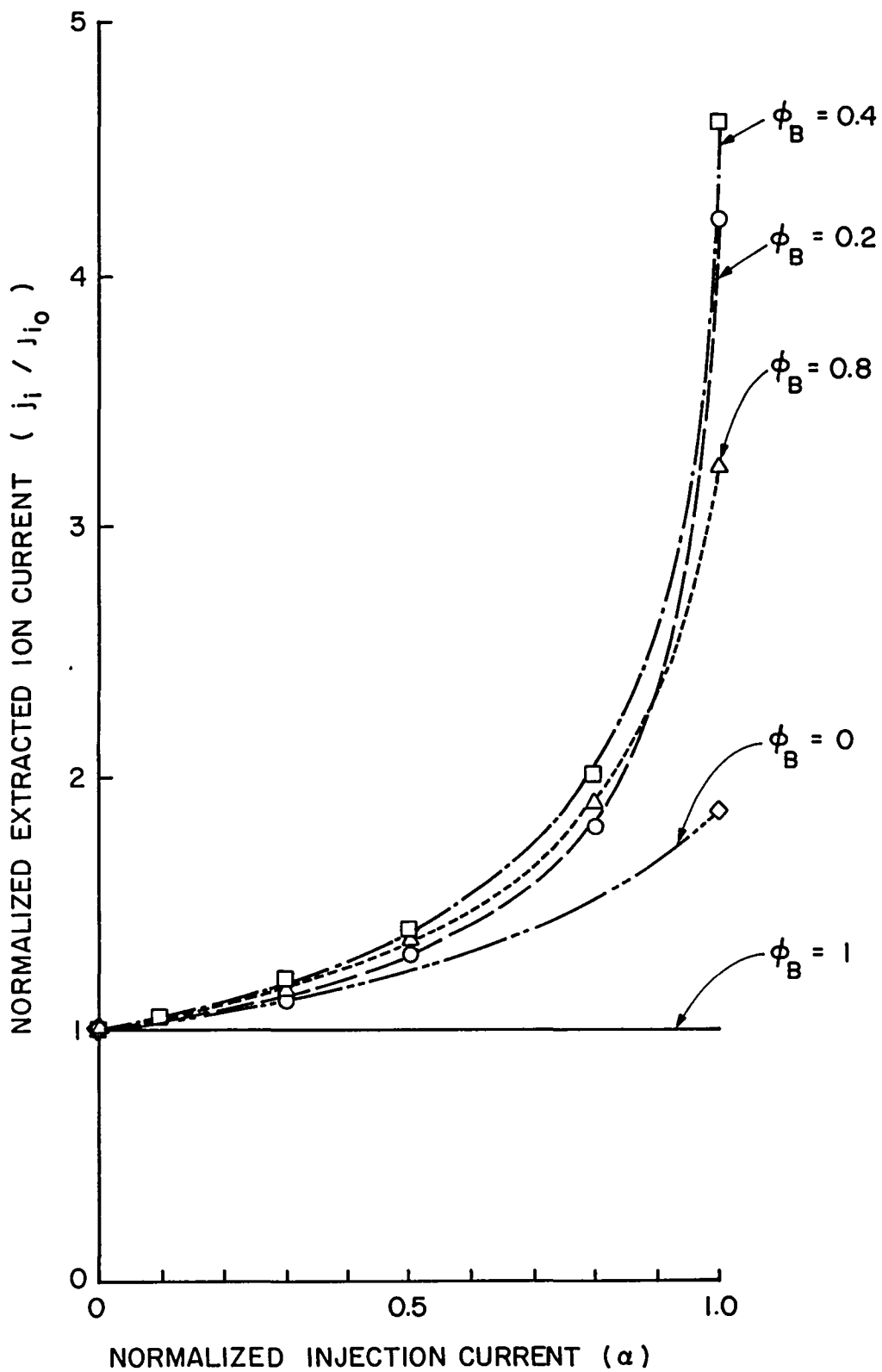
Electron Injection

Fig. 4 Effect of Injected Electron Current on Extracted Ion Current

respectively the conventional space charge limited ion current and the mass weighted electron current of Eq. (7). The figure suggests the highest ion current enhancement is realized at when emission occurs at $\phi_B = 0.4$ as suggested previously. It also shows that a reduction in the injected electron current from the maximum value ($\alpha = 1$) is accompanied by a dramatic decrease in the extracted ion current. This points out the drawback of electron injection because $\alpha = 1$ implies a large electron current (Eq. 20) and this in turn suggests a substantial input power to the electrons.

Electron Injection from Upstream of the Screen Grid

Let us now consider the effect of introducing negative electrons which are shot into the region between screen and accelerator grid from the upstream side of the screen grid with their velocity directed toward the accelerator grid. Because of the retarding field seen by the electrons as they enter the region between the grids, their velocity will decrease and at some distance from "A" (at plane "B" shown in Fig. 5) their velocity will become zero. They will then be accelerated back toward the screen grid. As before, we assume that the ions and electrons collide with neither the gas molecules nor with each other and that no appreciable number of ions or electrons is lost by recombination during the passage between the electrodes. As a consequence of electron injection to neutralize the ion space charge, the ion beam current density extracted by the grids will reach a value j_i.

The development of this problem parallels exactly the problem just solved. The only difference in the development being that the density the injected electrons at any given location is twice that for the case where electrons are emitted from a plane between the grids.

Solution of this problem shows that there is an optimum injection
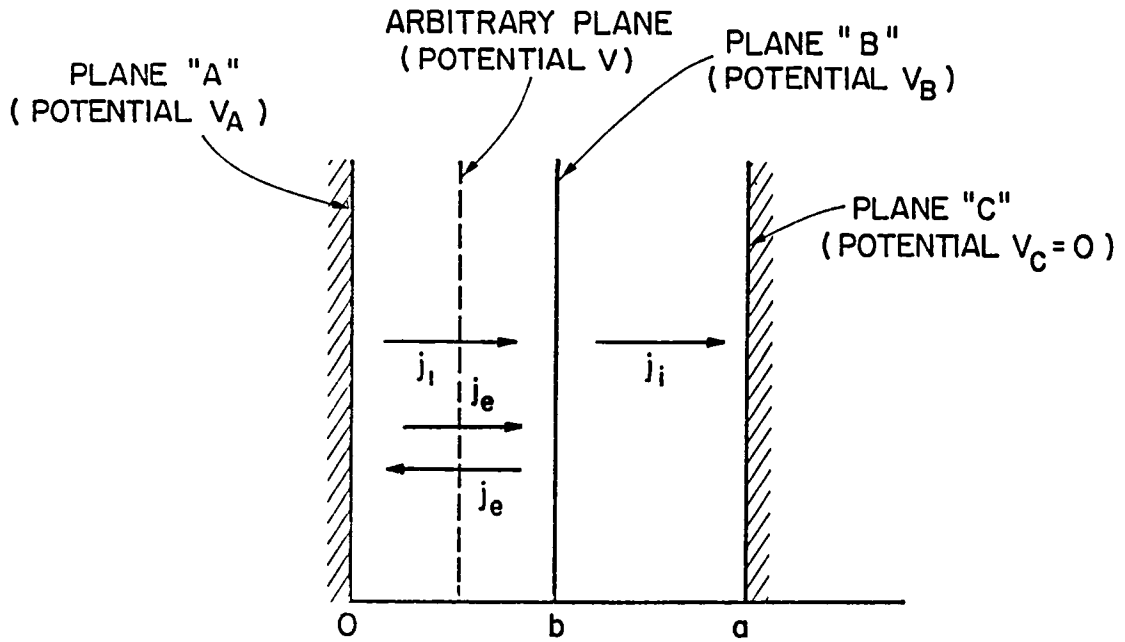
Fig. 5 Configuration for Electron Injection from Upstream of the
Screen Grid (Plane "A")
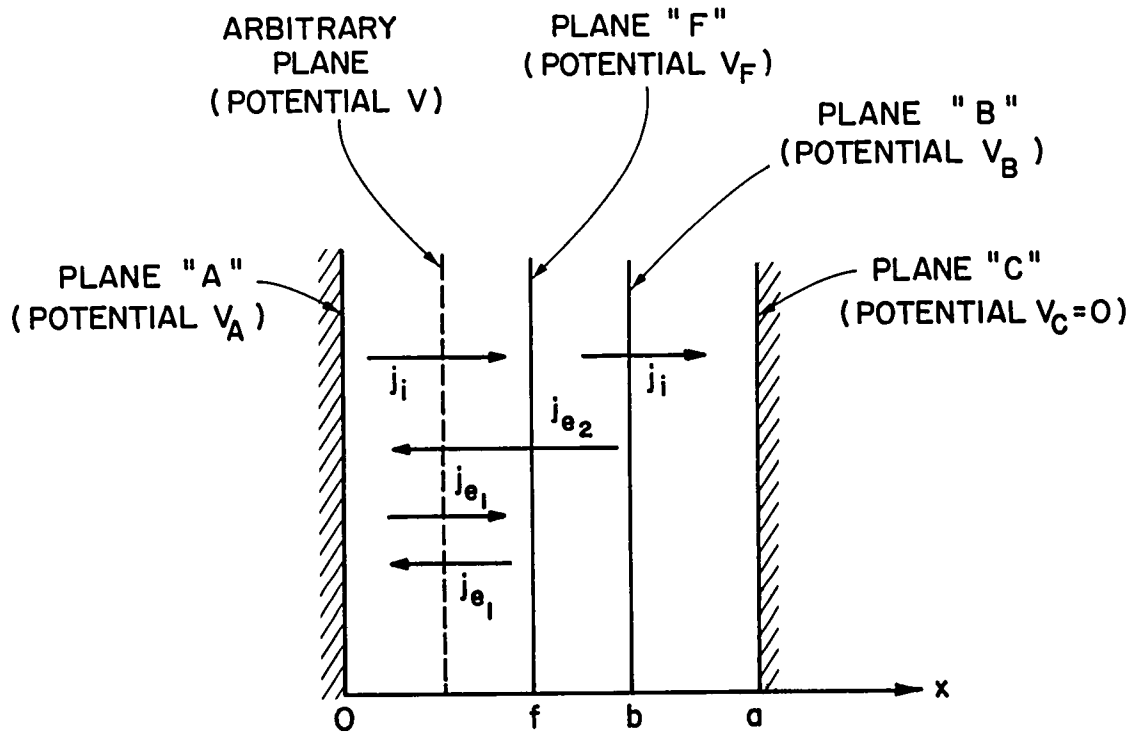
Fig. 6 Configuration for Simultaneous Upstream and
Intra-grid Electron Injection

energy corresponding to the location of the plane "B" where the velocity

goes to zero. As one would expect

$$\phi_{B\ opt} = 0.4$$

and

$$(j_i/j_{io})_{max} = 4.6 \quad .$$

Hence the same 4.6 fold increase in the ion current density that was

obtained using intra-grid electron injection can be effected by optimal

electron injection from upstream of the grids. Numerical integration of

the equations in this case can again be used to determine potential,

potential gradient and ion velocity profiles. These profiles are identical

to those shown in Fig. 3. The plot of extracted ion current as a function

of injected electron current is the same as Fig. 4, except for the fact

that the peak ion currents occur at a normalized injected electron current

(α) of one half. Hence one can conclude that the effect of electron injection

is the same regardless of the means of getting the electrons into the ion

acceleration region. The advantage of upstream electron injection is the

required electron current is half of that required for intra-grid injection

($\alpha = 1/2$ vs. $\alpha = 1$).

Electron Injection from both Sides of the Screen Grid

It is possible to inject electrons from both upstream and downstream

of the screen grid simultaneously in order to neutralize the space charge

within an ion beam. Figure 6 shows a physical model of this situation in

which electrons are injected from upstream of the screen grid at plane "A"

with a current density j_{e_1} and a velocity sufficient to enable them to reach

plane "F". These electrons pass both directions through the region A-F as

shown in Fig. 6. Electrons are also released at plane "B" with zero velocity

and they pass through region A-B going toward plane "A" as shown. As in the cases considered previously collisions are neglected and one computes the electron and ion charge density in each region as a function of the velocity of the electrons injected from upstream, the location of electron injection from between the grids and the current densities of the two injected electron beams. The charge densities are then used in the Poisson Equation describing each region, the resulting equations are integrated and potentials and potential gradients are matched at planes "B" and "F". The basic procedure is similar to the ones followed for the cases just discussed. As a result of this analysis one obtains the following expressions for the nondimensionalized locations of the planes "B" and "F" and the ratio of the ion current to the ion current without electron injection.

$$\lambda_F = \frac{3}{4}\left[\frac{j_i}{j_{i_0}}\right]^{\frac{1}{2}} \int_{\phi_F}^{1}\left\{2\alpha_1(\phi-\phi_F)^{\frac{1}{2}} + \alpha_2(\phi-\phi_B)^{\frac{1}{2}} + (1-\phi)^{\frac{1}{2}}\right.$$

$$\left. - \left[2\alpha_1(1-\phi_F)^{\frac{1}{2}} + \alpha_2(1-\phi_B)^{\frac{1}{2}}\right]\right\}^{\frac{1}{2}} d\phi \tag{25}$$

$$\lambda_B = \lambda_F + \frac{3}{4}\left[\frac{j_i}{j_{i_0}}\right]^{\frac{1}{2}} \int_{\phi_B}^{\phi_F}\left\{\alpha_2(\phi-\phi_B)^{\frac{1}{2}} + (1-\phi)^{\frac{1}{2}} - \left[2\alpha_1(1-\phi_F)^{\frac{1}{2}}\right.\right.$$

$$\left.\left. +\alpha_2(1-\phi_B)^{\frac{1}{2}}\right]\right\} d\phi \tag{26}$$

$$\frac{j_i}{j_{i_0}} = \frac{9}{16}\left\{\int_{0}^{\phi_B}\left\{(1-\phi)^{\frac{1}{2}} - \left[2\alpha_1(1-\phi_F)^{\frac{1}{2}} + \alpha_2(1-\phi_B)^{\frac{1}{2}}\right]\right\}^{-\frac{1}{2}} d\phi\right.$$

$$+ \int_{\phi_B}^{\phi_F}\left\{\alpha_2(\phi-\phi_B)^{\frac{1}{2}} + (1-\phi)^{\frac{1}{2}} - \left[2\alpha_1(1-\phi_F)^{\frac{1}{2}} + \alpha_2(1-\phi_B)^{\frac{1}{2}}\right]\right\}^{-\frac{1}{2}} d\phi \tag{27}$$

$$\left. + \int_{\phi_F}^{1}\left\{2\alpha_1(\phi-\phi_F)^{\frac{1}{2}} + \alpha_2(\phi-\phi_B)+(1-\phi)^{\frac{1}{2}} - \left[2\alpha_1(1-\phi_F)^{\frac{1}{2}} + \alpha_2(1-\phi_B)^{\frac{1}{2}}\right]\right\}^{-\frac{1}{2}} d\phi\right\}^{2}$$

The potential gradient expressions describing each of the regions of Fig. 6 are:

for region A-F

$$\frac{d\phi}{d\lambda} = -\frac{4}{3}\left[\frac{j_i}{j_{io}}\right]^{\frac{1}{2}}\left\{2\alpha_1(\phi-\phi_F)^{\frac{1}{2}} + \alpha_2(\phi-\phi_B)^{\frac{1}{2}} + (1-\phi)^{\frac{1}{2}} - \left[2\alpha_1(1-\phi_F)^{\frac{1}{2}} + \alpha_2(1-\phi_B)^{\frac{1}{2}}\right]\right\}^{\frac{1}{2}} \quad (28)$$

for region F-B

$$\frac{d\phi}{d\lambda} = -\frac{4}{3}\left[\frac{j_i}{j_{io}}\right]^{\frac{1}{2}}\left\{\alpha_2(\phi-\phi_B)^{\frac{1}{2}} + (1-\phi)^{\frac{1}{2}} - \left[2\alpha_1(1-\phi_F)^{\frac{1}{2}} + \alpha_2(1-\phi_B)^{\frac{1}{2}}\right]\right\}^{\frac{1}{2}} \quad (29)$$

for region B-C

$$\frac{d\phi}{d\lambda} = -\frac{4}{3}\left[\frac{j_i}{j_{io}}\right]^{\frac{1}{2}}\left\{(1-\phi)^{\frac{1}{2}} - \left[2\alpha_1(1-\phi_F)^{\frac{1}{2}} + \alpha_2(1-\phi_B)^{\frac{1}{2}}\right]\right\}^{\frac{1}{2}} \quad . \quad (30)$$

Application of the space charge limited conditions at planes "B" and "F" yields the normalized injected electron currents from Eqs. (28) to (30).

$$\frac{j_{e_1}}{j_i} = \alpha_1\sqrt{\frac{m_i}{m_e}} = \frac{(1-\phi_F)^{\frac{1}{2}}(1-\phi_B)^{\frac{1}{2}} + \left[(\phi_F-\phi_B)^{\frac{1}{2}} - (1-\phi_B)\right]^{\frac{1}{2}}}{2(1-\phi_F)^{\frac{1}{2}}(\phi_F-\phi_B)^{\frac{1}{2}}} [1-\phi_B]^{\frac{1}{2}}\sqrt{\frac{m_i}{m_e}} \quad (31)$$

and

$$\frac{j_{e_2}}{j_i} = \alpha_2\sqrt{\frac{m_i}{m_e}} = \frac{(2\alpha_1-1)(1-\phi_F)^{\frac{1}{2}}}{(\phi_F-\phi_B)^{\frac{1}{2}} - (1-\phi_B)^{\frac{1}{2}}}\sqrt{\frac{m_i}{m_e}} \quad . \quad (32)$$

Numerical integration of Eqs. (28) to (30) yields the potential variations through the ion acceleration region as a function of α_1, α_2, ϕ_B and ϕ_F. The maximum ion current density is observed for

$$\alpha_1 = 0.42,$$

$$\alpha_2 = 0.30,$$

$$\phi_F = 0.4$$

$$\phi_B = 0.16 = \phi_F^2 \ .$$

At the condition corresponding to these parameters the normalized ion current is

$$\frac{j_i}{j_{io}} = 11.7$$

and the normalized total injected electron current (from both sources) is required to be

$$\frac{j_e}{j_i} = 0.72 \sqrt{\frac{m_i}{m_e}} \ .$$

Hence in this case the ion current density can be increased over an order of magnitude above the value without injected electrons. As before, however, very large injected electron currents are required. Figure 7 shows the potential, potential gradient and velocity profiles associated with this maximum ion current density operating condition. In this case the electric field peak near plane "A" $(x/a = 0)$ is observed to be greater than it was for the case of electron injection at a single energy. It is this higher electric field that induces the higher ion current densities observed. It is noted that optimal electron injection from upstream at two energy levels produces profiles that are identical to those shown in Fig. 7. In this case however $\alpha_2 = 0.15$ and hence

$$\frac{j_e}{j_i} = (\alpha_1 + \alpha_2)\sqrt{\frac{m_i}{m_e}} = 0.57\sqrt{\frac{m_i}{m_e}} \ .$$

Multiple Energy Level Electron Injection

The logical extension of the preceding section of this paper is the analysis of the case where electrons are injected into the ion acceleration region at various energies. By doing this the injected electrons can induce space charge limited flow boundaries at an arbitrary number of locations
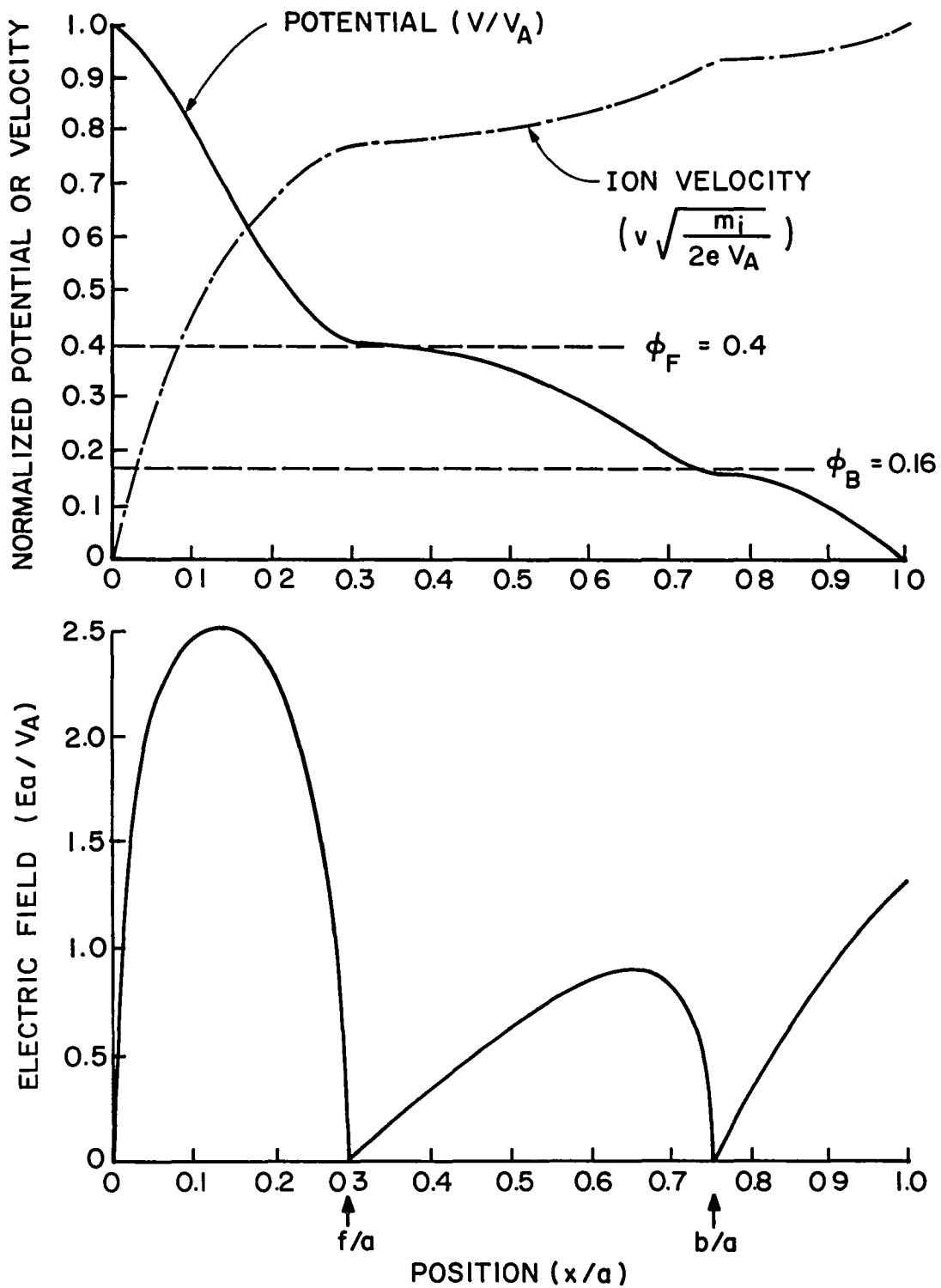
Fig. 7 Property Profiles for Optimal Injection of Two Electron Groups

within the ion acceleration region.

The basic one-dimensional model of this process is shown schematically in Fig. 8. The screen grid is represented by the plane "A" and is at a potential V_A. The accelerator grid represented by plane "C" is assumed to be at zero potential and is located a distance a from plane "A". Electrons are ejected from plane "A" at velocities $v_{e_{1_0}}$, $v_{e_{2_0}}$, $v_{e_{3_0}}$ . . . $v_{e_{n_0}}$ all directed at the accelerator grid (plane "C"). Because of the retarding field seen by the electrons as they enter the region between the planes their velocities will drop to zero at planes P_1, P_2 . . . . P_n which are at potentials V_1, V_2 . . . V_n respectively. The electrons will, after they come to rest, be accelerated back toward plane "A". Again it is assumed that the ions and electrons do not collide with each other or with neutral particles between the grids. As a result of electron injection at current densities j_{e_1}, j_{e_2} . . . j_{e_n} corresponding to injection velocities $v_{e_{1_0}}$, $v_{e_{2_0}}$ . . . . $v_{e_{n_0}}$ the ion current density will reach a level j_i. The ion charge density anywhere between the planes "A" and "C" is given by Eqs. (2) and (3) as in the preceding cases discussed. The electron charge densities will, however, depend on which region is being considered. In the region between planes "A" and "P_1", for example the total charge density is the sum of charge densities ρ_{e_1}, ρ_{e_2} . . . . ρ_{e_n} associated with each of the incident beams as well as the reflected ones that pass back through this region.
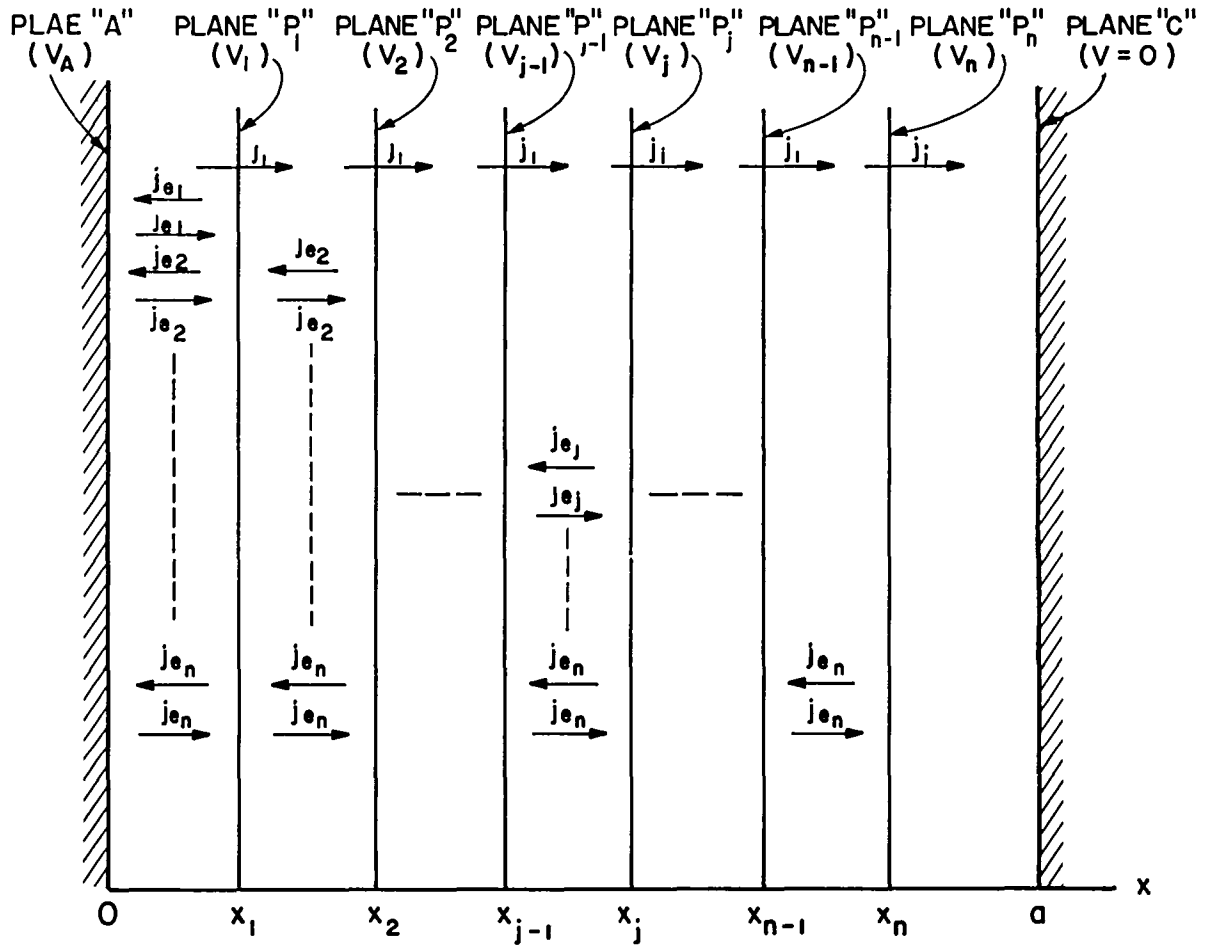
Fig. 8 Configuration for Multi-energy Electron Injection

$$\rho_{e_1} = \frac{j_{e_1}}{v_{e_1}(x)}$$

where

$$v_{e_1}(x) = \sqrt{v_{e_{1_0}}^2 - \frac{2e(V_A - V)}{m_e}}$$

and

$$v_{e_{1_0}} = \sqrt{\frac{2e(V_A - V_1)}{m_e}}$$

$$\cdot$$
$$\cdot$$
$$\cdot$$
$$\cdot$$
$$\cdot$$
$$\cdot$$
$$\cdot$$
$$\cdot$$
$$\cdot$$
$$\cdot$$
$$\cdot$$

(33)

$$\rho_{e_n} = \frac{j_{e_n}}{v_{e_n}(x)}$$

where

$$v_{e_n}(x) = \sqrt{v_{e_{n_0}}^2 - \frac{2e(V_A - V)}{m_e}}$$

and

$$v_{e_{n_0}} = \sqrt{\frac{2e(V_A - V_n)}{m_e}}$$

In the preceding expressions V is the potential at a location x between planes "A" and "P"$_1$. Poission's Equation in this region becomes:

$$\frac{d^2 V}{dx^2} = \sum_{k=1}^{n} \frac{2j_{e_k}}{\varepsilon_0 \sqrt{v_{e_{k_0}} - \frac{2e(V_A - V)}{m_e}}} - \frac{j_i}{\varepsilon_0 \sqrt{\frac{2(V_A - V)e}{m_i}}}$$

(34)

nondimensionalization using the parameters defined in Eqs. (1) and (7) enables one to rewrite Eq. (34) in the form

$$\frac{d^2\phi}{d\lambda^2} = \frac{4}{9}\left(\frac{j_i}{j_{i_0}}\right)\left[\sum_{k=1}^{n} 2\alpha_k(\phi-\phi_k)^{-\frac{1}{2}} - (1-\phi)^{-\frac{1}{2}}\right]. \tag{35}$$

In this equation j_{i_0} is the ion current density without electron injection and

$$\alpha_k \equiv \frac{j_{e_k}}{j_i}\sqrt{\frac{m_e}{m_i}}. \tag{36}$$

Integrating Eq. (35) and applying the space charge limited boundary condition $\frac{d\phi}{d\lambda} = 0$ at $\lambda = 0$ one obtains

$$\frac{d\phi}{d\lambda} = -\frac{4}{3}\left(\frac{j_i}{j_{i_0}}\right)^{\frac{1}{2}}\left[\sum_{k=1}^{n} 2\alpha_k(\phi-\phi_k)^{\frac{1}{2}} + (1-\phi)^{\frac{1}{2}} - \sum_{k=1}^{n} 2\alpha_k(1-\phi_k)^{\frac{1}{2}}\right]^{\frac{1}{2}}. \tag{37}$$

Integration of this equation using the boundary condition $\phi = 1$ at $\lambda = 0$ gives the normalized location (λ_1) of the plane P_1 in terms of the potential ϕ_1

$$\lambda_1 = \frac{3}{4}\left(\frac{j_{i_0}}{j_i}\right)^{\frac{1}{2}}\int_{\phi_1}^{1}\left[\sum_{k=1}^{n} 2\alpha_k(\phi-\phi_k)^{\frac{1}{2}} + (1-\phi)^{\frac{1}{2}} - \sum_{k=1}^{n} 2\alpha_k(1-\phi_k)^{\frac{1}{2}}\right]^{-\frac{1}{2}} d\phi. \tag{38}$$

In other regions groups of injected electrons that do not reach those regions are not included in the summations but the procedure followed above to obtain potential gradients and plane locations is similar. In the general region between planes P_{j-1} and P_j for example one obtains

$$\frac{d\phi}{d\lambda} = -\frac{4}{3}\left(\frac{j_i}{j_{i_0}}\right)^{\frac{1}{2}}\left[\sum_{k=j}^{n} 2\alpha_k(\phi-\phi_k)^{\frac{1}{2}} + (1-\phi)^{\frac{1}{2}} - \sum_{k=1}^{n} 2\alpha_k(1-\phi_k)^{\frac{1}{2}}\right]^{\frac{1}{2}} \tag{39}$$

and

$$\lambda_j = \lambda_{j-1} + \frac{3}{4}\left(\frac{j_{i_0}}{j_i}\right)^{\frac{1}{2}}\left[\int_{\phi_j}^{\phi_{j-1}}\sum_{k=j}^{n} 2\alpha_k(\phi-\phi_k)^{\frac{1}{2}} + (1-\phi)^{\frac{1}{2}} - \sum_{k=1}^{n} 2\alpha_k(1-\phi_k)^{\frac{1}{2}}\right]^{-\frac{1}{2}} d\phi \tag{40}$$

The preceding expressions are valid for $j = 2, 3 \ldots n$. For the last region to the right in Fig. 8 (Region P_n -C) one obtains

$$\frac{d\phi}{d\lambda} = -\frac{4}{3}\left(\frac{j_i}{j_{i_o}}\right)^{\frac{1}{2}}\left[(1-\phi)^{\frac{1}{2}} - \sum_{k=1}^{n} 2\alpha_k(1-\phi_k)^{\frac{1}{2}}\right]^{\frac{1}{2}} \tag{41}$$

which can be integrated to give

$$1-\lambda_n = \frac{3}{4}\left(\frac{j_{i_o}}{j_i}\right)^{\frac{1}{2}}\int_0^{\phi_n}\left[(1-\phi)^{\frac{1}{2}} - \sum_{k=1}^{n} 2\alpha_k(1-\phi_k)^{\frac{1}{2}}\right]^{\frac{1}{2}} d\phi \quad . \tag{42}$$

Adding the equations of the form of Eqs. (38), (40) and (42) describing the locations of the planes "P_1", "P_2" . . . . ."P_n" one obtains the normalized ion current density ratio:

$$\frac{j_i}{j_{i_o}} = \frac{9}{16}\left\{ \int_0^{\phi_n}\left[(1-\phi)^{\frac{1}{2}} - \sum_{k=1}^{n} 2\alpha_k(1-\phi_k)^{\frac{1}{2}}\right]^{-\frac{1}{2}} d\phi \right.$$

$$+ \int_{\phi_n}^{\phi_{n-1}}\left[2\alpha_n(\phi-\phi_n)^{\frac{1}{2}} + (1-\phi)^{\frac{1}{2}} - \sum_{k=1}^{n} 2\alpha_k(1-\phi_k)^{\frac{1}{2}}\right]^{-\frac{1}{2}} d\phi$$

$$\begin{matrix} \cdot \\ \cdot \\ \cdot \\ \cdot \\ \cdot \\ \cdot \\ \cdot \\ \cdot \end{matrix} \tag{43}$$

$$\left. + \int_{\phi_1}^{1} \sum_{k=1}^{n}\left[2\alpha_k(\phi-\phi_k)^{\frac{1}{2}} + (1-\phi)^{\frac{1}{2}} - \sum_{k=1}^{n} 2\alpha_k(1-\phi_k)^{\frac{1}{2}}\right]^{-\frac{1}{2}} d\phi \right\}$$

Applying the space charge limited current condition at each of the planes "P_1", "P_2". . . . . ."P_n" to Eqs. (37), (39) and (41) one obtains the following set of simultaneous equations

$$2\alpha_1(1-\phi_1)^{\frac{1}{2}}+2\alpha_2\left[(1-\phi_2)^{\frac{1}{2}}-(\phi_1-\phi_2)^{\frac{1}{2}}\right] + \ldots +2\alpha_n\left[(1-\phi_n)^{\frac{1}{2}}-(\phi_1-\phi_n)^{\frac{1}{2}}\right]=(1-\phi_1)^{\frac{1}{2}}$$

$$2\alpha_1(1-\phi_1)^{\frac{1}{2}}+2\alpha_2(1-\phi_2)^{\frac{1}{2}}+2\alpha_3\left[(1-\phi_3)^{\frac{1}{2}}-(\phi_2-\phi_3)^{\frac{1}{2}}\right]+\ldots+2\alpha_n\left[(1-\phi_n)^{\frac{1}{2}}-(\phi_2-\phi_n)^{\frac{1}{2}}\right]=(1-\phi_2)^{\frac{1}{2}}$$

$$\vdots \qquad\qquad\qquad\qquad\qquad\qquad \vdots \qquad\qquad\qquad\qquad (44)$$

$$2\alpha_1(1-\phi_1)^{\frac{1}{2}} + 2\alpha_2(1-\phi_2)^{\frac{1}{2}} + \ldots \ldots \ldots +2\alpha_n(1-\phi_n)^{\frac{1}{2}} = (1-\phi_n)^{\frac{1}{2}}$$

Simultaneous solution of Eqs. (44) was accomplished using Cramer's Rule to obtain expressions for the constants $\alpha_1 \ldots \ldots \alpha_n$ in terms of the normalized potentials $\phi_1 \ldots \ldots \phi_n$. The previous cases considered in this paper suggested that the maximum ion current density was realized when the normalized potentials of the planes "P_1" and "P_2" were $\phi_1 = 0.4$ and $\phi_2 = \phi_1^2 = 0.16$. Using the simplex method[9] for cases of two and three injected electron groups this result was verified for the two group problem and the potentials for the three group system were found to be $\phi_1 = 0.4$, $\phi_2 = \phi_1^2 = 0.16$ and $\phi_3 = \phi_1^3 = 0.064$. The logical extension of this is to establish injected electron energies such that the generalized potential is

$$\phi_k = (0.4)^k . \qquad\qquad (45)$$

Numerical integration of Eq. (43) carried out using values of α_k determined using Eq. (45) together with the solutions of Eq. (40) suggested that this criterion does indeed result in the maximum normalized ion current density for the general case. Normalized ion current densities have been computed for one through ten stages of electron injection and the results of this work are shown in Fig. 9. This figure shows that the ion current that can be extracted from a plasma increases monotonically with the number of stages of electron injection to a value over thirty times the uninjected Child's Law limit. This value of extracted ion current is realized when
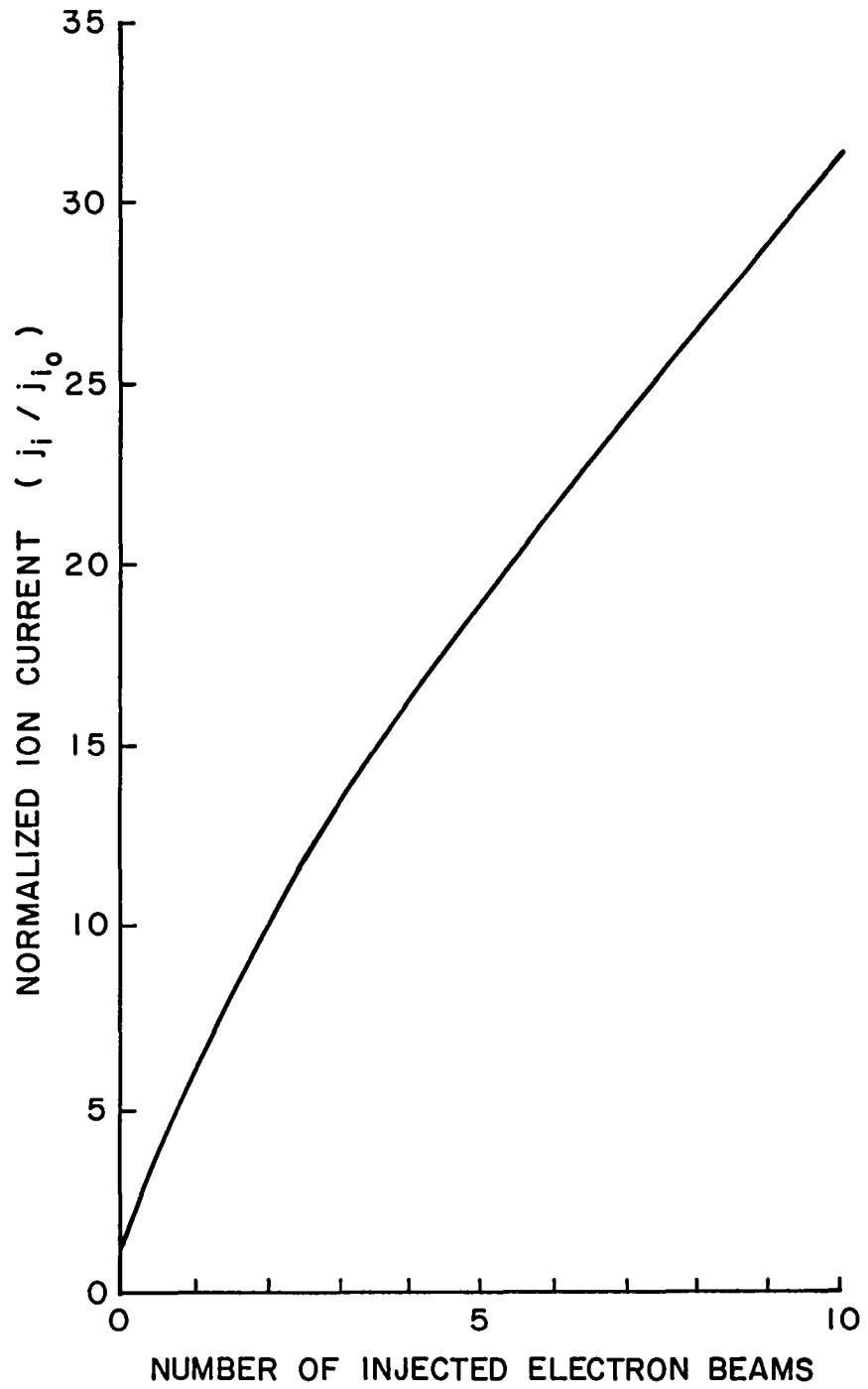
Fig. 9 Effect of Number of Optimally Injected Electron Beams
        on Extracted Ion Current

ten stages of injection are used. The normalized electron current density required for each injection stage at this optimized condition as a function of the number of injection stages is shown in Fig. 10. The greatest electron current densities are seen to be required for the first (lowest energy) stage regardless of the number injection stages used. The total electron current density required would be the sum of all of the values given by the curves that apply for the number of stages being used. For the cases of upstream electron injection investigated this value lies between 0.5 and 0.6 times the ion current and the square root of the extracted ion to injected electron mass ratio.

As an example consider the case of electron injection from the upstream side of the screen grid at two energies. In this case the potential, potential gradient and ion velocity profiles at the maximum extracted ion current density operating condition are exactly the same as those shown in Fig. 7 for the case of two injected electron groups, one injected from upstream of the grids and the other from between the grids. For the example where upstream injection of both beams is used, the maximum extracted ion current density is observed for

$$
\left.\begin{array}{l}
\alpha_1 = 0.42 \\
\\
\alpha_2 = 0.15
\end{array}\right\} \text{ from Fig. 10}
$$

$$
\left.\begin{array}{l}
\phi_1 = 0.4 \\
\\
\phi_2 = \phi_1^2 = 0.16
\end{array}\right\} \text{ from Eq. 45}
$$

At this condition the normalized ion current (j_i/j_{i_0}) from Fig. 9 is 11.7 and the total injected electron current has the same value as previously determined.

$$
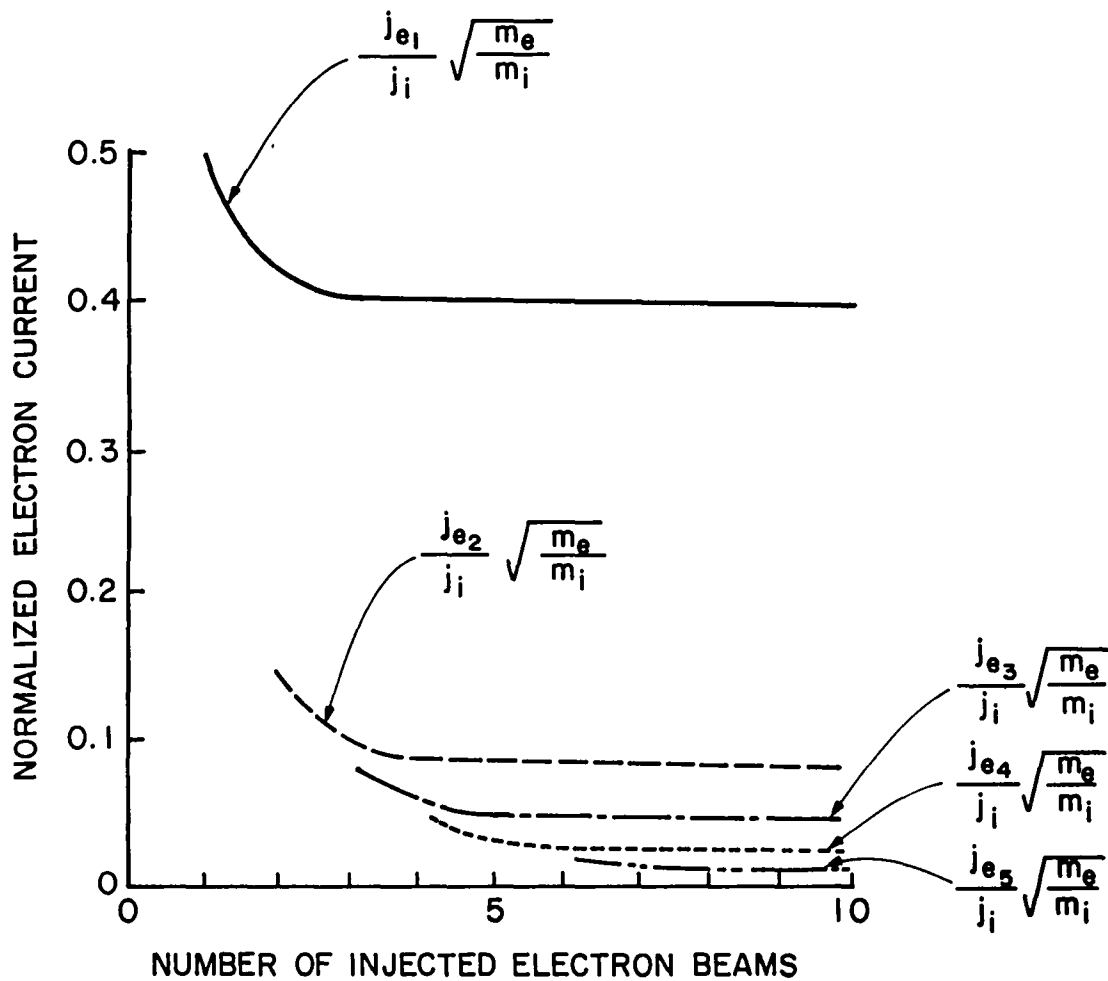\frac{j_e}{j_i} = (\alpha_1 + \alpha_2)\sqrt{\frac{m_i}{m_e}} = 0.57\sqrt{\frac{m_i}{m_e}}
$$

Fig. 10 Injected Electron Current Density Required to Yield the
Maximum Extracted Ion Current Density

Comparison of these results with those obtained previously for upstream injection of the primary electron beam (i.e. at ϕ_1) and intra-grid injection of the secondary one (i.e. at ϕ_2) shows that they are the same except for the fact that α_2 is 0.15 rather than 0.30 in the present case. This is simply a reflection of the fact that only half of the injected electron current density is required when upstream injection is used and the electrons pass through the space charge region twice rather than a single time.

It is appropriate to ask whether electron injection at a fraction of the optimum values given in Fig. 10 might not give substantial increases in extracted ion currents (i.e. a substantial fraction of the values shown in Fig. 9). The results shown in Fig. 11 suggest the answer to this question. In this figure the normalized extracted ion current is plotted against the normalized first stage of injected electron current for a typical electron injection case (three stages of injection with the second and third stages at optimal current densities). Unfortunately the figure shows that the ion current does not begin to increase substantially until the normalized electron current approaches its optimum value ($\sim$0.4 in this case). The figure also suggests one should just keep increasing the electron current above 0.4 to obtain still higher ion currents. It is however physically impossible to increase the electron current above the optimum value without inducing changes that alter the potential distribution between the grids in such a way that the normalized ion current decreases. Mathematically this is manifested in the equations by solutions for injected electrons current density that become imagainary.

It should be pointed out that while the analysis presented here has assumed the injected negative particle currents would be produced using electrons, the analysis is valid for negative ion injection. In this case the m_e appearing in the development would be the injected negative ions.
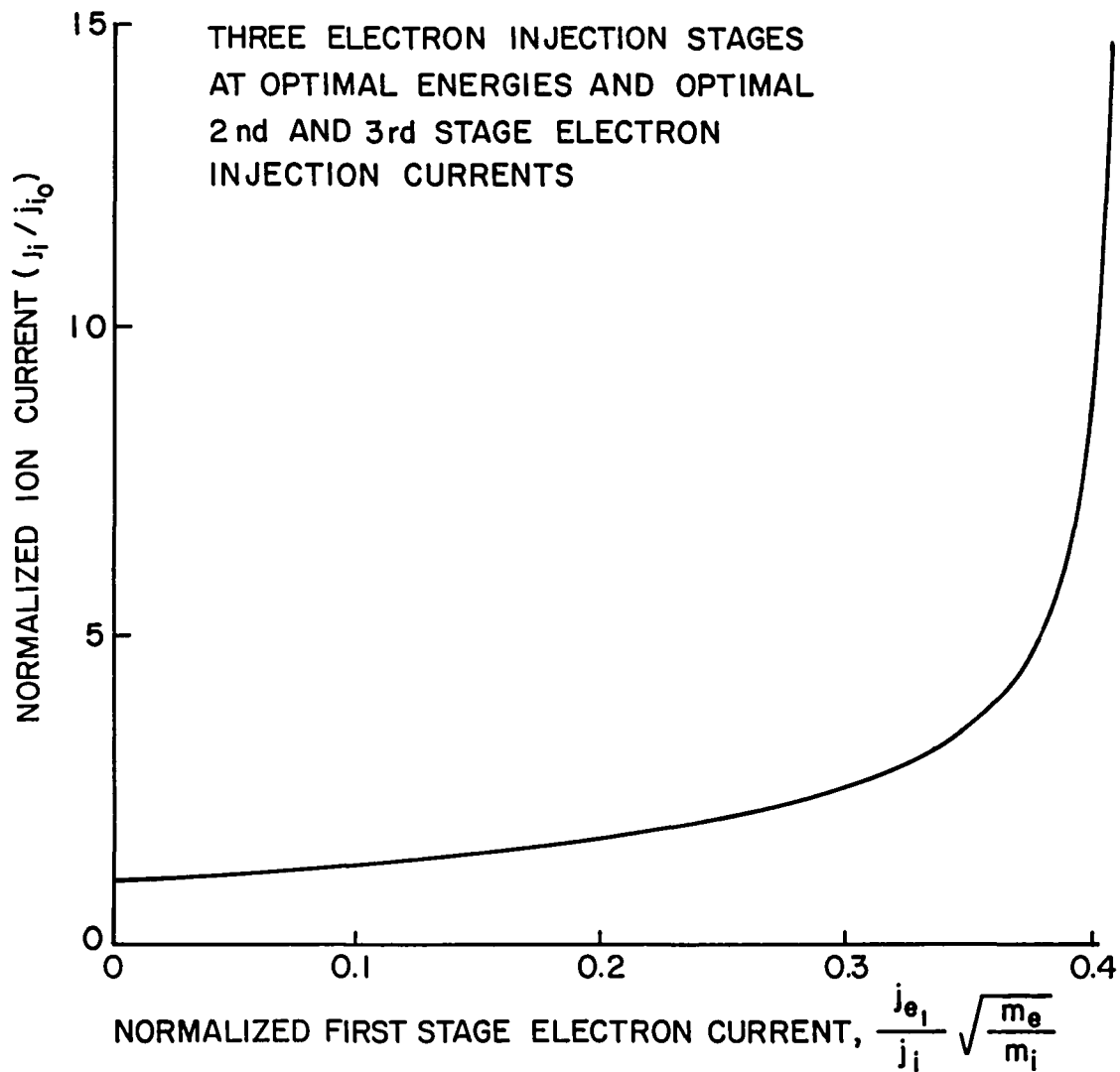
THREE ELECTRON INJECTION STAGES
AT OPTIMAL ENERGIES AND OPTIMAL
2nd AND 3rd STAGE ELECTRON
INJECTION CURRENTS

NORMALIZED ION CURRENT (j_i / j_{i_0})

NORMALIZED FIRST STAGE ELECTRON CURRENT, $\dfrac{j_{e_1}}{j_i} \sqrt{\dfrac{m_e}{m_i}}$

Fig. 11   Effect of First Stage Electron Injection Current
on Extracted Ion Current

Conclusions

The current density of a beam of charged particles being accelerated between two parallel plate electrodes can be increased substantially by injecting oppositely charged particles into the region between the electrodes. Multiple beams of oppositely charged particles can be used to produce the most substantial increases in the current density of the primary beam. The current density of this beam increases monotonically with the number of optimally selected, injected particle beams being used. There is an optimum injected particle current density and energy associated with each beam that yields the maximum primary beam current density for a given number of injection stages. It is perferable to inject the neutralizing particles from outside of the acceleration region rather than from within this region to minimize the required injected particle current densities. However either release of these particles in the acceleration region or injection with sufficient energy to carry them against an adverse electric field to the proper intra-grid potential produces the same solutions. The total required injected particle current density, regardless of the number of stages used, is of the order of the ion current density times the square root of the extracted ion-to-injected particle mass ratio. The primary beam current density that can be achieved decreases rapidly below its maximum value with small decreases in the injected particle current density below the optimum value. The fact that the extracted ion-to-injected particle mass ratio is high if electrons are the injected particle means that the injected particle electron current density would have to be very high for typical ion current densities. It is because they would have to be so high that the technique would probably be impractical for use in space propulsion applications. Negative ions could be injected and the required injected particle current density would decrease substantially. The required negative ion current

densities would however be comparable to the positive ion current densities produced in the beam for this case. Efficient production of such a beam however poses the same problem as generation of the positive ion beam that would be the objective of the final device. Recent experiments[10] suggest that these concepts are of interest however in ground based applications where power demand is a lesser concern.

THE ELECTROTHERMAL RAMJECT

Ben D. Shaw

In order to extend the practical uses of space for mankind it is de-
sirable (1) to reduce the cost for delivery of a payload into space from
earth, (2) to simplify the systems needed to make these launches and (3)
to improve their reliability. One system that holds some promise of
achieving these objectives involves the acceleration of a payload to a
sufficiently high velocity at the earth's surface so it would be able to
undergo passage through the earth's atmosphere and still have adequate
velocity to enable it to meet its mission objectives in space. One candi-
date propulsion system that has been analyzed and appears to hold promise
for use in such a launching scheme is the electrothermal ramjet.[11] It
appears to be capable of operation at the high thrust levels needed to
achieve the high launch velocities desired with a reasonably short launch
tube.

The concept of this launch scheme is illustrated in Fig. 12. To effect
the launch, propellant, preferrably a low molecular weight gas, would be dis-
tributed in the launch tube upstream of the projectile shown. This projec-
tile, which is also the payload, would be brought to an initial velocity
where efficient ramjet operation could begin by driving it with a light gas
gun driver.[11] At this point the projectile shown proceeding down the launch
tube in Fig. 12 would begin to process the propellant in the launch tube
through its annular intake diffuser. The diffused propellant would then
pass through a heat addition zone in the ramjet where energy would be added to
raise its stagnation temperature. Heat addition would be effected using either
electromagnetic energy radiated from pulsed lasers or directly deposited
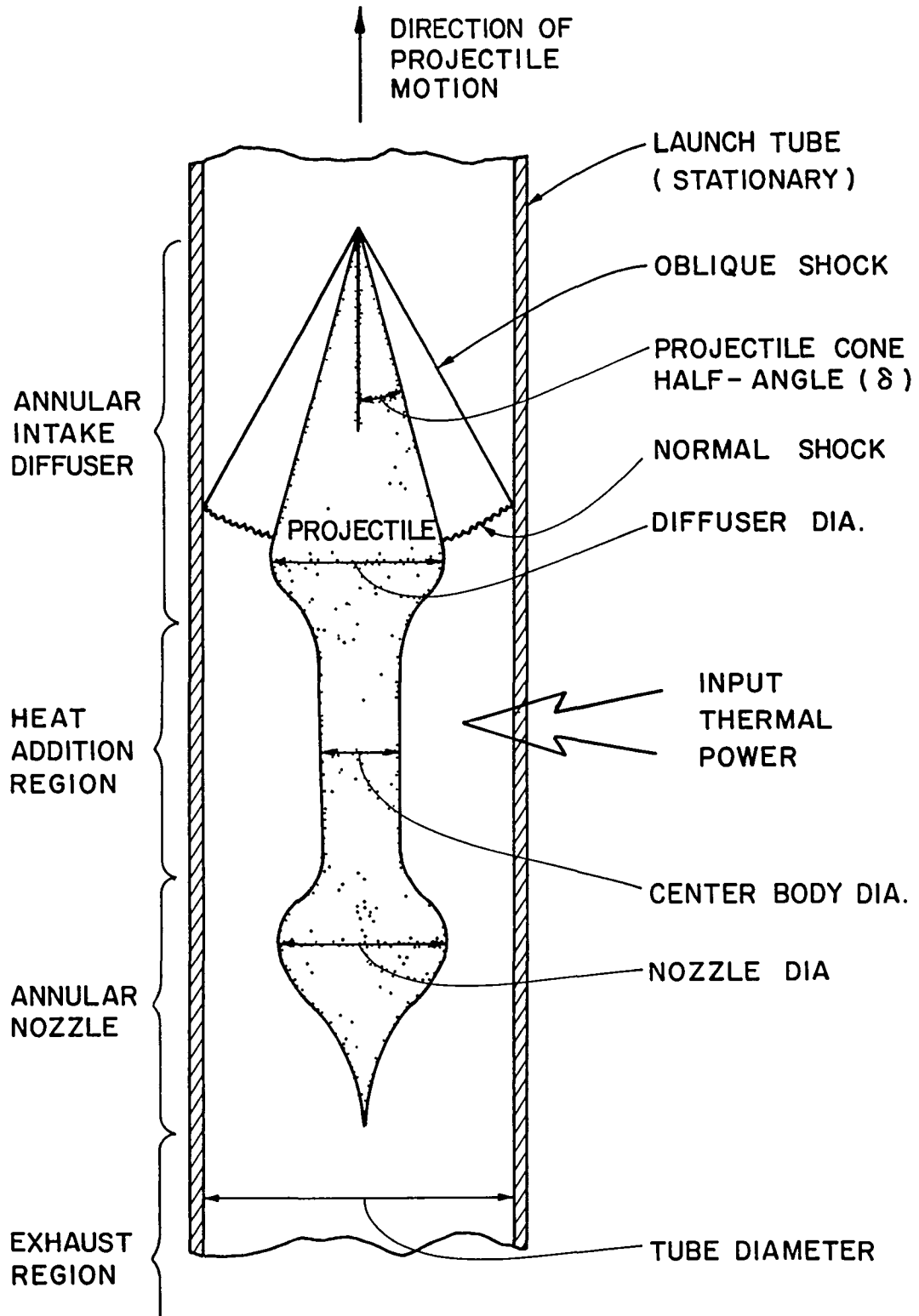energy from pulsed electrical discharges located along the tube wall.

Fig. 12 Electrothermal Ramjet Schematic

These devices would be triggered sequentially as the projectile passed down the launch tube. The heated propellant would then pass through the nozzle and would be expelled at a sufficiently high pressure and velocity to produce the desired thrust. The thrust level desired would actually be attained by adjusting the initial temperature and pressure of the propellant in the tube, the rate of heat addition to the propellant, and the ramjet geometry.

A preliminary analysis of this concept was conduced during the grant period and the results of this work were presented in the paper[11] inclued in Appendix A. In this work it was assumed that the diffusion process illustrated in Fig. 12 could be modelled as an isentropic one. It was recognized that this diffuser model was idealized and that the flow through the actual diffuser would encounter a system of shocks. The preliminary analysis based on the isentropic assumption suggested that the concept was workable and that reasonable energy utilization efficiences could be expected with it.

Theoretical Model of Diffuser Shock Losses

It was recognized that the diffusion process within an electrothermal plug ramjet (Fig. 12) would be non-isentropic because of shock losses. For this reason the first extension of the preliminary thermodynamic analysis of the electrothermal ramjet has been the incorporation of these losses. For supersonic operation a conical shock will either be attached to the nose of the projectile or a bow shock will be driven ahead of it. Which will occur depends on the velocity of the projectile and the geometric and boundary conditions associated with the flow. Of the two options the attached conical shock is preferrable because the stagnation pressure loss across a conical shock system is less than that across a bow shock seeing the same free stream flow. Consequently, flow conditions that enhance attachment of a conical

shock are desirable and a conical shock model has therefore been used in the analysis.

In order to incorporate shock losses into the complete analysis of the device, the flow conditions immediately downstream of the conical shock shown in Fig. 12 were first modelled. In an actual diffuser of the type shown, the attached conical shock would be followed by complex series of reflected shocks terminated by a normal shock. The location of this terminating normal shock would depend on the geometry of the device and the flow boundary conditions. Ideally the stagnation pressure loss associated with the initial conical shock and the series of reflected shocks will be less than that of a single conical shock terminated by a normal shock. However, a review of the literature on hypersonic wind tunnel diffusers (Ref. 12 for example) has shown that the actual stagnation pressure recovery that can be expected is very close to the stagnation pressure recovery prediced theorectically by assuming that all of the flow goes through the single conical shock followed by a normal shock. Because of this, the conical/normal shock model suggested in Fig. 12 was used in the analysis.

The thermodynamic properties of the working fluid will vary over the range of temperatures and pressures encountered during ramject operation primarily because of the effects of dissociation. For this analysis, however, it was desirable to avoid the complications of temperature and pressure dependent specific heats and gas constants. In addition, increases in propellant temperature predicted during ramjet operation are generally accompanied by corresponding increases in pressure. This being the case, it is not too unrealistic to use fixed values for the specific heats and the gas constant. The results contained in this analysis were obtained assuming ideal gas behavior and diatomic hydrogen was the working fluid. A gas constant (R)

of 4160 joules/kg°K and a ratio of specific heats (γ) of 1.4 were used. It is also noteworthy that the exhaust pressure for the device turns out to be quite high for the cases examined to date. This suggests that recombination rates in the exhaust will be high, that frozen flow losses will be small and this should also tend to make efficiencies computed using the ideal gas assumption reasonably accurate.

The model suggested in Fig. 12 implies an axi-symmetric (two-dimensional) conical flow field immediately downstream of the conical shock that must somehow be matched to the one-dimensional model used to describe the flow downstream of the normal shock. The marrying of these flow fields necessitated the development of an averaging procedure that provided single values of flow properties at the conical flow field exit for input into the one-dimensional normal shock relations. This was accomplished by determining a mass weighted average of each property using the mass, energy, and momentum conservation equations. Downstream of the postulated normal shock in the diffuser, all flow throughout the ramject was assumed to be well mixed and one-dimensional in nature. The flow exiting the diffuser passes through a constant area, frictionless passage where heat addition at a subsonic Mach number is assumed to occur. Next the flow passes through the nozzle where isentropic expansion to the maximum attainable supersonic Mach number is achieved under the constraint of the available exhaust area.

It is also assumed that the ramjet exhaust pressure can be maintained at that value dictated by the isentropic expansion through the nozzle. This static exhaust pressure required at the projectile base will vary with projectile position and control of its magnitude would have to be achieved in an actual device by proper design of the launch tube. Such a tube would consist of two sections, a cavity section into which propellant processed by the

ramjet would be collected and the launch section through which the projectile would pass. It has been assumed in this analysis that the cavity section would be designed to have the length and cross-sectional area needed to accommodate the propellant and to facilitate maintenance of the necessary projectile base pressure. While it seems possible to do this intuitively, the unsteady fluid mechanical analysis of this process has not yet been attemped.

The basic equations of fluid mechanics (conservation of mass and energy coupled with a thermodynamic path equation) were applied to all processes occurring within the ramjet. Solutions were obtained numerically. Propellant velocities were computed in the frame of reference of the moving projectile. The fact that the tube wall, which is the outer boundary to the flow, is moving in this frame of reference was assumed to have no effect on the flow behavior. This analysis assumes that the projectile has been accelerated to a high enough velocity before the initiation of ramject operation so that attachment of the conical shock to the diffuser nose is assured. Thrust was computed by applying the momentum equation in the frame of reference of the control volume moving with the projectile.

It should be noted that the boundary conditions associated with the annular flow ramjet are different than those associated with conventional ramjet operation. In the annular flow ramjet the inlet and outlet flow areas must be equal and the flow area in the heat addition zone must be less than this area. Further the ramjet inlet and outlet pressures will be different. For the conventional ramjet on the other hand the inlet, outlet and heat addition region flow areas are not constrained, but the inlet and outlet pressures must be equal.

Results for a Typical Supersonic Launch Cycle

In the analysis procedure that has been described it is assumed that the projectile will be acted upon by either the ramjet thrust or some externally applied force needed to produce the desired acceleration. As a result of this assumption the projectile trajectory is known. This in turn implies the projectile velocity is known and hence the propellant flow velocity into the ramjet diffuser is also known at each position along the launch track. In order to minimize the mechanical complexity of the projectile it has also been assumed that the projectile geometry remains fixed throughout the launch cycle. The diameter of the launch tube is allowed to vary as a function of axial position however so efficient ramjet operation can be achieved. Further, the present analysis requires that the flow through the ramjet is choked at the nozzle throat. While choking could occur at the diffuser throat rather than the nozzle throat, these two throat areas were selected so that choking would occur in the nozzle because this gave the best performance. Using the analysis one determines how the tube diameter and heat addition rate should vary so that a prescribed thrust can be maintained throughout the period of ramjet operation.

A typical case of electrothermal ramjet operation has been examined. In this case hydrogen propellant is placed in the launch tube at a pressure of 30 atmospheres and a temperature of 300°K. A 10 kg projectile having a 16 cm diffuser throat diameter (Fig. 12), an 8 cm center body diameter and a 16 cm nozzle throat diameter is used. These values were selected because they gave reasonable performance and were at the same time sufficient to ensure structural integrity during launch. It is also required that the thrust be sufficient to sustain the projectile at a constant acceleration level of 30,000 g until it reaches a final velocity of 15,000 m/sec.

The results of the analysis in which diffuser shock losses are included are compared to results obtained using an isentropic diffuser model in Fig. 13 for this particular case. Figure 13a shows how the projectile and exhaust velocities vary during the launch cycle. The projectile velocity (relative to the stationary launch tube) is observed to increase linearly with time as a consequence of the constant thrust and constant projectile mass that have been specified. The exhaust velocities (relative to the projectile) computed for the isentropic and non-isentropic cases are shown in Fig. 13a for times greater than 10 to 16 msec. Prior to these times, the conical shock would not attach, adequate thrust could not be produced regardless of the level of heat addition to the propellant, or the tube diameter became so large that the assumption of a one-dimensional flow model was seriously violated. During these initial phases a gun mode of operation would be required to accelerate the projectile to the velocities at which proper ramjet operation could be initiated. The parameter appearing in this figure (δ) is the half angle of the diffuser cone. A half angle of about 22.5° is observed to produce exhaust velocities that lie closest to the isentropic ones. At half angles greater or less than this value (5° and 45° are shown) the exhaust velocities are less at all times. The data of Fig. 13a show that $\sim$ 50 msec would be required to accelerate the projectile to a final velocity of 15 km/sec. This would require a launch tube about 400 m long.

Figure 13b indicates how the launch tube diameter would have to vary with time in order to maintain unity Mach number at the nozzle throat for these same isentropic and non-isentropic cases. It is important to hold the nozzle throat Mach number at unity to get the best performance from the device. If the tube diameter is less than the value indicated in the figure

a. VELOCITY PROFILES

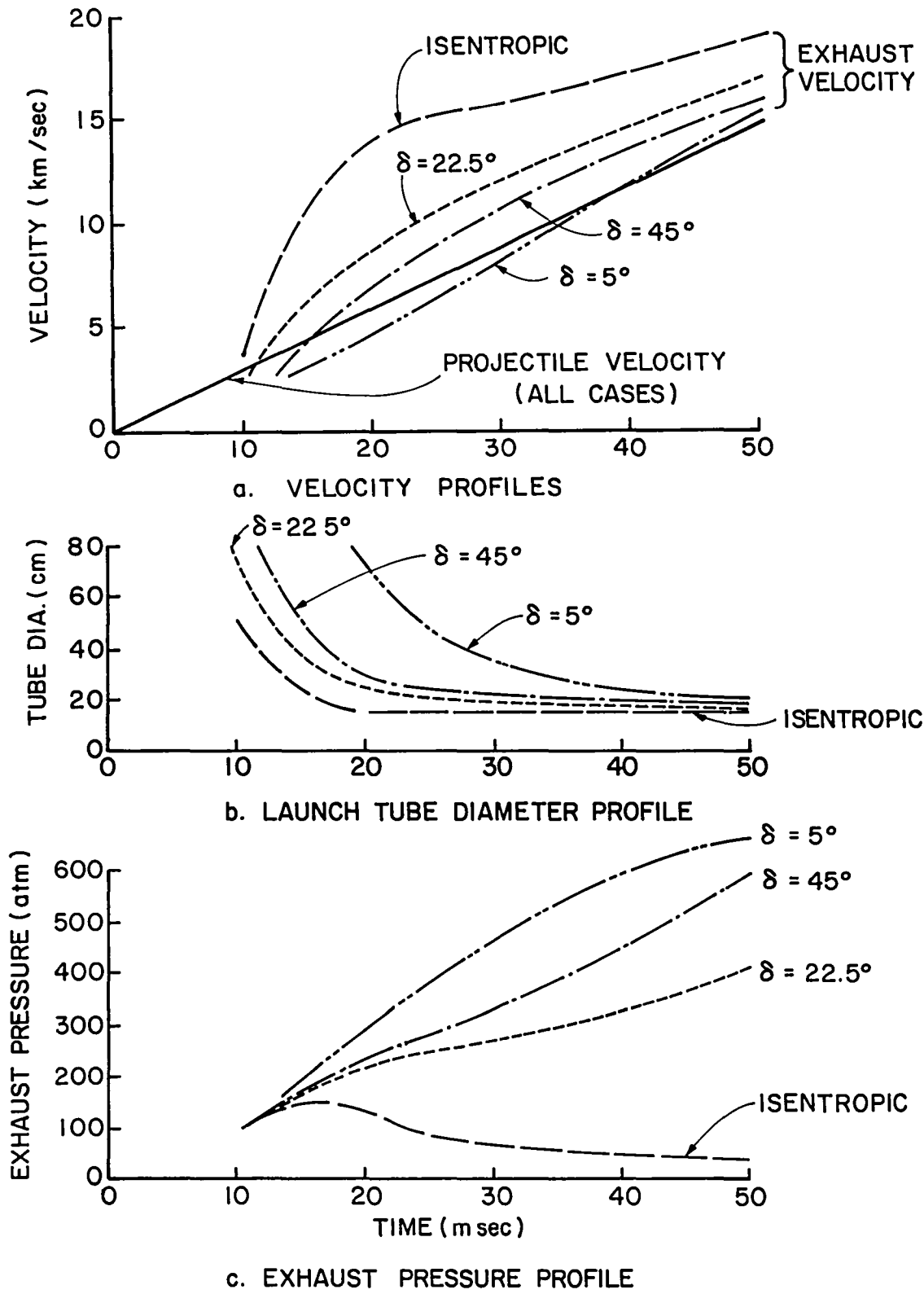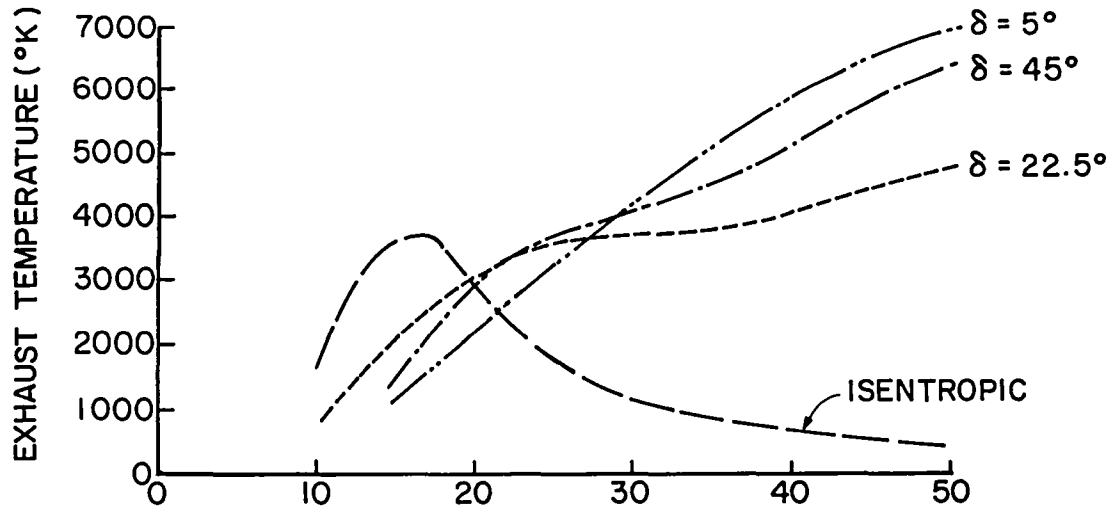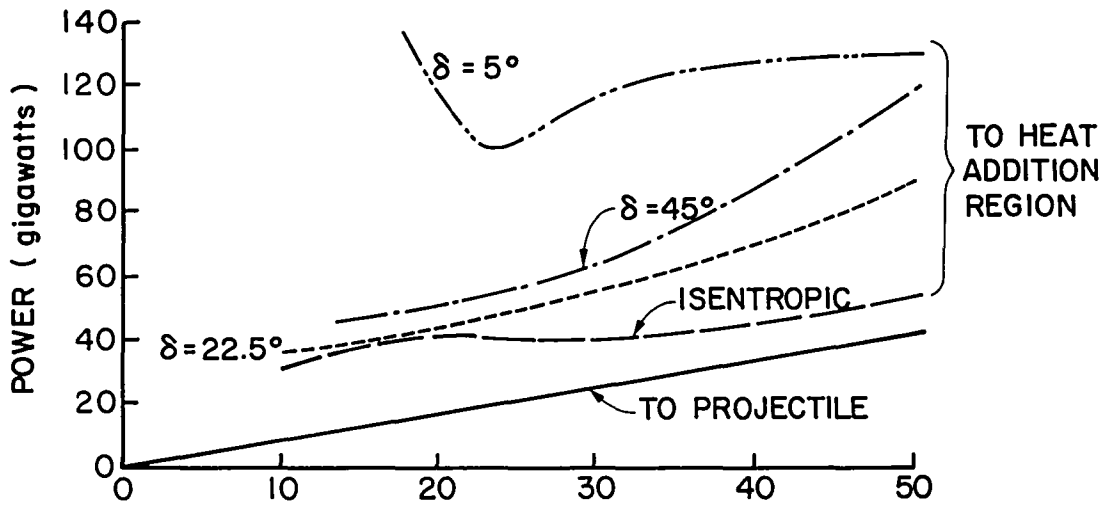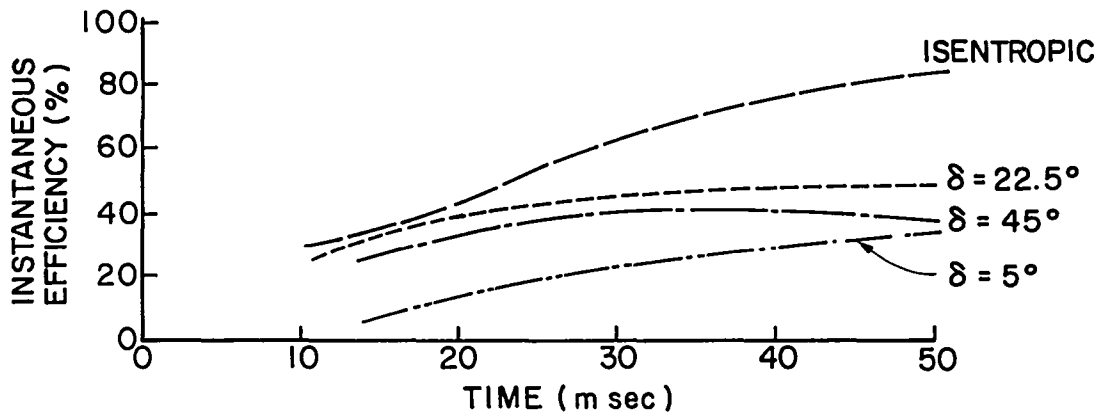b. LAUNCH TUBE DIAMETER PROFILE

c. EXHAUST PRESSURE PROFILE

Fig. 13   Typical Ramjet Launch Profile for a
10 kg Mass Accelerated at 30,000 g

d. EXHAUST TEMPERATURE PROFILE

e. POWER DEMAND PROFILE

f. EFFICIENCY PROFILE

Fig. 13 cont. Typical Ramjet Launch Profile for a
10 kg Mass Accelerated at 30,000 g

at a given time and all other input parameters are fixed, then the conical shock will detach and losses will increase. If the tube diameter is greater than this value the heat addition will be insufficient to maintain unity Mach number at the nozzle throat, the nozzle flow will go subsonic and poor ramjet efficiency will result. In the case of Fig. 13b one again observes that a diffuser cone half angle of 22.5° produces results that are closest to the isentropic ones.

Figure 13c illustrates the pressures required at the projectile base for the examples of ramjet operation being considered. The base pressures for the non-isentropic cases rise as the projectile travels down the launch tube. The non-isentropic cases are observed to exhibit higher exhaust pressure requirements over most of the launch sequence. Once again a diffuser cone angle of 22.5° yields conditions that approach the isentropic ones most nearly. It is of interest to note that at the beginning of ramjet operation, for each of the non-isentropic cases considered here the high projectile base pressure is the source of all of the required thrust, and the momentum change of the flowing propellant across the ramjet actually detracts from the thrust. As ramjet operation continues, the momentum change of the propellant begins to dominate the thrust, although not completely. For example, at the end of the operating period for the 22.5° cone angle device, $\approx$ 35% of the thrust is being provided by the pressure differential across the projectile, and $\approx$ 65% of the thrust is being provided by the momentum change of the propellant.

Figure 13d shows the temporal variation in propellant exhaust temperature that is induced by the heat addition profile shown in Fig. 13e. The temperatures and thermal input powers shown are high, but not excessive in light of the short launch times involved. The power going into the projectile is also shown in Fig. 13e and the ratio of this power to the thermal

input power at a given time is termed the instantaneous efficiency. This ratio is plotted as a function of time for the cases considered in Fig. 13f.

This figure shows that for the case under consideration the non-isentropic diffuser having a cone half angle of 22.5° again produces results closest to the isentropic ones. This suggests then that there is an optimum diffuser shape and that the optimum conical diffuser has a cone half angle of ∿ 22.5°. The isentropic efficiency is observed in Fig. 13f to be substantially greater than that for the best non-isentropic case (δ = 22.5°) over most of duration of the launch. The efficiency of the electrothermal ramjet equipped with this optimized realistic diffuser is however still very attractive. It exhibits an efficiency near the end of the launch of about 50% and the mean efficiency over the complete cycle beginning at 10 msec is observed to be greater than 40%. This efficiency is much greater than the efficiencies of chemical and light gas gun launchers and is competitive with efficiencies predicted for rail guns and mass drivers.

The reason why an optimum diffuser cone half angle is observed in the data of Fig. 13f can be understood by considering the fluid flow conditions associated with the limiting cone half angles (i.e. values of 0° and 90°). For the present model we are requiring subsonic heat addition so the flow in the diffuser section must pass through a normal shock wave at some location. For a specified incoming (free-stream) Mach number, each of these cones coupled with the diffuser, will produce identical stagnation pressure re-covery effects. The very shallow angle (∿ 0°) cone will produce a Mach wave at the diffuser entrance across which the Mach number of the flow remains constant. The flow will then enter the supersonic diffuser, where it must encounter a normal shock in order to reach the subsonic flows required in

the heat addition region. This means the stagnation pressure loss across the shock will correspond to the free-stream Mach number. The blunt cone will propagate a bow shock, which is essentially a normal shock, ahead of it. The bow shock will cause the flow entering the diffuser to become subsonic, and the stagnation pressure loss will again correspond to the free stream Mach number. This analysis has shown that a moderate cone half-angle (between 0° and 90°) and the corresponding conical shock coupled with a normal shock will produce more efficient stagnation pressure recovery than will either of these single normal shocks.

Conclusions

There is an optimum cone angle for the diffuser in an electrothermal ramjet which yields maximum energy efficiency. For a typical case considered here it is $\sim$ 22.5°. The efficiency of the electrothermal ramjet is degraded from the isentropic efficiency when account is taken for shock losses occurring in the diffuser. Overall energy efficiencies for a typical mission, where acceleration to 15,000 m/sec is effected, still lie in the very attractive range of 40 to 50% when these losses are considered.

CONSTANT PRESSURE ACCELERATION OF THE ELECTROTHERMAL RAMJET

Charles E. Mitchell

Introduction

No ramjet engine can operate efficiently until it has been accelerated to some minimum operational velocity. For the electrothermal ramjet system discussed in Reference 11 and elsewhere in this report this minimum operational speed is quite high. Preliminary calculations performed for a vehicle mass (m_r) of 10 kg, an acceleration rate (α) of 30,000 g, and employing diatomic hydrogen as the propellant indicated that this minimum speed could be as high as 5000 m/sec (Ref. 11). Although certain designs facilitate ramjet operation at considerably lower speeds it is assumed conservatively in the following analysis that the starting system would have to bring the ramjet to 5000 m/sec.

One method of obtaining speeds of this order in short time periods at acceleration levels of the order of those assumed for the electrothermal ramjet is acceleration in a light gas gun system. Devices of this type have been both analysed and constructed and are discussed in the literature (see for example Ref. 13). In what follows two acceleration systems based on the light gas gun concept will be described and analysed. Both systems are designed to produce a high level of constant acceleration (and therefore constant base pressure) for the ramjet. The mode of energy addition required to produce the acceleration is taken to be similar to that assumed for the ramjet mode of operation; that is, electrothermal in nature and controllable in time.

A general description of the acceleration process will be presented first. This will be followed by the analysis of an isentropic flow, piston

driven dual chamber device. This type of system is typical of previous light gas gun designs. Next a non-isentropic flow, single chamber design will be described and analysed. This latter device differs from conventional designs but appears attractive in the current application. Results of calculations for a specific example will be presented and the relative performance of the two designs compared.

Uniform Acceleration Flows - General Description

If a constant pressure is maintained at the rear surface of the ramjet then, in the absence of frictional effects, a constant acceleration of the ramjet vehicle will occur. (It can be pointed out in passing that available data (see Reference 14) indicate that frictional effects between the projectile (ramjet) and the launch tube should cause a decrease in velocity obtained of about 5%.) The basic problem is to devise a method by which a constant ramjet base pressure can be maintained. In Reference 11 a quasi-steady expansion was assumed so that all the gas in back of the ramjet (in the launch tube) was at a constant pressure during acceleration. The high pressure level necessary was to be maintained by heat addition. Since sound speeds of the order of 3000 m/sec and vehicle speeds up to 5000 m/sec are desired, it is clear that the quasi-steady approximation cannot be correct, and that the flow behind the ramjet is inherently unsteady.

One unsteady flow which does provide constant pressure at the ramjet is the flow which results if all fluid particles in back of the ramjet are accelerated uniformly. That is, the gas in back of the ramjet and the ramjet itself are accelerated as a solid body. Conceptually, this is the flow situation which would result if the ramjet and all the gas behind it began accelerating at the constant value α starting at some arbitrary time, say $t = 0$. The determination of the variation of the dynamic and thermo-

dynamic variables for this flow as a function of axial location x and time t is relatively straightforward.

Consider first the pressure-distance condition which must exist at t = 0. Since solid body acceleration is occurring, then for the gas in back of the ramjet it must be true that

$$\frac{dP}{dx_0} = -\rho\alpha \tag{46}$$

where P is local pressure, ρ local density and x_0 the axial distance along the tube at t = 0. This is of course, recognized as the usual gravitational equation with g replaced by α. If a property relationship between P and ρ is given (say isentropic or isothermal for example) then P as a function of x_0 along the tube axis could be found at t = 0. For later times the way in which the pressure must increase at any x location is determined by the uniform acceleration condition itself. For any fluid particle (and for the ramjet)

$$x = x_0 + \frac{\alpha t^2}{2} \tag{47}$$

where x is the instantaneous location of the particle and x_0 is its location at t = 0. Particle paths on an x, t diagram for the case where x_0 of the ramjet is zero, are shown in Fig. 14. Also, since the acceleration is uniform, the state of any fluid particle cannot change in time. That is

$$\frac{DP}{Dt} = 0, \quad \frac{Ds}{Dt} = 0, \quad \frac{D\rho}{Dt} = 0, \quad \frac{DT}{Dt} = 0 \tag{48}$$

where $\frac{D}{Dt}$ is the material derviative and T and s are temperature and entropy, respectively. From Eq. (47) the identity (x_0 value) of the fluid particle which passes location x at time t is immediately found as
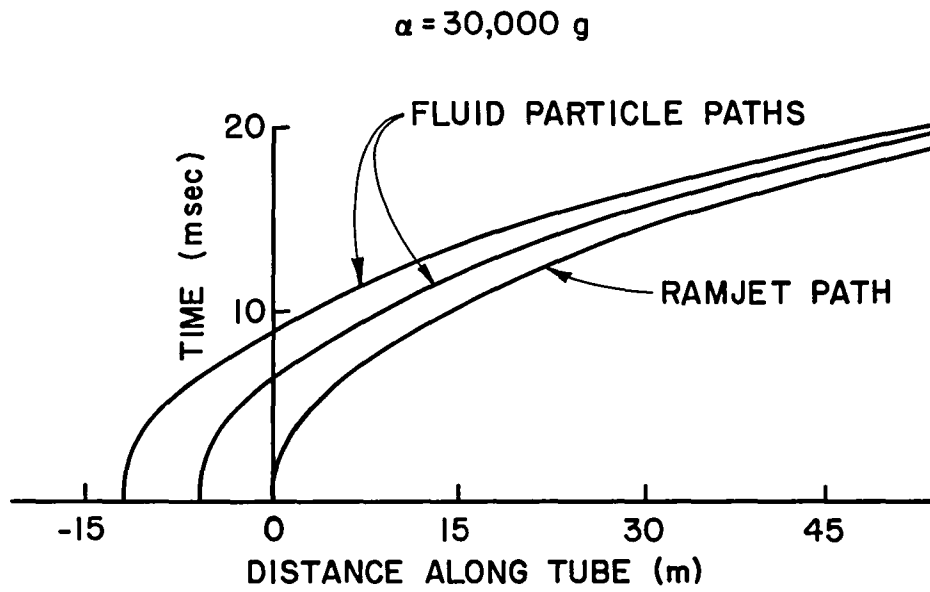
$$x_0 = x - \frac{\alpha t^2}{2} \tag{49}$$

$\alpha = 30,000$ g

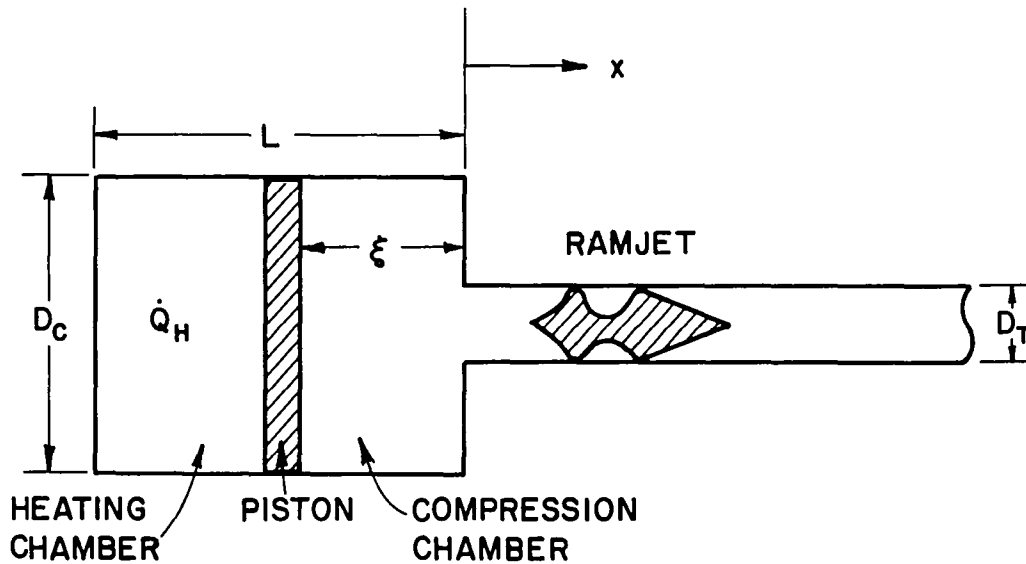
Fig. 14 Uniform Acceleration: Time vs. Distance

Fig. 15 Accelerator Design

Then, also,

$$\frac{dx_o}{dt} = - \alpha t \tag{50}$$

for any constant x location.

Combining Eqs. (50) and (46) gives

$$\frac{dP}{dt} = \alpha^2 \rho t \tag{51}$$

at any x station along the tube. Also at any x station

$$u = \alpha t \quad . \tag{52}$$

In order to integrate Eq. (51) a statement which relates P to ρ along the line t = 0, and permits the integration of Eq. (46) must be given, that is

$$P_o = P_o(\rho_o) \quad . \tag{53}$$

Since the pressure and density of every fluid particle remain constant for $t \geq 0$, then Eq. (53) is valid for all times

$$P = P(\rho) \quad . \tag{54}$$

Integration of Eq. (51) using Eq. (54), and application of Eq. (52) permits the specification of all thermodynamic and dynamic variables at any x location in the uniformly accelerating flow as a function of t.

The practical importance of such a specification to the ramjet acceleration problem can be seen as follows. If the ramjet is located at x = 0 at t = 0 and if P, u, ρ etc., take the values required by Eqs. (51) - (54) along x = 0 then the flow field for $x \geq 0$, $t \geq 0$ will be a uniform acceleration flow field. This means that if a flow with the required physical parameters at x = 0 can be <u>supplied</u> to the tube at x = 0 starting at t = 0 then a constant pressure acceleration of the ramjet will occur. In practice this could be

achieved through the use of a large diameter driving chamber attached to the launch tube at x = 0. Appropriate variation of pressure and density in the driving chamber (by piston motion or heat addition for example) would then give the required values of P, ρ, and u at x = 0. Two specific designs for providing the required parameters at x = 0 have been considered. The first of these, a dual chamber piston driven accelerator, will be discussed next.

Piston Driven Isentropic Accelerator

A sketch of this device is shown in Fig. 15. The general acceleration sequence would occur as follows. First, with the ramjet held at x = 0 the pressure in the compression chamber would be raised to the value required for the desired acceleration level. For an acceleration of α, this pressure would be

$$P_c = P_{oo} = \frac{m_r \alpha}{A_T} \tag{55}$$

where P_{oo} is the pressure at x = 0 and t = 0, m_r is the ramjet mass, A_T is the launch tube cross sectional area and P_c is the compression chamber pressure. The ramjet would then be released and the solution of Eqs. (51) to (54) would specify the required conditions at x = 0. These would be met through appropriate motion of the piston which would in turn be effected by heat addition in the heating chamber. This would continue until the ramjet reached its operational speed. A complicating factor is the possibility of choking the flow at x = 0. This will be discussed below.

Since the heat addition occurs in gas which is physically separated from the gas which will enter the launch tube, it is reasonable to assume that all gas entering the tube has the same entropy value and that the flow field in both the compression chamber and launch tube is homentropic (constant entropy everywhere). If in addition the gas is taken to be

perfect (ideal gas with constant specific heats) then the conditions at
x = 0 can be expressed in closed form as functions of time, as can the
heat addition rate in the heating chamber. It will also be assumed that
the diameter of the compression chamber is large compared with that of the
launch tube so that the properties in the compression chamber are constant
in space except for a negligibly thin acceleration region which connects
the chamber to the tube and which can be taken to the quasi-steady. Finally,
the mass of the piston and the friction associated with its motion are
neglected.

In solving the problem thus posed it is convenient to define the
following dimensionless variables

$$\bar{P} = P/P_{00} \quad , \quad \bar{\rho} = \rho/\rho_{00} \quad , \quad \bar{T} = T/T_{00} \quad , \quad \bar{t} = \frac{\alpha t}{a_{00}}$$

$$\bar{x} = \frac{\alpha x}{a_{00}^2} \quad , \quad \bar{\dot{Q}}_H = \frac{\dot{Q}_H}{P_{00} a_{00} A_c} \quad , \quad \bar{L} = \frac{\alpha L}{a_{00}^2} \quad , \quad \bar{\xi} = \frac{\alpha \xi}{a_{00}^2}$$

$$\bar{u} = \frac{u}{a_{00}} \quad , \quad \bar{a} = \frac{a}{a_{00}}$$

where the subscript oo indicates a quantity evaluated at x = 0 and t = 0,
$a_{00} = \sqrt{\gamma R T_{00}}$ is the reference state sound speed and γ and R are the ratio
of specific heats and gas constant, respectively.

The isentropic condition then gives

$$\bar{P} = \bar{\rho}^{\gamma} \tag{56}$$

which is a special case of Eq. (54). Using this relationship and non-
dimensionalizing Eq. (51) becomes

$$\frac{d\bar{P}}{d\bar{t}} = \gamma \left(\bar{P}\right)^{\frac{1}{\gamma}} \bar{t} \quad . \quad (x = 0) \tag{57}$$

Integrating, and using the ideal gas law, $\bar{P} = \bar{\rho}\,\bar{T}$, gives at x = 0
(superscript o)

$$\overline{P}^0 = \left[1 + \frac{(\gamma-1)}{2} \overline{t}^2 \right]^{\frac{\gamma}{\gamma-1}}$$ (58a)

$$\overline{\rho}^0 = \left[1 + \frac{(\gamma-1)}{2} \overline{t}^2 \right]^{\frac{1}{\gamma-1}}$$ (58b)

$$\overline{T}^0 = 1 + \frac{\gamma-1}{2} \overline{t}^2$$ (58c)

$$M^0 = \frac{\overline{u}}{\overline{a}} = \frac{\overline{t}}{[(\gamma-1)\overline{t}^2/2 + 1]^{\frac{1}{2}}} \quad \text{(Mach Number)}.$$ (58d)

Equation (58d) can be solved for $\overline{t}*$, the dimensionless time at which $M^0 = 1$. The result is

$$\overline{t}* = \left\{ \frac{2}{(3-\gamma)} \right\}^{\frac{1}{2}} .$$ (59)

Clearly, the solution as outlined above is only valid to this point. However, it must take some time for the information that the flow has choked to reach the ramjet. That is, there must be a period of time after $\overline{t} = \overline{t}*$ during which the ramjet will continue to accelerate at α with a base pressure P_{00}. The exact value of the time involved is determined by the intersection of the right running characteristic emanating from $\overline{x} = 0$, $\overline{t} = \left[\frac{2}{3-\gamma} \right]^{\frac{1}{2}}$, with the ramjet path on the $\overline{x}$, $\overline{t}$ plane. Without giving the details (see Ref. 14 for example) the resulting intersection time is

$$\overline{t}_{max} = \frac{(\gamma+1) \left[\frac{2}{3-\gamma} \right]^{\frac{1}{2}} - 2}{(\gamma-1)} .$$ (60)

This is the maximum time that the ramjet can experience uniform acceleration and constant base pressure, under the assumptions made here.

If the gas in the tube and compression chamber is assumed to be hydrogen, some numerical calculations can be made to assess the importance of the maximum acceleration time condition. For hydrogen, $\gamma = 1.4$ and thus $\overline{t}* = 1.118$ and $\overline{t}_{max} = 1.708$. Since $\overline{u}_{max} = \overline{t}_{max}$, and $u_{max} = \overline{u}_{max} a_{00}$, an estimate

of the T_{oo} necessary to reach a certain u_{max} in time t_{max} can be made.

For hydrogen this relationship is $T_{oo} = \left[\frac{u_{max}}{130.3}\right]^2$. If u_{max} is the conservatively high value of 5000 m/sec then $T_{oo} = 1472°K$. This temperature does not seem unreasonably high. Moreover, the maximum temperature which would occur would be at $\bar{t} = \bar{t}^*$ when $T_{max} = 1840°K$. If it is desirable or necessary to operate at lower temperatures and still reach 5000 m/sec, it is possible to accelerate the ramjet in a non-uniform fashion after $\bar{t} = \bar{t}_{max}$. The nature of the flow field in the tube after $\bar{t} = \bar{t}^*$ is, of course, non-uniform and must be determined using the method of characteristics. Solutions indicate nearly uniform acceleration at the ramjet can still be achieved by appropriate tailoring at $x = 0$ (see Ref. 15). For the purpose of the present analysis, the temperature condition will be taken as not overly restrictive and the $\bar{t}$ of interest will be taken to be $\bar{t} \leq \bar{t}_{max}$.

The values of $\bar{P}$, $\bar{\rho}$ and $\bar{T}$ as given by Eqs. (58a, b, c) lead through the quasi-steady assumption and the isentropic perfect gas relationships, to the following expressions for $\bar{T}_c$, $\bar{\rho}_c$, $\bar{P}_c$, the non-dimensional temperature, density and pressure in the compression chamber

$$\bar{T}_c = 1 + (\gamma-1)\ \bar{t}^2 \tag{61a}$$

$$\bar{\rho}_c = \left[1 + (\gamma-1)\ \bar{t}^2\right]^{\frac{1}{\gamma-1}} \tag{61b}$$

$$\bar{P}_c = \left[1 + (\gamma-1)\ \bar{t}^2\right]^{\frac{\gamma}{\gamma-1}}. \tag{61c}$$

The ideal gas law written for the compression chamber is

$$P_c\ \xi\ A_c - m_c\ R\ T_c \tag{62}$$

where m_c is the mass of hydrogen in the compression chamber at any instant and ξ is the instantaneous length of the compression chamber (see Fig. 15). Also the quasi-steady outflow at $x = 0$ implies that

$$\frac{dm_c}{d\bar{t}} = -\bar{\rho}^0 \ \bar{u}^0 = -\left[1 + \frac{-1}{2} \ \bar{t}^2\right]^{\frac{1}{\gamma-1}} \bar{t} \ . \tag{63}$$

Combination of Eqs. (62) and (63) leads after some manipulation to the following expression for $\bar{\xi}$, the non-dimensional compression chamber length

$$\frac{\bar{\xi}}{\bar{\xi}_0} = \frac{1 + \frac{1}{\gamma} \frac{A_T}{A_c} \frac{1}{\bar{\xi}_0}\left\{1 - (1 + \frac{\gamma-1}{2} \ \bar{t}^2)^{\frac{\gamma}{\gamma-1}}\right\}}{\left[1 + (\gamma - 1) \ \bar{t}^2\right]^{\frac{1}{\gamma-1}}} \ . \tag{64}$$

ξ_0 is the compression chamber length at t = 0. It is related to the final clearance length in the compression chamber which exists at $\bar{t} = \bar{t}*$. For example, if $\gamma = 1.4$, $\frac{A_T}{A_c} = \frac{1}{16}$, and $\bar{\xi} \to 0$ at $\bar{t} = \bar{t}*$, then $\bar{\xi}_0 = 0.0528$. This corresponds to $\xi = 1.540$ m if u_{max} is 5000 m/sec. The quantity $|\frac{d\bar{\xi}}{d\bar{t}}|$ is the non-dimensional piston speed. For the example just discussed $|\frac{d\bar{\xi}}{d\bar{t}}|$ takes a maximum value of 0.0622 which corresponds to a piston speed of about 183 m/sec for u_{max} = 5000 m/sec. The piston speed is thus quite small compared with the sound speed in the chamber ($\sim$ 3000 m/sec and the maximum ramjet velocity $\sim$ 5000 m/sec). This suggests that the assumption of uniform pressure, temperature and density in the compression chamber is probably not unreasonable.

Several methods for producing piston motion of the type required by Eq. (64) have been suggested in the literature (Ref. 15). In the present analysis it will be assumed that energy can be added to the heating chamber behind the piston by electric discharge or laser addition methods similar to those envisioned for the electrothermal ramjet itself. In particular it will be assumed that the rate of energy addition can be controlled closely enough to meet the requirements of the piston motion presented above. The necessary heat addition profile can be determined from application of the first law of thermodynamics to the heating chamber. This is

$$\overset{\circ}{Q}_H - \overset{\bullet}{W}_H = \frac{dU_H}{dt} \tag{65}$$

where $\overset{\bullet}{Q}_H$ is the required heat addition rate, $\overset{\bullet}{W}_H$ is the power necessary to move the piston as required by Eq. (64), and $\frac{dU_H}{dt}$ is the rate of energy storage in the gas in the heating chamber.

If the piston is massless and frictionless (these effects can be shown to be relatively small) then

$$\overset{\bullet}{W}_H = - P_H \frac{d\xi}{dt} A_C = - P_C \frac{d\xi}{dt} A_C \tag{66}$$

with $\frac{d\xi}{dt}$ determined from Eq. (64), while

$$\frac{dU_H}{dt} = m_H C_v \frac{dT_H}{dt} \tag{67}$$

where m_H is the (constant) mass of gas in the heating chamber and C_v is the specific heat at constant volume for the same gas. Application of the ideal gas law and substitution of Eqs. (66) and (67) into Eq. (65) gives after some rearrangement

$$\bar{Q}_H = \frac{\overset{\bullet}{Q}_H}{P_{oo} a_{oo} A_C} = \frac{\gamma}{\gamma-1} \left\{ \frac{A_T}{A_C} \left[1 + \frac{\gamma-1}{2} \bar{t}^2 \right]^{\frac{1}{\gamma-1}} + 2\bar{L} \left[1+(\gamma-1) \bar{t}^2 \right]^{\frac{1}{\gamma-1}} \right\} \bar{t} \tag{68}$$

where $\bar{L} = L \frac{\alpha}{a_{oo}^2}$ and L is the combined length of the compression and heating chambers (see Fig. 15). The value of L is somewhat arbitrary, though it does have an impact on the temperature rise in the heating chamber. This is readily seen upon application of the ideal gas law to the gas in the heating chamber. This gives

$$\frac{T_H}{T_{Ho}} = \frac{P_H}{P_{Ho}} \frac{(L-\xi)}{(L-\xi_o)} = \frac{P_C}{P_{Co}} \left[\frac{L-\xi}{L-\xi_o} \right] \tag{69}$$

If $\xi = 0$ at $\bar{t} = \bar{t}^* = 1.118$ then

$$\frac{T_H{}^*}{T_H} = 4.133 \frac{L}{L-\xi_o} \qquad . \tag{70}$$

It is clear from either Eqs. (69) or (70) that small values of L lead to large temperature rises. The maximum value of T_H, $T_H{}^*$ still depends on T_{Ho}. Since T_{Ho} need not be equal to T_{oo} a separate control on the maximum temperature is possible beyond that implied by the choice of L. In the numerical results to be presented shortly, L was taken quite arbitrarily to be $2\xi_o$. This means that at t = 0 the driving chamber is separated into two equal volumes by the piston. Other choices of L would lead to higher or lower values of T_H for the same T_{Ho}. As will be pointed out later the choice of L also affects the performance of the device as far as energy conversion efficiency is concerned.

The efficiency of the accelerating process at any instant of time can be measured by the ratio of the rate of change of the kinetic energy of the ramjet vehicle to the rate of heat addition to the heating chamber $\dot{Q}_H$. The rate of change of the kinetic energy of the ramjet is

$$\frac{d\left(m_r u^2/2\right)}{dt} = m_r u\frac{du}{dt} = m_r \alpha^2 t = m_t \alpha a_{oo} \bar{t} = P_{oo} A_t a_{oo} \bar{t} \quad .$$

Thus, using Equation (68)

$$\eta = \frac{\dfrac{d\left(m_r u^2/2\right)}{dt}}{\dot{Q}_H} = \frac{\gamma-1}{\gamma} \left[\left[1 + \frac{\gamma-1}{2}\bar{t}^2\right]^{\frac{1}{\gamma-1}} + 2\bar{L} \frac{A_C}{A_T} \left[1+(\gamma-1)\bar{t}^2\right]^{\frac{1}{\gamma-1}} \right]^{-1} \quad . \tag{71}$$

The dependence of η on $\bar{t}$ for γ = 1.4, $\frac{A_C}{A_T}$ = 16, $\bar{L} = 2\bar{\xi}_o$ = 0.1056 (L = 3.08 m) is shown in Fig. 16. The maximum efficiency is seen to be about 0.065 at $\bar{t}$ = 0. The efficiency decreases with increasing $\bar{t}$ and drops to 0.026 at $\bar{t} = \bar{t}^*$ = 1.118, the end of the heat addition period. These values can be compared with the equilibrium, constant pressure expansion value of $\frac{\gamma-1}{\gamma}$ = 0.286,
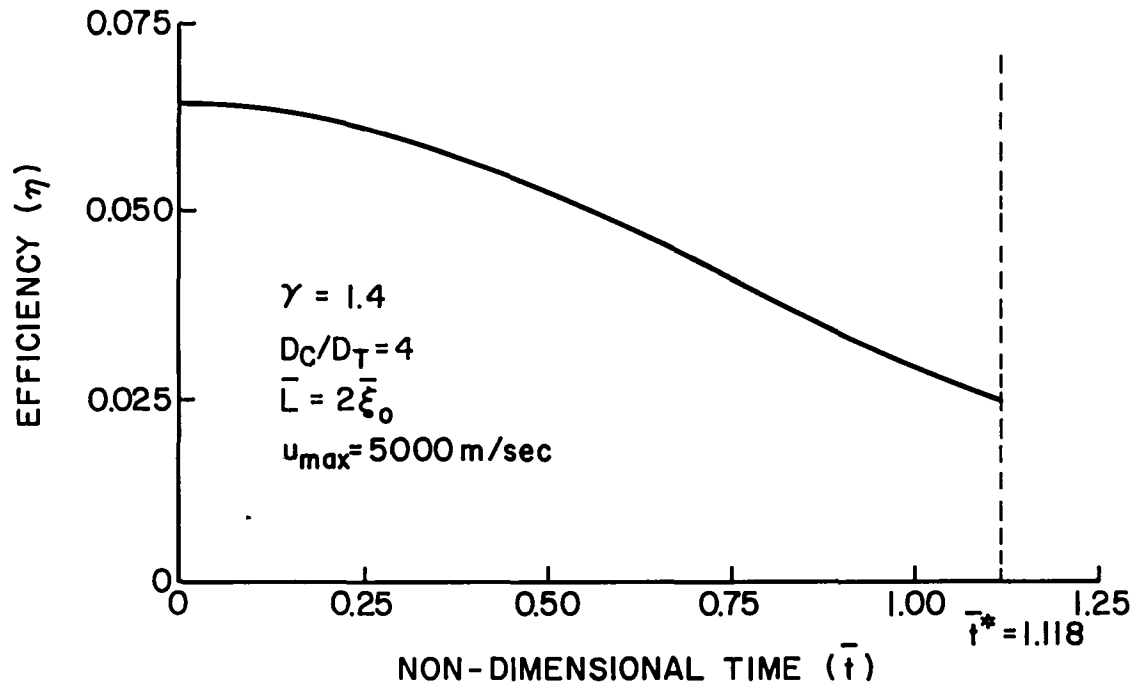
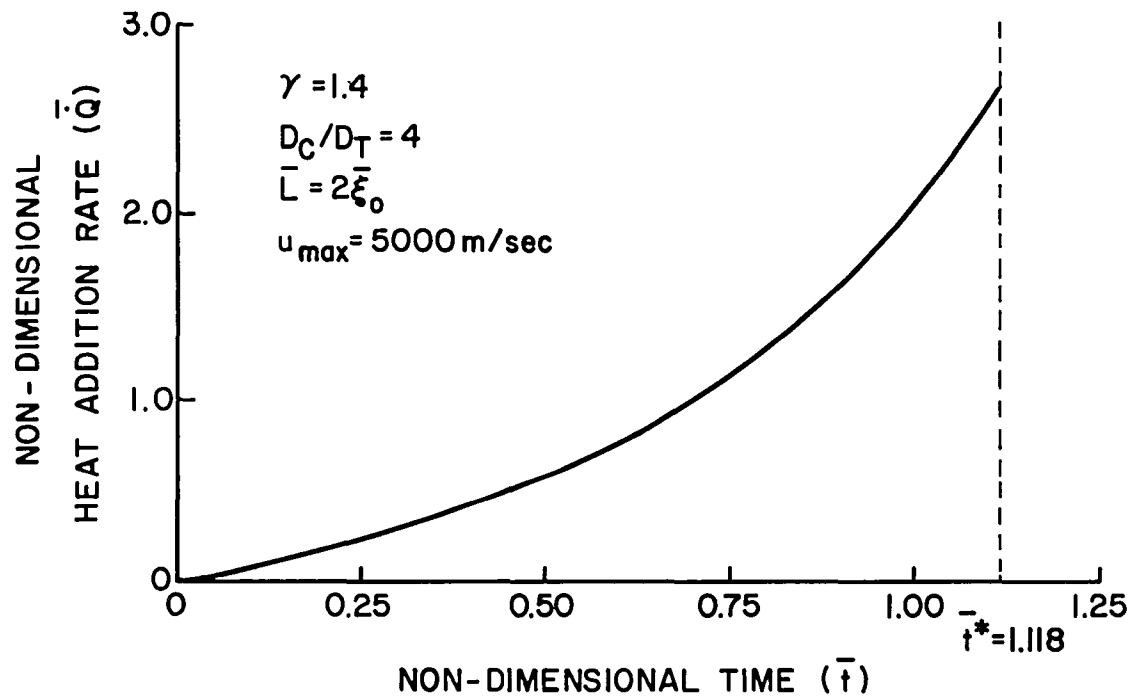Fig. 16 Efficiency of Piston Driven Accelerator

Fig. 17 Rate of Heat Addition: Piston Driven Accelerator

which could be realized if the ramjet were accelerating slowly (this is the value used in Reference 11). The factor multiplying $\frac{\gamma-1}{\gamma}$ in Equation (71) can thus be considered to be the loss incurred because of the unsteady acceleration process occurring in the piston driven device. Physically this loss can be traced to the fact that the pressures in the compression chamber and heating chamber must be maintained at values increasingly larger than P_{oo}, the pressure at the base of the ramjet, as time increases.

The effect of $\bar{L}$ on efficiency (η) can be seen in Eq. (71). Increasing values of $\bar{L}$ decrease efficiency through the second term in brackets. There is a limit on how small $\bar{L}$ can be. If $\bar{L} = \bar{\xi}_0$ (i.e. no heating chamber volume) then η at $\bar{t} = 0$ would increase to 0.106 and to 0.045 at $\bar{t} = 1.118$. Of course this represents an impossible situation physically, since, as can be seen from Eq. (70) that $T_H \rightarrow \infty$ if $\bar{L} \rightarrow \bar{\xi}_0$. The choice $\bar{L} = 2\bar{\xi}_0$ gives $\frac{T_H^*}{T_{Ho}} = 4.13$, still a substantial temperature rise. In general, relatively modest increases in efficiency can be obtained at the cost of large increases in $\frac{T_H^*}{T_{Ho}}$.

The heat addition rate ($\bar{\dot{Q}}_H$) as a function of time ($\bar{t}$) is shown in Fig. 17. From this figure it can be seen that the heat addition rate is nonlinear in time and must increase more and more rapidly as the acceleration process progresses. The maximum power required for accelerating a 10 kg ramjet to 5000 m/sec would be 370 gigawatts (at $\bar{t} = 1.118$).

An overall efficiency for the acceleration process can be defined as the ratio of the kinetic energy of the ramjet to the total amount of heat added to the heating chamber. Thus

$$\eta_0 = \frac{m_r u_r^2/2}{\int_0^t \dot{Q}_H dt} = \frac{(\gamma-1)}{2} \left[\frac{\bar{t}^2}{(1+\frac{\gamma-1}{2}\bar{t}^2)^{\frac{\gamma}{\gamma-1}} + \bar{L}\frac{A_C}{A_T}(1+(\gamma-1)\bar{t}^2)^{\frac{\gamma}{\gamma-1}} - (1+\bar{L}\frac{A_C}{A_T})} \right]. \quad (72)$$

Equation (72) is valid for any time, $\bar{t}$. However it must be remembered that for $\bar{t} \leq \bar{t}^* = 1.118$, $\bar{Q}_H = 0$. That is, once the flow chokes at $\bar{x} = 0$, the power to the heating chamber can be cut off while the ramjet continues at constant acceleration until $\bar{t} = 1.708$. The period from $\bar{t} = 1.118$ to $\bar{t} = 1.708$ thus represents a "free" acceleration period during which the over-all efficiency continually increases (and η is ∞). At $\bar{t} = \bar{t}^* = 1.118$ the overall efficiency (η_0) is 0.0386. At $\bar{t} = \bar{t}_{max}$ this efficiency reaches 0.0901. This last value represents the overall efficiency for the complete acceleration process. During ramjet mode operation, the efficiency of energy conversion remains above 40%, even considering shock losses. Consequently, it seems that once the ramjet can begin operation it is to be much preferred over the piston driven device just described as a mass accelerator.

Pistonless Single Chamber Accelerator

In the accelerator design discussed above a separation of the heating chamber from the isentropic compression chamber by a piston was assumed. This is consistent with the practice common in high velocity light gas gun design. The question arises as to what would happen if the piston were simply removed and both heating and compression occurred in a single chamber. Certainly a measure of design simplification would result. What would be the effect on efficiency?

In attempting to answer this question, the first thing which becomes clear is that the analysis of the problem is considerably more difficult mathematically. This is because the unsteady gasdynamic flow in the system can no longer be modelled as a constant entropy (homentropic) flow. In general each fluid particle in both the chamber and the tube will have a different entropy value associated with it since it is generated in the heating chamber at a different entropy. However, there is no reason to

expect that the entropy of each particle, once generated, might not remain

constant. That is, it seems reasonable to assume that $\frac{Ds}{Dt} = 0$, as before,

for x > 0. The solution for the flow field downstream of x = 0 still

poses a difficult problem in the method of characteristics, one that cannot

apparently be solved in closed form, but that is amenable to numerical

techniques (see Ref. 16). This solution has not yet been attempted. However,

a reasonable estimate of the performance of the single chamber design, based

on the uniform acceleration model discussed earlier, can be made.

As before, it is assumed that a solid body type acceleration of the gas

and ramjet occurs starting from t = 0 with the ramjet at x = 0. That is, it

is assumed Eqs. (46) to (54) apply. The basic physical design of the accel-

erator is also similar. Referring to Fig. 15, removal of the piston leads

simply and immediately to the design we wish to consider. The parameter L

now represents the heating chamber length, ahile ξ has no significance. The

ratio of A_C to A_T will be taken to be large as in the dual chamber design

so that a quasi-steady isentropic (not homentropic!) flow field connects the

heating chamber with the launch tube.

Because of the homentropic assumption appropriate in the piston driven

accelerator, it was possible to replace Eq. (54) by the relationship

$\overline{P} = \overline{\rho}^\gamma$ (Eq. (56)) and finally develop closed form expressions for $\overline{P}^0$, $\overline{\rho}^0$

and $\overline{T}^0$, the pressure, density and temperature at $\overline{x} = 0$, as functions of time $\overline{t}$.

in the single chamber design no relationship of this type can be written

down a priori. In fact, the relationship between pressure and density is

implicit in the complete solution. Though any choice of P(ρ) will lead under

the uniform acceleration assumption to the $\overline{P}^0$, $\overline{\rho}^0$ and $\overline{T}^0$ required to support

the solution at $\overline{x} = 0$; this flow must in general be generated in the upstream

region by a combination of piston motion and heat addition in the chamber

immediately before $\overline{x} = 0$. For the choice $\overline{P} = \overline{\rho}^{\gamma}$, only piston motion was required. For the present case where only heat addition is allowed the relationship between $\overline{P}$ and $\overline{\rho}$ at $\overline{x} = 0$ is unknown. If $\overline{P} = \overline{\rho}$ (isothermal) then both piston motion and heat transfer <u>out of</u> the chamber would be required.

The solution is pursued by writing down the necessary conservation and state equations at $\overline{x} = 0$, in the heating chamber, and for the region connecting them.

<u>At $\overline{x} = 0$</u>;

$$\frac{d\overline{P}^0}{d\overline{t}} = \gamma\overline{\rho}^0 \, \overline{t} \qquad \text{(uniform acceleration condition)} \qquad (73a)$$

$$\overline{P}^0 = \overline{\rho}^0 \, \overline{T}^0 \qquad \text{(ideal gas equation of state)} \qquad (73b)$$

<u>In the heating chamber</u>:

$$\overline{P}_H = \overline{\rho}_H \, \overline{T}_H \qquad \text{(ideal gas equation of state)} \qquad (74a)$$

$$\frac{d\overline{T}_H}{d\overline{t}} = \frac{A_T}{A_C} \frac{\overline{\rho}^0}{\overline{\rho}_H} \, \overline{T}_H \frac{1}{\overline{L}} \, \overline{t} + \frac{\overline{T}_H}{\overline{P}_H} \frac{d\overline{P}_H}{d\overline{t}}$$

$$\text{(conservation of mass)} \qquad (74b)$$

$$\dot{Q}_H = \overline{P}_H \, \overline{L} \left[\frac{\gamma}{\gamma-1} \frac{1}{\overline{T}_H} \frac{d\overline{T}_H}{d\overline{t}} - \frac{1}{\overline{P}_H} \frac{d\overline{P}_H}{d\overline{t}} \right]$$

$$\text{(first law of thermodynamics)} \qquad (74c)$$

<u>Across the connecting region</u>:

$$\overline{T}_H = \overline{T}^0 + \frac{\gamma-1}{2} \, \overline{t} \qquad \text{(first law of thermodynamics)} \qquad (75a)$$

$$\frac{d\overline{P}_H}{d\overline{t}} = \frac{\overline{P}_H}{\left[1 - \frac{\gamma}{2} \frac{\overline{t}^2}{\overline{T}^0} \right]} \left[\frac{1}{\overline{T}^0} \right] \left[2\gamma\overline{t} - \frac{\gamma}{2} \, \overline{t}^3 \frac{A_T}{A_C} \frac{\overline{\rho}^0}{\overline{\rho}_H} \frac{1}{\overline{L}} \right] \qquad (75b)$$

$$\text{(isentropic condition)}$$

The derivation of this system of equations requires extensive algebraic manipulations, which have not been reproduced here. The seven equations in the seven variables $\bar{P}^0$, $\bar{\rho}^0$, $\bar{T}^0$, P_H, $\bar{\rho}_H$, $\bar{T}_H$, $\bar{Q}_H$ can be solved numerically in a straightforward way by the method of finite differences using a forward marching technique in $\bar{t}$, recognizing that at $\bar{t} = 0$ all of the variables are unity except $\bar{Q}_H$, which is zero.

The next question which arises concerns how far the integration in $\bar{t}$ should proceed. Certainly if the desired final speed for the ramjet is u_{max}, then one answer is $\bar{t}_{max} = \bar{u}_{max} = \dfrac{u_{max}}{a_{oo}}$. For this solution it is only necessary to specify a_{oo} (or T_{oo}) in order to find the maximum time the ramjet can experience uniform acceleration $\bar{t}_{max}$. Unfortunately, two aspects of the problem would be left out with this conclusion. First, the question of choking at $x = 0$, and second the "free acceleration" period which must occur after heat addition is terminated. The question of choking does not turn out to be of major importance in this case because of the high temperatures which are present at $\bar{x} = 0$. The Mach numer at $\bar{x} = 0$ is

$$M^0 = \frac{u^0}{a^0} = \frac{\bar{t}}{\sqrt{\bar{T}^0}} \quad .$$

Numerical integration of the governing system of equations (Eqs. (73) through (75)) indicates that $\bar{T}^0$ increases rapidly enough so that $M^0 = 1$ is not approached in reasonable values of $\bar{t}$ and is never approached for some parameter selections (especially small $\bar{L}$ values). Thus, in this case there does not seem to be a "natural" termination of the uniform acceleration solution, as there was in the homentropic accelerator. For a given T_{oo}, then, higher final velocities can probably be achieved in the pistonless design.

The problem of the "free acceleration" period is more difficult to evaluate. Certainly it must take some finite time for information to travel along the right running characteristic which intersects the ramjet path in

x, t space. In order to find the exact time involved it is necessary to apply the method of characteristics to the non-homentropic flow field downstream of x = 0. As was mentioned earlier this has not been done yet. Consequently, we are left with making an estimate of what this period might be. It is reasonable to expect that it might be of the same order as that for the homentropic flow field.

For the sake of preliminary comparisons between the piston driven and pistonless accelerator it will be assumed that heat driven acceleration occurs until $\bar{t}$ = 1.2 and that from $\bar{t}$ = 1.2 to 1.708 a "free acceleration" period occurs. These numbers are arbitrary and will be corrected when the characteristic solution is completed. The parameter $\bar{L}$, the non-dimensional length of the heat addition region, also appears in the equations. As in the piston driven case, small values of $\bar{L}$ give better performance and higher maximum temperatures, large values give reduced performance and maximum temperatures. The exact dependencies are more obscure in the pistonless case. For the preliminary calculations that were performed for the sake of comparison with the piston driven accelerator, an $\bar{L}$ value of 0.05 was chosen. This is close to the dimensionless length of the compression chamber of the dual chambered accelerator.

Results of calculations are shown in Figs. 18, 19 and 20. The variations of $\bar{P}_H$, $\bar{T}_H$ and $\bar{P}^0$ with $\bar{t}$ are shown in Fig. 18. At $\bar{t}$ = 1.2, the end of the heating period, $\bar{P}_H$ = 2.32. $\bar{T}_H$ = 3.80, $\bar{P}^0$ = 1.78. Dimensionally these correspond to P_H = 344 MPa (49,900 psia), T_H = 5597°K, P^0 = 264 MPa (38,300 psia) for the example where a 16 cm dia, 10 kg ramjet is accelerated to 5000 m/sec. The maximum pressures attained are about half of those attained in the piston driven case. A comparison between maximum system temperatures for the two different designs is not really possible, because of the arbitrary nature of T_{Ho} in the piston driven case. If T_{Ho} were taken to be equal to T_{∞}, then the maximum
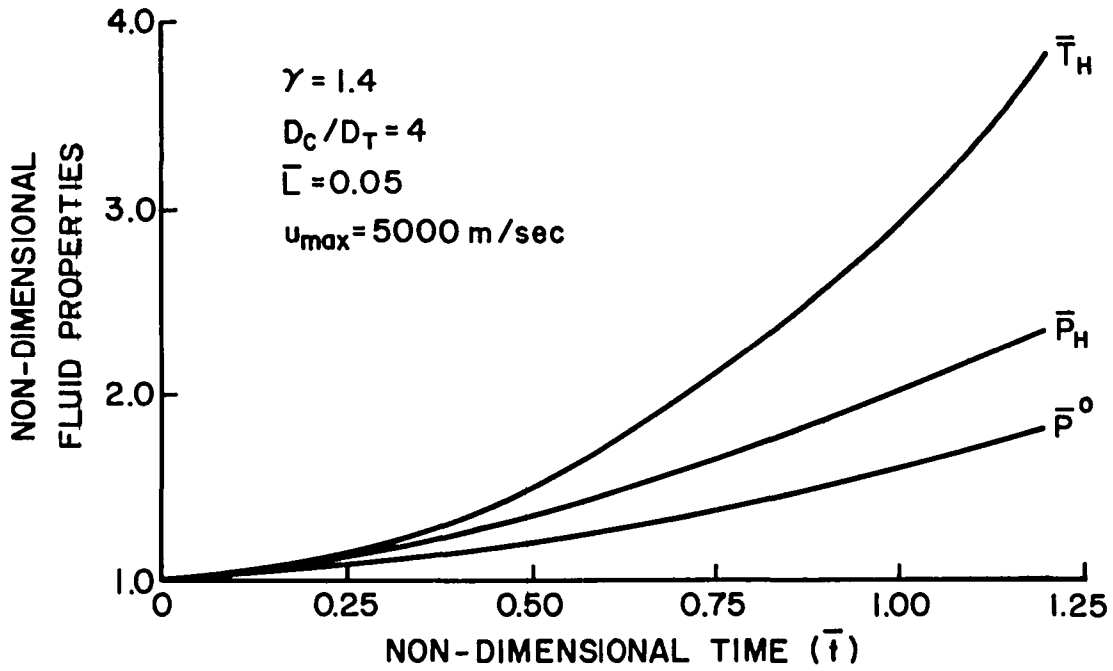
Fig. 18   Pressure and Temperature: Pistonless Accelerator
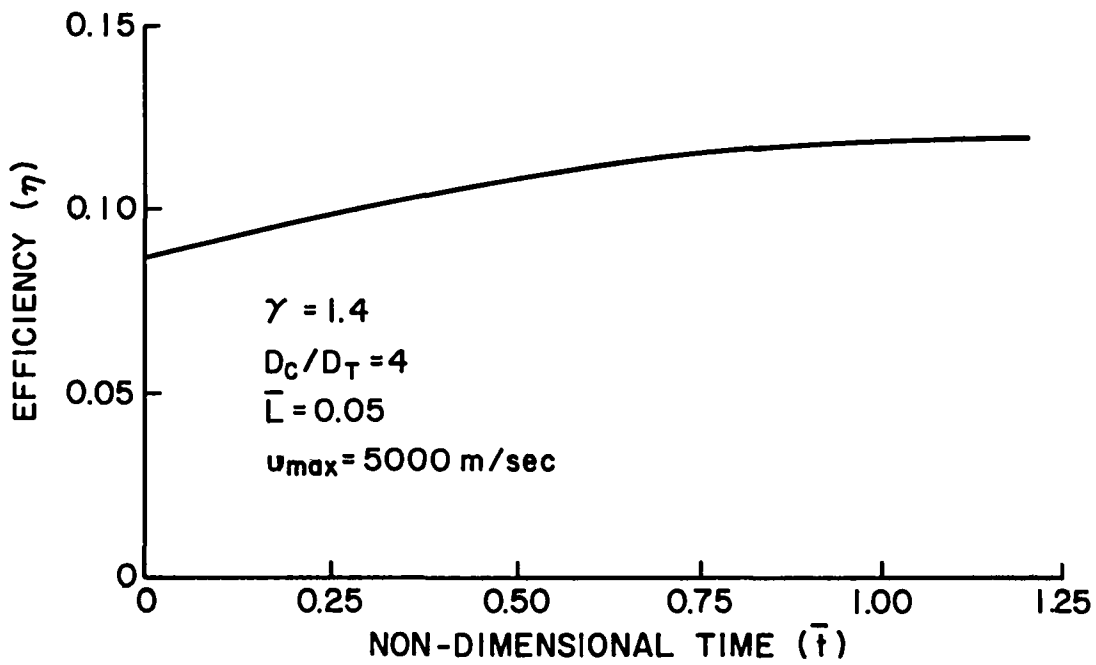

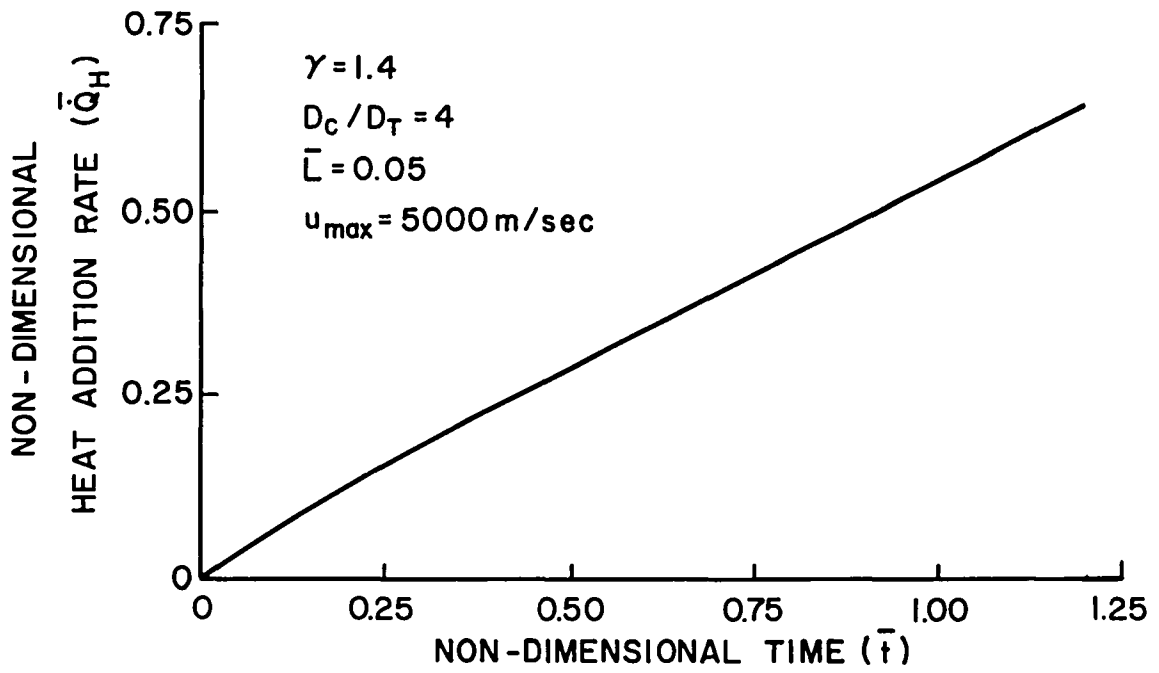Fig. 19   Efficiency of Pistonless Accelerator

Fig. 20 Rate of Heat Addition: Pistonless Accelerator

system temperature in the pistonless accelerator would be about 40% of that of the piston driven accelerator, for the example chosen here.

In Fig. 19 η the instantaneous efficiency defined earlier is shown as a function of time ($\bar{t}$). In contrast with the piston driven case (Fig. 16), the efficiency increases with time, reaching a maximum value of about 11.9% at $\bar{t}$ = 1.2. The total change in efficiency during the acceleration period is 30%. For the piston driven device it decreases by a factor of 2.5 during acceleration, starting from a maximum of 6.5%.

As shown in Fig. 20 the heat addition rate $\bar{\dot{Q}}_H$ increases nearly linearly with time (i.e. power input would have to increase linearly with time to provide the uniform acceleration desired). The maximum of $\bar{\dot{Q}}_H$ occurs at $\bar{t}$ = 1.2 and corresponds to a power input of 86.8 gigawatts. This compares favorably with the maximum power requirement of 370 gigawatts for the piston driven accelerator. The overall efficiency of the acceleration, η_o, including the "free acceleration" period from $\bar{t}$ = 1.2 to $\bar{T}$ = 1.708 is 23.4%, more than double that of the piston driven device.

Conclusions

Calculations indicate that gun-type, constant base pressure acceleration of an electrothermal ramjet vehicle to the speed necessary for effective ramjet mode operation is feasible. The efficiency of the acceleration process is not high compared with the ramjet itself. Overall efficiences (conversion of thermal to kinetic energy) of less than 25% are predicted for idealized accelerator operation. These compare unfavorably with effi- ciencies greater than 40% for ramjet mode operation, even when shock losses are considered. Two types of accelerator designs were evaluated: a dual chambered piston driven accelerator, and a single chambered accelerator with

no piston. Of the two, preliminary comparisons strongly favor the pistonless accelerator. It is mechanically simpler, provides higher efficiencies, has the potential for reaching higher maximum velocities, requires a much simpler power addition profile (linear vs nonlinear), and reaches lower maximum pressures during the acceleration process.

REFERENCES

1. Siegfried, D. E., "A Phenomenological Model for Orificed Hollow Cathodes," NASA CR-168026, Dec. 1982.

2. Siegfried, D. E. and P. J. Wilbur, "A Model for Mercury Orificed Hollow Cathodes: Theory and Experiment," AIAA Paper No. 82-1889, Nov. 1982.

3. Homa, J. M. and P. J. Wilbur, "Ion Beamlet Vectoring by Grid Translation" AIAA Paper No. 82-1895, Nov. 1982.

4. Brophy, J. R. and P. J. Wilbur, "The Flexible Magnetic Field Thruster," AIAA Paper No. 82-1936, Nov. 1982.

5. Rovang, D. C. and P. J. Wilbur, "Ion Extraction Capabilities of Very Closely Spaced Grids," AIAA Paper No. 82-1894, Nov. 1982.

6. Feng, Yu-Cai and P. J. Wilbur, "The Influence of Stray Magnetic Fields on Ion Beam Neutralization," AIAA Paper No. 82-1945.

7. Langmuir, I., "The Interaction of Electron and Positive Ion Space Charge in Cathode Sheaths," Phys. Rev., Vol. 33, June 1929, pp. 954-990.

8. Jahn, R. G., Physics of Electron Propulsion, Gordon & Breach, New York, 1970.

9. Anon., "Optimization Methods," Department of Mathematics, Nanjing University, China.

10. Ishikawa, J. et. al., "Ion Beam Extraction with Space-charge Compensation in Beam-plasma Type Ion Source," J.A.P. v. 53, No. 9, Sept. 1982. pp. 6018-6028.

11. Wilbur, P. J., C. E. Mitchell and B. D. Shaw, "The Electrothermal Ramjet," AIAA Paper No. 82-1216, June 1982.

12. Anderson, John D. Jr., "Modern Compressible Flow," McGraw Hill, New York 1982.

13. Krier, H. and M. Summerfield, Eds., <u>Interior Ballistics of Guns</u>, v. 66, Progress in Astronautics and Aeronautics Series, American Institute of Aeronautics and Astonautics, New York, 1979.

14. Lukasiewicz, J. "Constant Acceleration Flows and Applications to High-Speed Guns," <u>AIAA Journal</u>, v. 5, no. 11, pp. 1955-1963, 1967.

15. Smith, F., "Theory of Two-Stage Hypervelocity Launcher to Give Constant Driving Pressure at the Model," <u>J. Fluid Mech.</u>, v. 17, pp. 113-125, 1963.

16. Rudinger, George, <u>NonSteady Duct Flow</u>, Dover Publications, New York, 1969.

APPENDIX A

RECENT PAPERS DESCRIBING WORK

ACCOMPLISHED DURING THE PERIOD

COVERED BY THIS REPORT

AIAA'82

AIAA-82-1889
A Model for Mercury Orificed Hollow Cathodes: Theory and Experiment

D. Siegfried and P.J. Wilbur, Colorado State Univ., Ft. Collins, CO

AIAA/JSASS/DGLR 16th International Electric Propulsion Conference

November 17-19, 1982/New Orleans, Louisiana

A MODEL FOR MERCURY ORIFICED HOLLOW CATHODES.
THEORY AND EXPERIMENT*

Daniel E. Siegfried** and Paul J. Wilbur†
Colorado State University
Fort Collins, Colorado

Abstract

A model is presented which provides a useful qualitative description of the basic physical processes taking place within a mercury orificed hollow cathode and can predict, to first order, important cathode operating parameters such as emission length and insert temperature. The analytical formulation of the model is based on the concept of an idealized "ion production region" which is defined as the volume circumscribed by the emitting portion of the insert. The energy exchange mean free path for primary electrons is used as a criterion for determining the length (L_e) of this region. An ion production region aspect ratio (D/L_e) of two is suggested as a design criterion for minimizing keeper voltage. The model accounts for electrons produced in the ion production region both by surface emission and by volume ionization. Surface and volume energy balances are used to predict plasma density and plasma potential in this region. An empirical relation is presented which can be used to estimate cathode internal pressure (a necessary input to the model) from the discharge current and cathode orifice diameter. Calculations based on the model are compared with experimental results.

Nomenclature

a_o – theoretical constant (1.2×10^6 A/m^2 $^\circ$K^2)

A_c – area of end boundary of ion production region (m^2)

A_e – insert emission area (m^2)

A_s – total surface area of ion production region (m^2)

D – insert inner diameter (m)

d_o – orifice diameter (mm)

e – electronic charge (Coulombs)

E – electric field at insert surface (V/m)

I_D – total discharge current (A)

I_e – insert electron emission current (A)

I_i – total ion current to cathode surfaces (A)

j_i – Bohm current density (A/m^2)

j_{th} – field-enhanced, thermionic emission current density (A/m^2)

J – normalized emission current (Eq.1)

k – Boltzman's constant (1.38×10^{-23} J/$^\circ$K)

L_e – insert emission length (m)

$\dot{m}$ – propellant mass flow rate (mA equivalent)

m_i – ionic mass (kg/ion)

n_e – electron density in ion production region (m^{-3})

n_i – ion density in ion production region (m^{-3})

n_o – total neutral atom density in ion production region (m^{-3})

P – internal cathode pressure

$\dot{q}_{dx}$ – energy flux associated with de-excitation of excited states on the emission surface (W/m^2)

$\dot{q}_{ph}$ – energy flux due to plasma radiation (W/m^2)

$\dot{Q}_{th}$ – insert thermal power loss (W)

T_e – electron temperature in ion production region ($^\circ$K)

T_s – insert emission temperature ($^\circ$K)

V_p – plasma potential in ion production region (V)

ε_i – ionization potential (10.4V for Hg)

ε_o – permittivity of free space (8.85×10^{-12} F/m)

ε_{pr} – primary electron energy, equivalent to plasma potential V_p(eV)

λ_{ee} – electron-electron elastic mean free path (m)

λ_{El} – effective, energy exchange, elastic mean free path for primary electrons (m)

λ_{In} – effective inelastic mean free path for primary electrons (m)

λ_{pr} – primary electron, energy exchange mean free path (m)

φ_e – average effective work function (V)

φ_s – average surface work function (V)

Introduction

The results of previous experimental investigations of mercury orificed hollow cathodes [1,2]

showed that ~70% of the total cathode current is due to surface electron emission from a narrow band (~2mm long) on the downstream end of the low work function insert and that the dominant surface emission process is probably that of field-enhanced, thermionic emission. The results also indicated that the remaining 30% of the current is due to volume ionization which takes place in the very intense plasma discharge which is established adjacent to the emitting portion of the insert. A phenomenological model describing the emission and plasma production processes within the cathode was developed based on the results of those experiments [2]. The important cathode processes are shown schematically in Fig. 1. Surface electron production is from a narrow band on the downstream end of the insert, primarily from field-enhanced thermionic emission. These electrons are accelerated across the plasma sheath and, thereby, pick up sufficient energy to ionize mercury atoms (via multistep excitations) in the region adjacent to the insert. The total discharge current is made up of the sum of the currents due to both surface and volume electron production. The ions produced in the process leave the production volume at the Bohm velocity and are neutralized at internal cathode potential surfaces. Ions striking the insert surface provide the energy input which is required to maintain the insert at the emission temperature.

By defining an idealized ion production volume as the region adjacent to the emitting portion of the insert (indicated by dashed lines in Fig. 1) and assuming that the plasma properties are uniform in that region, the physical description above can be represented analytically in a rather simple form. The analytical model, as initially proposed, was presented in Ref. [2] and further developed in Ref. [3]. The development of the model is discussed in detail in those two references, so only the important assumptions and a summary of the final results will be presented here.

Summary of Model

Table I gives a summary of the equations developed in the model along with the physical basis for each equation and a brief comment indicating the important assumptions on which it is based. It should be noted that all of the equations in Table I are in MKS units EXCEPT for the empirical expression for the pressure (Eq. I.11) which has the units indicated in parentheses. Each of the equations in Table. I will be discussed briefly below.

The total cathode discharge current I_D is the sum of the surface electron emission current I_e plus the current of volume produced ions returning to the surface I_i. This is represented by Eq. I.1 of the table, where j_{th} is the field-enhanced thermionic current density coming from emitting area A_e of the insert (emission length L_e) and j_i is the Bohm current density of ions crossing the boundary of the ion production region which has a surface area A_s. This equation assumes that the current due to surface emission processes such as cold-field emission, photoemission, and secondary emission due to ions and excited state atoms is negligible. These emission processes are discussed in Ref.[3] where it is shown that the electric fields at the insert surface are too low to cause appreciable field emission and that photoemission is negligible because photons produced within the
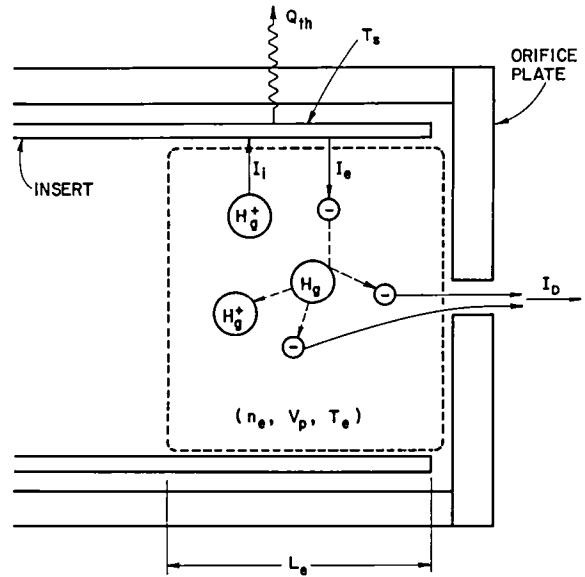

Fig. 1   Schematic of Ion Production Region

plasma by resonance de-excitations are effectively trapped due to the high neutral atom density, so cannot reach the surface in appreciable numbers. Secondary emission currents due to ions and excited state atoms are estimated to be less than 5% of the total current, so they are also neglected. Equation I.1 also neglects electron production within the orifice region and downstream of the orifice. Experimental results indicate that this is a reasonable assumption since these sources contribute only ~7% of the total discharge current.

Equation I.2 of Table I gives the current density J_{th} for field-enhanced thermionic emission from a surface at temperature T_s with an effective work function of φ_e. The effective work function φ_e is the surface work function ϕ_s (a material property) minus the reduction in the work function due to the electric field E at the emission surface and can be calculated using Eq. I.3. The electric field in Eq. I.3 is the field at the emission surface associated with the potential drop across the plasma sheath. It is estimated based on the theoretical analysis presented by Prewett and Allen [4] for the double sheath which forms at a hot cathode surface emitting electrons into a plasma. For the range of operating conditions typical of mercury hollow cathodes, Prewett and Allen's general analysis yields the approximation for the electric field given in Table I by Eq. I.4. This approximation holds for plasmas where the ratio of plasma potential (V_p) to electron temperature (T_e) is ~10 and the normalized emission current

$$J = J_{th} \left[n_o e \left(\frac{kT_e}{m_e}\right)^{1/2} \left(2\frac{V_p}{T_e}\right)^{3/2} \right]^{-1} \quad (1)$$

is less than ~10^{-3}. These criteria are satisfied for typical cathode conditions.

The Bohm current density j_i is estimated from an energy balance on the emitting surface. In such a balance, the power due to heating from ion neu-

Table I

Summary of Equations Used in Model

Physical Basis	Comments	Equation	No.
Current balance	Thermionic electron emission from insert only; ion flux based on Bohm criterion.	$I_D = I_e + I_i = J_{th}A_e + J_iA_s$	I.1
Field-enhanced thermionic emission	Model neglects all surface emission mechanisms, except this one.	$j_{th} = a_oT_s^2 \exp(-\frac{e\varphi_e}{kT_s})$	I.2
Effective work function	Based on electric field at emission surface	$\varphi_e = \varphi_s - \left[\frac{e\lvert E\rvert}{4\pi\varepsilon_o}\right]^{1/2}$	I.3
Double sheath analysis	Approx. based on theoretical analysis in Ref. [4]. Holds for $J < 10^{-3}$ (J from Eq.1)	$E \approx \left[\frac{n_e kT_e}{\varepsilon_o}\right]^{1/2} \left[2(1 + 2\frac{eV_p}{kT_e})^{1/2} - 4\right]^{1/2}$	I.4
Insert energy balance	Neglects energy input due to excited states and plasma radiation.	$J_i = \left[\frac{\dot{Q}_{th}}{\varphi_e} + I_D\right] \cdot \left[2A_c + A_e(1+\frac{a}{\varphi_e})\right]^{-1}$ where $a = (V_p + \varepsilon_i - \varphi_s)$	I.5
Energy balance on ion production region	Neglects energy loss due to excited states and plasma radiation.	$V_p = \frac{1}{I_D - j_iA_s}\left[\varepsilon_i j_i A_s + \frac{5kT_e I_D}{2e}\right]$	I.6
Bohm criterion	Assumes uniform or average plasma properties.	$n_e = \frac{j_i}{e[kT_e/m_i]^{1/2}}$	I.7
Existence length for primary electron	Criterion for emission/ion production region length.	$L_e = 2\lambda_{pr}$	I.8
Semi-empirical	Energy exchange mean free path based on results of computer model.	$\lambda_{pr} = \left[\frac{6.5\times10^{-17}n_e}{V_p^2} + \frac{10^3 n_o V_p}{2.83\times10^{23} - 1.5n_o}\right]^{-1}$	I.9
Ideal gas law	Assumes heavy particle temperature equal to insert temperature.	$n_o = \frac{P - n_e k(T_e + T_s)}{k T_s}$	I.10
Empirical	Neglects orifice plate thickness effect.	$P = \frac{\dot{m}}{d_o^2}(13.7 + 7.82 I_D)\times10^{-3}$ (Torr) where $\dot{m}$(mA) and d_o(mm)	I.11

tralization and de-excitation of excited states is equated to the power conducted and radiated from the surface plus the power removed by emitted electrons. The equation describing this is

$$j_i A_e (V_p + \varepsilon_i - \phi_s) + \dot{q}_{dx} A_e + \dot{q}_{ph} A_e = \dot{Q}_{th} + I_e \phi_e \quad (2)$$

where ϕ_e is the effective work function of the surface, ϕ_s is the surface work function (a material property), $\dot{Q}_{th}$ is the thermal power transferred away from the surface, V_p is the potential drop across the plasma sheath, and ε_i is the ionization potential. The terms $\dot{q}_{ph} A_e$ and $\dot{q}_{dx} A_e$ are the energy input due, respectively, to photons leaving the plasma and to surface de-excitation of excited atomic states. The photon flux is negligible because the resonance radiation is effectively trapped within the plasma. The term $\dot{q}_{dx} A_e$ due to excited states is believed to be relatively small though not necessarily negligible. Calculation of this term and various factors affecting it will be discussed in more detail in the last section of this paper. The term $\dot{Q}_{th}$ in Eq. 2 is the thermal power lost from the insert. In general, it is a function of the insert temperature T_s and must be estimated for the specific cathode thermal configuration on the basis of conduction and radiation from the insert. Neglecting the terms $\dot{q}_{dx} A_e$ and $\dot{q}_{ph} A_e$ in Eq. 2 and solving for the ion current density j_i gives Eq. I.5 of Table I. In expressing Eq. I.5 in terms of the total discharge current I_D, Eq. I.1 was used along with the fact that the total surface area of the ion production region is $A_s = A_e + 2A_c$ where A_c is the area of the end boundary of the region.

The plasma potential is estimated by a similar energy balance on the ion production region. Energy is convected into and out of this volume by the motion of the various particle species crossing the boundaries of the ion production region. This particle motion transports not only the random and directed kinetic energy of the particles but also their excitation potential energy. Again neglecting the energy flux due to excited state atoms $\dot{q}_{dx}$ and due to radiation $\dot{q}_{ph}$ leaving the volume, the energy balance can be written simply as

$$V_p I_e = \varepsilon_i I_i + \frac{5}{2} \frac{kT_e}{e} I_D \quad (3)$$

Here $V_p I_e$ is the rate at which energy is brought into the volume by the primary (surface emitted) electrons, $\varepsilon_i I_i$ is the rate at which energy leaves the volume in the form of ionized atoms, and $(5/2 \, kT_e I_D)$ is the rate at which energy leaves the volume due to the convection of Maxwellian electrons through the orifice ($5/2 \, kT_e$ is the enthalpy of the Maxwellian electron gas). Other energy terms such as the directed kinetic energy and enthalpy of the ions and neutrals can be shown to be small [3] and are neglected. Using the current balance of Eq. I.1 and solving Eq. 3 for V_p results in Eq. I.6 of Table I.

Calculation of the electric field E using Equation I.4 requires values for the plasma density n_e and the electron temperature T_e. Assuming that the plasma density ($n_e \approx n_i$) is uniform throughout

the ion production region and that the ions leave the region at the Bohm velocity $(kT_e/m_i)^{1/2}$, an equation for the ion current density from the production region can be written. Rearrangement of this equation gives Eq. I.7 where j_i is the ion current density from Eq. I.5. The electron temperature is also needed here. However, neither Eq. I.4 nor I.7 is very sensitive to the electron temperature because it appears as a square root. Probe measurements in the ion production region show that over the normal range of mercury hollow cathode operation the electron temperature is reasonably constant at 0.71 ± 0.1 eV. Therefore, it is suggested that this measured value be used in the equations.

To complete the model one requires a means of estimating the length of the ion production region. This length is determined by the collisional processes taking place within the ion production region. Energy input to the ion production region occurs mainly through the current of primary electrons emitted from the insert. The dominant energy exchange paths for a primary electron entering this region are inelastic collisions with a mercury atom (typically 10^9 collisions per second) and elastic collisions with Maxwellian electrons (typically 10^8 collisions per second). The elastic collision cross-section for an electron-electron collision is proportional to the inverse square of the projectile electron's energy. Therefore, once a primary electron gives up energy, either by small angle elastic or by inelastic collisions, it's collision rate increases and it is rapidly thermalized, losing it's identity as a primary. The fact that the primary electrons are required for the excitation reactions which sustain the plasma discharge suggests the length of the ion production region is probably on the order of the primary electron energy exchange mean free path. Primaries can lose energy both by elastic collisions over a mean free path of λ_{E1} and by inelastic collisions over a mean free path of λ_{In}. Therefore, the effective mean free path for the loss of a primary electron would be

$$\lambda_{pr} = (1/\lambda_{In} + 1/\lambda_{E1})^{-1}. \quad (4)$$

From where they are created, primary electrons will be scattered upstream to some extent by elastic collisions. Therefore, a reasonable criterion for the length of the ion production region is probably one to two primary electron energy exchange mean free paths. It will be seen in the next section that a length of two mean free paths gives the best agreement with experimental results. This criterion is indicated in Table I by Eq. I.8.

The primary electron mean free path criterion as well as the concept of an ion production region are clearly idealizations. The extent of the ion production region in reality will not be sharply defined; properties will not be uniform throughout the region and ionization will occur upstream of the boundary. In addition, ions produced in the region will diffuse upstream, heating the insert in the region upstream of the boundary. So far the diffusion of ions upstream has not been discussed, although to be consistent with the model, the

plasma density must fall off rapidly upstream of
the boundary. If this were not the case, signifi-
cant ion heating of the insert and related electron
emission would be expected to occur upstream of the
boundary defined by the mean free path criterion.
Experimental plasma density profiles show that, in
fact, the axial plasma density drops off exponen-
tially in the upstream direction. This indicates
that significant ion heating probably does not
extend far upstream of the ion production region
and is consistent with the observed rapid fall off
in surface temperature upstream of the emission
region. This observed behavior is also in agree-
ment with calculations based on ambipolar diffusion
of the ions and electrons. Such calculations show
that, by itself, volume recombination in the plasma
can result in a density decrease upstream of the
production region more rapid than that observed
experimentally. In the real situation, of course,
both volume ionization and wall recombination are
also taking place in conjunction with volume recom-
bination to determine the actual plasma density
profile in this upstream region.

In order to use Eq. 4 to estimate the emis-
sion length it is necessary to be able to calculate
the elastic (λ_{El}) and inelastic (λ_{In}) energy
exchange mean free paths. Elastic electron-ion and
electron-atom collision frequencies are relatively
low. Therefore, the effective elastic mean free
path for energy exchange is approximately equal to
the electron-electron mean free path, or

$$\lambda_{El} \approx \lambda_{ee} = \frac{\varepsilon_{pr}^2}{6.5 \times 10^{-17} n_e}. \tag{5}$$

Here the expression for λ_{ee} is based on a Coulomb
collision between a primary electron with energy
ε_{pr} and a low energy Maxwellian electron [5], and
n_e^{pr} is the Maxwellian electron density. The inelas-
tic
mean free path is given by the following expression

$$\lambda_{In} = \frac{1}{\sum_j n_\alpha \sigma_{\alpha\beta}^j} \tag{6}$$

where $\sigma_{\alpha\beta}^j$ is the collision cross-section for pro-
duction of excited state β from a target particle
of type α having a density n_α. The summation in
Eq. 6 is made over all of the important excitation
reactions in the ion production region. Evaluation
of λ_{In} using Eq. 6 requires the densities of the
various excited states of mercury in the ion pro-
duction region as well as the cross-section for all
of the important reactions. Peters [6] has com-
piled the necessary collision cross-section data
and developed a computer model which calculates
excited state densities for a mercury discharge.
The application of Peters' computer model for this
purpose is described in detail in Ref. [3], so only
the important results will be presented here.

The computer model was used to calculate
excited state densities and inelastic mean free
paths λ_{In} over a wide range of input parameters
typical of hollow cathode conditions. The results
of the computations are shown in Fig. 2 where λ_{In}
is plotted as a function of total neutral density
n_o using primary energy as a parameter. Although
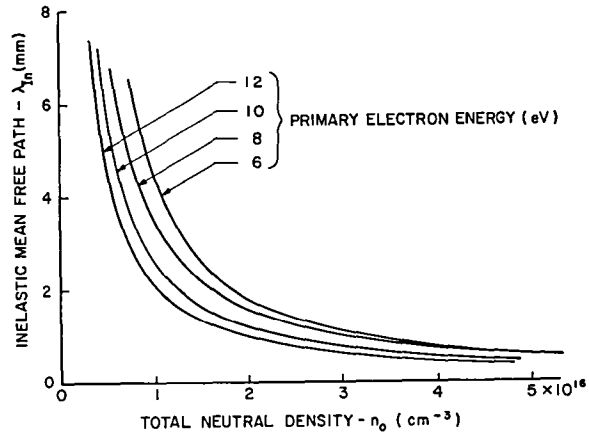all of the input parameters were varied over a con-

Fig. 2   Effect of Total Neutral Atom Density
on Primary Electron Inelastic Mean
Free Path

siderable range, the mean free path for inelastic
collisions was found to be sensitive only to total
neutral density and to primary electron energy.
The Maxwellian electron density n_e was also found
to have a slight effect on λ_{In}. However, this
effect is rather small amounting to an increase in
λ_{In} of less than 20% when electron density is
increased by a factor of five. For our purposes
here, this effect can be neglected.

Recognizing that the mean free path varies as
the inverse of the neutral density n_o, the results
of Fig. 2 are fitted with the following expression

$$\lambda_{In} = (\frac{2.83 \times 10^{23}}{n_o} - 1.5) \frac{1}{10^3 \varepsilon_{pr}}. \tag{7}$$

This expression fits the results shown in Fig. 2
within $\pm$ 5% over the full range of the parameters
except for values of ε_{pr} equal to 6.0V where λ_{In} is
overestimated by ~20% in the intermediate density
range. Using Eq.5 for the elastic mean free path
and Eq. 7 for the inelastic mean free path, the
effective primary electron mean free path for
energy loss due to both elastic and inelastic col-
lisions λ_{pr} is given by Eq.I.9 of Table I. It has
also been assumed in this equation that the primary
energy ε_{pr} is equal to the plasma potential V_p.
Equation I.9 provides an easy means of estimating
the insert emission length. Of particular impor-
tance is the fact that over the normal range of
cathode conditions, the results of Eq. I.9 are
dependent mainly on the neutral density and are not
very sensitive to the plasma potential (V_p is nor-
mally 8-12V) or electron density. This enables
one to make a reasonable estimate of λ_{pr} based only
on typical plasma conditions and the neutral den-
sity. It is worth pointing out that the curves in
Fig. 2 are relatively flat at densities
greater than ~2 x 10^{16} cm^{-3} resulting in typical
values of λ_{pr} near one millimeter. This is in good
agreement with the experiments, which show that for
internal pressures over a few Torr ($n_o \sim 2 \times 10^{16}$
cm^{-3}), the emission is confined to a region ~2 mm
long or less on the downstream end of the insert
but that the region extends significantly upstream

at pressures below a few Torr. Comparison with additional experimental results will be presented in the next section.

Finally, it is necessary to estimate the total neutral density n_o in the region upstream of the orifice. The presence of the cathode orifice plate simplifies this problem somewhat because most of the pressure drop is across the orifice and the pressure within the cathode cavity upstream of the orifice is essentially constant. The total pressure at any point in the cathode is the sum of the partial pressures of each species. Using the ideal gas law this can be expressed as

$$P = n_e kT_e + n_i kT_i + n_o kT_o \qquad (8)$$

where k is Boltzmann's constant, n is the density, T is the temperature, and the subscripts e, i, o refer to electrons, ions, and neutral atoms respectively. Given the local pressure, each of the temperatures, and the plasma density, Eq. 8 can be solved for the neutral gas density. Invoking quasi-neutrality of the plasma (i.e., $n_e \approx n_i$) and equilibrium of the heavy particles (ions and neutrals) with each other at the insert temperature, Eq. 8 takes the form given in Eq. I.10. The local pressure P used in Eq. I.10 is determined from a correlation of experimental results based on actual pressure measurements made over a wide range of mass flow rates, discharge currents, and orifice diameters [3]. This correlation is shown in Table I as Eq. I.11 where the units are P (Torr), $\dot{m}$ (mA equivalent), d_o (mm) and I_D(A). It is believed to be accurate to within $\pm 30\%$.

Given the mass flow rate $\dot{m}$, the orifice diameter d_o, the insert diameter D, the total discharge current I_D, the surface work function φ_s, the insert thermal power loss $\dot{Q}_{th}$, and the physical constants (e, k, m_i, ε_o, ε_i, a_o), the equations in Table I can be solved for all of the other parameters except the electron temperature. As discussed above, a value of 0.71 eV is a reasonable assumption for the electron temperature. Because Eq. I.2 can not be solved explicitly for the surface temperature T_s, the solution of these equations is necessarily iterative. However, the equations converge to a solution very rapidly (five place accuracy in six or seven iterations). The results of calculations based on this set of equations will be compared with experimental results in the next section.

Comparison with Experiment

An earlier paper describes an experiment in which a special quartz tube test cathode was used to determine the magnitude and origin of the various hollow cathode currents [2]. The predictions of the model will be compared here with the results of that experiment.

A schematic of the test cathode used in the experiment is shown in Fig.3. The cathode was fabricated from a quartz tube such that all of the internal surfaces were covered with tantalum foil and each surface of interest was isolated as a separate electrode. The insert was 2.2 mm long and had a diameter of 3.9 mm. The cathode had an orifice diameter of 0.96 mm. Both the insert and the cathode tube were coated with the low work function
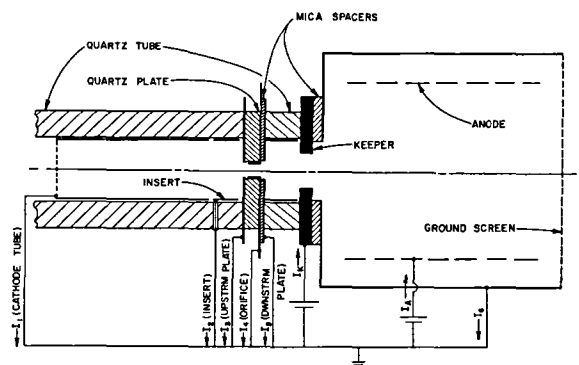

Fig. 3   Test Cathode for Current Accounting

chemical R-500*. The cathode discharge was coupled to a cylindrical anode which was completely enclosed within a stainless steel ground tube covered on its downstream end by a fine mesh screen. The current from each of the surfaces shown in Fig. 3 was measured separately for total discharge currents I_D of 1.3, 2.3, 3.3 and 4.3A at a mercury flow rate $\dot{m}$ of ~100mA. Data were also collected for an emission current of 3.3 A at internal cathode pressures P ranging from 1.3 to 5.5 Torr. The internal pressure was measured using a U-tube manometer and the insert temperature was measured using a micro-optical pyrometer.

Emission Length

A critical test of the model is its ability to predict the length of the insert emission region since this parameter strongly affects the predicted insert surface temperature for a given discharge current and surface work function. The model assumes that the insert emission length is between one and two primary electron free path lengths. The primary electron mean free path λ_{pr} was calculated with Eq. I.9 for the experimental conditions. In making these calculations, the neutral density was estimated from the measured cathode pressure using Eq. I.10 and the primary electron energy was taken to be 8.7 eV. The primary electron energy could have been estimated using Eq. I.6, but it will be seen shortly that this underestimates the plasma potential by ~2V. The value of 8.7 eV was chosen on the basis of plasma property measurements [3] which showed that over the range of normal operating conditions for this size cathode, the plasma potential in the ion production region is nearly constant at 8.7 $\pm$0.5 V.

The results of the mean free path calculation discussed above are plotted as the solid curve ($2\lambda_{pr}$) in Fig. 4. Insert emission lengths determined from the experimental results are indicated in the figure as circles. The agreement between the experimental data points and the calculated curve is quite good and supports the assumption of the model that L_e/λ_{pr} is approximately two. The data points above four Torr would have been in even closer agreement with the curve except that there was no way in this experiment to discriminate emission lengths shorter than the 2.2 mm long insert segment. Insert emission lengths, for conditions

---
*   A double carbonate mixture – (Ba/Sr) CO_3 – manufactured by the J.R. Baker Chemical Co., Phillipsburg, New Jersey.
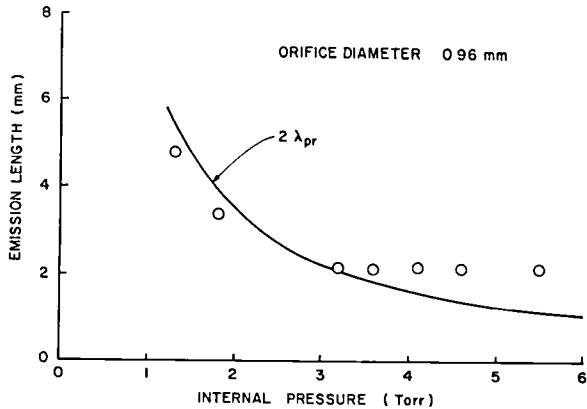
ORIFICE DIAMETER 0 96 mm

2 λ_{pr}

Fig. 4   Comparison of Emission Length with
Primary Electron Energy Exchange
Mean Free Path

where emission was taking place not only from the
insert (surface 2) but also from the cathode tube
(surface 1), were estimated by assuming that the
current density for emission from the tube was the
same as the measured average current density of the
2.2 mm long insert at that same condition.

It is worth noting here that, for operation at
a typical internal cathode pressure of ~3 Torr, the
2mm emission length is the same as the cathode
insert radius. These conditions correspond to a
pressure-diameter product of ~1 Torr-cm. It is
interesting to compare this with experimental
results reported by Lidsky et al. [7] for an open
tube cathode. Working with a number of different
gases (H_2, H_e, A, N_2), they determined experimen-
tally that the emission region locates itself where
the local pressure-diameter product is ~1 Torr-cm.
A pressure-diameter product of this magnitude
corresponds to a primary electron mean free path
which is on the order of the cathode radius. In
the open tube cathode, the local pressure varies
significantly along the tube. It is reasonable in
this situation that the ion production region
locates itself where conditions are such that pri-
mary electrons can reach the centerline of the
cathode. In the orificed hollow cathode, on the
other hand, most of the pressure drop occurs across
the orifice plate so that the pressure within the
tube is rather constant along the axis of the
cathode and can be adjusted independently without
significantly affecting the emission location.
However, a primary electron mean free path on the
order of the insert radius is probably a desireable
operating condition here as well. This is so even
though the orificed cathode can be forced to
operate under conditions both with shorter and
longer primary electron mean free paths. That a
primary electron mean free path on the order of an
insert radius is a desireable operating condition
is also suggested by experimental results [1,8]
which show that a keeper/discharge voltage minimum
will occur at a pressure-diameter product of a few
Torr-cm.

The above discussion suggests that, for design
purposes, the insert should be chosen to have a
radius on the order of a few primary electron mean
free paths. This would correspond to an insert
radius which is about the same as the emission
length and an ion production region which has an

aspect ratio (D/L_e) of approximately two. Such an
aspect ratio is also convenient with regards to
application of the model since it should result in
an ion production region with fairly uniform plasma
properties (a basic assumption of the model).

Other Predictions

The results of the experiment can also be com-
pared with the model's prediction of insert tem-
perature, plasma density, and plasma potential. In
order to do this, calculations using the model were
performed based on the following considerations

1) Rather than the mass flow rate, the measured
    pressures were used as input to the model.
    Equation I.11 could have been used to determine
    the pressure from the flow rate and orifice
    diameter, but in this case it underestimates
    the pressure by about 20%. A probable explana-
    tion for this discrepancy is that the effective
    diameter of the tantalum, foil-lined orifice
    was slightly smaller during operation than its
    measured diameter when cold. A small error in
    the orifice diameter results in a large error
    in pressure because it appears in Eq. IV.1 as
    an inverse square.

2) The surface work function ϕ_s for the insert was
    not known exactly, although it was believed to
    be between 1.8 and 2.0 eV. The value of 1.94 eV
    used in the calculation was arbitrarily chosen
    from this range to give agreement between the
    measured and the calculated temperature at the
    operating conditions where I_D was 3.3 A and $\dot{m}$
    was ~100 mA. The comparison between calculated
    and measured temperatures will, therefore, be a
    relative one valid mainly for checking the
    functional dependence on discharge current and
    pressure predicted by the model.

3) The thermal power loss used for the calcul-
    ations was taken from the dashed curve of Fig.
    A.1 in Appendix A.

4) The electron temperature was assumed to be the
    average measured value of 0.71 eV.

5) The ratio of emission length to mean free path
    L_e/λ_{pr} was assumed to be two.

The results of calculations using the model
based on the assumptions discussed above are shown
in Figs. 5, 6, and 7. Figures 5a and 5b show the
effect of discharge current and pressure on the
emission temperatures predicted by the model for
the assumed average surface work function of 1.94
eV. It should be recalled here that agreement with
the experimental temperature at a current of 3.3A
was assured by selecting a value of 1.94 for ϕ_s.
The significant feature of Fig. 5a, therefore, is
that the model accurately predicts the effect of
discharge current on the emission temperature.

Such good agreement is not obtained for the
effect of pressure on the emission temperature.
Fig. 5b shows emission temperatures plotted as a
function of internal pressure for a discharge
current of 3.3 A. Unfortunately, at the pressure
conditions indicated by the solid circles, insert
temperatures were not measured in this experiment.
The data indicated by the solid symbols were,
therefore, estimated using the results of another
experiment [1] which showed that for a cathode of

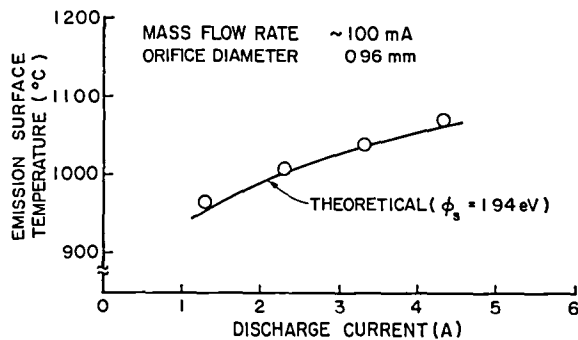Fig. 5a   Effect of Discharge Current on
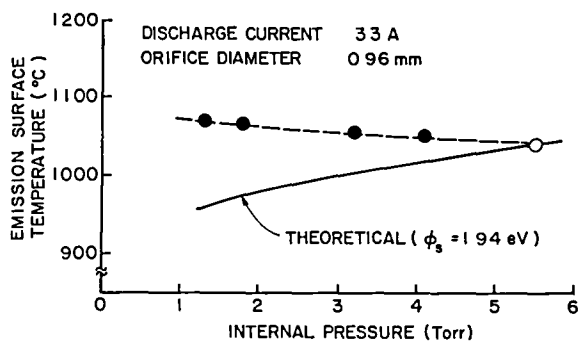   Calculated and Measured Emission
           Surface Temperatures

Fig. 5b   Effect of Internal Pressure on
           Calculated and Measured Emission
           Surface Temperatures

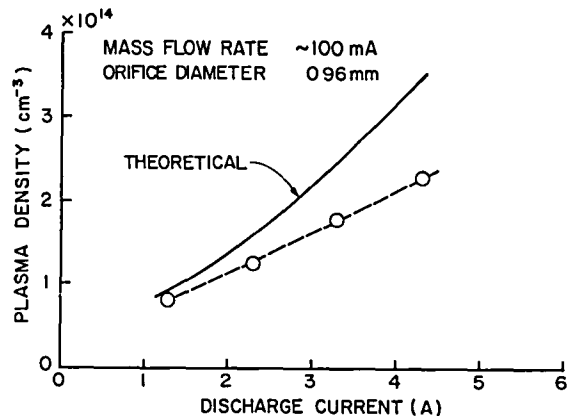
Fig. 6a   Effect of Discharge Current on
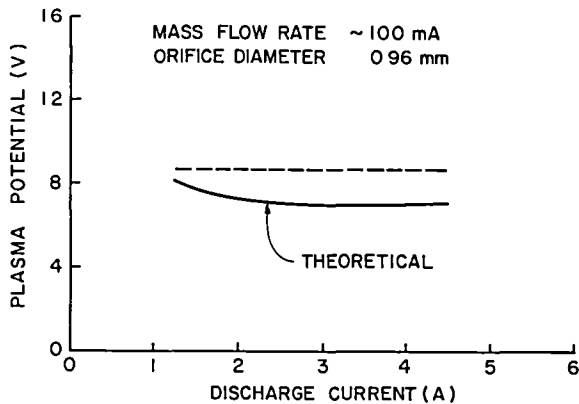   Calculated and Measured
           Plasma Densities

Fig. 6b   Effect of Internal Pressure on
           Calculated and Measured
           Plasma Densities

similar construction operating at a discharge current of 3.3A the maximum insert temperature decreased by ~ 7°C per Torr when internal pressure was increased. However, it is believed that this estimate is reasonably reliable, so it would not account for the differences between the two curves in Fig. 5b. The main reason for the differences between the two curves is that the temperatures indicated by the circles are the maximum emission temperature while the calculated temperatures (circles) are average values based on the assumption of uniform emission over the entire emitting length. While for short emission lengths, the uniform emission assumption is probably valid, the assumption apparently breaks down as the length of the emission region increases. This suggests that, for low pressures, emission temperature gradients become important and the simple, lumped parameter model does not provide an accurate description of the emission temperature.

The ion production region plasma density predicted by the model is plotted in Fig. 6a as a function of discharge current. (solid curve) For comparison, the plasma density n_3 adjacent to the upstream side of the orifice plate is plotted as the circles. These data points (n_3) were estimated from the measured current I_3 based on the Bohm criterion (Eq. I.7) and represent the average plasma density adjacent to the downstream boundary of the ion production region. Plasma densities are shown in Fig. 6b plotted as a function of internal pressure for a discharge current of 3.3A. In both cases (Figs. 6a and 6b), the agreement between experimental values and those predicted by the model is reasonably good,
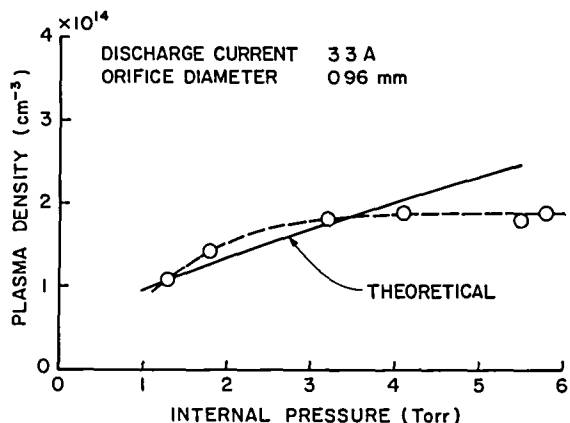
although in Fig. 6b the curve shapes for the measured and calculated values are different. This difference may be attributable, at least partially, to the assumption in the model of a uniform ion production region. This assumption is expected to hold best for operation at conditions where the primary electron mean free path is on the order of the insert radius. As the internal pressure is increased beyond this point (a few Torr), the primary electrons have a lower probability of reaching the centerline of the cathode, so that ion production is increasingly confined to an annular region bounded by the emission surface (as opposed to the assumed cylindrical volume). Such a reduction in volume could account for the fact that the average measured values of the plasma density adjacent to the orifice plate are nearly constant for pressures above a few Torr (Fig. 6b).

The fraction of the total discharge current that is due to volume electron production processes depends mainly on the plasma density. For the plasma densities predicted by the model, this fraction ranged from 0.30 to 0.34. This is in good agreement with results based on measured currents which showed current fractions due to volume ionization ranging from 0.27 to 0.31.

Finally, the plasma potential predictions of the model are shown in Figs. 7a and 7b where they are plotted, respectively, as a function of discharge current at a constant mass flow rate (~100 mA), and as a function of internal pressure at a constant discharge current (3.3A). Although the plasma potential was not measured in this experiment, results from Langmuir probe measurements made during another experiment on a similar cathode showed that the plasma potential in the ion production region was ~8.7V [3]. The average measured value of 8.7V from that experiment is indicated in the Figs. 7a and 7b as the dashed line. The value is shown as a constant (horizontal line) because the probe measurements indicated no clear correlation of the plasma potential in the ion production region with either current or pressure.

Fig. 7a Effect of Discharge Current on
          Calculated and Measured
          Plasma Potentials
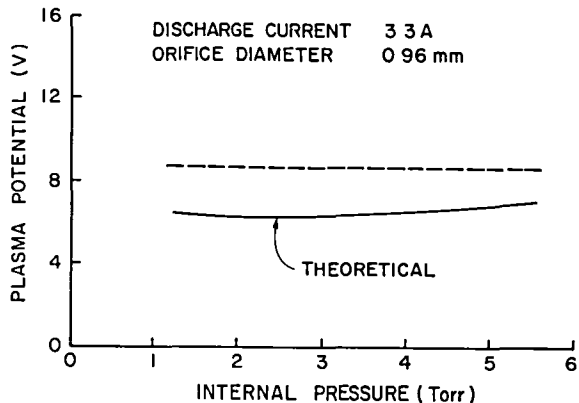
Fig. 7b Effect of Internal Pressure on
          Calculated and Measured
          Plasma Potentials

It should be recalled that both the plasma density and plasma potential predictions are based on energy balances for the ion production region and neglect the energy term due to the the flux of excited atoms. A rough estimate of the energy flux due to excited states was made in Ref.[3]. The estimate was based on excited state densities calculated using Peters' computer model and assumed that the excited atoms leave the ion production region at their thermal velocity carrying with them their excitation potential energy. Furthermore, it

was assumed that all of the excitation energy is deposited at surfaces outside of the boundary and that the de-excited atoms return with only their random thermal energy. The excited state energy flux based on those assumptions was found to be rather large [3] and gave predictins for both plasma density and plasma potential which were not realistic. On the other hand, the results in Figs. 6 and 7 indicate that the model predicts plasma densities and plasma potentials of the right magnitude when the excited state power term is neglected. (In both cases the model would provide better agreement if some fraction of the calculated excited state power were included – 0 to 30%). The over estimation of the excited state energy flux may be due to a number of factors. For example, it may be that the excited state densities near the boundary and, therefore, the particle fluxes are actually over estimated. Another possibility is that the particle fluxes are estimated correctly but that there is some mechanism for returning energy to the volume, such as reflection of excited particles or of resonance radiation from cathode surfaces. However, even in light of these uncertainties associated with calculation of the excited state energy flux, the model provides a useful and reasonable qualitative description of the basic physical processes taking place within the cathode.

Based on the above experimental results, it is suggested that for design purposes the average measured values ot the electron temperature (0.71 eV) and plasma potential (8.7V) should be used when making calculations with the model. The results also indicate that the best agreement between model and experiment is obtained when the ion production region aspect ratio (D/L$_e$) is on the order of two. This is also a condition which is expected to provide good cathode performance.

Conclusions

A phenomenological model has been presented which describes the physical processes underlying the operation of mercury orificed hollow cathodes of the type used in ion thrusters. This descriptive model is in good qualitative agreement with the experimental results indicating that our basic understanding of the important physical processes for these devices is essentially correct. By assuming an idealized ion production region within which most ot the plasma processes are concentrated, this phenomenological model has been expressed analytical as a simple set of equations which relate cathode dimensions and specifiable operating conditions, such as mass flow rate and discharge current, to such important parameters as insert temperature and plasma properties. Comparison with experimental results shows that, if the excited state energy flux is neglected, the model provides reasonably accurate predictions of emission length, emission surface temperature, plasma density and fraction of discharge current due to volume ionization. The plasma potential prediction of the model is rather low; and it is suggested that the average measured value of 8.7V be used in place of Eq. I.6 when making calculations using the model. An ion production region aspect ratio (D/L$_e$) of two is suggested as a design criterion for minimizing keeper voltage.

84

References

1. Siegfried, D. E. and Wilbur, P.J., "Studies on an Experimental Quartz Tube Hollow Cathode," AIAA Paper No. 79-2956, October, 1979.

2. Siegfried, D. E. and Wilbur, P. J., "A Phenomenological Model Describing Orificed Hollow Cathode Operation," AIAA Paper No. 81-0746, April 21-23, 1981.

3. Siegfried, D. E., "A Phenomenological Model for Orificed, Hollow Cathodes," Doctoral Dissertation, Colorado State University, December 1982.

4. Prewett, P. D. and Allen, J.E., "The Double Sheath Associated with a Hot Cathode." Proc. R. Soc. Lond. A, Vol. 348, No. 1655, April 1976, pp. 435-446.

5. Jahn, R. G., Physics of Electric Propulsion, McGraw Hill, New York, 1968, Ch. 4.

6. Peters, R. R., "Double Ion Production in Mercury Thrusters," NASA CR-135019, April 1976.

7. Lidsky, L. M., Rothleder, S.D., Rose, D.J., Yoshikawa, S., Michelson, C. and R.J. Macken, Jr., "Highly Ionized Hollow Cathode Discharge," Journal of Applied Physics, Vol. 33, No. 8, August 1962.

8. Martin, R. J. and Rowe, J. E., "Experimental Investigation of the Low-Voltage Arc in Noble Gases," Journal of Applied Physics, Vol. 39, No. 9, August 1968, pp. 4289-4298.

APPENDIX A

Thermal Power Loss from Emission Surface

The rate of heat transfer ($\dot{Q}_{th}$) away from the emitting portion of the insert due to conduction, convection and radiation is required for the energy balance calculations discussed above. An accurate value for the power loss $\dot{Q}_{th}$ for the experimental cathode is not easily determined, although bounds can be placed on its value and a reasonable estimate can be made. A maximum value can be determined by assuming that end of the quartz tube which holds the insert segment is at the same temperature as the segment (perfect thermal contact). The power loss is then calculated based on conduction down the quartz tube and radiation from its outer surface to ambient ($T_a \approx 300°K$). The quartz tube would then be analogous to a cylindrical fin one end of which is at the insert temperature. The results of this analysis are plotted in Fig. A.1 as a function of insert temperature and are indicated by the upper (maximum) curve. The minimum value of $\dot{Q}_{th}$ is calculated by assuming radiation from both outer and inner surfaces of the insert to surfaces at 700°C and by neglecting all losses due to conduction and convection from the insert. A temperature of 700°C was selected because the adjacent surfaces - non-emitting portion of insert, start-up heater, etc. - were at a temperature less than the minimum temperature detectable with the optical pyrometer (~700°C) used in making temperature measurements. The minimum value for $\dot{Q}_{th}$ calculated in this way is plotted as the lower curve in Fig. A.1.
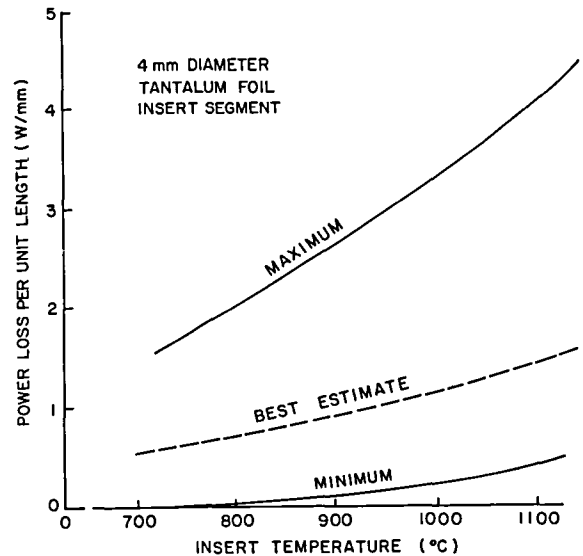

Fig. A.1 Thermal Power Loss for 2 mm Long Tantalum Foil Insert Segment.

Finally, a more probable value for $\dot{Q}_{th}$ is calculated by assuming direct radiation from the insert in addition to some contact between the insert and the quartz tube. The heat transfer between the insert and tube is estimated to be due to a combination of direct contact and transfer via the intervening mercury vapor. The heat transferred to the tube is then assumed to be conducted down its length and radiated from its median diameter to surfaces at $T_a \approx 300°K$. The results of this analysis are plotted in Fig. A.1 as the dashed (best estimate) curve.

AIAA'82

AIAA-82-1895
Ion Beamlet Vectoring by Grid Translation
J.M. Homa and P.J. Wilbur, Colorado State
Univ., Ft. Collins, CO

AIAA/JSASS/DGLR 16th International
Electric Propulsion Conference

November 17-19, 1982/New Orleans, Louisiana

ION BEAMLET VECTORING BY GRID TRANSLATION[+]

John M. Homa[*] and Paul J. Wilbur[**]
Colorado State University
Fort Collins, Colorado 80523

Abstract

An experimental study of ion beamlet vectoring is described. The results can be used to design accelerating systems in which the direction and focus of emerging beamlets are important. Deflection and divergence angle data were collected for two-grid systems as a function of the relative displacement of these grids. At large displacements, accelerator grid impingement becomes a limiting factor and this defines the useful range of beamlet deflection. Beamlet deflection was found to vary linearly with grid offset angle over this range. Values of deflection-to-offset angle ratio and useful range of deflection are given as functions of grid-hole geometries, perveance levels, and accelerating voltages. The divergence of the beamlets was found to be unaffected by deflection over the useful range of beamlet deflection. The grids of a typical dished-grid ion thruster are examined to determine where over the grid surface the grid offsets exceed the useful range. This defines the regions on this surface where high accelerator grid impingement is probably occurring.

Nomenclature

d_a accelerator grid hole diameter
d_s screen grid hole diameter
E_1 electric field, acceleration region
E_2 electric field, deceleration region
f thin lens focal length
h dish depth
j current density
J beam current per hole
ℓ_e' effective acceleration length
ℓ acceleration length
ℓ_g grid separation distance
m_i ion mass
NP/H normalized perveance per hole
q charge
R net-to-total acceleration voltage ratio
R_c radius of curvature
t_a accelerator grid thickness
t_s screen grid thickness
V_N net accelerating voltage
V_T total accelerating voltage

α beamlet divergence half-angle
β beamlet deflection angle
β_u useful beamlet deflection range
δ grid offset angle
δ_u useful grid offset angle range
ϵ relative grid displacement
ϵ_a fractional change in accelerator grid hole spacing
ϵ_0 free space permittivity

Introduction

The study of grid translation effects on ion beam optics has two important applications in the design of electrostatic thrusters. First, for a dished grid pair, hole misalignments are used to redirect the emerging beamlets in order to minimize off-axis thrust. A study that would yield correlations or a model of this phenomenon would facilitate design of these grids. Second, for some applications a vectorable beam is desired[1] and grid translation is one method of producing a moderate thrust vectoring capability. In addition, beam focusing may be desirable to increase the current density in such ground-based applications as sputtering.[2] Again a model or correlations describing the effects of hole misalignment on grid optics would be useful in designing the hardware needed for these tasks.

Work done by Aston[3,4] has shown the effects of such parameters as grid separation, grid hole diameter and net-to-total accelerating voltage ratio on the optical performance of a two-grid system with aligned apertures. Optical performance in this context was defined as the beamlet divergence variation with beam current as well as the maximum perveance that could be obtained before accelerator grid impingement became excessive. The present study of grid translation is intended to examine the effects of grid geometry and operating parameters on grid performance for vectored beams. Of particular importance in this study are the degradation of optical performance as a function of relative grid displacement, the functional relationship between beamlet deflection angle and grid displacement, and the maximum usable beamlet deflection.

Definitions and Linear Optics Theory

Figure 1a shows a two-grid configuration in which the accelerator grid hole is displaced a distance ϵ relative to the screen grid hole. As a consequence the beamlet undergoes a deflection through an angle β (degrees) with respect to the screen grid centerline, while diverging with a half-angle α (degrees). Figure 1a also illustrates pertinent grid dimensions including screen and accelerator grid aperture diameters (d_s and d_a), grid thickness (t_s and t_a) and the grid separation distance (ℓ_g). The grid offset angle δ also shown in Fig. 1a is defined in terms of the relative grid displacement ϵ by the equation:

$$\delta = \tan^{-1}\left(\frac{\epsilon}{\ell_g + t_s}\right). \qquad (1)$$

Figure 1b shows typical potential variations with position for the two-grid aperture configuration of Fig. 1a. As the figure suggests the ions are first accelerated through a total potential, V_T, and then decelerated to a final ion velocity corresponding to V_N. The ratio of net-to-total
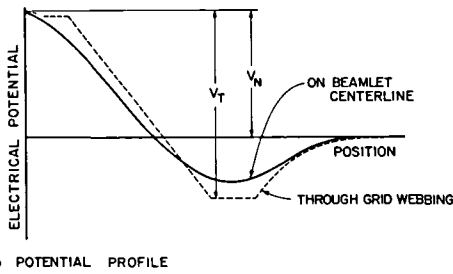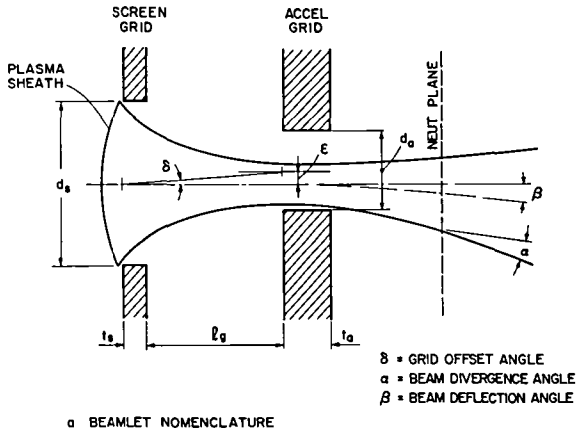
a BEAMLET NOMENCLATURE

δ = GRID OFFSET ANGLE
α = BEAM DIVERGENCE ANGLE
β = BEAM DEFLECTION ANGLE

b POTENTIAL PROFILE

Fig. 1. Beamlet Nomenclature and Potential
Variation.

voltage is designated as the R-value.

$$R = \frac{V_N}{V_T} \text{ .} \tag{2}$$

The results of this study will be presented as
a function of the normalized perveance per hole at
which the grids are operating. This quanity desig-
nated herein as "NP/H" is based on the theoretical
Child's law current density limit for ion extrac-
tion between parallel plates due to the accumulation
of space charge in the intervening gap. This law is
expressed as:

$$J = \frac{4}{9} \varepsilon_0 \left(\frac{2q}{m_i}\right)^{\frac{1}{2}} \frac{V_T^{3/2}}{\ell^2} \tag{3}$$

where j is the maximum current density, ε_0 is the
permittivity of free space, q is the charge of the
ion, m_i is the ion mass, V_T is the total accelerat-
ing voltage and ℓ is the acceleration length. If
one considers the effective acceleration length
appropriate to Fig. 1a to be the one from the
plasma sheath to the intersection of the screen
hole centerline and the upstream surface of the
accelerator grid then the length in Eq. 3 is given
by

$$\ell_e' = [(\ell_g + t_s)^2 + d_s^2/4]^{\frac{1}{2}} \text{ ,} \tag{4}$$

the theoretical limiting value of normalized per-
veance per hole is given by

$$\text{MAX. NP/H} = \frac{J_{MAX}}{V_T^{3/2}} \left(\frac{\ell_e'}{d_s}\right)^2 = \frac{\pi}{9} \varepsilon_0 \left(\frac{2q}{m_i}\right)^{\frac{1}{2}} \text{ ,} \tag{5}$$

where J_{MAX} is the maximum current per hole, and d_s
is the screen hole diameter. For the argon propel-
lant used in this study, the maximum normalized
perveance per hole is 6.8×10^{-9} A/V$^{3/2}$. It is
noted that beamlet deflection can only be achieved
at values of NP/H significantly below this limit.

Beamlet deflection can be estimated using
linear optics theory,[5,6] and modeling the accelera-
tor aperture of a two-grid system as a thin lens
with a focal length f. The focal length is given
by

$$f = 4 \frac{V_T}{(E_2-E_1)} \text{ ,} \tag{6}$$

where V_T is the potential of the accelerator grid
with respect to the screen grid and E_1, E_2 are the
potential gradients on the acceleration and decel-
eration sides of the accelerator grid, respectively.
The beamlet deflection angle, β is then given by:

$$\beta = \frac{\varepsilon}{f} \text{ ,} \tag{7}$$

where ε is the relative grid displacement. When E_1
is assumed to be equal to the total accelerating
voltage divided by the grid separation distance,
this becomes

$$\beta = -\frac{\varepsilon}{4\ell_g} \left(1 - \frac{E_2}{E_1}\right) \text{ .} \tag{8}$$

In the case where $E_2 \ll E_1$ this simplifies to:

$$\beta = -\frac{\varepsilon}{4\ell_g} \text{ ,} \tag{9}$$

or

$$\beta = -14.3 \frac{\varepsilon}{\ell_g} \text{ (} \beta \text{ in degrees).} \tag{10}$$

The minus sign indicates that beamlet deflection
occurs in the direction opposite to that of accel-
erator grid displacement. It should be noted that
in Eq. 8, E_2 and E_1 are of opposite sign so when E_2
is significant, the ratio (β/ε) should be greater
than the value given by Eq. 10.

Apparatus

The beamlet vectoring study has been conducted
on an 8 cm dia. divergent field ion source in which
the grids have been masked down to a 1 cm^2 active
area. This masking of the grids results in very
uniform plasma properties at each aperture and
hence a uniform beam. The thruster uses a tungsten
filament for both the main and neutralizer cathodes
and it operates with argon as the propellant.

The grids are fabricated from graphite sheets
with a nineteen hole array arranged in a hexagonal
pattern on them. A screen grid hole diameter of
2.06 mm was selected for the study and mica sheets
were used to maintain the spacing between the grids.
While the accelerator is held fixed, the screen
grid can be translated along one axis during thrus-

ter operation by a mechanical system in the manner suggested by Fig. 2. The screen grid was selected as the translating grid, because such an arrangement facilitated grid spacing and accelerator grid alterations.

The beam emerging from the grids is probed by a collection of molybdenum, flat plate probes each 1 cm^2 in area, arranged in the manner suggested in Fig. 2. Twenty of these probes are situated along a horizontal line 14 cm downstream from the grids. In addition, a line of probes extends vertically downward from each end of the horizontal probe rake. By using these three probe rakes it is possible to intercept the full beam profile over the complete range of grid translation. A 70% open area screen is placed in front of the probes, and is biased 24 v negative relative to ground in order to reflect neutralizer electrons. The probes themselves are biased 18 v positive relative to ground to reflect low energy, charge-exchange ions produced downstream of the grids. The rake assembly is designed so it can be rotated in the manner suggested in Fig. 2 to facilitate rake axis alignment with the beam axis in the plane perpendicular to the direction of grid translation.
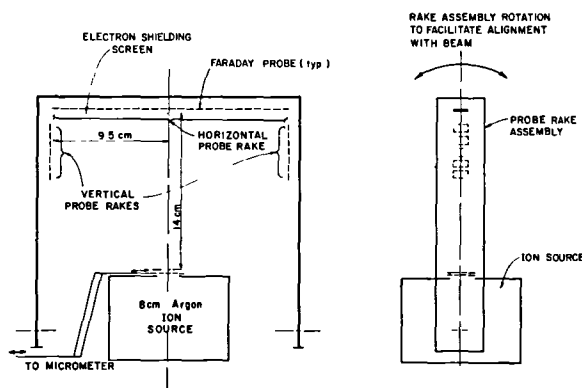
Fig. 2. Deflecting Beamlet Test Apparatus.

Procedure

A complete set of beam profiles is collected by first achieving stable ion source operation with the screen grid displaced to produce a substantial negative ion beam deflection. Once the ion beam has been probed, the screen grid is displaced in 0.05 mm increments and the beam is probed after each displacement. This process continues until the beam is displaced sufficiently positive so the accelerator grid impingement current reaches ∿ 25% of the beam current. Since a grid displacement of 0.05 mm has been shown to produce measurable beam deflection, careful alignment of the grids in the direction perpendicular to the direction of grid translation and reduction of play in the movable grid are crucial to the generation of accurate data.

Beam current density profiles are analyzed using a computer routine. This routine first uses the current density data obtained from the three segment probe rake to compute the current density on a circular arc located 17 cm from the grid center. From this profile the point of maximum current density is identified. An initial estimate of the deflection angle is then computed as the

angle between the thruster axis and the line from the screen grid center through the point of maximum current density. Next the two segments of the current density profile on either side of the maximum are averaged and the total beam current is estimated by integrating this average profile for an assumed axi-symmetric distribution about the line of maximum current density. The deflection angle value which best fits the data is then obtained by iterating assumed deflection angle values and solving for the minimum integrated beam current. The final beam current obtained in the analysis is then compared to the measured beam current to insure that they agree to within 5 to 10%. The divergence angle (α in Fig. 1) is computed as the half angle of the cone enclosing 95% of the integrated beam current determined in the aforementioned analysis. This definition of half angle is the same as the one used by Aston[3,4] in the study of divergence characteristics of aligned grids.

Initially, current density data were collected manually by reading a meter that could be switched to read each Faraday probe in the rake. These results showed the linear relationship between the grid offset angle (ϵ) and the deflection angle (β) suggested by Eq. 10 but, inconsistencies were observed when data from various runs were compared. It was determined that these inconsistencies were due in part at least to variations in ion source operating conditions that occurred while the probe currents were being read. In order to minimize this drift the manual data collection was eliminated in favor of automated collection using a Hewlett Packard 3054 Data Logger. Results obtained using the data logger have been very reproducible and self-consistent.

In order to isolate the effects of various parametric changes to be introduced in the experiment a standard grid geometry was selected and then one grid parameter was varied while other parameters were held at their standard value. The standard case selected is defined by the following geometrical and operating conditions:

Screen hole diameter (d_s)	2.06 mm
Total accelerating voltage (V_T)	600 volts
Net-to-total accelerating voltage ratio (R)	0.70
Screen grid thickness ratio (t_s/d_s)	0.18
Accelerator grid thickness ratio (t_a/d_s)	0.37
Accelerator grid hole diameter ratio (d_a/d_s)	0.64
Grid separation ratio (ℓ_g/d_s)	0.49

As suggested by the above list, the geometrical grid parameters of Fig. 1 are normalized using the screen hole diameter, which was held constant at 2.06 mm for all tests. The range of variation of the parameters investigated in this study were:

Total accelerating voltage (V_T)	600 - 1100 volts
Net-to-total accelerating voltage ratio (R)	0.35 - 0.90

Screen grid thickness
ratio (t_s/d_s)   0.18 - 0.37

Accelerator grid thickness
ratio (t_a/d_s)   0.12 - 0.74

Accelerator grid hole dia.
ratio (d_a/d_s)   0.64 - 1.00

Grid separation ratio (ℓ_g/d_s)   0.49 - 1.00

In addition, the discharge voltage was main-
tained at 40 v and the bell jar pressures were held
between 6 - 8 x 10^{-6} Torr. An argon flow rate of
10 mA equivalent was used throughout the experiments
because it was sufficiently high to produce stable
discharge chamber operation while being low enough
to keep the charge exchange ion production less
than one percent of the beam current.

Results

A typical beam ion current density profile
collected in the manner outlined in the previous
section is shown in Fig. 3a. As this figure sug-
gests, the profiles are relatively symmetrical.
This symmetry is retained within the useful range of
beam deflections. Using the information on this
profile one can determine the beamlet divergence and
deflection associated with this particular grid geo-
metry and relative grid offset. A typical plot of
deflection angle vs. grid offset angle is presented
in Fig. 3b; this one for the standard grid set
operating at a normalized perveance per hole (NP/H)
of 1.02 x 10^{-9} A/V $^{3/2}$ where

$$NP/H = \frac{J}{V_T^{3/2}} \left(\frac{\ell_e}{d_s}\right)^2 \qquad (11)$$

Figure 3b shows the expected linear relationship
between deflection angle (β) and grid offset (δ) up
to a grid offset angle of ~ 15° where the beamlets
begin to intercept the accelerator grid. The de-
flection angle at the onset of this non-linear
behavior is designated β_u (for β useful), as sug-
gested in Fig. 3b. The data shown is for the
standard case accelerator grid hole diameter ratio
of 0.64. At accelerator hole ratios near 1.00 the
beam deflection beyond β_u levels off rather than
increasing as shown in Fig. 3b. This change in the
slopes above the point where impingement begins to
increase is probably related to the observation that
the beam profiles become increasingly asymmetrical
at high grid offset angles. It should be noted,
however, that the non-linear beam deflection always
occurs at relatively high impingement levels which
are outside of the normal thruster operating regime.

The experimental deflection characteristics
illustrated in Fig. 3b can be compared with the
theoretical relation expressed in Eq. 10. From
Fig. 3b, a deflection angle (β) of 6° corresponds
to a grid offset angle (α) of 15.5° within the
linear region. Using Eq. 1 to determine ε, one
arrives at an experimental correlation of the same
form as the theoretical value given in Eq. 10,
namely

$$\beta = - 15.8 \frac{\varepsilon}{\ell_g} \quad (\beta \text{ in degrees}) , \qquad (12)$$

ARGON
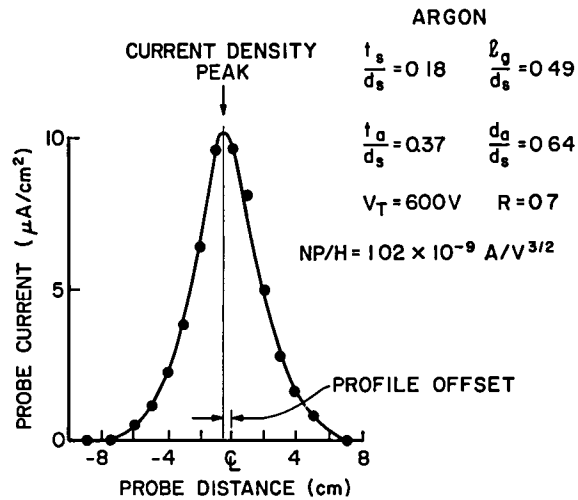
a BEAM CURRENT DENSITY PROFILE
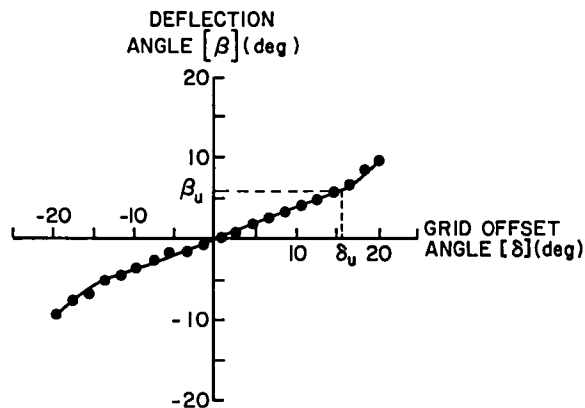
b DEFLECTION CHARACTERISTIC

Fig. 3. Typical Standard Grid Data.

The coefficient in this equation is reasonably
close to the theoretical constant of 14.3°
(1/4 rad) and is also in reasonable agreement with
previously measured values.[8] It is also noteworthy
that Eq. (8) predicts an increase in this constant
if the deceleration field E_2 is significant, as it
should be for the data of Fig. 3 where the net-to-
total accelerating voltage ratio (R) is less than
unity.

Typical divergence and impingement character-
istics for the grid set of Fig. 3 are given in
Fig. 4. It can be seen in Fig. 4a that the di-
vergence angle (α) does not vary significantly over
the useful range of grid offset angles where the
impingement currents are acceptably low and opera-
tion would normally occur. With a larger accelera-
tor grid hole diameter ratio (d_a/d_s) the divergence
angle drops slightly from the value at a significant
offset to a minimum at zero offset. Even in this
case, however, the total variation in divergence
angle over the useful range of grid offset angle
was not observed to exceed two degrees. The rapid
decrease in divergence angle apparent in Fig. 4a at
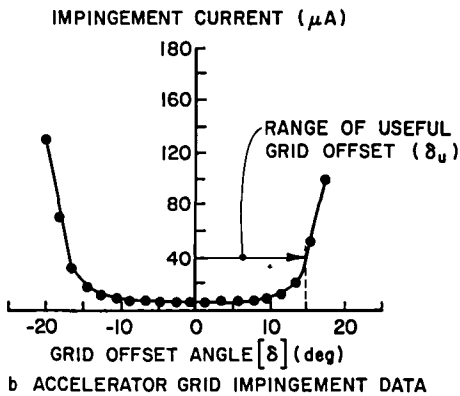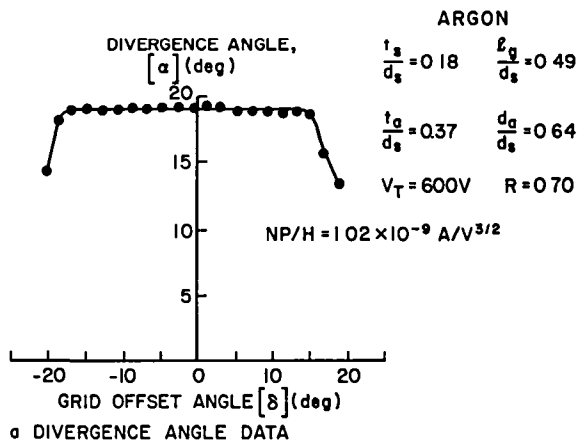large grid offset angles is probably due to inter-

90

Fig. 4. Typical Standard Grid Data.

Fig. 5. Effect of Grid Offset on Impingement Current.

ception of the most divergent ions from the beamlets by the accelerator grid. In Fig. 4b this rapid increase in accelerator grid impingement current is apparent and it defines the range of useful grid offset angles (δ_u). In order to quantify this range it is defined here rather arbitrarily as the grid offset angle at which the impingement current reaches 10% of the beam current. This sets the limit on the useful range of beam deflection (β_u) which is indicated on Fig. 3b.

The useful range of the grid offset angle (δ_u) is a function of both the geometrical parameters of the grids and the perveance at which they are operating. Figure 5 illustrates the effect of perveance on typical impingement current vs. grid offset angle plots. The two values of useful range of grid offset angle (δ_u) appropriate to the two levels of perveance are identified and they show that the limiting offset angle drops as the perveance is increased. This presumably occurs because the beamlet more nearly fills the accelerator grid aperture at the higher perveance level. Using a collection of data like those shown in Figures 3 and 4, one can define a group of parameters that characterize the optical behavior of deflected ion beamlets. The parameters that have been selected for use here are:

1. The useful ion beamlet deflection range (β_u)

2. The deflection-to-offset angle ratio in the useful range (β/δ)

3. Divergence angle in the useful range (α)

Effect of Grid Offset on Beamlet Divergence

The assumption that a single divergence angle characterizes the beamlets over the range of useful deflection (3 above) is supported by the results of Fig. 6, which show that the divergence angle is independent of grid offset angle over the full range of perveance. The divergence angle results also agree to within $\pm 2°$ with those obtained by Aston[3] using aligned grids. In comparing these results it should be noted that a slightly different definition of the effective ion acceleration length is used to compute the perveances.[9] In Aston's results the effective acceleration length is defined as:

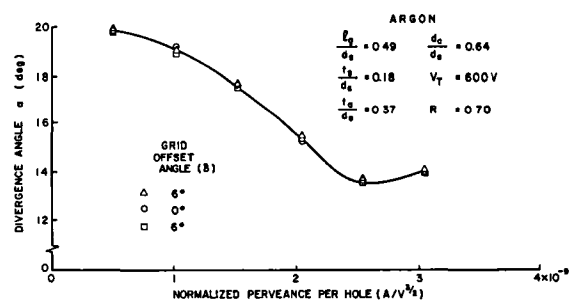$$\ell_e = \left[\ell_g^2 + d_s^2 \frac{}{4}\right]^{\frac{1}{2}},$$

Fig. 6. Effect of Grid Offset on Beamlet Divergence.

whereas in the present work the screen grid thickness is also incorporated in the definition of acceleration length as·

$$\ell_e' = \left[(\ell_g + t_s)^2 + \frac{d_s^2}{4}\right]^{\frac{1}{2}} \quad .$$

Figure 7 shows the effects of net-to-total voltage ratio (R) on beamlet divergence (α). These typical curves again agree reasonably well with those obtained by Aston.[3] Because of this agreement divergence curves will not be presented here for each parameter investigated, rather the reader is referred for divergence angle data to Aston's work[3] which utilized fixed grids and is therefore considered to give more accurate divergence angles than the present study.
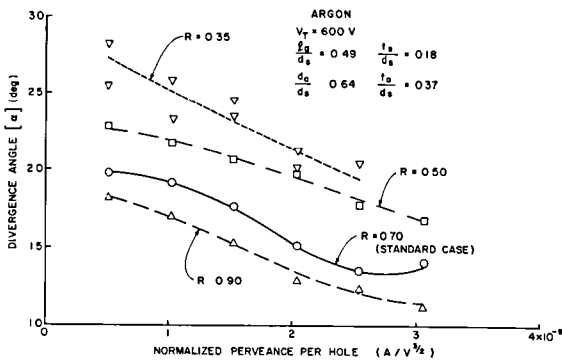
Fig. 7. Effect of Net-to-Total Accelerating Voltage Ratio on Divergence.

Effect of Normalized Perveance Per Hole

The effect of increasing the normalized perveance at which the grid set is operating always has the effect of decreasing the usable deflection angle range. As perveance is increased an unacceptable impingement level is eventually observed even at the zero grid offset condition. If a moderate beamlet steering capability is desired, this suggests the grid-hole pair must be operating well below the maximum obtainable, aligned-grid perveance. Figure 6 shows the shape of a typical divergence angle vs. perveance curve. One would generally want to operate at the minimum of this curve, but this corresponds to a rather high perveance condition where the beamlet cannot be deflected substantially without inducing a high impingement. Consequently, although the divergence angle shows little change with grid offset, the beamlets would generally have to be operating at a perveance below the one for minimum divergence in order to facilitate operation at a moderate offset without high impingement. All of the experiments suggested that perveance had no significant effect on the deflection-to-offset angle ratio (β/δ).

Effect of Grid Separation Distance

The deflection angle range is observed in Fig. 8 to decrease as the separation distance between the grids is increased. This can be explained by noting that the total voltage remains constant as the separation distance is increased and

that this results in a weaker electric field between the grids. Linear optics theory suggests this will result in less beamlet deflection for a given grid displacement (the grid separation appears in the denominator of Eq. 8). Figure 9 shows that the ratio of the beamlet deflection angle to the grid offset angle is independent of the grid separation ratio over the full range of perveance investigated. This is not surprising because one can combine a first order expansion of Eq. (1) and Eq. (9) together and obtain the expression for this deflection-to-grid offset ratio. It shows this ratio should indeed be independent of the grid separation ratio to first order for this case of a thin screen grid. The independence of the deflection angle-to-grid offset ratio also confirms its preference as a correlating factor over other factors such as the ratio of deflection angle to the linear offset displacement (β/ϵ).
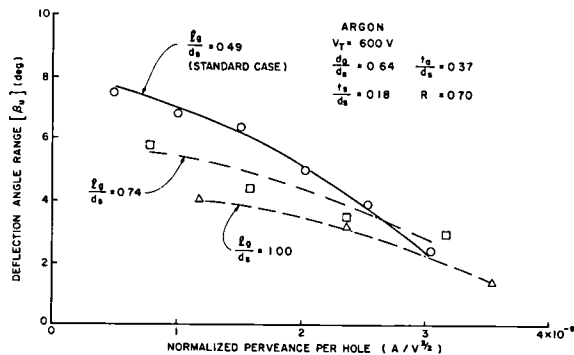
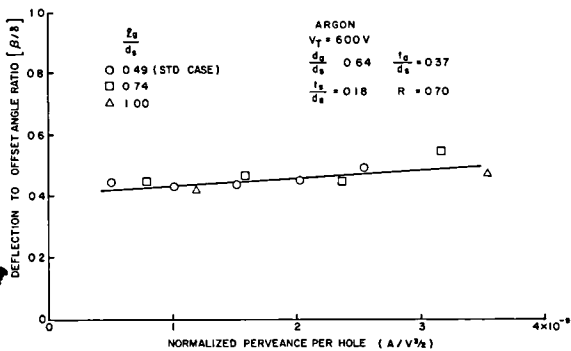Fig. 8. Effect of Grid Separation Distance on Deflection Angle Range.

Fig. 9. Effect of Grid Separation Distance on Deflection-to-Offset Angle Ratio.

Effect of Accelerator Hole Diameter

Accelerator hole diameters larger than the standard value enable grid sets to operate over much larger deflection angle ranges, as shown in Fig. 10. This is presumably due to the fact that the beamlets have more room to deflect before being intercepted by the accelerator grid. Figure 10 also shows that larger accelerator holes will permit a given beamlet deflection at a much higher perveance level; power supply limitations prevented operation at impingement limited perveance levels with the larger accelerator grid hole diameters

used in this study. As Fig. 11 shows, the accelerator hole diameter had no significant effect on the deflection-to-offset angle ratio.
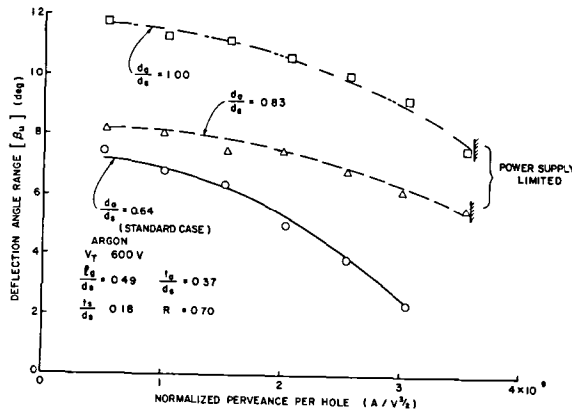

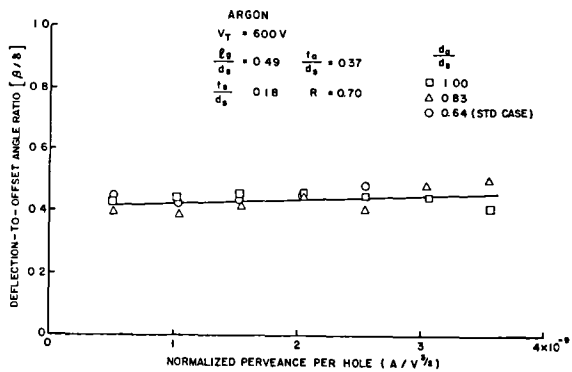Fig. 10. Effect of Accelerator Grid Hole Diameter on Deflection Angle Range.

Fig. 11. Effect of Accelerator Grid Hole Diameter on Deflection-to-Offset Angle Ratio.

Effect of Net-to-Total Accelerating Voltage Ratio

The net-to-total voltage ratio (R) has a moderate effect on the deflection-to-offset angle ratio (β/δ). As the R-value decreased from 0.90 to 0.35, β/δ increased from 0.4 to 0.6, as shown in Fig. 12. This is explained by considering that at a constant total voltage, a decrease in the R-value is accompanied by a decrease in the net acceleration voltage and hence in the ion velocity. The ion is then subjected to the lens effect of the accelerator aperture for a longer time and this results in a larger deflection angle for a given grid displacement. The deflection angle ranges as depicted in Fig. 13, show only a slight dependence on the R-value as long as it is greater than about 0.5. When the R-value is reduced to about 0.35 however the deflection range becomes more restricted at the higher perveances. This effect is presumably due to the fact that beamlets which become more divergent at low R-values begin to intercept the accelerator grid at a lesser grid offset angle.
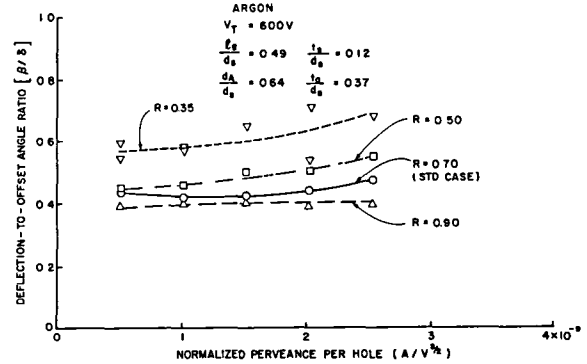
Fig. 12. Effect of Net-to-Total Accelerating Voltage Ratio on Deflection-to-Offset Angle Ratio.
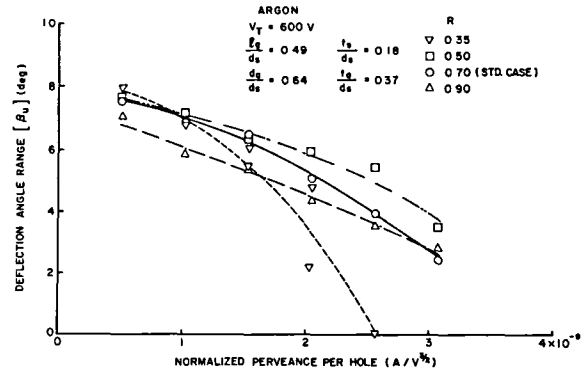

Fig. 13. Effect of Net-to-Total Accelerating Voltage Ratio on Deflection Angle Range.

Effect of Accelerator Grid Thickness

As shown in Fig. 14, the accelerator grid thickness had no significant effect on the deflection-to-offset angle ratio. However, in Fig. 15 the thick accelerator grid is seen to exhibit a pronounced reduction in deflection angle range. This is considered to be due to the fact that interception of the beamlet on the downstream edge of the accelerator grid occurs at a much smaller grid displacement with the thickest grid. It is noteworthy that a very thin accelerator grid showed no improvement in the deflection angle range over that observed for the standard case thickness.
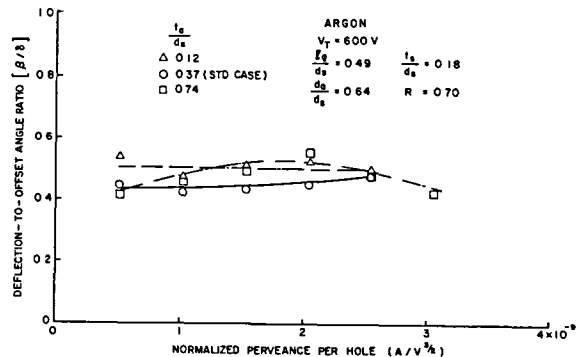

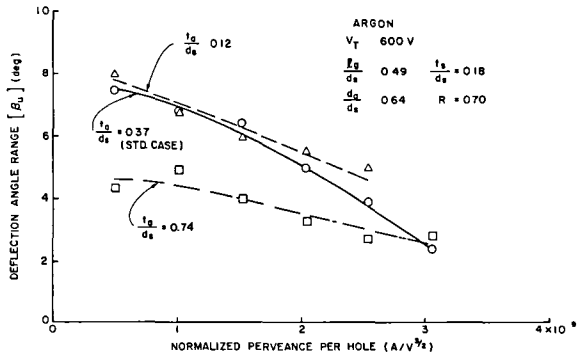Fig. 14. Effect of Accelerator Grid Thickness on Deflection-to-Offset Angle Ratio.

Fig. 15. Effect of Accelerator Grid Thickness on
Deflection Angle Range.

Effect of Screen Grid Thickness

The effect of doubling the standard screen
grid thickness on the deflection characteristics of
beamlets is examined in Figs. 16 and 17. This
change had only a slight effect on the beamlet de-
flection characteristics. A slight reduction in
deflection range was observed for the thicker screen
grid as illustrated in Fig. 16. This is supported
by previous work by Aston[3] which shows that thinner
screen grid geometries are capable of achieving
slightly higher perveances. This is consistent with
the fact that the thinner screen grid exhibits a
slightly higher deflection angle range at a given
perveance level. There appears to be a slight dif-
ference in the deflection-to-offset ratio for dif-
ferent screen grid thicknesses as shown in Fig. 17.
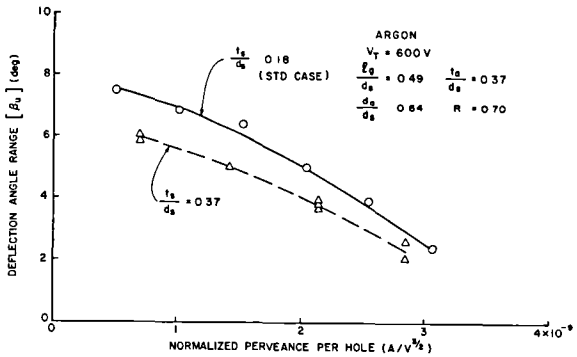

Fig. 16. Effect of Screen Grid Thickness on
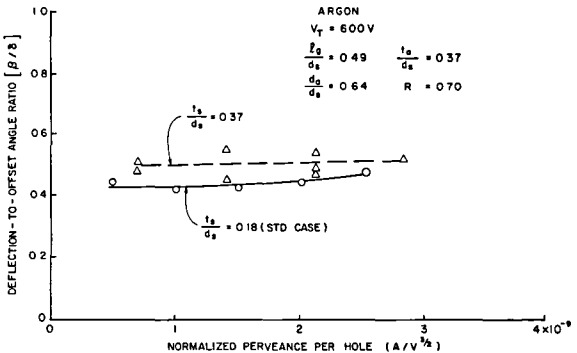Deflection Angle Range.

Fig. 17. Effect of Screen Grid Thickness on
Deflection-to-Offset Angle Ratio.

Effect of Total Acceleration Voltage

An inspection of Eq. 8, which pertains to
linear optics theory, reveals that the total ac-
celeration voltage does not appear so this para-
meter would not be expected to affect the beamlet
deflection parameters to first order. Figures 18
and 19 do show however that these parameters were
affected somewhat by a change in total accelerating
voltage from 600 v to 1100 v. Figure 18 reveals a
larger deflection angle range over the complete
perveance range at the higher voltage. Figure 19
shows that while the magnitudes of the deflection-
to-offset angle ratio are comparable at the two
voltages, changes in perveance seem to induce a
greater change in this ratio at the higher voltage.
It should be noted that some of the data on
Figs. 18 and 19 involved operation of the ion
source at a slightly higher discharge voltage and
magnet current. This did not appear to alter the
data trends. It was done so the ion source dis-
charge could be sustained at the higher beam cur-
rents associated with operation at the 1100 v
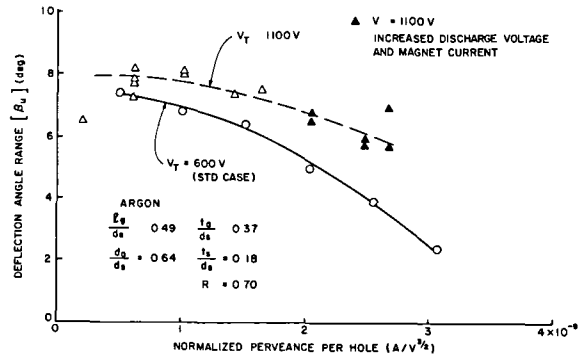condition.

Fig. 18. Effect of Total Accelerating Voltage on
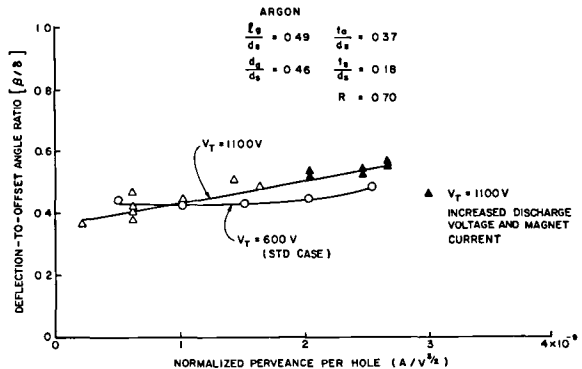Deflection Angle Range.

Fig. 19. Effect of Total Accelerating Voltage on
Deflection-to-Offset Angle Ratio.

Dished-Grid Example

In this section the beamlet vectoring data
presented in the previous section of this paper
will be used to examine the beamlet deflections that
would be expected in a sample dished-grid geometry.
The objective is to determine the effects of such
design factors as dish depth and beamlet steering on

94

the impingement characteristics of a dished-grid set. In order to conduct this analysis the current density profile and thermal distortion characteristics of a typical dished-grid system will be examined.

The parameters used to define the particular spherically dished grid set considered here are shown in Fig. 20. The beamlet pattern shown suggests aligned screen and accel grid holes that would cause the beamlets to emerge in this divergent pattern. Using current density profile data for a typical ion source together with reasonable values for grid geometric parameters, the radial screen/accel grid hole displacement profile needed to correct this condition will be determined. At this operating condition the beamlets would be aligned with the thruster axis. In addition, the impingement limited perveance will be calculated as a function of grid radius using the deflection angle range data present in this paper. This will enable one to determine where high impingement might be expected over the surface of the grids.
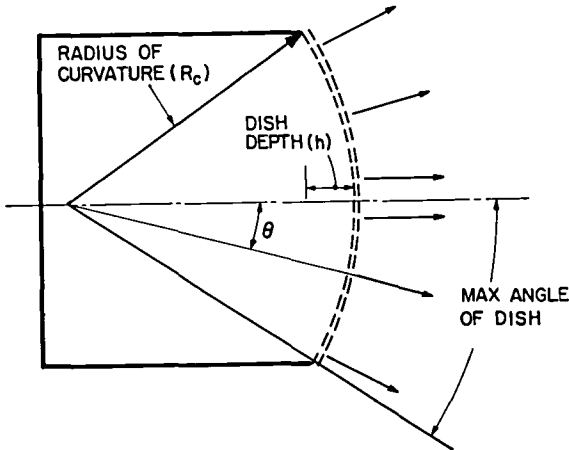

Fig. 20. Dished Grid Geometry.

The thruster selected was the 30 cm dia. 800 series Engineering Model Thruster. The current per hole data required as input for analysis of the grids when this thruster is operating at a 2.0 A beam current are shown in Fig. 21.[10] These data were obtained using mercury propellant, so the current per hole cited in Fig. 21 had to be multiplied by the square root of the mercury to argon atomic mass ratio to obtain the allowable perveance data needed for comparison. In order to determine the grid separation distance and relative hole positions at operating temperature, the linear expansion model of Rawlin, Banks, and Byers[11,12] was applied to the molybdenum grids and support rings. This model may not be applicable to all grid assemblies, but it is useful here to illustrate the application of beamlet vectoring data to the analysis of dished-grid accelerator systems.

When grids are dished and then provided with the desired separation distance, the screen-accelerator hole pairs become mis-aligned, and the beamlets are directed severely off-axis. This requires hole-pattern compensation, which for grids
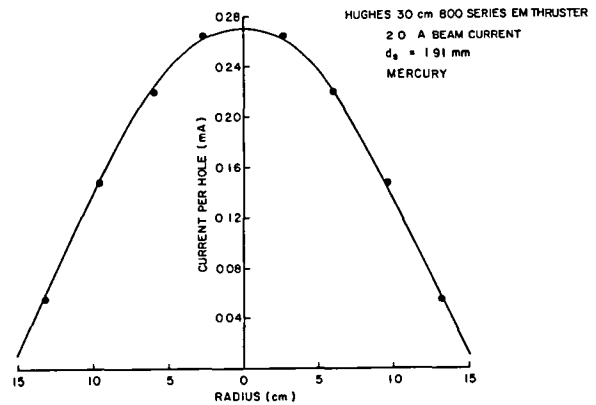

Fig. 21. Current per Hole Profile for Sample 30 cm Thruster.

dished convex downstream (Fig. 20), implies an accelerator grid hole pattern with center-to-center hole spacings increased or a screen grid with hole spacings reduced. By using some compensation a grid-hole pair can be re-aligned to the zero offset angle condition, however, an additional amount will be required in order to cause each beamlet to be directed parallel to the thruster axis. In order to accomplish this the accelerator grid hole spacings are designed to be $(1 + \epsilon_a)$ times the screen hole spacings. Figure 22 shows how the grid hole offset angles vary for a given grid dish depth as a function of radius under the influence of the indicated compensations (ϵ_a's) and the thermal gradients that the grid thermal model[10,11] predicts. Also shown in Fig. 22 as a solid line is the grid offset required as a function of radius to produce para-axial beamlets. It is determined from a deflection-to-offset plot (Fig. 12 for R = 0.70 in this case) using as input the angular separation between the thruster centerline and the normal to
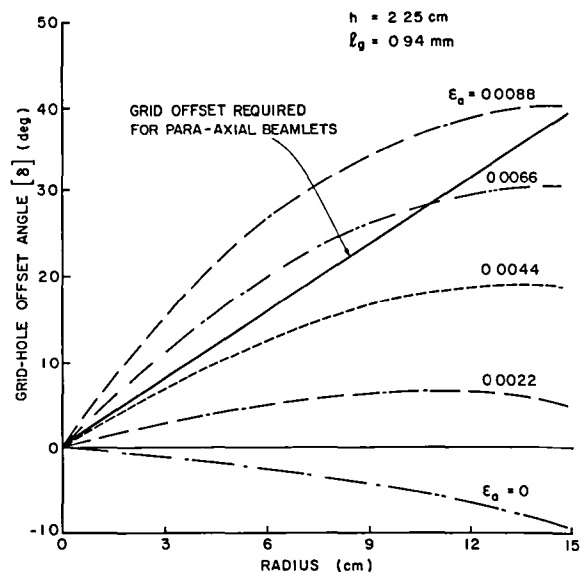

Fig. 22. Dished Grid Offset Angles for Varying Accelerator Grid Compensation, h = 2.25.

the accel grid surface at each radius for the 30 cm thruster (θ's in Fig. 20). Figure 23 presents the same type of data as Fig. 22 but in this case the dish depth is less. The magnitude of the dish depth affects the value of grid offset needed to re-align beamlets with the thruster centerline. A comparison of Figs. 22 and 23 shows that the smaller dish depth requires much less grid offset for the outer radius holes, and therefore it would be expected that the outer holes could then be operated at higher perveance levels. The drawback to using a smaller dish depth is that this leads to greater variations in the screen hole to accelerator hole separation distance as a function of operating temperature. It is apparent from Figs. 22 and 23 that a single value of accel grid compensation (ε_a) does not produce the required grid offset over the entire grid surface for the thermal deformations assumed here. This situation worsens as the dish depth is reduced.
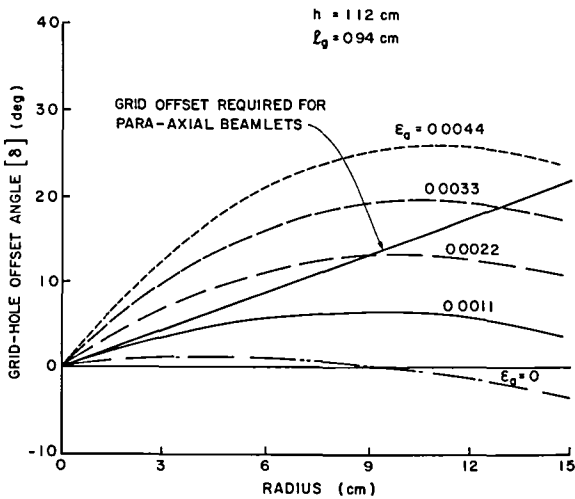
optimum dish depth seems to fall approximately midway between h = 2.25 cm and h = 1.12 cm. At zero radius, the estimated perveance profile drops with decreasing dish depth. This is due to the decrease in separation gap which is a maximum at the centerline and is more pronounced at small dish depths (the screen grid is assumed to be hotter than the accelerator grid and therefore expands more). These problems could be alleviated somewhat by varying the initial grid separation and accelerator grid hole size as a function of thruster radius.
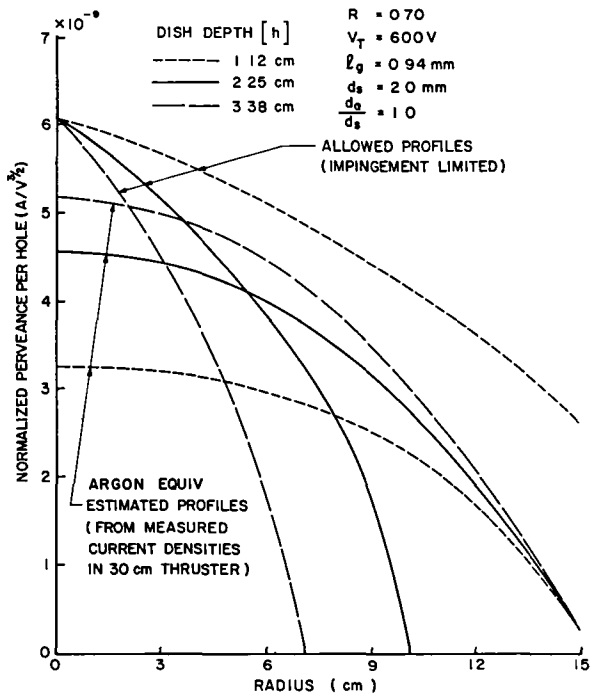

Fig. 23. Dished Grid Offset Angles for Varying Accelerator Grid Compensation, h = 1.12.

Fig. 24. Typical Comparison of Allowed Perveance and Estimated Perveance for 30 cm Dished Grids of Varying Dish Depths

Figure 24 shows perveance limit design plots for the sample case being considered. The allowed perveance profiles in this figure were determined by computing the angular displacement between the thruster centerline and normal to the grid surface at each radial location (θ's in Fig. 20). This information is then used to enter the useful deflection range plots (Fig. 10 for d_a/d_s = 1.00 in this case) in this paper to determine the maximum perveance allowed for a given deflection angle at each radial location before direct accelerator grid impingement becomes excessive. Also shown in Fig. 24 are the estimated perveance profiles that would be observed in the 30 cm thruster operating at the current per hole values of Fig. 21 with the dish depths indicated on Fig. 24 and the computed grid thermal distortions. It can be seen from Fig. 24 that the allowed profile for the shallowest dish depth (h = 1.12 cm) is above the corresponding estimated profile at all radii. This indicates the impingement levels will be low over the entire accelerator grid surface in this case. For the greater dish depth curves however the allowed profiles fall below the estimated ones at the greater radii. In this case impingement would be expected to be more substantial. For the case under consideration the

A potential problem also exists for large diameter multipole thrusters and is worthy of mention. As seen in Figs. 22 and 23 relatively large offset angles may be required for the apertures at the outer edges of the grids on large diameter thrusters. Because of the flatter plasma density profiles in multipole thrusters, these outer radius holes may be expected to operate at higher perveance values and this would be expected to create even more severe impingement problems when the beamlets are re-directed parallel to the thruster axis than was observed in Fig. 24 for the 30 cm divergent field thruster.

Conclusion

Ion beamlet deflections of several degrees can be accomplished by displacing the screen and accelerator grid holes relative to each other. This deflection is limited to a useful range by the onset of high accelerator grid impingement currents. This range is primarily dependent on the perveance at which the grid is operating and the diameter of the accelerator grid aperture. The useful range is

also dependent to a lesser extent on the net-to-total voltage ratio, grid separation distance, grid thicknesses, and the total accelerating voltage. Over the useful range of beam deflections the beamlet divergence angle is independent of deflection. In this range the deflection angle is also a linear function of the grid offset angle. The constant of proportionality between these angles exhibits a dependence on the net-to-total accelerating ratio but is relatively independent of the other parameters studied. Good agreement between the theoretical approximation and experimental results for this constant has been demonstrated. The beamlet deflection data developed in this study can be used to design large diameter dished-grid accelerator systems in which the ion beamlets are to be directed along the thruster axis. An important design parameter that is crucial to the maintenance of low impingement currents in these designs is the grid dish depth.

References

1. Latham, W. C. and W. B. Adam, "Theoretical Analysis of a Grid Translation Beam Deflection System for a 30 cm Diameter Kaufman Thruster," NASA TM X-67911, 1971.

2. Kaufman, H. R., J. M. E. Harper, and J. J. Cuomo, "Focused Ion Beam Design for Sputter Deposition," Journal of Vac. Science & Tech., May/June 1979, pp. 899-905.

3. Aston, G., "The Ion-Optics of a two-Grid Electron-Bombardment Thruster," NASA CR-135034, May 1976.

4. Aston, G., Kaufman, H. R., and Wilbur, P. J., "The Ion Beam Divergence Characteristics of Two-Grid Accelerator Systems," AIAA Journal, Vol. 16, No. 5, May 1971, pp. 516-524.

5. Kaufman, H. R., "Technology of Electron Bombardment Ion Thrusters," Advances in Electronics and Physics, Vol. 36, Academic Press Inc., San Francisco, 1974, pp. 324-327.

6. Whealton, J. H., "Linear Optics Theory of Ion Beamlet Steering," Rev. of Sci. Instrum., Vol. 48, No. 11, 1977, pp. 1428-1429.

7. Spangenberg, K. R., Vacuum Tubes, McGraw Hill, New York, 1948, pp. 350-356.

8. Stewart, L. D., Kim, J., and Matsuda, S., "Beam Focusing by Aperture Displacement in Multi-ampere Ion Sources," Rev. Sci. Instrum., Vol. 46, No. 9, Sept. 1975, pp. 1193-1196.

9. Wilbur, P. J., Advanced Space Propulsion Thruster Research, NASA CR-165584, pp. 127-130.

10. Poeschel, R, L., et. al., "High Power and 2.5 kw Advanced Technology Ion Thrusters," NASA CR-135163, 1977, p. 34.

11. Rawlin, V. K., Banks, B. A., and Byers, D. C., "Design, Fabrication, and Operation of Dished Accelerator Grids on a 30-cm Ion Thruster," NASA TM X-68013, 1972.

12. Rawlin, V. K., Banks, B. A., and Byers, D. C., "Dished Accelerator Grids on a 30-cm Ion Thruster," Journal of Spacecraft and Rockets, Vol. 10, No. 1, Jan., 1973, pp. 29-35.

AIAA'82

AIAA-82-1936
The Flexible Magnetic Field Thruster

J. R. Brophy and P. J. Wilbur, Colorado State
Univ., Fort Collins, CO

AIAA/JSASS/DGLR 16th International
Electric Propulsion Conference

November 17-19, 1982/New Orleans, Louisiana

THE FLEXIBLE MAGNETIC FIELD THRUSTER*

John R. Brophy** and Paul J. Wilbur+
Colorado State University
Fort Collins, Colorado 80523

Abstract

The flexible magnetic field thruster is a unique research tool for studying the behavior of direct current electron-bombardment thrusters. It utilizes a long wire anode shielded by a circumferential magnetic field. The magnetic field around the anode, which is produced by passing a direct current of up to 150 amperes through the wire, restricts primary electron flow from the discharge plasma to the anode. Different magnetic field configurations can be created by routing the anode wire in various ways through the discharge chamber. Divergent, cusped and multipole magnetic field configurations have been created in this manner. The thruster is also designed so ion currents to various internal surfaces can be measured directly and these measurements facilitate calculation of the distribution of ion currents within the discharge chamber. Experiments indicate that the distribution of ion currents inside the discharge chamber is strongly dependent on the shape and strength of the magnetic field but independent of the discharge current, discharge voltage, and neutral flow rate. Measurements of the energy cost per plasma ion indicate that this cost decreases with increasing magnetic field strength due to increased anode shielding from the primary electrons. Energy costs per argon plasma ion as low as 50 eV were measured. The energy cost per beam ion was found to be a function of the energy cost per plasma ion, extracted ion fraction and discharge voltage. Part of the energy cost per beam ion goes into creating many ions in the plasma and then extracting only a fraction of them into the beam. The rest of the energy goes into accelerating the remaining plasma ions into the walls of the discharge chamber. Measurement of ion fluxes across a virtual anode surface appear to indicate that ions cross this surface with velocities approaching their random thermal velocity rather than the Bohm velocity.

Introduction

A great deal of effort has been expended over the last two decades on research to improve the efficiency of electron-bombardment ion thrusters. Much of this effort has centered on the containment of the high energy or primary electrons in the main discharge region of the thrusters, and has resulted in a rather interesting evolution of the thruster magnetic field configurations.[1,2] In spite of this effort the energy cost per beam ion (in electron volts) for most thrusters is still on the order of

15 to 30 times the first ionization potential energy of the propellant atoms.‡ For example, the J-series thruster[3] using mercury, operates with a discharge power of 190 eV/beam ion at a beam current of 2 amps and a 32 volt discharge. This is a factor of 18 greater than the first ionization potential for mercury. For SERT II[4] this factor is about 22. Ramsey's magnetoelectrostatic thrusters[5] typically operate with factors of 16 for both argon and xenon as did Sovey's argon line-cusp thruster.[6] Multipole thrusters of Isaacson,[7] using xenon, and Longhurst,[8] using mercury, operated with discharge power losses around 18 and 26 times the respective ionization potentials.

Dugan and Sovie[9] have shown that the energy required to produce an argon ion in plasmas similar to that commonly found in ion thrusters should be on the order of 50 eV. That this energy is greater (by approximately a factor of 3) than the ionization potential is due primarily to the fact that the ionization process is accompanied by some excitation of the neutral atoms. Inherent in this analysis is the assumption that electrons lose energy through inelastic collisions with the neutral atoms exclusively, i.e. that electron energy losses to the walls are negligible. In the case of ion thrusters, this condition is approximately satisfied when the primary electrons are prevented from reaching the anode by a magnetic field and when only low energy electrons are removed from the plasma at the anode. Thus, it should be expected that a properly designed ion thruster (i.e., one which prevents primary electrons from having direct access to the anode) would produce argon ions in the plasma at an approximate energy cost of 50 eV.

This indicates that the high energy cost per beam ion of typical thrusters is not the result of inefficient plasma ion production, but rather it is the result of the fact that the fraction of these ions being extracted into the beam is substantially less than unity. If every ion produced in the plasma was extracted into the beam, the thruster would be operating at a discharge power level of 50 eV/beam ion (50 watts/beam ampere). This is probably the maximum energy efficiency that could be expected for an argon thruster.

To approach this maximum efficiency one must understand the behavior of, and be able to control, the ion currents inside the discharge chamber. The flexible magnetic field thruster was developed to study the behavior of these ion currents. The unique features of this thruster are that it allows drastic changes in its magnetic field configuration to be accomplished quickly and easily, and that it is designed so ion currents can be measured to its various interior surfaces. Changes in magnetic field configuration are made possible through the use of a copper wire anode through which a direct

---

** Research Assistant, Department of Mechanical Engineering.

+ Professor, Department of Mechanical Engineering, Member AIAA.

‡ For operation at the "knee" of the discharge power-propellant utilization curve.

99

current on the order of 100 amps is passed. This current sets up a circumferential magnetic field around the anode. The anode wire may then be bent into any shape inside the discharge chamber to produce the magnetic field configuration of interest. Axial, mildly divergent, strongly divergent, cusped and multipole magnetic field configurations have all been created with this thruster.

This paper provides a detailed description of the flexible magnetic field thruster design and some of the results obtained with it. These results include the measurement of ion currents to all thruster cathode potential surfaces. From these data the total ion production rate, energy cost per plasma ion and extracted ion fraction were calculated. In this study these performance parameters were monitored as magnetic field configuration and strength, discharge current, discharge voltage and neutral flow rate were varied.

Apparatus and Procedure

The primary feature of the flexible magnetic field thruster is the anode. It is made from a 3.2 mm diameter copper tube through which a relatively large direct current is passed. In designing the thruster the magnitude of the currents needed to produce fields that will prevent primary electrons from reaching the anode surface were first computed to insure they would be reasonable. This was done by recognizing that the magnetic flux density (B) at a radius (r) from the centerline of a wire carrying a current (J_f) is given by

$$B = \frac{\mu_0 J_f}{2\pi r} , \qquad (1)$$

where μ_0 is the permeability of free space. It has been assumed in writing this equation that the radius (r) where the field is sought is greater than the wire radius (r_0). In order to prevent collection of electrons having an energy E_e (in eV) Isaacson found the following condition on the integral of the magnetic flux density had to be satisfied in a similar geometrical situation[10]

$$\int_{r_0}^{r_1} B dr \geq 6.74 \times 10^{-6} \sqrt{E_e} . \qquad (2)$$

In this expression r_1 is either the radius at which the magnetic flux density drops to a negligible value or the radius at which electrons are injected into the magnetic field, whichever is less. Combining Eqs. 1 and 2 and performing the indicated integration one can solve for the current required through the wire. After substituting for the permeability one obtains

$$J_f = \frac{33.7 \sqrt{E_e}}{\ln\left[\frac{r_1}{r_0}\right]} . \qquad (3)$$

For 40 eV primary electrons, a 1.6 mm radius wire and a radius of electron injection in the radius range of 1 to 2 cm the required magnetic field current given by Eq. 3 is about 100 A. This is large, but not unacceptably so. For a 1.6 mm radius anode of the order of a meter in length further analysis suggests that copper can carry the required current with a small voltage drop over the one meter tube

length (~ 0.1 V) as long as the wire is maintained at a sufficiently low temperature ($\sim 80°C$). Computations suggest this temperature can be maintained by using commercially available 3.2 mm dia. copper tube and circulating water through it at a flow rate of a few tens of ml/min.

The basic stainless steel, sheet metal chamber used to house the anodes in this study is shown schematically without an anode in Figure 1d. For all of the data presented here this chamber was 17 cm in diameter and 12 cm long. The other sketches in Fig. 1 show perspective cutaway views of anode configurations examined in this study. The magnetic field shapes produced by these windings are also shown. The refractory wire cathode used

a) DIVERGENT CONFIGURATION   RESULTING FIELD SHAPE

b) CUSPED CONFIGURATION   RESULTING FIELD SHAPE

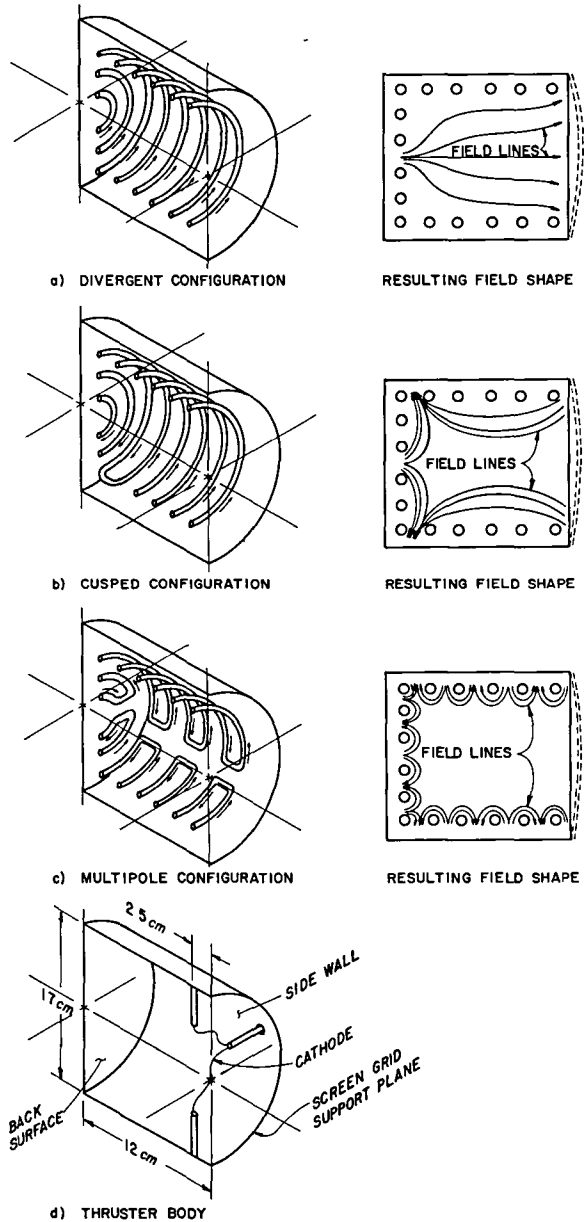c) MULTIPOLE CONFIGURATION   RESULTING FIELD SHAPE

d) THRUSTER BODY

Fig. 1   Flexible Magnetic Field Thruster Configurations.

in the tests was positioned 2.5 cm upstream of the grids in the manner suggested in Fig. 1d for all anode configurations. The cathode employed 0.25 mm dia. tungsten wire about 30 cm in length. This wire was heated using alternating currents in the range 12 to 15 A from a center-tapped power supply. Argon propellant was used because of the ease with which flow rates could be set and maintained. Tests were conducted at flow rates of 740, 1270 and 1580 mA equivalent. Thruster performance was measured at discharge voltages through the range of 30 V to 50 V above the cathode center tap potential. The discharge current was adjusted through the range 2 A to 6 A by controlling the alternating current through the refractory cathode.

The grids used in the tests had a 67% open area screen and a 30% open area accelerator. They were operated at a total accelerating voltage of 1500 V and a net-to-total accelerating voltage ratio of 0.67 with a cold grid spacing 0.75 mm. Beam neutralization was accomplished using a refractory wire cathode. All tests were conducted in the 1.2 m dia x 4.6 m long vacuum test facility at Colorado State University.

To facilitate the measurement of ion currents to various thruster surfaces the following features were incorporated into the design of the discharge chamber. The thruster back surface, cylindrical side wall, screen grid and cathode were all electrically isolated from each other. The positive high voltage was connected directly to the cathode center tap. The back surface, side wall and screen grid were connected to this point through one ohm resistors and through a power supply that was used to bias these surfaces negative of cathode potential. During thruster operation, these surfaces could be biased to -70 V (relative to cathode potential). At this bias, electron collection on these surfaces was eliminated and the ion current to each surface could be determined by measuring the voltage drop through each resistor. It is noted that ion currents going to the anode surface and recombining there are not counted when measurements are made in this way. Due to the difficulty of measuring the ion current to the anode surface it was decided to treat the ion-electron recombination there as if it were a volume recombination process. That is the energy lost as a result of ion neutralization at the anode surface was included in the overall average energy cost to produce a plasma ion. Further, the anode area exposed to the plasma was relatively small compared to the area of the cathode potential surfaces and was held constant for each of the configurations of Fig. 1. Thus the ion current to the anode could be safely neglected when measurements of the total ion production rate were made.

Applying a large negative bias to the various discharge chamber surfaces did not significantly alter the discharge chamber operation. When the bias was applied, the current from each surface rose from zero (at floating potential) to the value corresponding to the ion current being collected. As the negative bias on a surface was increased the discharge and beam currents would also increase. The discharge current increase was caused by the collection, at the anode, of additional electrons which had previously neutralized the ions at the walls by coming directly from the plasma. When the negative bias was applied these electrons could no longer neutralize the ions at the walls directly from the plasma, but rather they had to be collected by the anode and then be passed through the discharge power supply so they could reach the walls. The beam current increase associated with biasing discharge chamber surfaces is a result of the increase in discharge current brought on by the phenomenon just described. In conducting the tests it was found that when the discharge current was restored to its original value the beam current would also return to its original value. This indicates that the thruster discharge chamber efficiency was the same, regardless of whether the back, side and screen surfaces were allowed to float, or were biased strongly negative of cathode potential -- provided the discharge current was held constant. At first glance, this is a rather remarkable result. In the floating case the ions reaching the walls are neutralized there by high energy electrons from the plasma. In the other case the ions are neutralized by electrons from the discharge supply which are primarily low energy electrons collected by the anode and then pumped up to the discharge chamber surface potential through the anode power supply. That these two conditions should result in identical discharge chamber efficiencies requires an explanation.

With the walls floating the discharge current, J_D, is the sum of the cathode emission current, J_E, and the beam current, J_B, so that,

$$J_D = J_E + J_B \ . \tag{4}$$

In this case the ions are neutralized at the walls by high energy electrons emitted by the cathode. When the walls are biased sufficiently negative of the cathode potential so that no electrons from the plasma can reach them, the discharge current becomes,

$$J_D = J_E' + J_B + J_W \tag{5}$$

where J_W is the magnitude of the ion current to the walls -- a current that remains unchanged as the walls are biased negatively. Now, if the discharge currents of Eqs. (4) and (5) are to be made equal and if, at this condition the beam currents are equal, then the cathode emission current (J_E') in Eq. (5) must be decreased by an amount equal to J_W. That is the rate at which high energy electrons are injected into the plasma for the case where the walls are highly negative must be reduced by an amount exactly equal to the rate at which high energy electrons were lost to the walls in the first case. This results in the density of high energy electrons being the same in both cases, and since everything else was held constant, the efficiency must be unchanged.

By measuring the ion current to the thruster body and screen grid in the manner suggested above one is provided with a powerful tool for evaluating thruster performance. It is really an extension of the Langmuir probe technique proposed by Sovey[6] and is essentially the same approach used by Siegfried in studying hollow cathodes.[11] In this case however the back surface, side wall and screen grid act as probes. The value of the measurement lies in the fact that the sum of the body and screen grid ion currents represents the current of ions produced in the chamber but not extracted through the grids. The sum of this current and the beam

current is the total ion production rate (expressed as a current). Knowing this total ion production rate one can compute the fraction of ions produced that are extracted (beam current-to-total production rate ratio) and the energy cost of a plasma ion (discharge power-to-total production rate ratio). The first of these parameters indicates the efficiency of the discharge chamber in directing ions through the grids; the second the efficiency of discharge chamber electrons in producing ions.

Results and Discussion

Existing Thruster Designs

In the first part of this study three thruster magnetic field configurations were examined: the divergent field, the single cusped field and the multipole configuration. Each of these configurations was easily created with the flexible field thruster. Figure 1 shows these configurations and how the anode wire must bend in order to create each particular magnetic field shape. In each of these three configurations the loop separation was approximately 2 cm and the total anode length exposed to the plasma was 280 cm. In addition, the volume and surface area of the region bounded by the anode was the same for each configuration. The effect of increasing the magnetic field strength for the divergent field thruster configuration is illustrated in Fig. 2. In this figure the fractions of total ion current produced (J_p) which go to: the back surface (J_{back}/J_p), the side wall (J_{side}/J_p), the screen grid (J_{screen}/J_p), and the beam (J_B/J_p) are plotted as functions of normalized magnetic field current through the anode wire. These data were taken at a discharge current of 2.0 A, a discharge voltage of 50 V and a neutral flow rate of 1580 mAeq. However, it was found that the ion current distribution in the discharge chamber was independent of discharge current, discharge voltage, and neutral flow rate over the ranges investigated. Because of this independence from discharge conditions, the curves shown in Fig. 2 can be considered generally applicable to the divergent magnetic field configuration. Examination of Fig. 2 indicates that the fraction of the total ion current extracted in the beam increases with increasing field current. In addition, the fractions of the total ion current going to the back surface and screen grid increase slightly while that to the side wall decreases. This is clear evidence that the magnetic field strength can influence the distribution of ion currents inside the discharge chamber. The decrease in the fraction of ion current to the side wall is believed to be primarily the result of a radial plasma density distribution in the discharge chamber that becomes increasingly non-uniform as the field current is increased. Most of the ion current going to the back surface is assumed to be going there through the "hole" in the magnetic field on the centerline of the thruster.

The distribution of ion currents for the cusped field thruster (Fig. 1b) configuration is shown in Fig. 3. Again the fractions of ion currents to each surface are plotted against the normalized magnetic field current. Here the same basic trends exhibited by the divergent field configuration are seen. However, in this case the redistribution of ion currents is less pronounced than in the previous case. This appears to indicate that the plasma
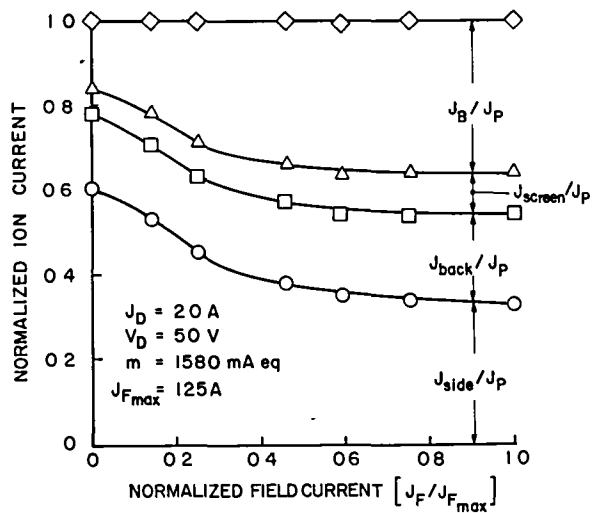

Fig. 2   Ion Current Fractions to Various Thruster Surfaces vs. Field Current for the Divergent Field Configuration.
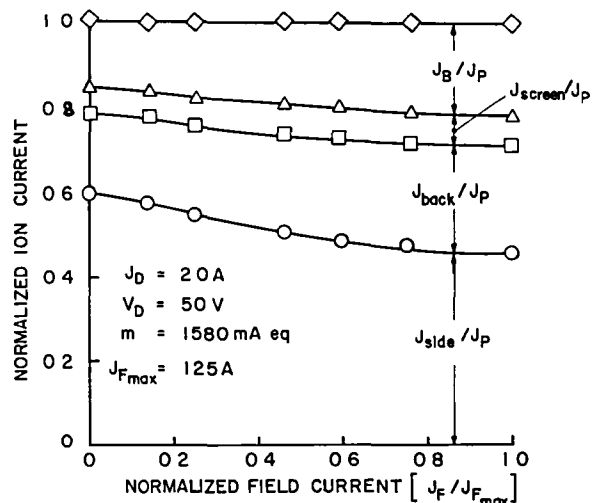

Fig. 3   Ion Current Fractions to Various Thruster Surfaces vs. Field Current for the Cusped Field Configuration.

density remains more uniform at high field strengths in the cusped configuration than in the divergent field geometry. This plasma uniformity is also reflected in the respective ion beam profiles which are more uniform in the cusped field configuration than they are for the divergent one.[2] It is believed that an additional factor which causes the side wall current fraction to be higher for the cusped configuration than for the divergent one is the plasma leakage that occurs at the cusp.

Finally the distribution of currents for the multipole configuration (Fig. 1c) are shown in Fig. 4. Here, interestingly enough, the magnetic field strength has no effect on the gross distribution of ion currents inside the discharge chamber. Further, the fraction of current to each surface was found to be exactly equal to the area of that
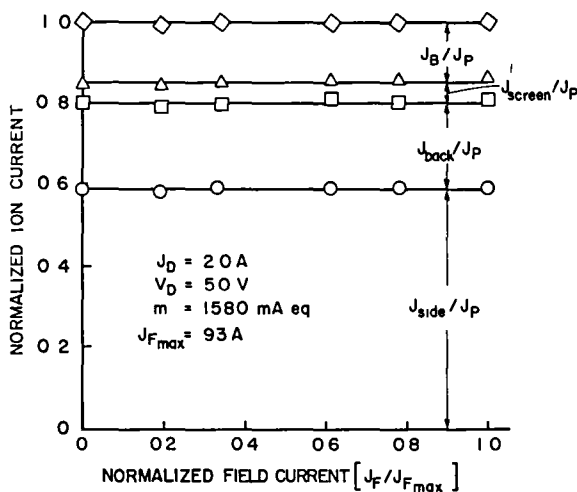
Fig. 4 Ion Current Fractions to Various Thruster Surfaces vs. Field Current for the Multipole Configuration.

Fig. 5 Normalized Ion Current Directed Toward Grids vs. Field Current.

surface divided by the total area of the primary electron region. This was true only at zero field current for the first two configurations. This appears to indicate that the ions move toward the walls with nearly equal probably in all directions in a multipole thruster. It should be noted here that this result applies only to low field strength multipole thrusters. It was not possible to create the 0.3 Tesla magnetic fields now found at the pole pieces of some multipole designs.[12] The improved performance of these designs suggests that some redirection of ion currents is indeed occurring. In any case, the uniform ion current distribution of low field strength multipole thrusters is clearly demonstrated here. The fact that ions are lost uniformly in all directions from the plasma implies that the extracted ion fraction should always be less than 50% for multipole thrusters of low field strength design.

For comparison purposes, the fraction of ions directed toward the grids, $(J_B + J_{screen})/J_p$, is plotted against the magnetic field current in Fig. 5 for the three thruster configurations. The advantage of the divergent field geometry in terms of the fraction of ions directed toward the grids is clear.

Plasma Ion Production

The energy required to create an ion in the plasma has, as one would expect, a strong influence on the overall thruster efficiency. The relationship between this energy cost per plasma ion and that per beam ion can be related using quantities measured in the tests described in this paper. The energy cost per plasma ion (P_p-in electron volts) is defined by

$$P_p = \frac{(J_D - J_p)V_D}{J_p} , \qquad (6)$$

where V_D is the discharge voltage. The ion production rate (J_p) can be written as the sum of the beam current and ion current to the discharge chamber walls (J_W), i.e.,
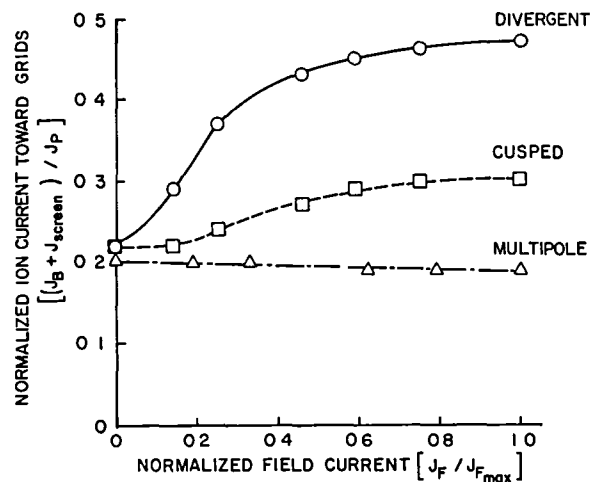
$$J_p = J_B + J_W . \qquad (7)$$

Substituting Eq. (7) into Eq. (6) yields,

$$P_p = \frac{[J_D-(J_B + J_W)] V_D}{J_B + J_W} . \qquad (8)$$

This can be rewritten as,

$$P_p = \frac{(J_D-J_B)V_D}{J_B} \left\{ \frac{J_B}{J_B+J_W} \right\} - \frac{J_W V_D}{J_B} \left\{ \frac{J_B}{J_B+J_W} \right\} . \qquad (9)$$

Recognizing that $(J_D-J_B) V_D/J_B$ is the discharge power P_D (in eV/beam ion), and letting f be the extracted ion fraction defined by,

$$f = \frac{J_B}{J_B+J_W} , \qquad (10)$$

then, Eq. (9) can be written in the form,

$$P_D = \frac{P_p}{f} + \frac{(1-f)V_D}{f} . \qquad (11)$$

This is the desired relation between the energy cost per plasma ion and the energy cost per beam ion. The first term on the right hand side of this equation reflects the energy lost because ions are produced that recombine on the walls and are not extracted into the beam. The second term represents the energy used to accelerate the plasma ions that go to the walls of the discharge chamber into these surfaces.

The plasma ion energy cost has been determined for each thruster configuration and at each operating point considered in this study using Eq. (6). A sample of the results obtained with the cusped field thruster are shown in Fig. 6. These data indicate that the energy cost per plasma ion decreases with increasing magnetic field strength (due to increased anode shielding from primary electrons). In addition, it indicates that the cost increases with discharge current and decreases with neutral flow rate. However, it is relatively
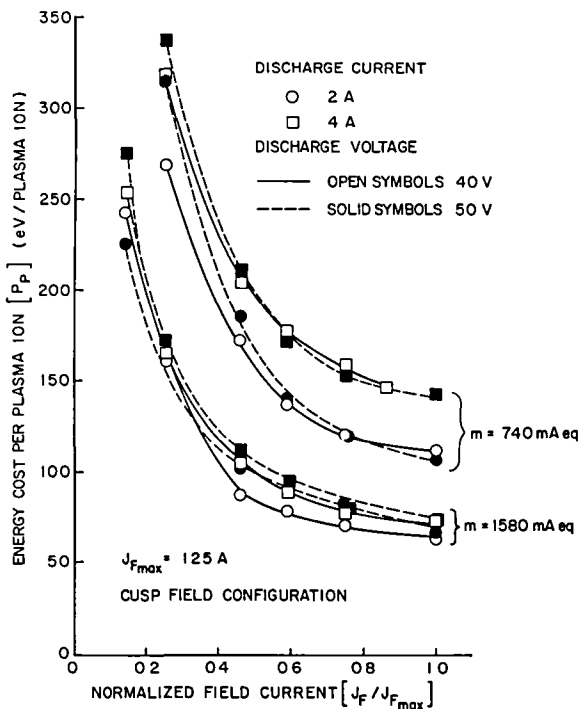
Fig. 6 Plasma Ion Energy Cost in the Cusped Field Configuration.

Fig. 7 Comparison of ion Production Rate and Beam Current to the Neutral Flow Rate for the Cusped Field Configuration.

independent of discharge voltage. While these data were obtained with the cusped field configuration results obtained with the other thrusters showed similar trends. These and other data indicate that the energy cost per plasma ion can be made as low as 50 to 60 eV for the argon propellant used.

In the course of measuring the total ion production rate it was noticed that this rate was frequently much greater than the neutral flow rate in equivalent milliamperes. An example of this is shown in Fig. 7 for data collected on the cusped field thruster. The ion production rate being greater than the neutral flow rate is an indication that the walls of the discharge chamber behave as a virtual source of propellent atoms. Also shown on this figure is the beam current. This figure indicates rather dramatically how the ion production rate can be significantly greater than the neutral flow rate and yet the beam current is still significantly less than the flow rate. This does not mean, however, that if every ion produced could be extracted into the beam that one would get a beam current greater than the flow rate. Instead, the neutral density would decrease causing a corresponding decrease in the ion production rate such that the beam current (assuming only singly charged ions) would always be less than the neutral flow rate.

Other Considerations

In addition to the tests described above, several other configurations of the flexible field thruster were tested in an effort to reduce ion losses to the walls still further. The number and type of configurations that can be tested is limited only by the imagination of the researcher. To date, no configuration of the flexible field thruster has directed a greater fraction of ions toward the grids than the divergent field configuration. However,
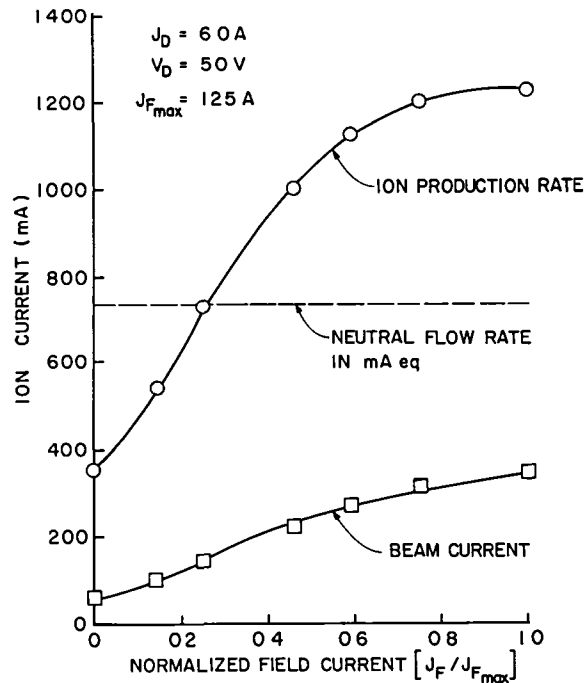
in the course of this effort a very interesting phenomenon was observed. Tests were being run on the flexible field thruster in an axial magnetic field configuration as shown in Fig. 8. In addition to the solenoidal anode the thruster was equipped with an external solenoid. This allowed the magnetic field in the discharge chamber to be created by 1) passing a current through the anode wire only, 2) passing a current through the external solenoid only, or 3) passing currents in opposing or adding directions through both wires simultaneously to produce a wide range of magnetic field conditions. With this thruster configuration it was observed that at any given flow rate, discharge current and discharge voltage, the ion current to the side wall was smaller when the magnetic field was created with the external solenoid alone than it was when a magnetic field of identical strength was created with the internal solenoid alone. This indicates that the plasma is being contained better when the magnetic field is created by the external solenoid than it is when the internal anode wire is used. Why this should occur was not immediately apparent.

The reason the external coil gives better performance than the internal one can be understood, however, by considering Fig. 8 further. Figure 8a shows the magnetic field lines for the case where the field is produced entirely by passing a current through the anode wire. Figure 8b shows the field lines when the field is produced entirely by the external solenoid. The anode wire in this second case serves only as the anode. In Fig. 8b we notice that certain field lines intercept the anode surface directly. As we progress outward from the centerline of this thruster along a radius, the surface of revolution of the first field line that we encounter which intercepts the anode surface is

a) INTERNAL ANODE SOLENOIDAL FIELD
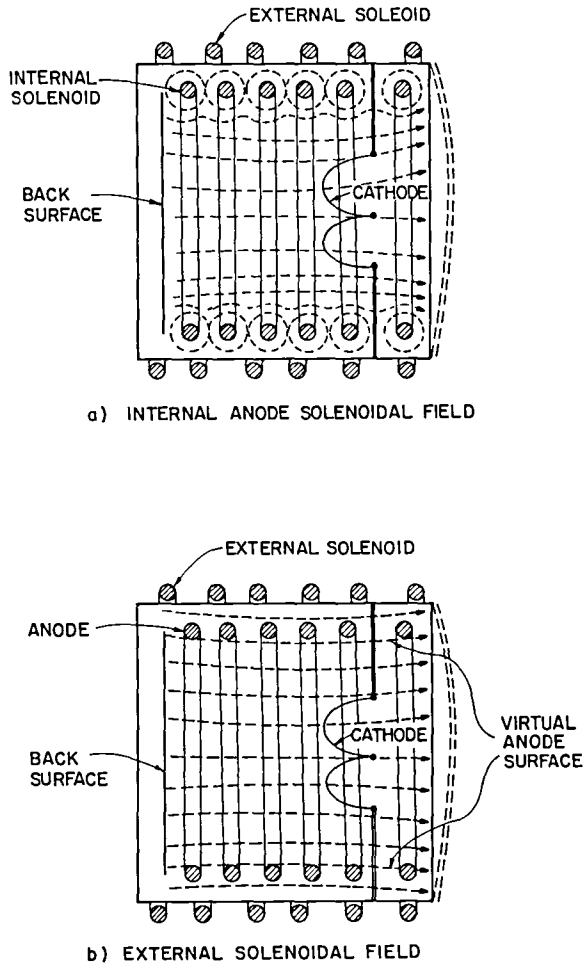

b) EXTERNAL SOLENOIDAL FIELD

Fig. 8 Axial Magnetic Field Thruster Configurations.

called the virtual anode surface. It is so called because once an electron becomes attached to a field line on this surface it has a high probably of being collected by the anode. Consequently, few electrons would be expected to be found at radial locations greater than that of the virtual anode surface. This in turn implies that the plasma density should be reduced substantially in the region outside of this surface. It appears that the reduced ion flux to the side wall is a result of the reduced plasma density in this region. For the case of Fig. 8a (magnetic field created by the internal solenoid), however, it is seen that no field lines intercept the anode directly. Instead they tend to form concentric circles around the anode wire. Consequently there is no virtual anode surface. Further, the field strength between adjacent turns of the anode wire goes to zero. These two factors apparently enable the plasma to leak out of the volume bounded by the anode wire and the result is an ion current to the side wall greater than that observed with the external solenoid.

When the virtual anode surface is present, as mentioned earlier, ion losses to the side wall can be greatly reduced. It was postulated that this reduced ion loss to the wall was the result of a greatly reduced plasma density adjacent to it. Further, this reduction in plasma density was be-

lieved to occur across the virtual anode surface because of the removal of electrons from the plasma by the anode. If this is indeed the case, that is, if the plasma density is reduced dramatically across the virtual anode surface, then the ions must cross this surface with an average velocity substantially less than the Bohm[13] velocity. This must be so for if the ions crossed this surface from a region of high density to a region of low density with the Bohm velocity, then an excess of positive charge would very quickly be built up in the low density region. This excess charge would serve to reduce the ion velocity across the virtual anode surface to the point where the flux of positive charges across the surface was consistant with the condition of quasi-charge neutrality in both the high and low density regions.

To see if this was indeed the case the following experiment was performed. A thruster having the configuration shown schematically in Fig. 9 was constructed. The anode consisted of a washer-shaped piece of 0.025 cm thick stainless steel. An axial magnetic field was created in the discharge chamber through the use of a six turn solenoid wrapped around the cylindrical thruster body. The cathode consisted of a tungsten wire bent into a circle 10.2 cm in diameter. With this configuration the entire side wall was protected by the virtual anode surface but the physical anode area exposed to the plasma was extremely small. This allowed the ion current to the side wall to be measured very accurately since the ion current to the physical anode was negligible. The actual ion currents to each thruster surface are shown in Fig. 10 for an argon flow rate ($\dot{m}$) of 1270 mA, a discharge current (J_D) of 2.0 A and a discharge voltage (V_D) of 50 V. It is noteworthy that this discharge chamber gave a higher extracted ion fraction than the divergent field design (Fig. 1a and Fig. 5). The remarkable aspect of the results of Fig. 10 is however that as the ion current toward the grids ($J_B + J_{screen}$) increases by approximately a factor of 5, due to an increase in the magnetic field current from zero to 100 A, the ion current to the side wall actually decreases. This shows that the virtual anode surface does a remarkable job of containing the plasma. It is believed that this occurs because ions cross this surface with velocities approaching their random thermal velocity rather than the Bohm velocity. The following rough calculation supports this hypothesis.

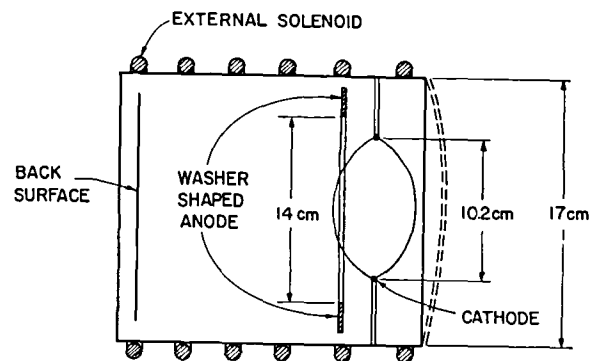Assuming that the ions reach the accelerator

Fig. 9 Axial Magnetic Field Thruster with Washer-Shaped Anode.

$\dot{m} = 1270$ mA eq
$J_D = 2.0$ A
$V_D = 50$ V

ION CURRENT (mA)

FIELD CURRENT $[J_F]$ (amp)

$J_B + J_{screen}$
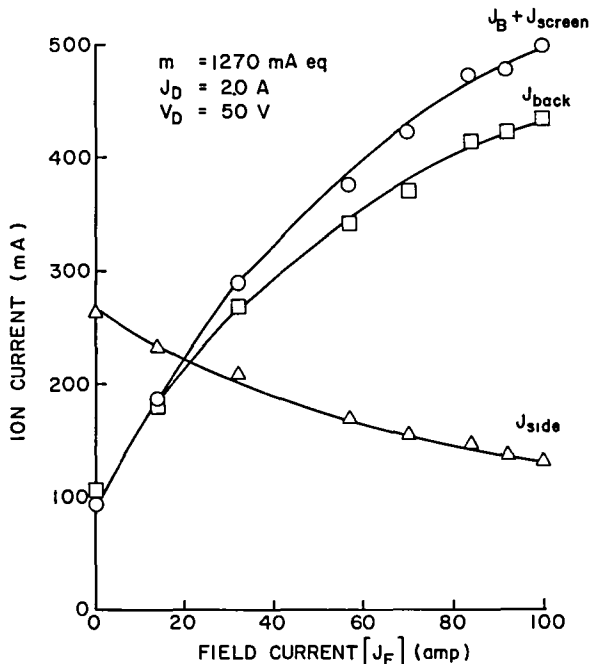
J_{back}

J_{side}

Fig. 10 Ion Currents to Various Thruster Surfaces for the Axial Field Thruster with Washer-Shaped Anode.

system with the Bohm velocity based on an estimated electron temperature of 5 eV, the plasma density just inside of the virtual anode surface was estimated from an ion beam current density profile to be $2.4 \times 10^{-16} m^{-3}$. If the ions crossed the virtual anode surface with the Bohm velocity, then the current to the side wall would be given by the formula,

$$J_{side} = neA_s v_B \qquad (12)$$

where n is the plasma density(just cited), e is the charge for singly charged ions in coulombs, A_s is the area of the virtual anode surface and v_B is the Bohm velocity corresponding to an electron temperature (T_e) of 5 eV. If, on the other hand the ion current depends on the ion random thermal velocity, then

$$J_{side} = \frac{1}{4} neA_s <v> \qquad (13)$$

where

$$<v> = \sqrt{\frac{8kT_i}{\pi m_i}} , \qquad (14)$$

and T_i is the ion temperature (assumed to be equal to 600°K), k is Boltzmann's constant and m_i is the ion mass. Using the density cited previously, Eq. (12) gives a ion current to the side wall of 1010 mA, whereas Eq. (13) gives a current of 40 mA. The measured current at the maximum magnetic field was 113 mA. If the one-fourth factor in Eq. (13) is eliminated, then the equation would correspond to the current due to a directed thermal velocity and the result is a current of 160 mA. Admittedly these calculations are somewhat crude but they are believed to be accurate to better than a factor of two. On the basis of these results it is suggested that the ions cross the virtual anode surface with

their thermal velocity rather than their Bohm velocity.

This phenomenon can also be used to explain the low ion flux across the virtual anode surface observed in the SERT II thruster.[14] In this case the average current density across this surface was measured and found to be approximately 15% of the average current density toward the grids. Rough calculations suggest that if the ions have the Bohm velocity at this surface, then the average current density would be on the order of 250% of the average current toward the grids. If they are assumed to have the random thermal velocity however the calculated current density is about 10% of the current toward the grids. It appears that the ions do not cross the virtual anode surface with the Bohm velocity. It should be pointed out that these results are still preliminary and final judgement must await detailed probing of the plasma around the virtual anode surface.

In light of this ion velocity phenomenon it should be noted that the flexible magnetic thruster does not produce any virtual anode surfaces regardless of its configuration (for the reasons discussed with regard to Fig. 8a). This implies that the flexible field thruster does not imitate exactly those thruster designs which do create virtual anode surfaces. This includes virtually all current designs. However, based on results obtained with the thruster configurations shown in Figs. 8a and 8b, it is believed that the ion flux distributions obtained with the flexible field thruster are still qualitatively correct, and meaningful comparisons can be made between different magnetic field configurations using this technique.

Conclusions

The ability to make drastic changes in magnetic field configurations, together with the ability to measure ion currents to different thruster surfaces makes the flexible magnetic field thruster a powerful tool for the study of magnetic field configuration effects on thruster operation. With this thruster it was observed that the distribution of ion currents inside the discharge chamber was strongly dependent on the shape and strength of the magnetic field. This distribution of ion currents, however, was found to be independent of the discharge current, discharge voltage and the neutral flow rate. With no magnetic field the ions move to the thruster walls with equal probability in all directions, and the fraction of current to each surface bounding the plasma is equal to the area of that surface divided by the total surface area of the primary electron region.

The fraction of ion current to each thruster surface was found to vary as a function of magnetic field strength for both the divergent and cusped field configurations. Generally the fraction of ion current to the side wall would decrease and the fraction of ion current toward the grids would increase as the field strength was increased for these configurations. No such redistribution of ion currents was observed for the multipole configuration. In this case, the ion current distribution remained the same as it was for the zero magnetic field condition.

Measurements of the energy cost per plasma ion

indicated that this cost decreased with increasing magnetic field strengths. This effect was attributed to increased shielding of the anode from the primary electrons. Energy costs per argon plasma ion as low as 50 eV were measured.

The energy cost per beam ion was found to be a function of the energy cost per plasma ion, the extracted ion fraction, and the discharge voltage. Part of the energy cost per beam ion goes into creating many ions in the plasma when only a fraction of them is extracted into the beam. The rest of the energy goes into accelerating the remaining plasma ions into the walls of the discharge chamber.

The flexible field thruster does not exactly imitate the discharge chambers of existing thruster designs due to its inability to produce virtual anode surfaces. However, the ion current distributions measured with it are still believed to be qualitatively correct. The virtual anode surface provides a boundary between high and low density plasma regions. Ions from the high density region cross this boundary with velocities approaching their random thermal velocity. This indicates that ion losses from typical ion thruster discharge chambers can be reduced by bounding the plasma with virtual anode surfaces.

References

1. Robinson, R. S., "Physical Processes in Directed Ion Beam Sputtering," NASA CR-159567, March 1979.

2. Beattie, J. R., "Cusped Magnetic Field Mercury Ion Thruster," NASA CR-135047, July 1976.

3. Bechtel, R. T., "The 30 cm J Series Mercury Bombardment Thruster," AIAA Paper No. 81-0714, 1981.

4. Wilbur, P. J., "Experimental Investigation of a Throttlable 15 cm Hollow Cathode Ion Thruster," NASA CR-121038, Dec. 1972.

5. Ramsey, W. D., "Magnetoelectrostatic Thruster Physical Geometry Test," AIAA Paper No. 81-0753, 1981.

6. Sovey, J. S., "Performance of a Magnetic Multipole Line-Cusp Argon Ion Thruster," NASA Technical Memorandum 81703, 1981.

7. Isaacson, G. C. and Kaufman, H. R., "15-cm Multipole Gas Ion Thruster," J. of Spacecraft and Rockets, Vol. 14, No. 8, August 1977, pp. 469-473.

8. Longhurst, G. R. and Wilbur, P. J., "Multipole Mercury Ion Thruster," AIAA Paper No. 78-682, 1978.

9. Dugan, J. V. and Sovie, R. J., "Volume Ion Production Costs in Tenuous Plasmas: A General Atom Theory and Detailed Results for Helium, Argon, and Cesium," NASA TN D-4150, 1967.

10. Isaacson, G. C., "Multipole Gas Thruster Design," NASA CR-135101, June 1977.

11. Siegfried, D. E., "A Phenomenological Model Describing Orificed Hollow Cathode Operation," Appears in, "Ion and Advanced Electric Thruster Research - 1980," NASA CR-165253, Dec. 1980.

12. Sovey, J. S., "Improved Ion Containment Using a Ring-Cusp Ion Thruster," AIAA Paper No. 82-1928, 1982.

13. Bohm, D., "Minimum Ionic Kinetic Energy for a Stable Sheath," The Characteristics of Electrical Discharges in Magnetic Fields, A. Guthrie and R. K. Wakerling, eds., McGraw-Hill Book Co., Inc., 1949, pp. 77-86

14. Wilbur, P. J., "Advanced Space Propulsion Thruster Research," NASA CR-165584, Dec. 1981, pp. 82.

AIAA'82

AIAA-82-1894
Ion Extraction Capabilities of Very Closely
Spaced Grids

D.C. Rovang and P.J. Wilbur, Colorado
State Univ., Fort Collins, CO

AIAA/JSASS/DGLR 16th International
Electric Propulsion Conference

November 17-19, 1982/New Orleans, Louisiana

ION EXTRACTION CAPABILITIES OF CLOSELY SPACED GRIDS[+]

D. C. Rovang[*] and P. J. Wilbur[**]
Colorado State University
Fort Collins, Colorado 80523

Abstract

An experimental investigation into the ion extraction capabilities of accelerator systems with small screen hole diameters ($\leq$ 2.0 mm) at net-accelerating voltages of 100, 300, and 500 V is described. The apparatus developed for this study is shown to be well suited for measuring the impingement-limited perveance, electron backstreaming, and electrical breakdown characteristics of two-grid ion accelerator systems. Results suggest that the impingement-limited perveance is not dramatically affected by reductions in screen hole diameter to 1.0 mm, but impingement-limited performance was found to be dependent on the grid separation distance, the discharge-to-total accelerating voltage ratio, and the net-to-total accelerating voltage ratio. Results obtained with small hole diameters and closely spaced grids suggest a new mode of grid operation where high current density operation can be achieved with a specified net acceleration voltage. In this mode the grids are operated at a high net-to-total acceleration voltage ratio rather than the low ones that have heretofore been considered to yield higher current densities. Under these conditions it appears to be the onset of electron backstreaming that ultimately determines the extractable ion current density. Beam current densities as high as 25 mA/cm^2 were obtained using grids with 1.0 mm diameter holes operating at a net accelerating voltage of 500 V.

Introduction

In order to reduce the number of electrostatic ion thrusters required for a space propulsion mission and hence the cost and mass of the thruster subsystem, it is generally desirable to increase the thrust densities of these devices above those attainable with currently available ion thrusters. To keep the thrusters operating at their optimum specific impulse this should be accomplished by increasing the ion beam current density extracted from the ion optics system without increasing the exiting ion velocity. This can be done under the constraint of the space-charge effect by reducing the grid spacings and hole diameters below the values used on present-day accelerator systems. The need for this type of accelerator system becomes even more apparent when one considers the current trend away from heavy propellants such as mercury to lighter propellants such as argon and xenon. To achieve the optimum specific impulse for a typical mission, these lighter propellants require a lowering of the net accelerating voltages below those

being used for current accelerator system designs. In terms of the extracted current densities this means that the trend to lighter propellants necessitates the use of accelerator systems with smaller grid holes and closer grid separations in order to maintain current densities at their present levels.

Although existing experimental performance data for accelerator systems with relatively large screen hole diameters ($\geq$ 2 mm) is quite extensive,[1,2,3] this same information for smaller screen hole diameters is somewhat limited. Previous experimental results have suggested that there might be a reduction in the ion extraction capabilities of thrusters utilizing grids with small screen hole diameters (< 2.0 mm).[1,2,3] Because of this possible degradation due to hole size, it was felt that before any future high thrust density designs could be attempted an improved understanding of the ion extraction capabilities of grids utilizing these small diameter holes (< 2.0 mm) was needed. It is for this purpose that the present detailed investigation was undertaken.

Background and Theory

The essential components of a basic two grid ion accelerator system are shown in Fig. 1a. Although the side view of a single aperture is depicted, it should be noted that a multi-aperture system is implied. The accelerator system is placed adjacent to a discharge chamber containing a low density ionized plasma at a potential of a few tens of volts above that of the screen grid. Around each screen hole a plasma sheath is formed which defines the boundary between the discharge plasma and the acceleration region. Potentials applied to the grids produce an electric field that accelerates the ions and repels the electrons coming into the sheath from the discharge plasma. Figure 1b illustrates the variation of these electrical potentials associated with the grid geometry of Fig. 1a. The solid line of Fig. 1b shows how the potential drops slightly from the plasma to the relatively high positive potential in the grid. It remains constant through the screen grid area then drops almost linearly in the space between the grids. It is constant through the accel grid and then rises to the potential far downstream of the accelerator grid. In this downstream region electrons are available to maintain charge neutrality in the plasma associated with the ion beam. The dotted line of Fig. 1b shows how for a normally operating grid the potential varies with position through the center of the grid holes rather than through the grids themselves. The difference between the solid and dotted lines is induced by the space charge effects of the ions passing through the grids. Table 1 defines and names the symbols shown in Figs. 1a and 1b.
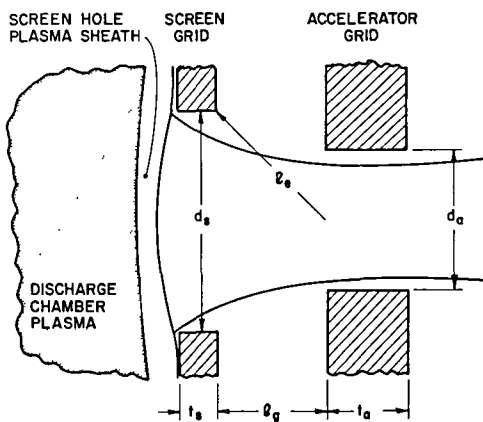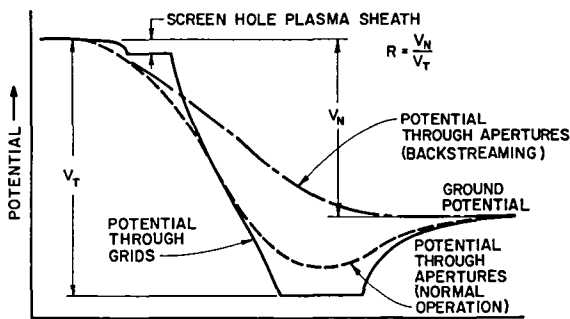
a) GRID GEOMETRY

b) POTENTIAL VARIATION

Fig. 1 Two-Grid Acceleration System

Table 1
Accelerator System Nomenclature

t_a = Accelerator grid thickness

t_s = Screen grid thickness

d_a = Accelerator hole diameter

d_s = Screen hole diameter

ℓ_g = Grid separation distance

ℓ_e = Effective acceleration length

V_N = Net accelerating voltage

V_T = Total accelerating voltage

R = Net-to-total accelerating voltage ratio

The current density extraction capability of an accelerator system aperture like the one shown in Fig. 1a is generally limited by space charge effects to the value given by Child's Law.

$$J = \frac{4}{9} \epsilon_0 \ (\frac{2q}{m_i})^{\frac{1}{2}} \frac{V_T^{3/2}}{(\ell)^2} \qquad (1)$$

In this equation, representative of a one-dimensional model of the ion acceleration process, ϵ_0 is the permittivity of free space, q is the ion charge, m_i is its mass and ℓ represents the length through

which the ions are accelerated by the applied total accelerating voltage (V_T). In the case of the parallel plate vacuum diode, for which this equation was originally derived, ℓ refers to the physical distance between the parallel plates. However, in the case of the extraction aperture the emissive surface is not defined by a plate whose position is fixed, but rather by a plasma sheath whose position is dependent on the ion current being extracted. The current density of ions arriving at the plasma sheath, from the upstream plasma is determined by the Bohm condition for a stable sheath, i.e.,

$$J = n_i \ q \sqrt{\frac{eT_e}{m_i}} \ . \qquad (2)$$

In this equation the discharge plasma ion density (n_i) is equal to the associated electron density (n_e) and the electron temperature (T_e) of the plasma is in electron volts. The quantity "e" is the electron charge.

Experimental results obtained by Aston showed that increasing the Bohm current density, by increasing the plasma density caused the sheath to move closer to the screen hole.[4] These results lead one to the conclusion that the acceleration length ℓ adjusts itself so that Child's Law is always satisfied. In normal operation the shape of the plasma sheath is similar to that shown in Fig. 1a. As the plasma density and as a result the ion current density increase, the sheath moves closer to the screen hole and begins to flatten out. Eventually, an operating point is reached where the sheath can no longer focus the ions through the accelerator grid aperture and direct ion impingement upon the accelerator grid begins to occur. At this point the acceleration length ℓ required by Child's Law has reached a value less than a physical acceleration length required to produce a well focused ion beam. This physical acceleration length is dictated by the geometry of the accelerator system. In past theoretical and experimental investigations, the physical acceleration length used to correlate the performance of various grid geometries is the effective acceleration length ℓ_e where

$$\ell_e = [\ell_g^2 + \frac{d_s^2}{4}]^{\frac{1}{2}} \ . \qquad (3)$$

Replacing ℓ in Eq. 1 with ℓ_e, and setting the beam current density (J) equal to the beamlet current (J_B) divided by the area of a screen grid hole, Eq. 1 can be written

$$\frac{J_B}{V_T^{3/2}} \ (\frac{\ell_e}{d_s})^2 = \frac{\pi \epsilon_0}{9} \ (\frac{2q}{m_i})^{\frac{1}{2}} \ . \qquad (4)$$

The left side of this expression is known as the normalized perveance per hole and it will be used in this paper to correlate the performance of accelerator grid systems as a function of the various grid geometries and the operating conditions investigated. Of particular interest will be the impingement-limited normalized perveance per hole defined as the perveance per hole at the onset of excessive accelerator grid ion impingement. It should be noted that the right-hand side of Eq. 4 has a fixed value for a particular propellant. This value is indicative of the perveance where one would expect to encounter the impingement limit.

110

In the case of argon, the propellant used in this study, this limiting value is computed to be 6.8×10^{-9} A/V$^{3/2}$. Assuming the grids can be held parallel at any separation distance there are two additional phenomena that limit the operating range of an ion acceleration system. These are electrical breakdown through the region between the grids and electron backstreaming into the discharge plasma from the plasma downstream of the grids. In practice the occurrence of these phenomena constrains the absolute lower limits of grid separation distances that can be realized and thus limits the ion current which can be extracted from the accelerator system. Electrical breakdown occurs when the electrical field strength between the grids (total accelerating voltage minus the discharge voltage all divided by the grid separation distance) exceeds the breakdown limit. When this occurs excessive electron currents begin to flow between the grids. This limit is determined by the geometry of the grids as well as such factors as the grid surface finish and the density of charged and neutral particles between the grids.

Electron backstreaming occurs when electrons in the downstream ion beam plasma find a path along which they can be accelerated through grid apertures directly into the discharge chamber. This condition occurs when the potential variation through the apertures is similar to that shown by the centerline in Fig. 1b. When this type of potential profile exists, the electrons in the beam plasma are no longer repulsed by the negative potential on the accelerator grid and they are therefore able to backstream into the discharge chamber.

Many factors influence the onset of backstreaming, and traditionally those factors pertaining to the accelerator system have been lumped together to form a dimensionless parameter known as the electron backstreaming parameter.[5] The parameter used herein is

$$B = (1 - R_{max}) \left(\frac{\ell_g}{d_a} \right) \left(\exp\left[\frac{t_a}{d_a} \right] \right).$$

This parameter is slightly different from the one used in previous theoretical investigations where instead of (ℓ_g/d_a) the factor (ℓ_c/d_a) was used.[6] This change was made because the factor (ℓ_g/d_a) gave a better correlation of the electron backstreaming data collected in this study.

Apparatus

All testing has been conducted on a 8 cm diameter by 10 cm long ion source with a mildly divergent magnetic field. The magnetic field was derived from a long solenoidal winding wrapped around the outside of the thruster body. A cylindrical copper anode was used and apart from this, nonmagnetic stainless steel construction was employed throughout the source. Refractory tungsten filaments were used for both the neutralizer and cathode emitters. The emission levels for both of these was controlled by adjusting the current flowing through the filaments from their ac power supplies. This source design was selected because it provided the high current density capability needed to assure a proper test of the grids, and it provided a stable discharge. To minimize the discharge chamber noise further, the voltage drop across the refractory cathode was reduced by using two short filaments in parallel. It is believed

that this reduces the noise because it reduces the range of primary electron energies coming off of the cathode.

The ion current extraction capability of various nineteen aperture grid sets investigated in this study were each characterized by a different screen aperture diameter. The grid aperture pattern used was a hexagonal array with a center-to-center hole spacing of 2.5 mm for all aperture diameters. The grids were made from thin sheets of commercially available graphite, and to help ensure proper grid hole alignment, the screen and accelerator grids were simultaneously match drilled. As a result of this the screen and accelerator grids both had the same diameter apertures. The thicknesses of the screen and accelerator grids were both the same in each test and as hole size was varied for the different tests the grid thicknesses were also varied to hold the ratio of hole diameter to grid thickness constant at 0.25.

Because the grid separation distance was a very important parameter in this study, the test apparatus was designed so it could be varied continuously while the ion source was being operated. This is accomplished, using the apparatus shown schematically in Fig. 2, by moving the fork-spaced wedge in the manner suggested by the large arrow. As this wedge is moved toward the grids it forces the accelerator and screen grid support plates apart and hence the screen and accelerator grids attached to these plates are also separated. All materials used in the construction of this apparatus are capable of withstanding high temperatures. Graphite was used for both the grids and grid support plates to minimize the differential thermal
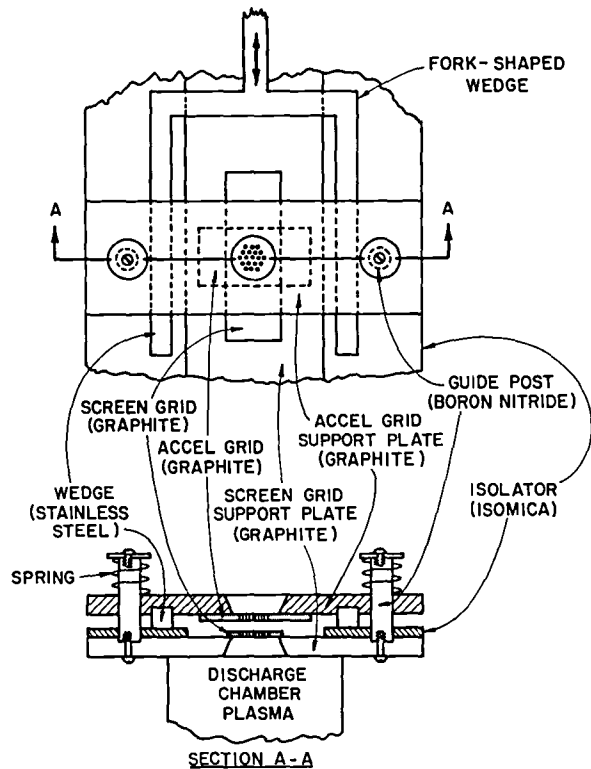

Fig. 2 Variable Grid Spacing Apparatus

expansion between these components that could cause grid warpage. The distance over which the grids were supported was also minimized to minimize the effects of grid warpage. Initial alignment of the grids was accomplished manually by positioning and clamping each grid and then checking the alignment visually beneath a large illuminated magnifying glass. This alignment is maintained during operation by the boron nitride guide posts shown in Fig. 2. Electrical isolation is assured by the sheet of Isomica between the screen grid support plate and the wedge. The wedge is mechanically connected to a micrometer used to measure and adjust its translation from the outside of the vacuum system.

Immediately after each period of data collection, while the source was still hot, the grid separation distance was reduced until the measured electrical resistance between the grids went essentially to zero. This reference point on the micrometer (assumed to correspond to zero separation) along with the geometry of the wedge could then be used to calculate the grid spacing from the micrometer readings recorded during the testing. This procedure for defining the reference point was usually repeated two or three times for each test setup to determine if the reference point had changed for some unknown reason. Based on repeated observations, it is believed that the grid separation distance was known to within $\pm$ 0.01 mm.

Test Procedure

Because the objective of this study was to define the limitations of the accelerator system and not those limitations that might be source related, every effort was made to operate the ion source so the highest possible impingement-limited perveance would be realized with each grid configuration. This was accomplished by optimizing the propellant flow rate, discharge voltage (V_D) and magentic field strength for each grid configuration tested. In general, it was found that discharge voltage and magnetic field strength could be maintained at a single optimum value for a particular net accelerating voltage. However, the propellant flow rate was more critical and had to be optimized for every grid separation investigated. This optimum flow rate was almost always equal to the minimum flow rate at which the source operated stably over the full range of beam currents investigated. The conduct of the tests involved the establishment of this optimum flow with a particular grid set, grid spacing and net accelerating voltage and then increasing the cathode emission current in steps to induce increases in the beam and impingement currents. These currents were recorded manually from high accuracy digital gauges at each step. This process continued until the impingement current reached a high value ($\approx$10% of the beam current). At this time, the cathode emission was reduced and the procedure for collecting electron backstreaming data was executed.

The collection of backstreaming data was accomplished by reducing the accelerator grid potential (V_T-V_N) while watching for the rather sudden increase in beam current that is indicative of electron backstreaming into the discharge chamber. This procedure yielded a minimum accelerator grid voltage which could be used along with the net accelerating voltage (V_N) to calculate the upper limit on the net-to-total accelerating ratio (R_{max}) which could

not be exceeded without inducing electron backstreaming. Since the grid separation and grid geometry were known, the value of the electron backstreaming parameter could be calculated from these data. It will be shown later that the electron backstreaming parameter is somewhat dependent on the beam current or normalized perveance per hole. The value of this parameter at the impingement-limited perveance is probably of the most interest, however, so most of the backstreaming data was collected at this high perveance condition. After the impingement-limited perveance and backstreaming data had been collected, the grid separation distance was reduced and the preceeding procedures were repeated.

Because of the potentially destructive nature of the electrical breakdown phenomenon, the electrical breakdown characteristic of each of the graphite grid pairs were measured after the perveance/impingement characteristics and electron backstreaming data had been obtained. The background pressure was held constant for electrical breakdown testing at a pressure of 2.0×10^{-5} Torr because this represented an average value of the bell jar pressures encountered during all testing. The data was collected by establishing a given grid spacing with the ion source operating at a moderate beam current. The screen and accelerator voltages were then increased in magnitude until electrical breakdown occurred. These tests indicated that either the screen or accelerator voltage could be increased to induce breakdown, i.e. the sum of the two voltages was the critical variable in determining when breakdown occurred.

Results

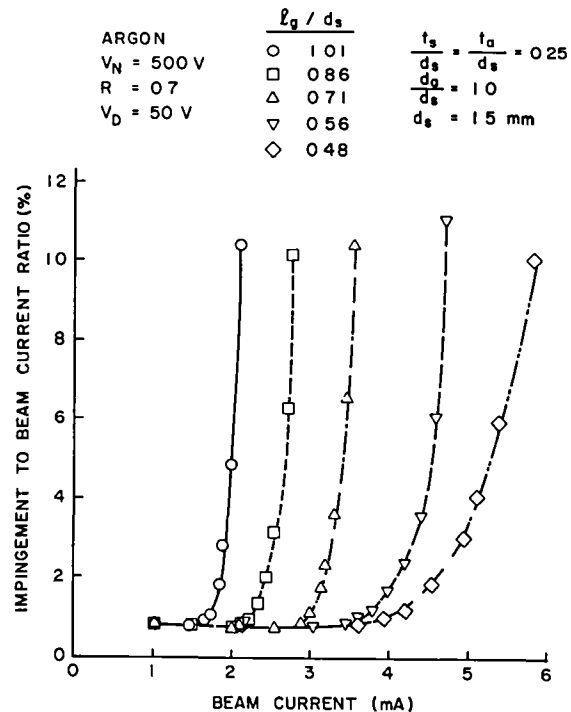Figure 3 displays a set of typical curves showing how impingement current (normalized using

Fig. 3 Effect of Grid Separation on Impingement Curves - Nineteen Hole, Two-Grid Systems

beam current) was observed to vary with beam current and grid separation distance. The figure shows that closer grid separations facilitate operation at higher beam currents before direct ion impingement levels become excessive. The data of Fig. 3 also show that the sharpness of the "knee" or rate of increase to high impingement becomes less dramatic as the grid spacing is reduced. These curves pertain specifically to the impingement data collected for the screen and accel grid hole diameters of 1.5 mm at a net accelerating voltage of 500 V and a net-to-total accelerating voltage ratio (R) of 0.7. Data similar to those in Fig. 3 were collected at each of the screen hole diameters, net accelerating voltages and net-to-total accelerating voltages investigated. Instead of presenting all of the performance data in the form shown in Fig. 3, it is more convenient and more meaningful for comparison purposes to define a maximum beam current for each grid separation, i.e., the beam current at which the direct accelerator grid impingement current becomes excessive. Since the total accelerating voltage, the grid separation distance, and the hole size are known, this impingement-limited beam current can be divided by the number of apertures and then used to calculate the impingement-limited normalized perveance per hole using Eqs. 3 and 4. The normalized perveance based on this definition facilitates comparison of the ion extraction capabilities of various grid geometries over a range of operating conditions. The impingement condition selected somewhat arbitrarily to define the impingement-limited beam current corresponds to an impingement-to-beam current ratio of one percent. It should be noted here that a normalized impingement current of 1% is only slightly above the baseline (charge exchange induced) impingement level shown in Fig. 3. This limit on the beam current was based on such a modest change in impingement current because it yielded consistent results close to the operating condition where an ion thruster would be expected to operate. A careful examination of representative data showed that this criterion yielded impingement-limited beam currents that on the average were 10% ± 3% higher than those beam currents that might be associated with negligible direct ion impingement.

Effect of Hole Size

Using the impingement-limited normalized perveance per hole, obtained from plots like those of Fig. 3, as the performance yardstick, the results of Figs. 4, 5, and 6 were obtained. These figures compare the performance of the various screen hole sizes investigated as a function of the normalized grid separation distance. Each figure presents data for a different net accelerating voltage. For each voltage, the curves corresponding to the different hole sizes all exhibit similar behavior. As the normalized grid separation is reduced the perveance remains constant or increases slightly and then it falls off as the grid separation drops below the value where focusing becomes poor and accelerator impingement begins to limit performance. The poor focusing that causes this reduction in performance is believed to be a result of intra-grid equipotential lines which become progressively less planar as the grid separation is reduced.

Figures 4, 5, and 6 do not appear to show any dramatic trends that would indicate a decrease in performance with decreasing hole size. This observation differs from what was expected based on pre-
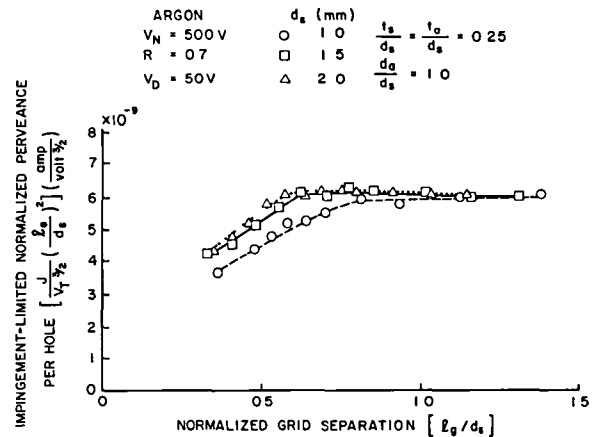

Fig. 4 Effect of Aperture Diameter on Two-Grid System Ion Extraction Performance for a Net Acceleration Voltage of 500 V
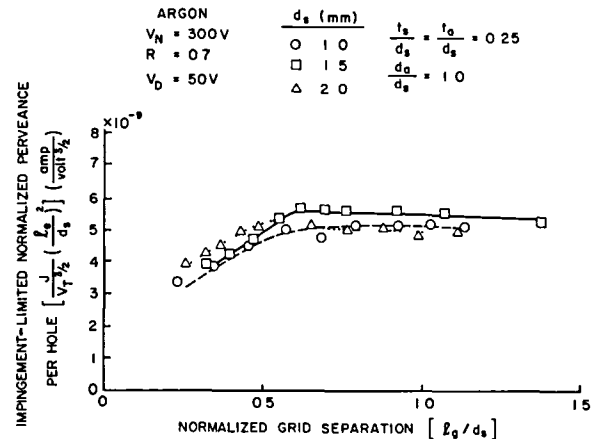

Fig. 5 Effect of Aperture Diameter on Two-Grid System Ion Extraction Performance for a Net Accelerating Voltage of 300 V
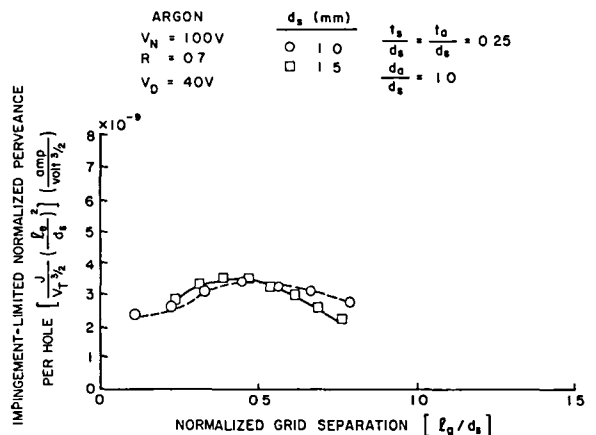

Fig. 6 Effect of Aperture Diameter on Two-Grid System Ion Extraction Performance for a Net Accelerating Voltage of 100 V

vious experimental investigations that reported a decrease in performance for screen hole diameters below 2.0 mm.[1,2,3] It is believed that results obtained in these tests differed from those measured in previous ones because of the experimental procedures used. During the present study it was found for example that it was important that the ion source be capable of producing Bohm current densities toward the grids significantly greater than the current densities being demanded by the grids when they were operating near the impingement limit. This ensured that it was the grids rather than the ion source that was limiting ion extraction. To accomplish this the source must be operated at the progressively higher plasma densities and hence smaller Debye lengths that are demanded as hole size and grid separation are reduced. It is noted in addition that some adjustment in flow rates was required to achieve the discharge chamber operating condition that would yield the highest impingement-limited current densities. It was also determined that the stability of the discharge chamber influenced the ion extraction capabilities of the grids. During a segment of the tests the discharge chamber was changed to a design that operated less stably (arc discharge noise being being apparent on an oscilloscope). The onset of high impingement currents occurred at lower beam current levels with this design than it did with the more stable one.

To help visualize the dramatic effect that decreasing hole size has on current density the data of Fig. 4 has been replotted in Fig. 7 with current density rather than perveance as the dependent variable. The current densities shown here were calculated by dividing the impingement-limited beam current per hole by the area of a screen hole. It is noteworthy that the current densities continue to rise as grid separation is reduced below the value where perveance began to drop off in Fig. 4 (ℓ_g/d_s = 0.6 to 0.7) and that current densities increase markedly as hole size is reduced. The current density of $\sim$ 25 mA/cm^2 measured with
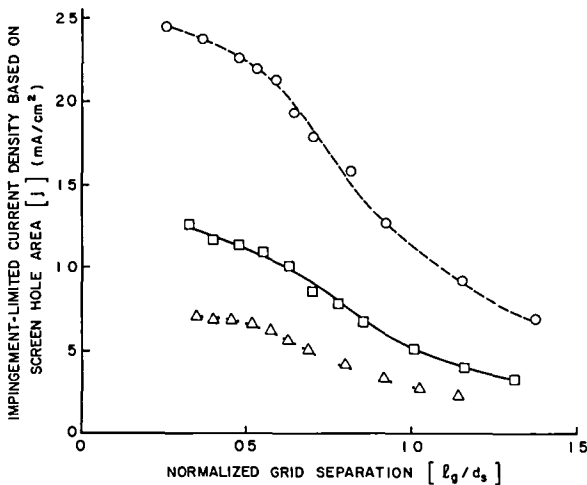
the 1.0 mm diameter holes is observed to be the maximum value realized at a net acceleration voltage of 500 V for the case considered here where the screen and accel grid hole diameters were equal and the impingement was limited to 1% of the beam current. When impingement levels of several percent were allowed this maximum current density increased to about 35 mA/cm^2. This substantial increase in current density can be realized when impingement is allowed to increase because impingement does not rise percipitously with beam current when the grids are spaced very close together (see Fig. 3 for example).

Effect of Net Accelerating Voltage

Although there is no apparent reduction in the impingement-limited perveance capabilities of grids as hole size is reduced, Figs. 4, 5, and 6 do show that there is a definite trend toward lower impingement-limited perveance per hole values as net accelerating voltages are reduced. Aston[3] has also reported that the net acceleration voltage level can affect the impingement-limited perveance capabilities of grid systems. He suggests that the ratio of discharge voltage-to-total accelerating voltage is a suitable correlating parameter for data of this sort. This parameter has been used in Fig. 8 to show how changes in total accelerating voltage associated with the data in Figs. 4, 5, and 6 induce changes in the impingement-limited perveance per hole. The data symbols and error bars in Fig. 8 pertain to the data from the horizontal portions of the curves in these figures. Figure 8 shows an almost linear decrease in performance as the ratio of discharge-to-total accelerating voltage increases.
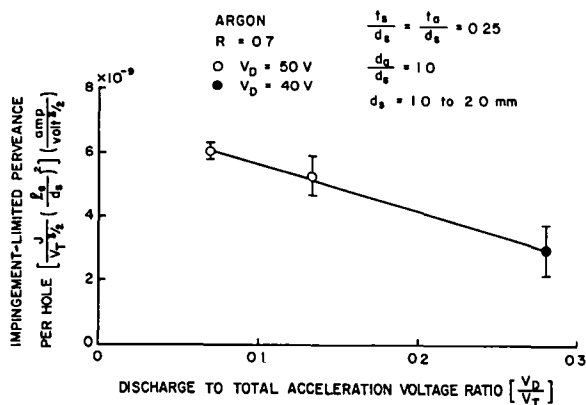

Fig. 8 Effect of Discharge-to-Total Acceleration Voltage Ratio on Ion Extraction Performance

Discharge and total accelerating voltages are known to alter the screen hole sheath shapes and positions and this could be the cause of the effect shown in Fig. 8. One might also speculate that this reduction results from a plasma related blockage of the screen grid hole. Such a situation could occur at low net accelerating voltages where low current densities with their attendant low plasma densities and larger Debye lengths are observed. It is also considered possible that discharge voltage influences the off-axis velocity component of ions entering the sheath while

Fig. 7 Effect of Aperture Diameter on Extracted Ion Current Density

total accelerating voltage determines their on-axis component. The ratio of these two voltages would then be expected to determine the relative trajectory of ions toward the accelerator grid webbing. In any case, this effect is believed to be a real effect and to avoid substantial decreases in performance at very low total accelerating voltages, it appears that it will be necessary to use thrusters which exhibit stable operation at high current densities with low discharge voltages.

Effect of Net-to-Total Accelerating Voltage Ratio

Figure 9 shows the effect of variations in the ratio of the net-to-total accelerating voltage on the impingement-limited perveance per hole characteristics of grids as a function of normalized grid separation for a typical case (d_S = 1.5 mm, V_N = 300 V). It shows that increases in the net-to-total acceleration voltage ratio (R) cause the characteristic impingement-limited perveance vs. grid separation curves to shift to the left. This means that operation is possible at a given net acceleration voltage at closer grid separation and hence higher current densities at the higher net-to-total acceleration ratios (R). This appears to be a result of the improved focusing associated with the higher values of R. Although Aston[3] reported large variations in beam divergence with R, his data did not indicate such a dramatic effect of R on the impingement-limited perveance per hole as that suggested by the results of Fig. 9. The reason for this difference is uncertain at this time but it may be related to a difference in the screen-to-accel grid hole diameter ratio which was different in the two tests.
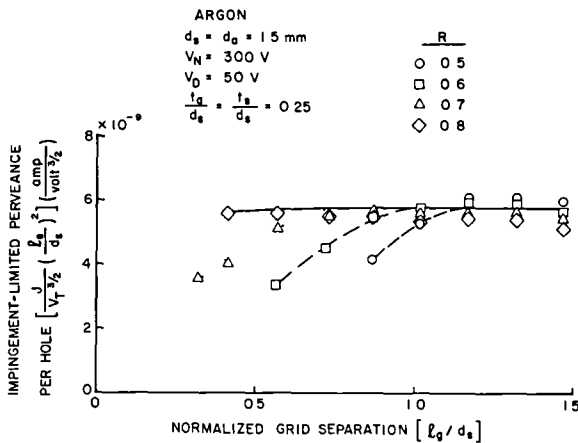
Fig. 9 Effect of Net-to-Total Acceleration Voltage Ratio on Ion Extraction Performance for 1.5 mm Diameter Grid Apertures

The significance of the results shown in Fig. 9 can be seen more readily if the impingement-limited current density (current per hole/hole area) is used as the dependent variable in place of the impingement-limited normalized perveance per hole. This has been done in Fig. 10. Even though the potential difference between the grids decreases as the net-to-total acceleration voltage ratio is increased, Fig. 10 indicates the current density can be increased by doing this. This can be accomplished because increasing the net-to-total acceleration voltage ratio facilitates better focusing and the

opportunity to reduce the grid separation to progressively lower values before accelerator grid impingement becomes excessive. Unfortunately, the process of increasing the net-to-total accelerating voltage cannot continue indefinitely, because the operation of the grids is eventually limited by the onset of backstreaming. It should be noted that the results of Fig. 10 were obtained with an accelerator grid hole diameter equal to the screen hole diameter and the observations just made could be altered somewhat if the accelerator grid hole diameter were reduced.
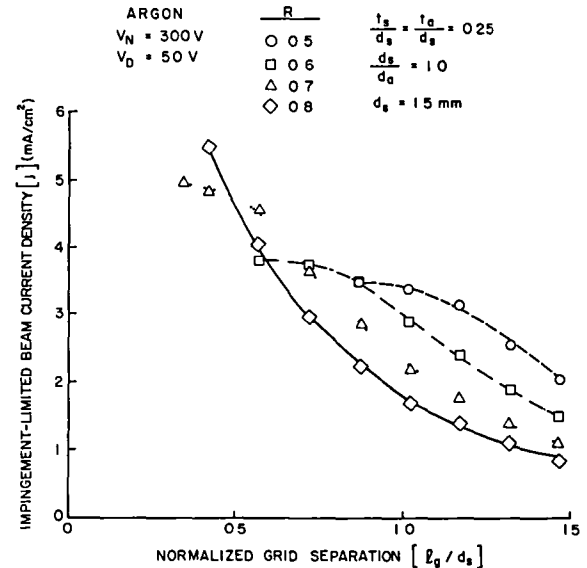
Fig. 10 Effect of Net-to-Total Acceleration Voltage Ratio on Current Density Capability of 1.5 mm Diameter Grid Apertures

Electron Backstreaming

Figure 11 shows the effect of variation in the screen/accelerator hole size on the electron backstreaming parameter as a function of normalized
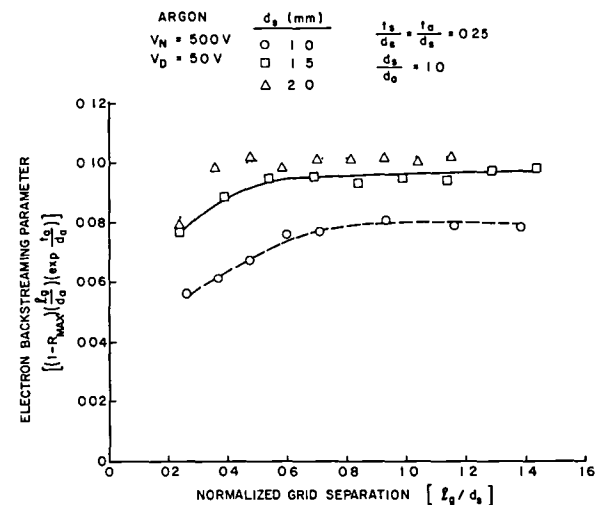
Fig. 11 Effect of Screen/Accelerator Grid Aperture Diameter on the Electron Backstreaming Parameter

grid separation length. Qualitatively, all the curves are observed to be similar. As the normalized grid separation is reduced, the electron backstreaming parameter remains fairly constant, and then falls off slightly at the lower grid spacings. The reason for this drop off is uncertain at this time, but it should be noted that at the lower grid separations under some conditions it was difficult to distinguish between increases in beam current due to improved focusing and increases due to backstreaming. There is also a trend in Fig. 11 toward lower electron backstreaming parameters with decreasing hole size. It is also possible that this lowering of the backstreaming parameter might be related to an increase of screen webbing area between the holes which accompanied reductions in screen hole diameter in the present experiments. This occurred because the hole-to-hole spacing was held fixed while the hole diameter was varied. Additional experiments are needed to determine which of these parameters induce the observed effect. The less significant effect of net accelerating voltage on the electron backstreaming parameter, for the typical case where the screen hole diameter is 1.5 mm, is shown in Fig. 12.
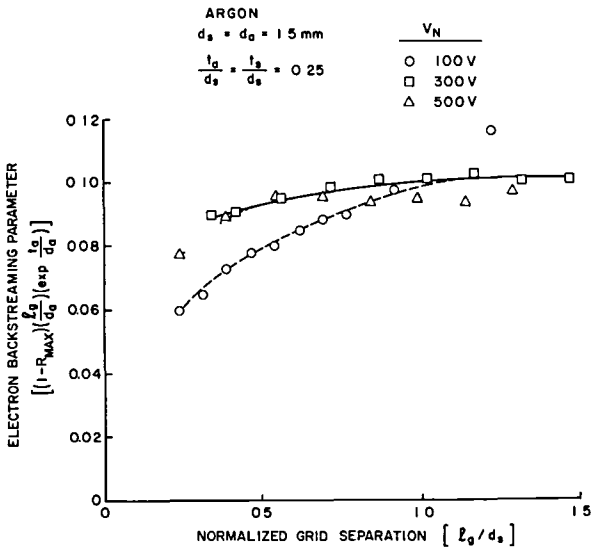

Fig. 12 Effect of Net Acceleration Voltage on the Electron Backstreaming Parameter for 1.5 mm Diameter Grid Apertures

Figure 13 shows the typical results indicative of the effect of the perveance at which a grid is operating on the electron backstreaming parameter. The rate at which the electron backstreaming parameter decreases appears to increase with decreasing perveance levels. Similar qualitative results were reported by Kaufman on the basis of numerical solutions for the electron backstreaming problem.[6] In summary, Figs. 11 to 13 indicate that there are secondary effects due to hole size (or open area fraction), net accelerating voltage, and perveance on the electron backstreaming parameter. Disregarding these minor effects the figures suggest that there is an upper limit on the electron backstreaming parameter of ~ 0.10.

Electrical Breakdown

The apparatus used in the conduct of the ex-
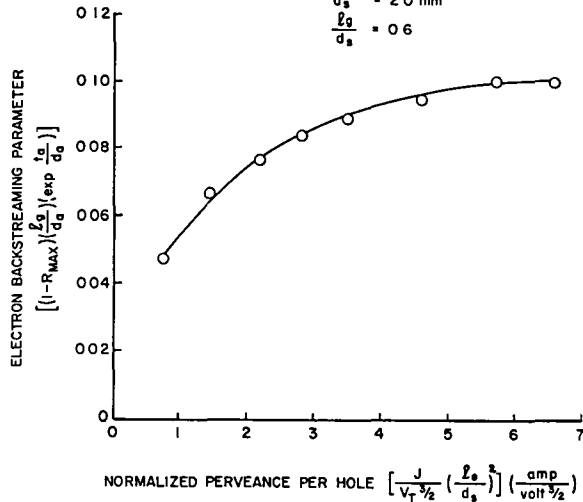
Fig. 13 Effect of Perveance on the Electron Backstreaming Parameter for 2.0 mm Diameter Grid Apertures

periments described herein were particularly well suited to the conduct of tests on the electrical breakdown characteristics of grid pairs for ion sources. The reasons for this were that 1) the grid separation could be varied to determine when breakdown would occur and 2) the grids were small so the effects of electrostatically and thermally induced deformations could be minimized. Figure 14 shows that the electrical breakdown characteristics
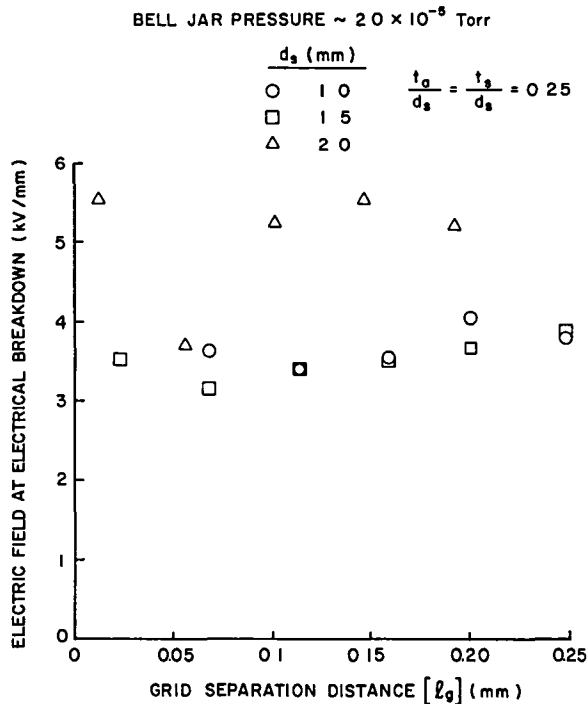
Fig. 14 Electrical Breakdown Characteristics of Graphite Grid Pairs

of each of the different graphite grid pairs remained fairly constant over the range of grid separations investigated in the range of 3 to 5.5 kV/mm. All of the data lies above an electrical breakdown limit of 3 kV/mm. This is slightly higher than generally accepted limit of 2 kV/mm for ion thruster accelerator systems.[5] No special effort was made to ensure the quality of the finishes on the grid surfaces and it is believed that this caused the scatter in the electrical breakdown limits shown in Fig. 14. There is no effect of grid aperture diameter or grid spacing on the breakdown electric field apparent from the data of Fig. 14. Additional tests also suggested that neither the net acceleration voltage nor the perveance at which the grids were operating influenced this breakdown electric field measurably.

Conclusions

Apparatus for testing two-grid accelerator systems has been developed which is well suited to evaluating the impingement-limited current density capabilities and the electron backstreaming and electrical breakdown characteristics of such systems. The basic relationships defining the current density capabilities of ion optic systems appear to be valid for screen grid hole diameters as small as 1 mm and it is expected that these relationships will be valid for even smaller screen grid hole diameters. Tests show, however, that the impingement-limited perveance per hole at which the grids can be operated degrades as the ratio of discharge-to-net accelerating voltage increases. The results also show that operation at the highest current densities are realized at close grid separations when the net-to-total accelerating voltage ratio is high. In general, at close grid separations there is an optimum range of net-to-total accelerating voltages. To operate in this optimum range, the ratio of net-to-total accelerating voltage must be high enough to avoid poor focusing yet low enough to prevent electron backstreaming. Electric fields greater than 3 kV/mm were obtained before electrical breakdown occurred between the pairs of graphite grid tested.

References

1. Kerslake, W. R. and E. V. Pawlik, "Additional Studies of Screen and Accelerator Grids for Electron-Bombarment Ion Thrusters," NASA Technical Note D-1411, 1963.

2. Rawlin, V. K., "Studies of Dished Accelerator Grids for 30-cm Ion Thrusters," AIAA Paper No. 73-1086, Oct/Nov. 1973.

3. Aston, G., Kaufman, H. R., and Wilbur, P. J., "The Ion Beam Divergence Characteristics of Two-grid Accelerator Systems," AIAA Journal, Vol. 16, No. 5, May 1978, pp. 516-524.

4. Aston, G., "Ion Extraction from a Plasma," NASA CR-159849, June 1980.

5. Kaufman, H. R., "Technology of Electron Bombardment Thrusters," Advances in Electronics and Physics, Vol. 36, Academic Press Inc., San Francisco, 1974.

6. Kaufman, H. R., "Accelerator System Solutions for Broad Beam Ion Sources," AIAA Journal, Vol. 15, July 1977, pp. 1025-1034.

AIAA'82

AIAA-82-1945
The Influence of Stray Magnetic Fields on Ion Beam Neutralization

Feng Yu-Cai, Chinese Academy of Science,
Beijing, People's Republic of China; and
P.J. Wilbur, Colorado State Univ., Fort
Collins, CO

AIAA/JSASS/DGLR 16th International Electric Propulsion Conference

November 17-19, 1982/New Orleans, Louisiana

THE INFLUENCE OF STRAY MAGNETIC FIELDS ON ION BEAM NEUTRALIZATION+

Feng Yu-Cai* and P. J. Wilbur**
Colorado State University
Fort Collins, Colorado

Abstract

An experimental investigation is described in which a comparison of the ion beam neutralization characteristics of a local neutralizer (within ∿ 5 cm of the beam edge) with those associated with a distant one (∿ 1 meter away from thruster) were compared. The influence of magnetic fields in the vicinity of the neutralizer cathode orifice which were either parallel or normal to the neutralizer axis were studied. Plasma property profiles which reflected the influence of the magnetic fields were measured. The results indicate that magnetic fields at the region of a neutralizer cathode orifice influence its ability to couple to the ion beam. They show that there is a potential jump from the neutralizer cathode orifice to the plasma which exists close to the orifice. This potential drop increases as the axial component of magnetic flux density increases. A magnetic field perpendicular to the neutralizer axis induces a potential rise a few centimeters further downstream of the neutralizer cathode. Test results indicate the path length from the neutralizer to the beam along magnetic field lines also has an effect on the beam-to-neutralizer plasma potential difference but this effect was typically smaller than the other two effects. The results suggest that in order to minimize the adverse effects of stray magnetic fields, a region as free of magnetic fields as possible should be selected for placement of the neutralizer.

Introduction

Recent tests conducted in space on the SERT II Spacecraft included an investigation of the process of ion beam neutralization from an electron source located far from the ion beam. This was accomplished by using the neutralizer or unaccelerated thruster plasma of a thruster located a meter or so away from the thruster operating at high voltage.[1,2] One of the results observed in this test was that the potential difference between the neutralizer and beam plasma potential could be lower with the distant neutralizer than it was when the local one was used. In order to determine if local magnetic fields could be the cause of this and to develop an understanding of neutralization phenomena that would aid in the design of future neutralizers, the study described herein was conducted. The experiments undertaken included a comparison of the ion beam neutralization characteristics of a local

neutralizer with those associated with a distant one. A study of the influence of magnetic fields in the vicinity of a neutralizer cathode orifice on ion beam neutralization was also undertaken. The plasma property profiles which reflected the effects of changes in magnetic fields near the neutralizers were measured.

Apparatus and Procedure

The experiments were conducted in the 1.2 m diameter by 4.6 m long stainless steel tank shown schematically in Fig. 1. The operating pressure
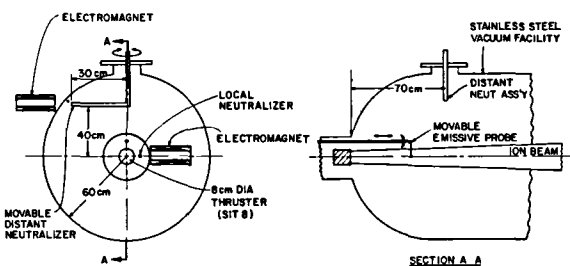

Fig. 1 Neutralization Test Apparatus

in the vacuum system was in the range of 5 ∿ 7 x 10⁻⁶ torr during the tests. At this pressure the electron collision frequency is small compared to a typical cyclotron frequency so the conditions of this test should model the collisionless environment of the space tests adequately. Further the potential of the plasma in the vacuum tank was typically several volts above ground, so most neutralizer electrons should have been reflected from the tank walls; a condition that also facilitates modeling of the space plasma. The SIT-8 mercury ion thruster[3] identified in Fig. 1 is located at one end of the test facility in such a way that its ion beam is directed along the tank axis. Neutralization of this beam is accomplished by either the standard SIT-8 hollow cathode mercury neutralizer[3] located adjacent to the thruster or by the distant neutralizer shown in Fig. 1. Both neutralizers utilize conventional 0.32 cm dia. mercury hollow cathodes. Each of the neutralizers is equipped with a rolled tantalum foil insert, and a toroidal keeper electrode located ∿ 0.08 cm downstream of the orifice plate. The distant neutralizer cathode has a 0.04 cm dia. orifice while the local one is 0.025 cm in diameter. In order to achieve stable and reproducible operation of the neutralizers, the distant one was operated at a mercury flow rate of ∿ 60 mA while the local one operated at ∿ 12 mA. The lower flow rate was presumably required for the local neutralizer because it had a smaller orifice diameter and because it utilized an enclosed keeper configuration.

The distant neutralizer was attached to a rod passing through the top of the tank as shown in Fig. 1. When this rod was rotated the neutralizer

moved through a 180° arc from one side of the tank to the other. Because the vacuum tank is stainless steel the influence of the earth's magnetic field is felt within it. This field has a magnitude of ∿ 0.5 gauss and is inclined at an angle of 65° from the direction of the ion beam in the plane of section A-A in Fig. 1. Movement of the neutralizer support rod through its 180° travel is sufficient to place the neutralizer at positions where it lies on earth magnetic field lines that either intersect the ion beam centerline or miss it by distances up to ∿ 30 cm. Each neutralizer cathode was equipped with power supplies that controlled keeper potential, cathode tip heater current and neutralizer bias potential. Keeper currents for the cathodes were maintained at either 0.3 or 0.4 A and the neutralizer bias was adjusted so it was sufficiently negative to effect the neutralizer emission required to match the ion beam current. Auxiliary magnetic fields of variable magnitude were generated in these experiments by using the two electromagnets shown in Fig. 1. These magnets were located immediately adjacent to the particular neutralizer they served. Magnetic fields of the order of 15 to 30 gauss could be induced at the neutralizer cathodes with these magnets.

Evaluation of the effects of parametric variations introduced in the experiments required the measurement of the neutralizer bias voltages, profiles of the plasma potential, and magnetic field shapes and magnitudes. The neutralizer bias voltage could be measured directly but the beam plasma potential had to be measured by an emissive probe as suggested by Fig. 1.

In a second series of experiments the distant neutralizer was moved to the vicinity of the vacuum feedthrough in the configuration shown in Fig. 2. In this configuration the neutralizer cathode axis was pointed at the ion beam rather than away from it as it had been in the configuration shown in Fig. 1. It was also installed so emitting and non-emitting spherical Langmuir probes could be used to measure plasma properties along the neutralizer axis through that region ranging from immediately adjacent to the distant neutralizer into the ion beam. The emissive probes were used to measure plasma potential profiles while the non-emitting one gave electron density and temperature information as well. The details of the operation of these probes are described in Refs. 4 and 5. In this second series of tests two electromagnets were installed to facilitate control of the magnetic field in the vicinity of the distant neutralizer in the manner suggested in Fig. 2. The intensities and shapes of magnetic fields in all of these tests were determined from gaussmeter and iron filings map measurements.

Experimental Results

Neutralization in the Unaltered Environment of the Magnetic Fields of the Thruster and Earth

The initial investigations into the neutralization of the ion beam were conducted with the electromagnets shown in Fig. 1, turned off. The magnetic field in the region between the distant neutralizer and ion beam is in this case the weak one (∿ 0.5 gauss) associated with earth only. In the region between the local neutralizer and ion beam the net magnetic field as induced by the thruster and earth was about 18 gauss. At a beam
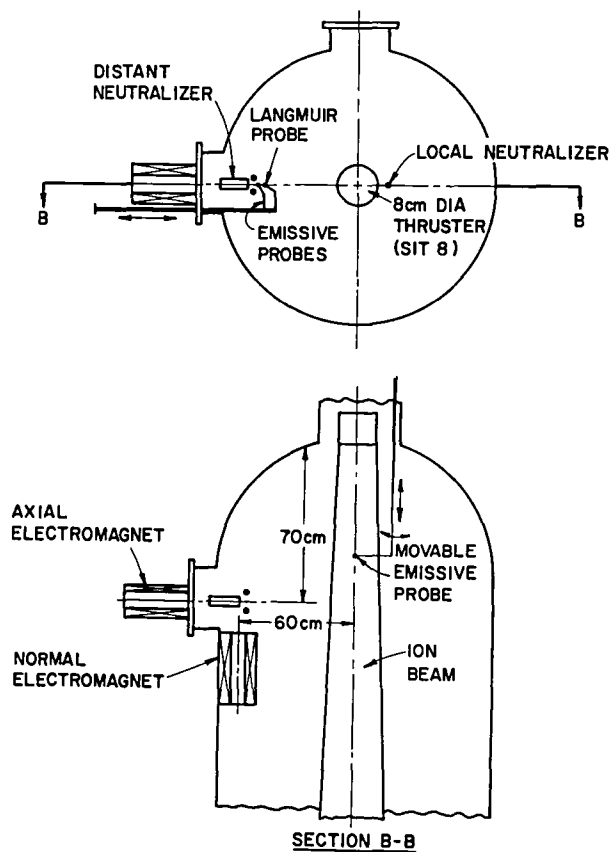

SECTION B-B

Fig. 2 Neutralization Test Apparatus

current of 100 mA with the distant neutralizer positioned as shown in Fig. 1, so electrons emitted from it would pass about 30 cm from the beam centerline, the plasma potential profiles represented by the dotted and dashed curves of Figure 3 were observed. These profiles were measured through the ion beam at the indicated distances downstream of the ion source screen grid and during data collection for these curves, the local neutralizer was not operating. When the distant neutralizer was turned off and the local neutralizer was started the higher plasma potentials represented by the solid and centerlines were observed at the two axial locations identified. The higher plasma potentials observed here with the local neutralizer are reminiscent of results obtained during some of the SERT-II tests[1,2] conducted in space. The plasma potential profile at the 6 cm location is also seen to be broader when the local neutralizer is being used, a condition that was also observed in the space tests. Both of these effects are believed to be manifestations of an impedence between the beam and local neutralizer plasmas that is higher than the one between the distant neutralizer and beam plasma. This postulate is also supported by the observation that the neutralizer cathode bias voltage relative to ground (V_c) required to effect neutralization was also considerably lower in magnitude when the distant neutralizer was used.

In a second experiment the local neutralizer was secured, the distant neutralizer was moved with respect to the ion beam while the thruster was operating. The effect of this movement on the ion
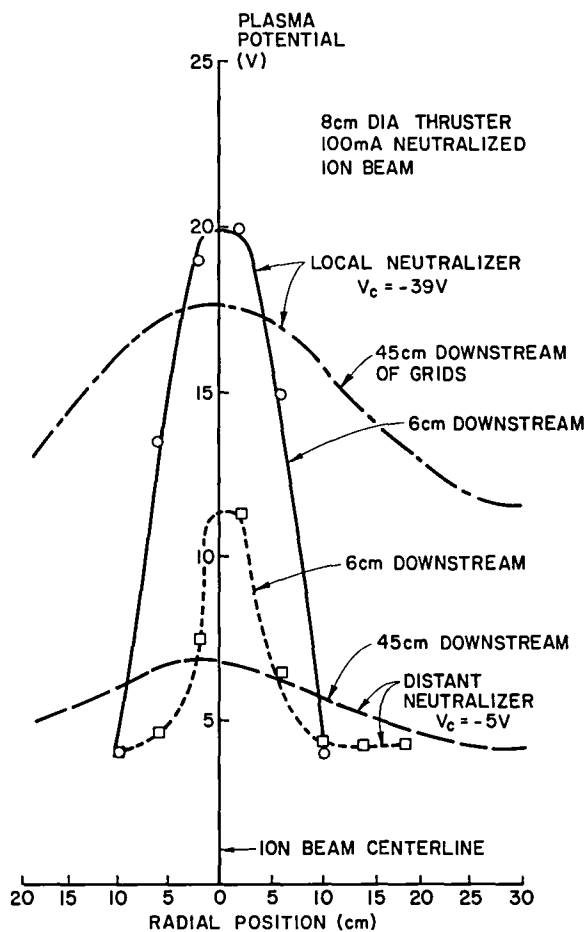
120

Fig. 3 Effect of Neutralizer Location on Ion Beam Plasma Potentials

a NEUTRALIZER ON FIELD LINE MISSING BEAM ℄ BY ~30cm

b NEUTRALIZER ON FIELD LINE INTERSECTING BEAM ℄

Fig. 4 Effect of Distant Neutralizer Position in the Earth's Magnetic Field

beam plasma profile was examined. This neutralizer movement was accomplished by rotating the arm supporting the distant neutralizer (Fig. 1) so the neutralizer plasma was moved from the earth magnetic field line missing the ion beam centerline by ∿ 30 cm to one passing through the ion beam centerline and the beam potential profiles shown in Fig. 4 were obtained. As indicated on the figure, profiles were measured at axial locations downstream from the grids (x) of 6, 29 and 52 cm. The results shown in this figure are as expected in that the beam plasma potentials dropped when the neutralizer was moved to the field line intercepting the beam axis. The fact that this drop was small (∿ 3v) could be due to the fact that the neutralizer plasma was not moved very far away from the edge of the beam plasma. In this regard it is noted that 1) the beam plasma potentials suggest substantial beam spreading with axial position and 2) the electron gyro radius in the tank plasma and earth's magnetic field is about 10 cm. The fact that the gyro radius is less than the 30 cm distance between the magnetic field line passing through the neutralizer plasma and the beam centerline is consistent with the observed change in the plasma potential profiles. It is also noted that the neutralizer bias voltage (V_c) required to effect neutralization of the 100 mA beam current tracked with the changes in plasma potentials. It has been suggested[6] that fluctuations in beam

plasma potentials of the order of several volts observed during the SERT-II space tests could have been caused by spacecraft motion in the earth's magnetic field. These fluctuations were originally attributed to a spacecraft wake effect but the relative motion of the distant neutralizer and beam in the earth's magnetic field could have also caused this effect in much the same way it was induced in the test just described.

The Influence of Magnetic Field at the Distant Neutralizer

For this series of tests the electromagnet at the distant neutralizer in the Fig. 1 test configuration was positioned so its solenoidal magnet field was aligned with the neutralizer axis as suggested by the inset sketch in Fig. 5. As the electromagnet current was varied the shapes of the field lines shown in Fig. 5 were not altered but the field strengths did change. The beam plasma potential profiles at axial locations of 6, 29 and 52 cm downstream of the grids were measured as this change was effected. The relative shapes and magnitudes of these profiles at these three axial positions were however consistent with the trends shown in Figure 5. As a result the plasma potential at the beam centerline 6 cm downstream of the grids was selected as representative of the state

121

Fig. 5   Effect of Magnetic Field at Distant
         Neutralizer on Beam Plasma and Neutralizer
         Potentials

of the beam plasma potential. Figure 5 shows that
the magnitudes of both this representative beam
plasma potential and the neutralizer bias voltage
increase as the magnitude of the solenoidal mag-
netic field at the neutralizer tip is increased.
The same behavior is observed at beam currents of
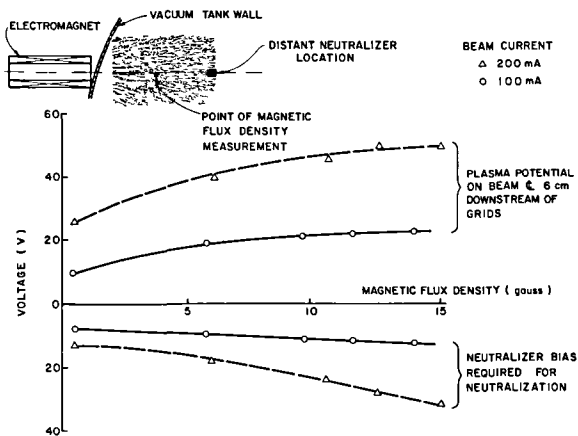100 mA and 200 mA although the magnitudes of both
voltages are higher at the higher beam current.

Figure 6 shows that the coupling voltages be-
tween the neutralizer and beam plasmas (i.e., total
voltage drop from beam plasma to neutralizer tip)
taken from the data of Figure 5 are nearly directly
proportional to magnetic flux density at both beam
currents. Further, these voltage difference levels
increase in direct proportion to the beam current
level. Visual observation of the neutralizer
plasma when the solenoidal magnetic field current
was increased showed that an increase in the field
strength caused the luminous region associated with
the cathode discharge to contract. As the magnetic
field strength was increased to ~ 15 gauss, the
hollow cathode discharge appeared as a very tiny
bright spot at the orifice.

In order to further clarify the influence of
the magnetic field on the neutralizer's ability to
couple to the ion beam, another series of tests
were undertaken. In these tests the distant neu-
tralizer was positioned so its axis was perpendic-
ular to the thruster axis as shown in Fig. 2. The
magnetic fields were arranged so one was aligned
with the neutralizer axis and another was normal to
it as suggested by the sketch of section B-B in
Fig. 2. Each of the magnets could be controlled
independently. Again as the current was varied to
either electromagnet the shapes of the field lines
were not altered but the field strengths did change.

The plasma potential profiles along the neu-
tralizer axis from the cathode to the ion beam
center observed when the axial magnetic field was
on and the normal magnetic field was off are shown
in Fig. 7a. These curves show that there is a
steep potential jump between the neutralizer
cathode and the plasma close to the cathode orifice.
Most of the voltage increase between the neutra-
lizer cathode and the beam plasma is seen to occur
in this region. Further the magnitude of this
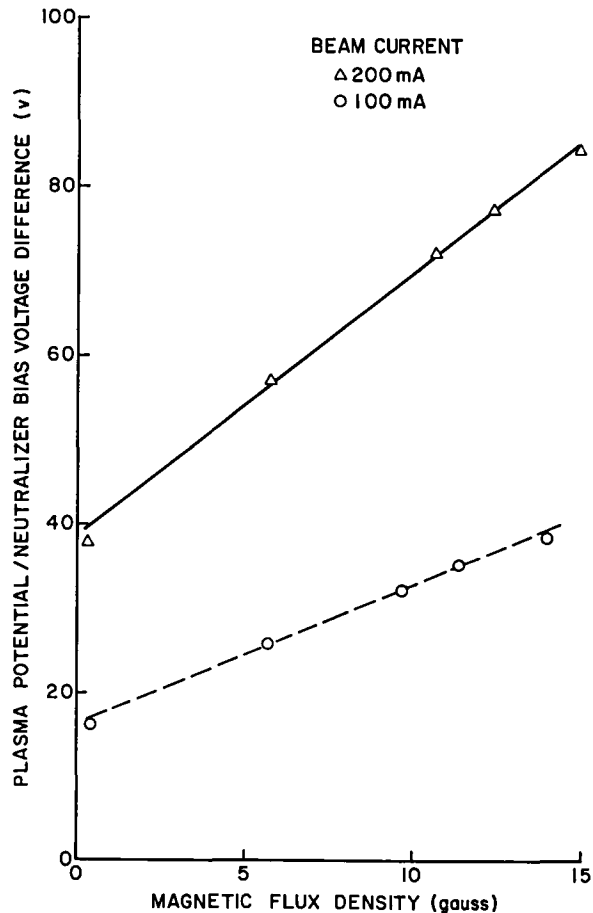
Fig. 6   Effect of Magnetic Field at the Distant
         Neutralizer on Voltage Difference Between
         the Neutralizer and Ion Beam

voltage rise is observed to increase with axial
magnetic flux density at the neutralizer tip. It
is noteworthy that the data points at the cathode
orifice (on the vertical axis) in Fig. 7a corres-
pond to the neutralizer bias voltage while those
further downstream were measured using the emis-
sive probes. After the initial voltage jump, its
rise is observed to be approximately linear with
distance and of the order of a few to several volts.
As the axial magnetic field (the component along
the direction of the neutralizer axis) was in-
creased by increasing the current to the axial
electromagnet (Fig. 2), Fig. 7a shows the magni-
tudes of the plasma potentials increased and the
cathode potential required to induce a 100 mA emis-
sion current decreased. Fig. 8 shows this same
effect in the form of plots of the beam plasma
(i.e., 60 cm from the neutralizer), the neutralizer
plasma (i.e., ~ 0.3 cm from the neutralizer) and
the neutralizer cathode potentials as a function of
the magnetic flux density at the neutralizer ca-
thode orifice. It is noted the plasma density pro-
file measured along the neutralizer axis and shown
in Fig. 9 as function of axial magnetic field does
not seem to be affected significantly by this field.
These results suggest that the axial magnetic field
affects the capacity of a neutralizer to couple to
the ion beam principally because it induces a po-

a) PLASMA POTENTIAL PROFILES ON NEUTRALIZER AXIS

b) AXIAL MAGNETIC FLUX DENSITY PROFILES ON NEUTRALIZER AXIS

Fig. 7   Effect of Axial Magnetic Field

Fig. 8   Effect of Axial Magnetic Field on Neutralizer and Beam Potentials
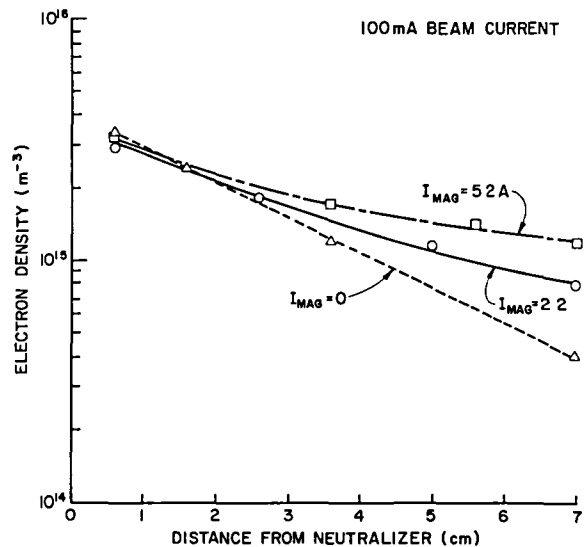
Fig. 9   Electron Density Profile for Axial Magnetic Field Case

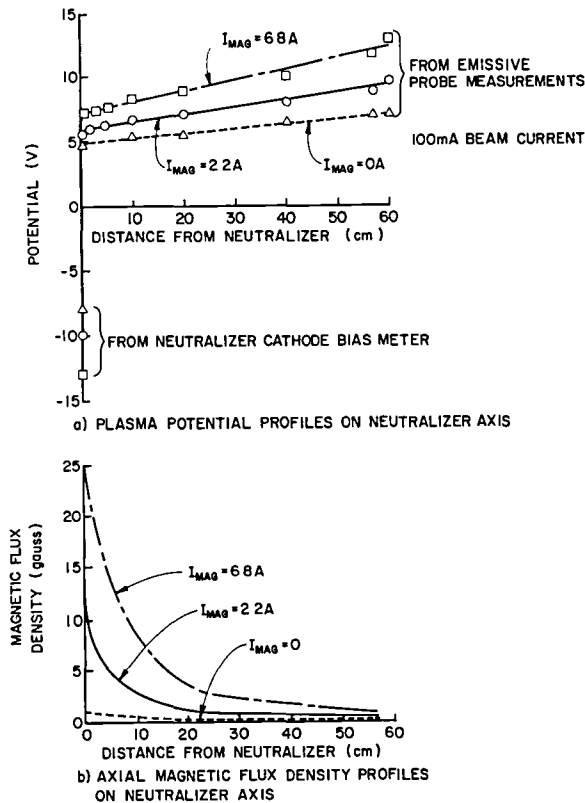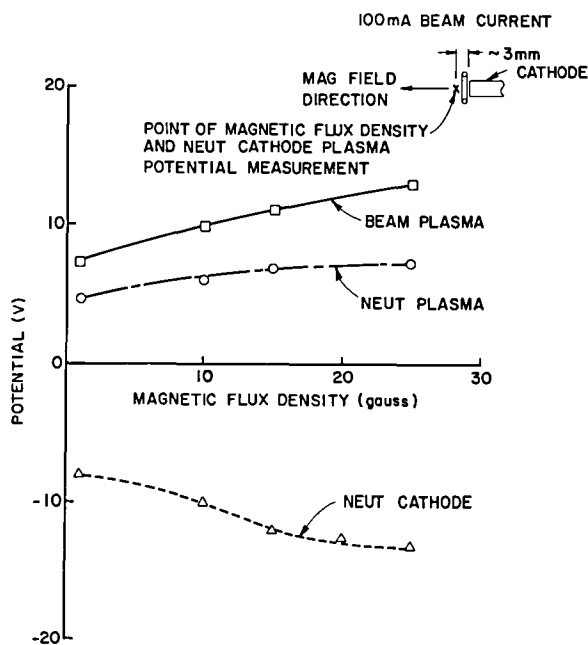tential drop close to the cathode orifice. Finally it is noted that the coupling voltage between the neutralizer and beam plasma is nearly directly proportional to the magnetic flux density.

Plasma potentials were also measured for the case where the axial magnetic field was turned off and the normal magnetic field was turned on. Figure 10 shows how this magnetic field component affects the plasma potential profile. In contrast to Fig. 8, where the axial field was observed to cause an increase in the potential difference very close to the cathode ($\lesssim$ 0.3 cm), the normal magnetic field induces a potential difference over a much longer distance (a few centimeters). The increase in potential difference through this region is presumably caused by the plasma impedance induced by the magnetic field aligned perpendicular to the direction of current flow. Figure 11 shows that the variation in plasma density along the neutralizer axis when the normal magnetic field is applied. Comparison of this Figure with Fig. 9 reveals a much more dramatic drop in plasma density along the neutralizer axis when the normal field is applied in place of the axial one. In Figure 12 the potentials of the beam plasma, neutralizer plasma and neutralizer cathode are plotted as a function of the normal magnetic field flux density. This Figure again shows that the potential rise at the cathode does not increase in the immediate vicinity of the cathode as it did in the case of the axial magnetic field. As suggested by Fig. 10 most of the potential rise occurring between the beam and neutralizer plasmas is observed within a few centimeters of the neutralizer cathode.

The Influence of the Magnetic Field at the Local Neutralizer

The test results obtained with the local SIT-8 neutralizer showing the influence of stray magnetic fields in its vicinity on neutralization performance indicators are shown in Fig. 13. In this case the neutralizer is located in the magnetic field associated with the thruster itself; this

a) PLASMA POTENTIAL PROFILES ALONG NEUT AXIS

b) NORMAL MAGNETIC FIELD FLUX DENSITY
PROFILES ON NEUT AXIS

Fig. 10   Effect of Normal Magnetic Field

Fig. 11   Electron Density Profile along Neutralizer
Axis - Normal Magnetic Field

Fig. 12   Effect of Normal Magnetic Field on
Neutralizer and Beam Potentials

field is oblique to the local neutralizer axis. The
test involved altering this field with an external
magnet and measuring the resulting changes in beam
and neutralizer bias potentials. The central iron
filings map in Figure 13 shows the unaltered mag-
netic field associated with the thruster as well as
the location of the neutralizer in this field. In
the filings maps to the left of center the external
magnet acts to cancel the thruster field thereby
reducing the magnitude of magnetic flux density at
the neutralizer and bending the field lines passing
through the neutralizer toward the ion beam. In
the filings maps on the right, the external magnet
is used to increase the magnetic field magnitude
and draw the field lines passing through the neu-
tralizer still further away from the beam. The
arrows associated with each filings map indicate
the magnitude of magnetic flux density at the neu-
tralizer corresponding to that filings map.
Figure 13 shows that when the magnetic flux density
magnitude is increased and the field lines passing
through the neutralizer are drawn further away from
the beam, the neutralizer bias and beam plasma po-
tentials are increased. Conversely, reducing the
magnetic flux densities and directing the field
lines toward the beam reduces the magnitudes of
these potentials somewhat. As with the distant
neutralizer (Fig. 5), operation at high beam cur-
rents requires higher potential differences between
the beam and neutralizer in order to effect neu-
tralization. The results of Fig. 13 are observed
to be qualitatively consistent with results obtain-
ed with the electromagnets used in tests associated
with the distant neutralizer.
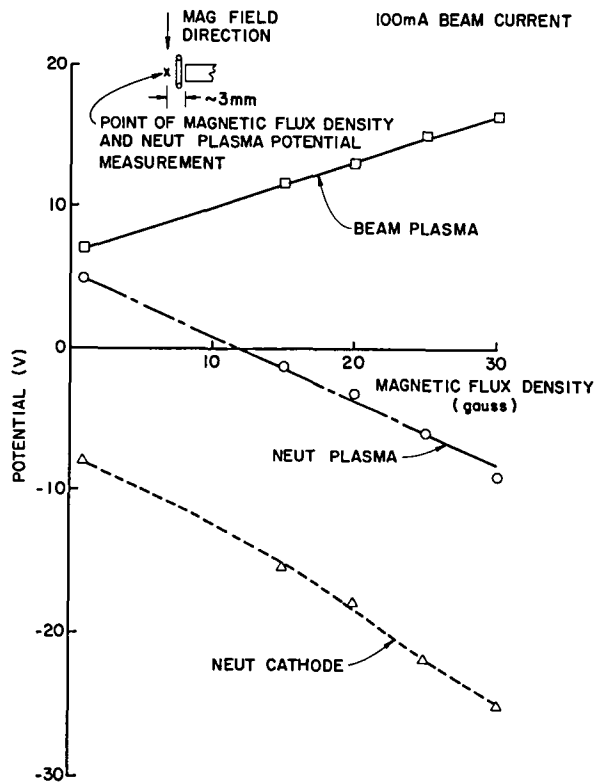
Fig. 13 Effect of Magnetic Field at Local
Neutralizer on Beam and Neutralizer
Potentials

A Phenomenological
Discussion of Test Results

The Influence of Axial Magnetic Field on
Neutralization

The experiments have suggested that the plasma
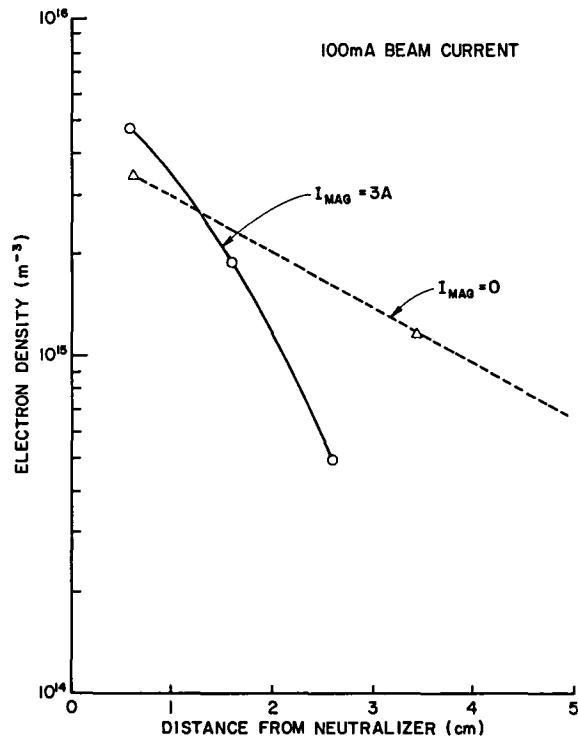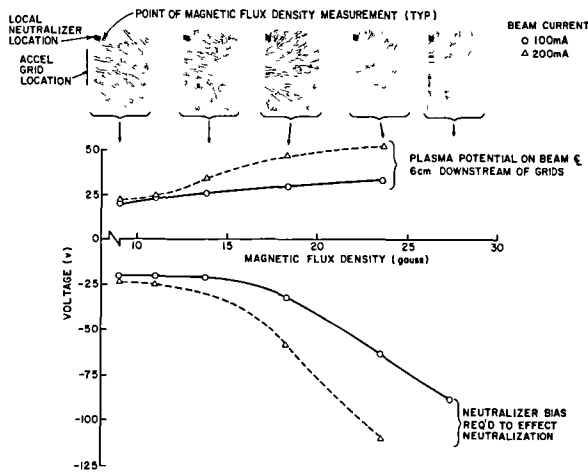between the neutralizer cathode and the ion beam
can be described as three separable regions. The
first will be defined as the thin layer (sheath)
immediately adjacent to the cathode orifice. The
next (intermediate) region is assumed to extend
from this cathode region through the first few cen-
timeters immediately downstream of it. The final
(distant) region is assumed to extend from the edge
of the second region to the ion beam. Based on the
experimental results obtained the following model
describing the influence of low intensity stray
magnetic fields in these three regions is proposed:

1) The sheath region is affected by the axial
   magnetic field,

2) The intermediate region is affected by the
   normal magnetic field, and

3) The distant region is not affected signif-
   icantly by either component of magnetic
   field.

At the hollow cathode orifice emitted electrons
and ions are both present so a double sheath is
formed. When no magnetic field was applied in the
experiments the bulk of the neutralizer-to-beam po-
tential rise occured across this sheath. As the
axial magnetic field strength was increased this
sheath potential rise increased in magnitude. It
is postulated that with no magnetic field present
the sheath is curved because the electrons exiting
the orifice can move both radially and axially
toward the keeper and/or the beam. As the axial
magnetic field strength is increased it is argued
that the electrons are confined to move along field
lines and the sheath moves from a curved to a flat
configuration. In order to model the effect of the
axial magnetic field on the sheath potential rise

consider the sheath with no field present to be
hemi-spherically convex.

For the purposes of this analysis the poten-
tial through the sheath will be measured relative
to the downstream sheath plasma boundary where the
potential is taken to be zero. Position will be
measured from the neutralizer cathode orifice exit
surface where $r = r_0$ as shown in Fig. 14. Assuming
the thickness of sheath to be one Debye length (λ_d)
analysis shows in the test under consideration that
$\lambda_d < \lambda_m$ is satisfied where λ_m is the electron mean
free path for elastic collisions. Therefore the
particles are assumed to move without collision or
ion production within the sheath. The sheath
plasma is assumed to be composed of three particle
groups, namely electron drawn from the cathode in-
terior, ions from the downstream plasma, and elec-
trons from this same plasma. The electrons from
the cathode interior are assumed to enter the
sheath with a negligible velocity and to have a cur-
rent density J_e and a mass m_e. Ions entering from
the other side have a current density J_i, a mass m_i
and a velocity determined by the Bohm criterion.
The potential equivalent of their velocity is given
by

$$V_0 = \frac{kT_e}{2e} \qquad (1)$$

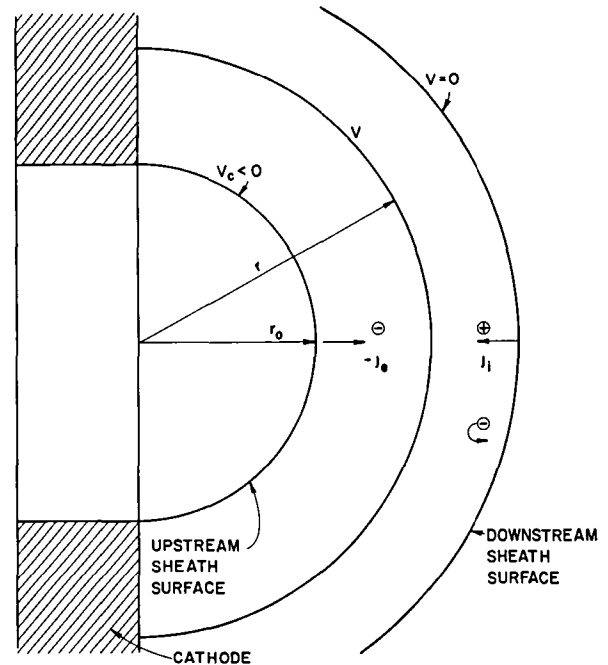where T_e is the electron temperature in the down-
stream plasma.

Fig. 14 Schematic Diagram of Cathode Sheath

The plasma electrons entering the sheath from
the downstream plasma will have a Boltzmann dis-
tribution so that their density n_e will decay ex-
ponentially into the sheath. Their charge density
can be expressed as

$$\rho_{e_1} = en_e = en_{e_0} \exp [eV/kT_e] \qquad (2)$$

where n_{e_0} is the density of electrons at sheath edge where $V = 0$. These three plasma constituents combine to determine the potential variation through the plasma sheath. In this case we assume spherical symmetry and a sheath dimension that is small compared to the orifice radius so the effect of curvature can be neglected.[7] For this case Poisson's equation can be used to describe the physical situation in one dimension.

$$\frac{d^2V}{dr^2} = \frac{J_e}{\epsilon_0 \sqrt{\frac{2e(V-V_c)}{m_e}}} - \frac{J_i}{\epsilon_0 \sqrt{\frac{2e(V_0-V)}{m_i}}}$$

$$+ \frac{1}{\epsilon_0}\left(en_{e_0}\right)\exp(eV/kT_e) \quad (3)$$

where ϵ_0 is the permittivity of free space. Using the definition

$$\alpha = \frac{J_i}{J_e}\left[\frac{m_i}{m_e}\right]^{\frac{1}{2}}$$

and applying the space charge limiting boundary conditions

$$\left.\frac{dV}{dr}\right|_{r=r_0} = 0$$

$$\left.\frac{dV}{dr}\right|_{r=r_0+x_s} = 0$$

where x_s is the sheath thickness Eq. (3) integrates to

$$\frac{dV}{dr} = \left\{ \frac{4J_e}{\epsilon_0}\left(\frac{m_e}{2e}\right)^{\frac{1}{2}}\left[(V-V_c)^{\frac{1}{2}} + \alpha[(V_0-V)^{\frac{1}{2}} - (V_0-V_c)^{\frac{1}{2}}]\right]\right.$$

$$\left. + \frac{2n_{e_0}kT_e}{\epsilon_0}\exp(\frac{eV}{kT_e}) \right\}^{\frac{1}{2}} \quad (4)$$

The sheath thickness can be expressed as

$$x_s = \int_0^{-V_c} dV \left[\frac{4J_e}{\epsilon_0}\left(\frac{m_e}{2e}\right)^{\frac{1}{2}}\left\{(V-V_c)^{\frac{1}{2}} + \alpha[(V_0-V)^{\frac{1}{2}}\right.\right.$$

$$\left.\left. - (V_0-V_c)^{\frac{1}{2}}]\right\} + \frac{2n_{e_0}kT_e}{\epsilon_0}\exp(\frac{eV}{kT_e})\right]^{-\frac{1}{2}} \quad (5)$$

where

$$\alpha = \frac{\frac{4J}{A}\left(\frac{m_e}{2e}\right)^{\frac{1}{2}}(-V_c)^{\frac{1}{2}} + 2n_{e_0}kT_e}{\frac{4J}{A}\left(\frac{m_e}{2e}\right)^{\frac{1}{2}}[(V_0-V_c)^{\frac{1}{2}} - V_0^{\frac{1}{2}}]} \quad (6)$$

In this expression J is the sum of the keeper current and the ion beam neutralization current and A is the surface area of sheath through which the electron current flows. This area is taken to be the surface area of the sector of a sphere of radius R intersecting the cathode orifice circle. If one

assumes the potential of electrons entering the sheath from the cathode interior is approximately equal to the potential of the cathode and that the potential at the downstream sheath surface is equal to the potential which was measured $\sim$ 3 mm downstream of the cathode the sheath thickness in the absence of a magnetic field is found to be $\sim$ 0.024 mm from Eq. (5).

In the presence of a magnetic field, as mentioned earlier the surface should tend to become more planar (i.e., R increases). In the limit of a high magnetic field $R \to \infty$ and the sheath surface is equal to the area of the cathode orifice. If we assume the sheath thickness is independent of the axial magnetic field strength then the difference in the potential rise from the cathode to the neutralizer plasma for these two extremes (R = r_0 and R = ∞) can be computed. This change in potential for the conditions pertaining to the present problem is found to be $\sim$ 12v, (assuming T_e = 0.8 eV[8], and using measured values for the other quantities in Eqs. (5) and (6)).

The measured changes in the neutralizer plasma-to-cathode potential difference ranged in value up to 7 or 8 volts at axial magnetic flux densities near 25 gauss. It is believed that magnetic flux densities near 50 gauss would be sufficient to induce the computed change in potential difference of 12 volts. At any rate the relative agreement between the measured and computed values is considered significant.

For this case of an axial magnetic field the experiments suggest that the potential drop through the intermediate and distant regions is only a few volts and that it varies linearly with distance. Axial magnetic field strength seemed to have a minimal effect on the voltage rise through these regions. It is postulated that this condition exists because the magnetic and electric fields are approximately parallel. Under this condition the conduction current dominates so the plasma conductivity is not influenced substantially by magnetic field strength. In addition the collision frequency is relatively small and this is also essential to the small rise observed through these regions. The small increase in potential rise that is observed through these regions with changes in axial magnetic field is considered to be due primarily to small changes in the path length from the neutralizer to the ion beam.

The Influence of a Normal Magnetic Field on Neutralization

The experiments indicate that a normal magnetic field effects a voltage rise in the intermediate region rather than the sheath region. It is argued in this case that electrons in the intermediate region are affected by both the electric and magnetic field that exist there and that these fields tend to be mutually perpendicular. It is also argued that in this intermediate region the neutral density is sufficiently low so the ratio of gyro frequency to collision frequency is moderate and as a result the Hall Current is significant. As the normal magnetic field is increased under these circumstances there should be a substantial increase in the path length of electrons passing between the sheath and distant regions. It is believed that this increase in path length

through a region of moderate to low collision frequency causes the observed increase in potential difference.

For this case where a normal magnetic field is applied the voltage rise through the sheath is not affected by the field strength. This is expected because the sheath thickness is small compared to the gyro radius. In the distant region the magnet induces a small change in the magnetic field. The magnetic field there is quite weak and generally parallel with the electric field. Hence the effect of field strength on the potential rise through the distant region is relatively small as it was in the case where an axial magnetic field was applied.

Combined Axial and Normal Magnetic Field Effects

When the local neutralizer is used both normal and axial magnetic field components are present. Under this condition the axial magnetic field component should cause the potential rise at the sheath to increase while the normal magnetic field component should cause a potential rise through the intermediate region. Comparison of the results of Figs. 8 and 12 with those of Fig. 13 suggest that the potentials observed in this configuration are however higher than one would predict considering both of the separate voltage rise components due to separate axial and normal magnetic fields. It is considered likely in this case that the conduction path length in the distant is increasing substantially as magnetic field is varied so that the potential rise in the distant region also becomes significant.

Conclusions

The magnetic field at a neutralizer cathode orifice influences the neutralizer's ability to couple to the ion beam. A magnetic field which is aligned with the neutralizer axis influences the potential rise at the neutralizer cathode sheath which exists between the neutralizer cathode and the plasma immediately adjacent to it. This potential difference between the neutralizer and adjacent plasma increases linearly with axial magnetic flux density. When a magnetic field that is perpendicular to the neutralizer axis is applied the region over which the potential rise occurs is extended over several centimeters.

Stray magnetic fields associated with ion thruster themselves are sufficiently large to cause substantial increases in the potential difference between the neutralizer and the beam plasma. In order to minimize this effect a region as free of magnetic fields as possible should be selected for placement of the neutralizer. The neutralizer does not seem to have any difficulty coupling to the ion beam over distance of the order of 1 meter as long as the magnetic field levels are low (of order 0.5 gauss or less). If a neutralizer must be located in the region of a stray thruster magnetic field, an external magnet which is properly arranged to alter the magnetic field so it is directed toward the ion beam can improve coupling. Application of such a field does not seem to alter thruster performance measurably. Magnetic fields of the order of those associated with the earth ($\sim$ 0.5 gauss) can effect small beam plasma potential changes (of order 1v) when they are interposed between an ion beam

and a neutralizer located on the order of 1 meter away.

References

1. Kerslake, W. R. and S. Domitz, "Neutralization Tests on the SERT-II Spacecraft," AIAA Paper No. 79-2064, Oct/Nov., 1979.

2. Kerslake, W. R. and L. R. Ignaczak, "SERT-II 1980 Extended Flight Thruster Experiments," AIAA Paper No. 81-0665, April, 1981.

3. Hyman, J., et. al., "One-Millipound Mercury Ion Thruster," AIAA Paper No. 75-386, March, 1975.

4. Aston, G., "Ion Extraction from a plasma," NASA CR-159849, June 1980.

5. R. H. Huddlestone and S. L. Leonard, Plasma Diagnostic Techniques, New York, 1965, P. 113-198.

6. Kerslake, W. R., NASA Lewis Research Center, Private Communication, January, 1982.

7. Langmuir, L. and K. B. Blodgett, "Currents Limited by Space Charge Between Concentric Sphers," Phy. Rev. 23, 49 (1924).

8. Siegfried, D. E., and P. J. Wilbur, "Studies on an Experimental Quartz Tube Hollow Cathode," AIAA Paper 79-2056, October, 1979.

AIAA-82-1216
The Electrothermal Ramjet
P.J. Wilbur, C.E. Mitchell and B.D. Shaw,
Colorado State Univ., Fort Collins, CO

THE ELECTROTHERMAL RAMJET*
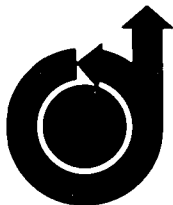
P. J. Wilbur,[**] C. E. Mitchell[**] and B. D. Shaw[+]
Colorado State University
Fort Collins, Colorado

ABSTRACT

An electrothermal ramjet confirguration is examined as a possible alternative to rail guns and mass drivers for high acceleration launch missions. For a specific mission (earth escape) the idealized performance of the electrothermal ramjet, the electrothermal rocket and the electromagnetic acceleration system are compared. This comparison indicates that the gross performance of the ramjet compares favorably with that of the ideal electromagnetic acceleration system. A specific configuration for the ramjet is chosen and models for the dynamics, thermodynamics and fluid mechanics are presented. Results of calculations for a typical supersonic launch cycle suggest that pressure, temperature and power demand profiles associated with ramjet operation should be reasonable. A light gas gun is proposed to accelerate the vehicle to the critical velocity where efficient ramjet operation can begin. The theoretical performance of the ramjet is also shown to be substantially better than that of the light gas gun at high velocities.

INTRODUCTION

The relatively massive expenditure of chemical fuel and oxidizer associated with the launch phase of space missions adds substantially to the cost of such missions. Not only are the propellants costly, but the additional mass of tankage and structure required to hold the propellant mass detracts from the payload mass and therefore adds substantially to the cost of the delivered payload. It is also desirable to simplify these launch systems and improve their reliability. For some missions where high acceleration levels can be tolerated such alternative launch schemes as light gas guns[1], rail guns[2], and mass drivers[3] have been proposed as substitutes for conventional rockets. These missions could include ones in which various materials would be directed into space either for disposal or application there. While the capital investment in such systems is expected to be large, they hold the promise of lower cost per launch because of the large number of launches that should be realized over their design lifetimes.

Because of the high acceleration levels at which these devices could operate, the associated launch tracks could be relatively short and the terminal launch velocity could be achieved while the payload was close to the earth's surface. Achieving terminal velocity in a short distance is considered desirable because the launch could be effected in a tube of reasonable size which would be sealed during the launch sequence if it became necessary to abort the launch. This could facilitate containment if toxic or radioactive materials were being launched.

Another propulsion concept which may be useful in these high acceleration level missions is the electrothermal rocket concept.[4] In these devices on-board propellant is heated electrically and then discharged through a nozzle to produce thrust. Because the heating is accomplished electrically, hydrogen propellant with its attendant high specific impulse capability can be selected. There are several types of electrothermal rockets. In the resistojet, for example, the propellant is heated by passing it over current-carrying, resistive elements and exhaust velocities as high as 8500 m/sec have been achieved.[4] Higher exhaust velocities can be realized if the material limitations imposed by the heating elements are eliminated and joule heating is accomplished by passing current directly through the propellant in an arcjet thruster. Exhaust velocities as high as 15000 m/sec have been demonstrated in these devices.[4]

A basic electrothermal rocket vehicle which might be used in this application is shown conceptually in Figure 1a. This rocket would carry on-board propellant which would be metered into the heating chamber where its temperature could be raised by energy either beamed there electromagnetically or carried there in the form of electrical current from rails located in the launch tube.

For the mission under consideration here, where the launch is accomplished in a relatively short distance close to the earth's surface, it is also practical to distribute the propellant in the launch tube. When this is done a ramjet engine can be used to collect the propellant, heat it and produce the desired thrust as it moves down the tube. Physically the ramjet would operate in the manner suggested by Figure 1b by simply drawing propellant in from the tube through an intake diffuser, heating it electrically and then expelling it through a nozzle. Energy could again be transported into the heating chamber either electromagnetically or in the form of electrical current. No compressor or other rotating equipment would be needed although

an initial velocity would have to be imparted to the vehicle. This might be accomplished by a booster rocket, a light gas gun or a low terminal velocity electromagnetic driver.
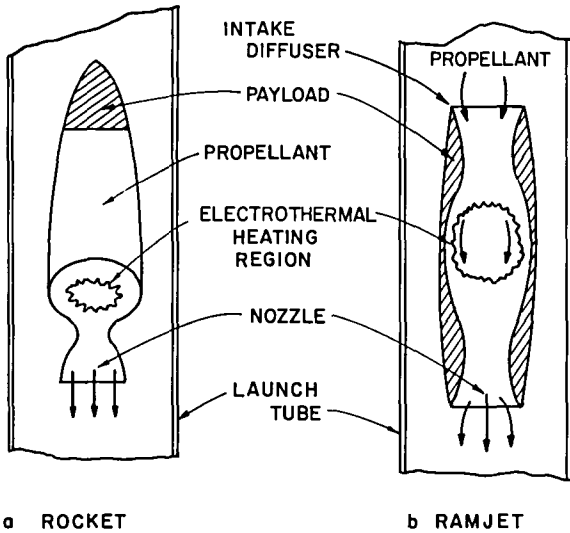

a ROCKET   b RAMJET

Fig. 1. Electrothermal Thruster Concepts

The purposes of this study are 1) to determine the potential of the electrothermal ramjet concept by comparing its gross performance capabilities with those of rocket and electromagnetic accelerator systems, 2) to select a ramjet configuration that appears to be promising and 3) to examine the fluid mechanics and thermodynamics of operation of this configuration. The execution of this work should point out any basic physical limitations that make the concept impractical and illustrate its potential advantages over other launch vehicle concepts.

GROSS PERFORMANCE COMPARISON

In order to compare the performance of various propulsion systems a high acceleration earth escape mission was selected. In this mission sufficient velocity would be imparted to the payload at the earth's surface so it would be at earth escape velocity when it reached an altitude where atmospheric drag would be negligible. The thrusters to be compared are characterized by their exhaust velocities with the following values being selected as typical of the capabilities of the devices indicated:

Thruster	Exhaust Velocity (U)
Chemical Rocket	4,500 m/sec
Resistojet Rocket	8,500 m/sec
Arcjet Rocket	15,000 m/sec
Resisto-ramjet	8,500 m/sec
Arc-ramjet	15,000 m/sec

Each of these thrusters will, for this preliminary analysis, be assumed to operate at a constant exhaust velocity. This is probably a reasonable assumption for the rockets, but it is not obvious that the ramjet is modeled adequately as a constant exhaust velocity device. Work contained in the

next section of this paper shows, however, that from a theoretical point of view it is quite reasonable to model the ramjet in this way. In addition an ideal electromagnetic launcher will be used in the comparison. This device is idealized in the sense that all of the electrical energy input is assumed to be transferred to the moving payload mass and it therefore represents the ultimate launcher.

The velocity required at the surface of the earth by a payload intended to escape the earth and the maximum acceleration that such a payload can endure are also necessary as inputs to the problem under consideration. These quantities can be defined if one considers the expulsion of the payload to consist of two phases, namely the launch phase illustrated in Figure 2 and the subsequent phase of vehicle passage through the atmosphere. A vertical launch trajectory is specified and initially the vehicle is assumed to be at rest and to have a mass m_i. When the thruster is started it generates a constant thrust F which produces an initial acceleration σ_i. The launch phase is assumed to continue until time t_f when a terminal launch velocity v_f is reached. At this point the vehicle mass is m_f, the acceleration is σ_f and the axial location measured from the initial location is x_f. Thrusting stops and the phase of vehicle passage through the atmosphere begins at this point. During this second phase the vehicle velocity decreases as a result of atmospheric drag and gravitational effects.
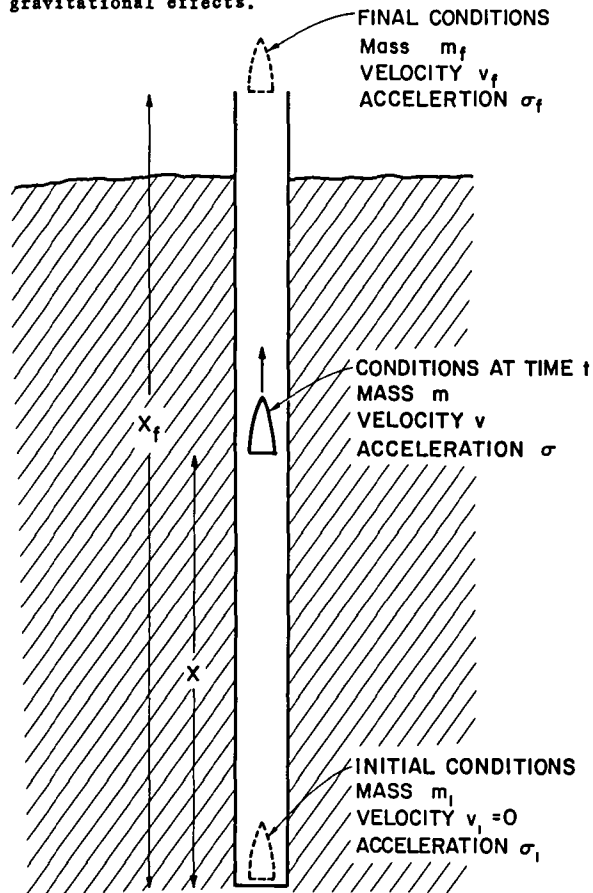

Fig. 2. Launch Phase Nomenclature

The maximum acceleration σ_f occurs at the end of the launch phase. In order to minimize track length this acceleration should be as large as the vehicle can withstand, a value that is ultimately determined by the mechanical strength of the vehicle. If one assumes the basic vehicle is cylindrical and has a diameter d, the compressive stress S at the base of the vehicle is equal to the thrust force F divided by its cross sectional area.

$$S = \frac{4F}{\pi d^2} = \frac{4 m_f \, \sigma_f \, g}{\pi d^2} \qquad (1)$$

In this equation σ_f, the final (maximum) acceleration, is in G's and g is the acceleration due to gravity. The ballistic coefficient of the vehicle B which characterizes vehicle drag during its movement through the atmosphere after launch, is given by

$$B = \frac{C_D \, \pi \, d^2}{4 \, m_f}. \qquad (2)$$

In this equation C_D is the vehicle drag coefficient and it should have a value near 0.1 for the velocities under consideration here.[5] Combining Eqs. 1 and 2 and solving for the maximum acceleration one obtains

$$\sigma_f = \frac{BS}{C_D \, g}. \qquad (3)$$

Figure 3, which was obtained from data supplied by the NASA Lewis Research Center[6], shows the ratio of the velocity at the start of passage through the atmosphere to that after this passage as a function of the ballistic coefficient of the vehicle. For the case under consideration here the velocity after atmospheric passage is the earth escape velocity as the vertical axis title suggests. From this figure it appears that a low but realistic ballistic coefficient might be $2 \times 10^{-5} \, m^2/kg$. At this value the ratio of atmospheric entrance velocity to the earth escape velocity ($v_{esc} = 11,200$ m/sec) is just under 1.2 and the terminal launch velocity (v_f) would therefore have to be about 13,000 m/sec. If one specifies an allowable stress in the vehicle of 1.4×10^9 nt/m² (200,000 psi) then the maximum allowable acceleration (Eq. 3) becomes 30,000 G's. This acceleration, while high, is not considered unattainable. Light gas guns[1] have in fact been operated at projectile acceleration levels an order of magnitude higher than this. For our case, however 30,000 G's should not be exceeded if compressive stresses are to be held below 1.4×10^9 nt/m² during launch to a velocity of 13 km/sec. This velocity will be sufficient to enable escape from the earth when the vehicle diameter is given by Eq. 2. For a 10 kg mass having the ballistic and drag coefficients mentioned this would correspond to a vehicle several centimeters in diameter.
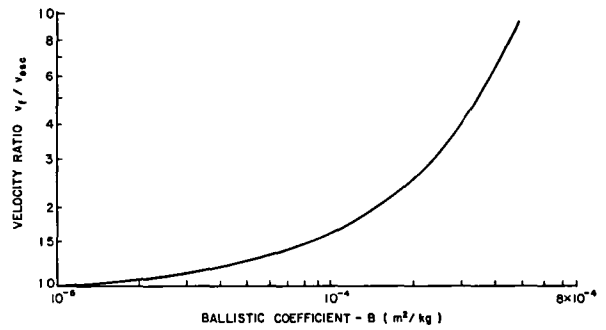
Fig. 3. Velocity Loss Through Atmospheric Drag

Results

A simple mathematical model based on a dynamical force balance and an energy conservation analysis can be applied to each of the thruster cases considered. In each of these cases a constant thrust and constant exhaust velocity in the frame of reference of the rocket or ramjet have been assumed. The basic equations used are given in Reference 7. The results were obtained for a particular case where a 10 kg final mass was launched vertically on the earth escape trajectory. The 10 kg final mass was selected rather arbitrarily but the basic trends and comparisons made here are not affected by this selection.
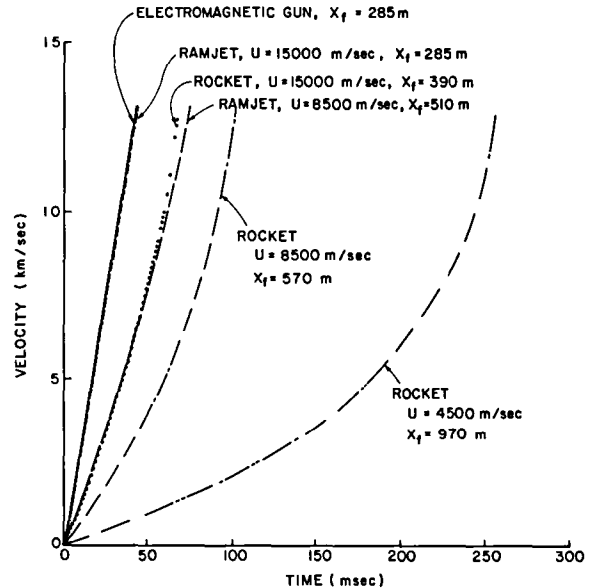
Fig. 4. Velocity Profile Comparison

Figure 4 shows the velocity profiles for the six thruster options being compared. The effect of increasing rocket exhaust velocity from 4,500 to 15,000 m/sec is observed to be a three-to-fourfold reduction in the launch time and a two-to-threefold reduction in the required launch track length (x_f).

131

This points out the great benefit of using the high exhaust velocity electrothermal rocket rather than the conventional chemical rocket motor which is characterized by the lower exhaust velocity. By using a ramjet rather than a rocket further reductions in launch times and track lengths are realized at a given exhaust velocity. This occurs because there is no on-board propellant being accelerated in the case of the ramjet. At an exhaust velocity of 15,000 m/sec the ramjet performs essentially the same as the electromagnetic accelerator in that it requires the same track length (285 m) and launch time (44 msec). The 8,500 m/sec ramjet is seen to exhibit performance comparable to the 15,000 m/sec rocket.

Figure 5 shows the time profile of the vehicle acceleration for the various thrusters. The acceleration is limited to 30,000 G's and this implies considerably lower initial accelerations for the conventional rockets in which the vehicle mass must decrease with time as on-board propellant is discharged. The shorter launch times and track lengths given in Figure 5 occur of course for the cases where the acceleration remains closer to the limiting value throughout the launch.

CONSTANT THRUST
CONSTANT EXHAUST VELOCITY
σ_f = 30000 G's

Fig. 5. Acceleration Profile Comparison

A discussion of the variation in acceleration for the 8.5 km/sec ramjet will facilitate an understanding of some of the physical characteristics of this thruster. 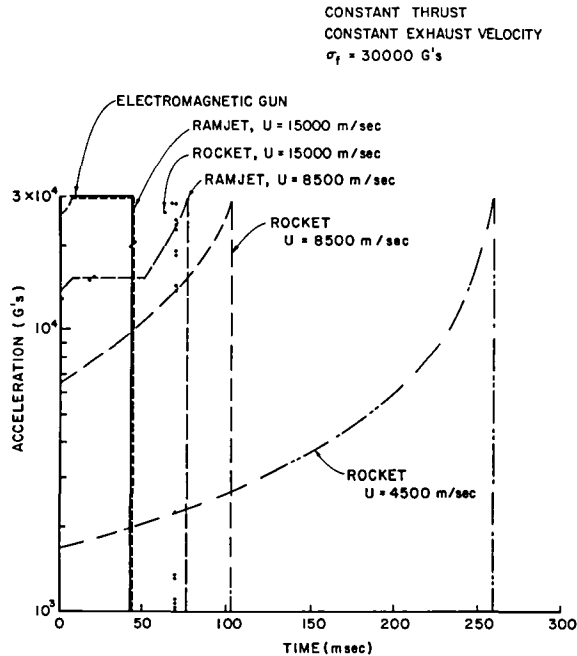Before a ramjet can be operated it is necessary to accelerate it, using an alternative force, to that velocity where it is processing adequate propellant mass. For the ramjet cases in Fig. 5 this is arbitrarily presumed to be accomplished using an auxiliary rocket motor. During the first ten milliseconds or so the acceleration of the 8.5 km/sec ramjet increases because this auxiliary rocket is operating and on-board mass is being expelled to accelerate the vehicle to the point where the ram pressure is sufficient to effect ramjet operation. This decrease in mass

causes the acceleration level to increase with time. During the interval from 10 to 50 milliseconds, ramjet operation occurs and the vehicle acceleration is constant. Near the 50 millisecond point the vehicle velocity gets sufficiently close to the thruster exhaust velocity so that the ramjet can no longer produce adequate thrust.* This means on-board propellant must again be used and acceleration again increases with time. This use of on-board propellant continues until the desired final velocity (13 km/sec) is realized.

For the 15 km/sec ramjet the final phase wherein on-board propellant is used is not required because the desired final velocity is significantly less than the exhaust velocity. As this discussion suggests it is desirable to have a ramjet exhaust velocity that is substantially greater than the desired vehicle velocity at the end of the launch phase. It is interesting to note at this point that constant exhaust velocity, constant thrust operation of a ramjet implies constant mass flow rate operation. This would seem at first to be difficult to achieve in this case where the projectile velocity is continuing to increase. A constant mass flow rate can be realized however by either varying the ramjet intake area or the distribution of mass in the launch tube.

Figure 6 shows the variation in vehicle mass with time for each of the thrusters. These curves simply reflect the variations in acceleration observed in Figure 5. It is noteworthy however that the 4,500 m/sec conventional rocket requires an initial mass of 180 kg to deliver a final mass of 10 kg at 13 km/sec while the 15,000 m/sec ramjet can do it with 11.5 kg and the ideal electromagnetic thruster requires only the desired 10 kg as an initial mass. It is also important to note that propellant tankage, structure and thruster masses are neglected in this analysis. If these masses were included in the analysis the differences between required initial masses would be even greater.

CONSTANT THRUST
CONSTANT EXHAUST VELOCITY
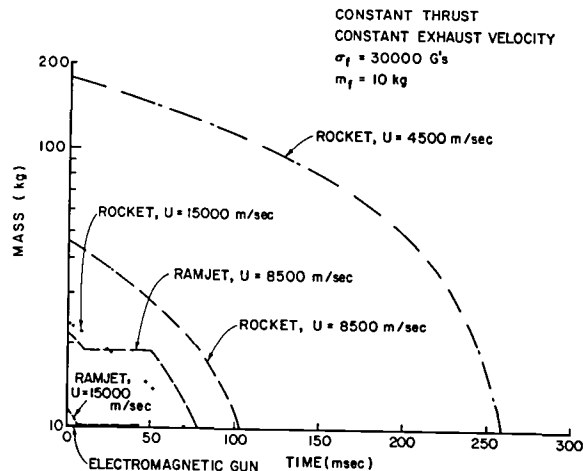σ_f = 30000 G's
m_f = 10 kg

Fig. 6. Mass Profile Comparison

---

* Application of the momentum balance equation demonstrates that the thrust ($F = \dot{m}$ [U–v]) goes to zero as the vehicle velocity (v) approaches the exhaust velocity (U).

132

The power profiles for each operating condition are compared in Figure 7. The total energy (E) required to accelerate the payload to the specified final velocity for each option is obtained by integrating under the power curves and is also shown in this figure. The variation in total energy required for the launch is seen to be relatively modest between the various modes, but the ramjet and electromagnetic designs are seen to require substantially greater peak power levels. Figure 7 shows that the peak power levels of the high exhaust velocity ramjet and the electromagnetic gun are comparable. The electromagnetic gun is observed to require the least energy of any option, but it is important to note that this is a highly idealized model. The energy stored in the magnetic fields of this device, when the vehicle leaves the launch track, as well as joule heating losses will be substantial and they have not been included here. Their inclusion could well make the energy required for the electromagnetic gun more comparable to values obtained with the rockets and ramjets.
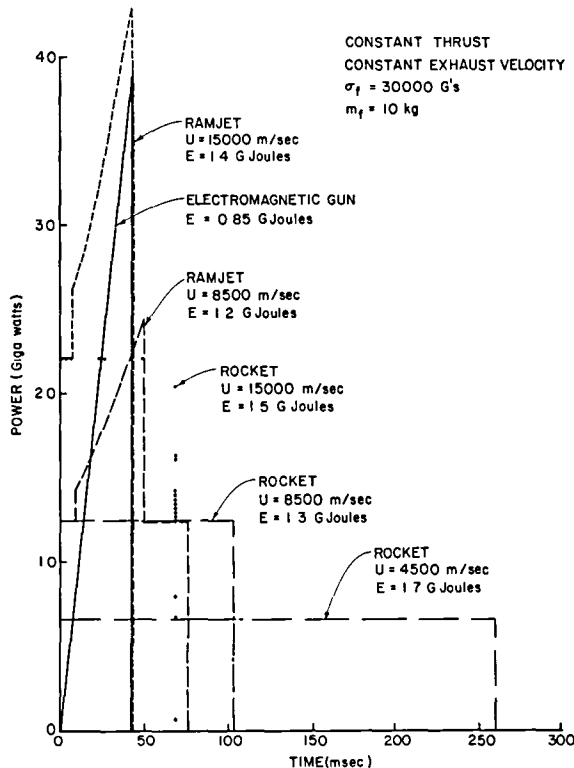

Fig. 7. Power Profile Comparison

The modeling that has been used in this study is highly idealized. For example losses due to aerodynamic and frictional drag and residual thermal energy in the propellants have been neglected for the launch phase, as have propellant pumping powers and losses associated with energy transport through conductors or windows. These could change absolute numbers significantly although the comparative results are considered correct, and the suggest the hydrogen ramjet thruster could exhibit performance that is comparable to that associated with idealized electromagnetic thruster. It is

therefore appropriate to examine specific ramjet configurations and to determine the mechanical complexity that might be required and the extent of the thermodynamic losses associated with their operation.

RAMJET DESIGN FEATURES

The conventional ramjet design shown in Fig. 1b could be used in the present application. In this configuration it would fly down the launch tube processing a portion of the hydrogen and bypassing the remainder through the region between its exterior surface and the launch tube wall. Such a design has several drawbacks typified by the following examples of major design problems:

- Transmission of electrical or electromagnetic energy through the ramjet sidewall into the heat addition core.

- Control of the ramjet geometry to effect shock swallowing and efficient operation over the large vehicle velocity range that will be encountered.

- Control of the radial position of the vehicle within the tube.

A more suitable design would be one in which the heat addition zone was located external to the ramjet and the tube wall could serve to guide it down the tube. Figure 8 shows a schematic diagram of such a design which is designated the annular flow ramjet configuration. This axisymmetric design utilizes a launch tube of circular cross section. All of the propellant flow is forced to pass through the ramjet. The converging–diverging diffuser and nozzle passages are observed to be formed by the undulating configuration of the projectile coupled with the essentially straight launch tube wall. The conceptual advantages of this configuration over the conventional design are

- Heat addition can be effected outside the ramjet body directly from the tube wall. This eliminates the need for windows in the ramjet for the case of beamed energy heating and sliding current contacts for arc discharge heating schemes.

- Shock losses will probably be lower with the annular flow design because a conical shock attached to the projectile would be expected while a bow shock would be driven ahead of the conventional ramjet.

- Direct mechanical or fluid mechanical forces induced between the tube wall and projectile should tend to stabilize and center it.

- The structural design of the projectile appears to be relatively simple.

- Variations in fluid flow areas needed to achieve proper flow conditions as the projectile velocity increases can be introduced by varying the cross-sectional area of the launch tube as a function of axial position.
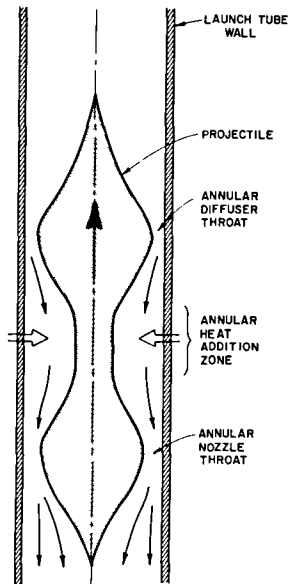

Fig. 8. Annular Flow Ramjet Configuration

It is noteworthy that by eliminating the need to transfer electrical energy to the projectile itself and introducing the self-centering capability just alluded to, one mitigates two of the problems associated with such electromagnetic devices as the rail gun. These problems relate to the design of sliding electrical contacts and the maintenance of a tight tolerance on launch track straightness. Relaxation of the tolerance should for example permit longer track lengths and lower acceleration levels than those required for railguns.

FLUID MECHANICS MODEL

Since fluid mechanical forces propel the vehicle it is appropriate to begin an analysis of the annular flow ramjet by determining the magnitudes of thermodynamic and fluid mechanical variables required to produce the desired thrust level. This analysis must be considered preliminary and as a result very much simplified. The first major assumption in this analysis is that the process can be considered quasi steady. It is recognized that at the acceleration levels being considered this cannot in fact be accurate. However, including unsteadiness introduces major complications in the analysis. Estimates of the errors involved have indicated that though they are fairly substantial, they are not so large as to render these prelim-

inary calculations valueless.

Starting the projectile through the application of an external force will be addressed later. For purposes of this analysis we assume the projectile has been accelerated to a substantial supersonic velocity. Though it is likely that there will be a conical shock attached to the nose of the projectile, the strength of this shock can be controlled to some extent by the contour and half angle of the projectile nose. Consequently, for this preliminary analysis the diffusion process is modeled as an isentropic one. After diffusion the hydrogen working fluid undergoes heat addition at a subsonic velocity in a constant area duct and this is followed by an isentropic expansion to a supersonic exhaust velocity. For this analysis propellant velocities were computed in the frame of reference of the moving projectile. The fact that the tube wall which is the outer boundary to this flow, is moving in this frame of reference was assumed to have no effect on the behavior of the flow. The basic equations of compressible fluid mechanics (conservation of mass and energy coupled with a thermodynamic path equation) were applied separately to the diffusion, heat addition and expansion processes.

Thrust was computed by applying the momentum equation in the frame of reference of the control volume moving with the projectile. It should be noted that the boundary conditions associated with the annular flow ramjet are different than those associated with conventional ramjet operation. In the present case the inlet and outlet flow areas are equal and the flow area in the heat addition zone must be less than this inlet/outlet area. In the conventional ramjet case the static inlet and outlet pressures are set equal while in the annular flow ramjet the static pressure of the outlet stream will typically be greater than that at the inlet.

The thermodynamic properties of the hydrogen working fluid will vary over the range of temperatures and pressures encountered during ramjet operation primarily because of the effect of dissociation. For this preliminary analysis however it was desirable to avoid the complications of temperature and pressure dependent specific heats and gas constants. Figures 9 and 10 show how the values of the ratio of specific heats and gas constant for hydrogen vary with temperature and pressure. In general, during ramjet operation, increases in temperature are accompanied by corresponding increases in pressure. This being the case Figures 9 and 10 suggest that it is not too unrealistic to treat these two parameters as constants. For the results contained in this paper ideal gas behavior was assumed and a ratio of specific heats (γ) of 1.4 and a gas constant (R) of 4160 joules/kg$^\circ$K were used.

Extensive analysis of the early phase of ramjet operation when a bow shock was propagated ahead of the projectile was also undertaken. Modeling of this phase of operation was successful and showed that with proper launch tube design the bow shock would become attached as an conical shock without difficulty. However it also showed that positive ramjet thrust could not be produced at the subsonic diffusion inlet condition that accompanies operation with a bow shock. It was therefore assumed that acceleration to supersonic speeds and initia-

134

tion of the isentropic diffusion process would be accomplished by some alternative acceleration scheme.
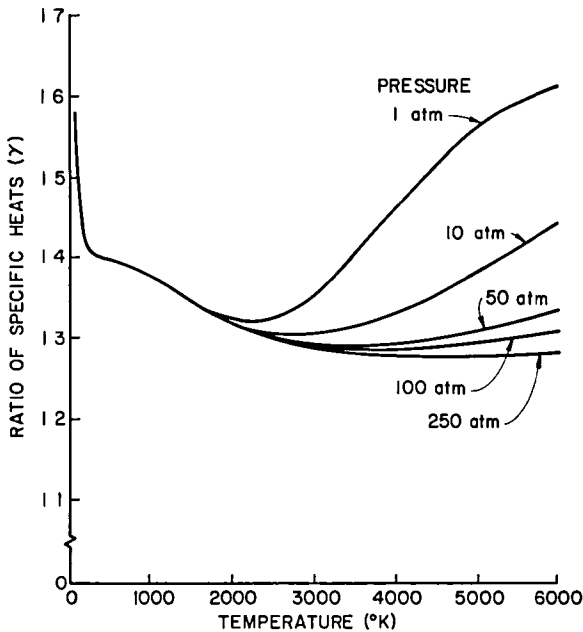

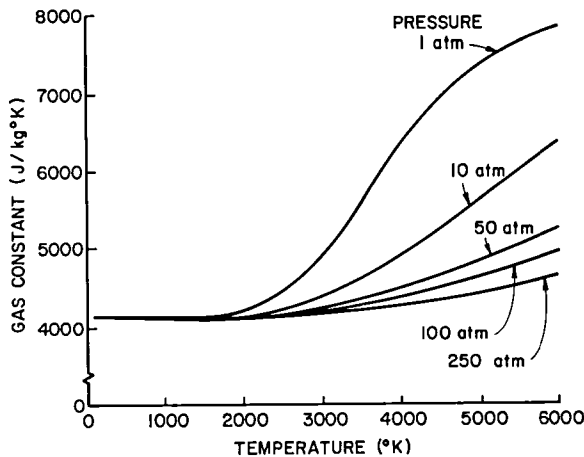Fig. 9. Ratio of Specific Heats for Equilibrium Hydrogen

Fig. 10. Gas Constant for Equilibrium Hydrogen

TYPICAL SUPERSONIC LAUNCH CYCLE

If one assumes that the projectile will be acted upon by either the ramjet force or some externally applied force needed to produce the desired acceleration, the projectile trajectory will be known. With the projectile velocity profile known the propellant flow velocity relative to the ramjet is known at each position along the launch track. One can now prescribe the diffuser throat area required at each position along the tube so that the flow will remain sonic at this throat. One can also prescribe the heat supplied

in the subsonic heat addition region so that the specified thrust will either be produced or the mach number at the exit of the heating region (in the projectile frame of reference) reaches its maximum allowable value of unity. After heat has been added, the flow is accelerated isentropically in the nozzle to the maximum supersonic mach number achievable under the constraint of the area change available. The static pressure at the nozzle exit is determined by this expansion and it will vary with projectile position. Proper control of this pressure at the base of the projectile would have to be achieved in an actual device by proper design of the launch tube. Such a tube would consist of two sections, a cavity section into which hydrogen processed by the ramjet would be collected and the launch section through which the projectile would pass. It has been assumed in this analysis that the cavity section could be designed to have the length and cross sectional area needed to accommodate the propellant and facilitate maintenance of the necessary projectile base pressure. While it seems possible to do this intuitively, the examination of the unsteady fluid mechanics describing the process has not yet been attempted.

Figure 11 shows the results of such an analysis for the case where a constant thrust of 3 x 10^6 Newtons is maintained on a 10 kg mass and the hydrogen in the launch tube is initially at 300°K (T_i) and 30 atmospheres(P_i). The projectile selected for this example has a fixed 16 cm diameter at the diffuser throat and an 8 cm diameter in the heat addition region. These diameters are considered adequate to assure the structural integrity of the projectile during launch. As Figure 11a shows the projectile velocity (in the launch tube frame of reference) increases linearly with time. Since the propellant is initially at rest, relative to the tube wall the projectile velocity is equal to the propellant inlet velocity in the projectile frame of reference. The exhaust velocity (in the projectile frame of reference) is observed to be equal to the inlet velocity during the first ~8 msec of operation so during this time interval essentially no net thrust is produced through the mechanism of momentum change of the propellant. After about 16 msec of operation, however, the exhaust velocity has risen to about 15 km/sec and begun to level off. During the time between ~8 to ~16 msec all of the heat that can be added without choking the flow (achieving unity mach number at the end of the heat addition region) is being added.

As Fig. 11b shows the net ramjet thrust is inadequate to meet the 3 x 10^6 neuton thrust requirement at times less than 16 msec. Thus, an alternative accelerating scheme such as the constant pressure gun (discussed in the next section) would have to be used during this time interval. As the projectile velocity increases, more heat can be added and this causes the increase in exhaust velocity shown in Fig. 11a. After ~16 msec both the exhaust velocity and the mass flow rate have risen to the point where the desired thrust level can be produced and the mach number after heat addition begins to drop below unity.

Figure 11c, which indicates projectile position as a function of time for this case of constant acceleration, shows a launch tube about 400 m long would be required to accelerate the 10 kg mass to the terminal velocity of 15,000 m/sec in ~50

msec. Figure 11d indicates the variation in tube and projectile diameters that would have to be effected to satisfy fluid mechanical constraints imposed on the ramjet. As the sketch suggests, the projectile diameter at the diffuser throat and in the heat addition region have been treated as fixed at 16 cm and 8 cm respectively. The reduction in tube diameter required to yield unity mach number at the diffuser throat as the projectile velocity increases is shown by the solid line. Data from this line taken together with the position profile of Fig. 11c specify how the tube diameter would have to vary along its length. Figure 11d also shows that the projectile diameter at the nozzle throat would have to increase as the projectile velocity increases and the input power is varied to induce the desired thrust level. The fact that this diameter must change during the launch cycle represents a significant mechanical complication in the system. It is noted however that the amount of change in this diameter becomes very small after about 20 m sec when the projectile velocity is ~5 km/sec. It is anticipated that a pressure or temperature sensitive scheme might be designed to facilitate this change in projectile diameter at the nozzle throat. Alternatively one could hold the projectile diameter in the nozzle region fixed, reduce the tube diameter slightly more rapidly that Fig 11d suggests and abrade the diameter of the projectile at the diffuser throat using protrusions from the tube wall.

a. Velocity Profiles

b. Thrust Profile

c. Projectile Trajectory
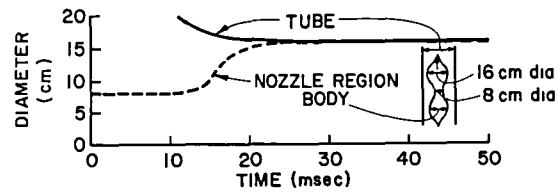
d. Required Variation in Geometry
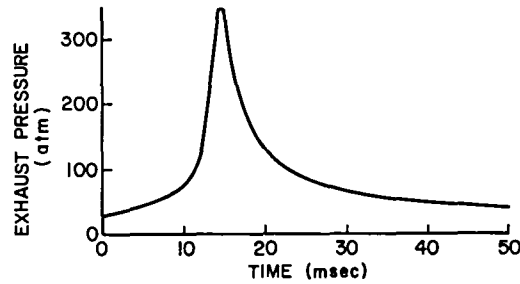
e. Projectile Base Pressure Profile
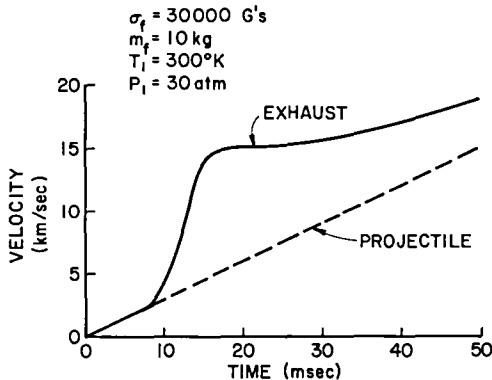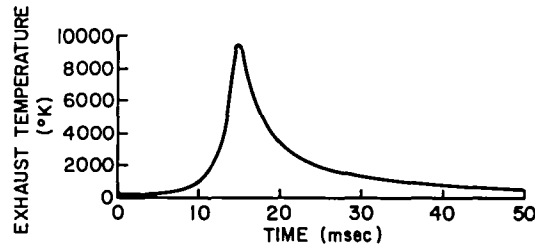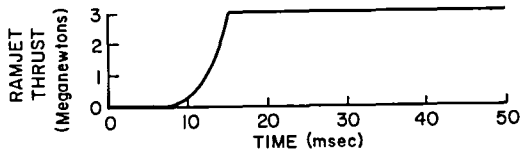
f. Exhaust Temperature Profile
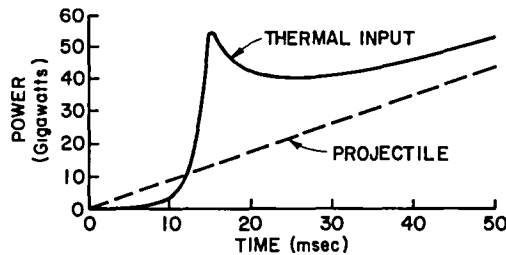
g. Power Profiles
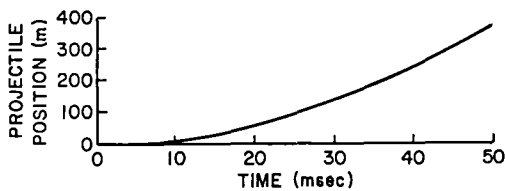
Fig. 11. Typical Electrothermal, Hydrogen Ramjet Launch Cycle

Figures 11e and 11f indicate how the static pressure and temperature at the nozzle exit should vary to conform to the problem specifications. The peaks in temperature and pressure occur at the point where the power input is a maximum (Fig. 11g). This in turn occurs at the time when the thrust has just reached its design value and the mach number at the end of the heat addition region is still at unity. At this condition the exhaust velocity is still relatively low and the bulk of the thrust is being produced by the static pressure difference across the projectile. If one did not start using the ramjet until after ~20 msec into

the launch, we see that the exhaust pressure and temperature would lie in a very moderate range throughout the period of ramjet operation. Note that it is the pressure profile of Fig. 11e that would have to be matched through proper design of the cavity section of the launch tube. This might be achieved by selecting not only the length and cross sectional area of this section but also by the inclusion of accumulator chambers that could be connected into the tube at the proper time.

The temperatures of Figure 11f are observed to be relatively low. So low in fact that it would probably not be possible to add energy to the hydrogen using electromagnetic radiation to couple to the plasma using the mechanism of inverse bremmstrahlung[8]. It is noted however that this is not the case in the heat addition region where temperatures in the $10,000^{\circ}K$ range needed to effect this energy addition mechanism do prevail.

Figure 11g shows the thermal power input profile required to effect operation as well as the actual profile of mechanical power input to the projectile. After the ~20 msec period over which the auxiliary starting force would be applied it is observed that the ratio of projectile power to thermal input power rises above ~50%. (An approximate mathematical relationship for this ratio is given in the next section.) The ramjet is observed to become increasingly efficient as the launch cycle proceeds. This suggests that the ramjet will be more efficient at the higher velocities where the efficiencies of electromagnetic launchers drop off. The difference between the projectile and thermal input powers represents the power being deposited as kinetic and thermal energy in this hydrogen propellant. It should be noted here that frozen flow losses in the nozzle and electrical-to-thermal power conversion losses as well as frictional losses have been neglected in this preliminary analysis.

Analyses similar to the one leading to the results of Fig. 11 have been carried out at other values of parameters such as the initial tube pressure and the diameter of the projectile at the diffuser throat. They suggest that inadequate mass flow rates are brought on by low projectile diameters and low initial tube pressures. This in turn leads to excessively high exhaust pressures and temperatures as well as extremely high thermal power demands. It has also been determined that the device will work if the nozzle is used as a diffuser and the propellant is exhausted at a subsonic mach number and a high static pressure.

CONSTANT PRESSURE GUN - RAMJET COMBINATION

As discussed above efficient ramjet operation does not occur until some critical projectile velocity is attained. Below this speed an auxiliary thrust device is required in order to maintain the constant acceleration level assumed. In the example whose characteristic parameters are shown in Figure 11 this velocity was reached at approximately 20 milliseconds. At this point the projectile velocity was about 5900 m/s and the distance down the tube about 59 m. One way of attaining this necessary velocity would be to accelerate the projectile as in a gun and delay ramjet operation until this velocity was reached. In this process

energy would be added to a fixed quantity of gas at the base (in back of) the projectile and the projectile would completely occupy the tube cross section. If acceleration is to be constant and the tube cross sectional area and projectile mass are constant, then the pressure in the tube must be maintained at a constant value as well during the acceleration. It is anticipated that the transition from the gun to the ramjet phases of operation would be accomplished when the projectile passed through a diaphragm containing the hydrogen in the section of the tube to be used for ramjet operation. The section of tube between the initial projectile location and the diaphragm would be at low pressure initially so no significant amount of gas would be compressed ahead of the projectile during the constant pressure phase.

A simple relationship between the required rate of energy deposition to the gas $\dot{Q}$ and the projectile velocity v is obtained easily for the constant pressure (gun) phase of acceleration from the principle of energy conservation if frictional effects are ignored. This relationship is.

$$\dot{Q} = \left(m_f \; \sigma_f \; g \; v \right) \frac{\gamma}{\gamma - 1} \qquad (4)$$

Since the rate of kinetic energy increase of the projectile is $m_f \; \sigma_f \; g \; v$ the efficiency of the process (ratio of rate of kinetic energy increase to rate of energy supplied to driven gas) must be $(\gamma -1)/\gamma$. If hydrogen is taken to be the driver gas, $\gamma = 1.4$, the efficiency is about 28.6%. This is constant throughout the acceleration process. The energy not appearing as kinetic energy of the projectile must reside in the thermal energy of the driver gas. The temperature of the gas driving the projectile must therefore increase substantially during the acceleration. The magnitude of the rise is, of course, dependent on the mass of driver gas used.

Once the velocity necessary for effective ramjet operation is reached, operation of the projectile as a ramjet in the mode described in the preceeding section is initiated. It is of interest to develop an expression for the efficiency of this process and to compare it with the efficiency of the constant pressure gun process. Application of conservation of energy to the ramjet results in the following expression:

$$\dot{Q} = \dot{m} \; \frac{U^2 - v^2}{2} + \dot{m} \; (h_e - h_i) \qquad (5)$$

where the subscripts e and i denote exit and inlet conditions for the device, and h and $\dot{m}$ represent respectively enthalpy and mass flow rate. Combination of this relationship with the thrust equation $F = \dot{m} \; (U - v) + (P_e - P_i)A$, where A is the tube cross sectional area, and P is the pressure gives after rearrangement:

$$\dot{Q} = \frac{F(U+v)}{2}\left(1 - \frac{(P_e - P_i)A}{F} + \frac{\dot{m} \; C_p \; (T_e - T_i)}{\frac{F(U+v)}{2}} \right) . \qquad (6)$$

Since $F = m_f \sigma_f g v$, the expression above can be written

$$\dot{Q} = m_f \sigma_f g v \left(\frac{U}{2v} + \tfrac{1}{2} \right) \left(1 - \frac{(P_e - P_i)}{F} A + \frac{\dot{m} C_p (T_e - T_i)}{\frac{F(U+v)}{2}} \right) \qquad (7)$$

Comparing this to the rate of kinetic energy gain of the projectile, $F = m_f \sigma_f g v$ allows the definition of the ramjet efficiency,

$$\eta_R = \left[\left(\frac{U}{2v} + \tfrac{1}{2} \right) \left(1 - \frac{(P_e - P_i)}{F} A + \frac{\dot{m} C_p (T_e - T_i)}{\frac{F(U+v)}{2}} \right) \right]^{-1} \qquad (8)$$

The efficiency clearly varies with the projectile velocity v. At the beginning of ramjet operation, for the case given in Figure 11, at t = 20 milliseconds,

$$\eta_R = \frac{1}{(1.25 + 0.5)\ (1 - .062 + .212)} = 0.497 \qquad (9)$$

and at t = 50 milliseconds (end of acceleration)

$$\eta_R = \frac{1}{(.624 + .5)\ (1 - .007 + .023)} = 0.876 \ . \qquad (10)$$

These calculations indicate that the efficiency of the ramjet is always substantially higher than that of the constant pressure acceleration (0.286) and increases with increasing projectile velocity.

The overall efficiency of the ramjet acceleration process can be estimated easily if the term

$$1 - \frac{(P_e - P_i)A}{F} + \frac{\dot{m} C_p (T_e - T_i)}{\frac{F(U+v)}{2}}$$

is taken to be unity and if U is taken to be constant. The first assumption introduces a fairly small error of about 15% at the start of ramjet operation and a very small error of about 1.6% at the conclusion of the acceleration. The constancy of U depends on the ramjet parameters chosen. For the example of Figure 11 it is not a bad approximation. With these two assumptions the expression for the rate of energy consumption becomes

$$\dot{Q} = \left(\frac{U}{2v} + \tfrac{1}{2} \right) m_f \sigma_f g v \ . \qquad (11)$$

Integrating the above expression over any period of time, say between t_1 and t_2

$$Q = m_f \sigma_f g(x_2 - x_1) \left[\frac{U}{2\bar{v}} + \tfrac{1}{2} \right] \ , \qquad (12)$$

where $\bar{v} = (v_1 + v_2)/2$ is the average projectile velocity between t_1 and t_2. Since $m_f \sigma_f g(x_2 - x_1)$ is equal to the change of kinetic energy of the projectile, the overall efficiency for the ramjet acceleration process becomes

$$\bar{\eta}_R = \frac{1}{\left[\frac{U}{2\bar{v}} + \tfrac{1}{2} \right]} \ . \qquad (13)$$

For the example of Figure 11, $\bar{\eta}_R = 77.3\%$. For the combined constant pressure acceleration-ramjet acceleration process the efficiency is approximately 68%.

CONCLUSIONS

Much analysis remains to be done to investigate completely the effects of all of the parameters of concern. In particular the effects of high acceleration and unsteady gas dynamic effects need to be considered and solutions that yield higher system efficiencies and/or more readily accommodated geometry changes need to be sought. Results presented in Figure 11 suggest however that the electrothermal ramjet designed to produce thrust after being given an initial velocity cannot be rejected on the basis that it violates a basic principle of fluid mechanics or thermodynamics. Moreover, on the basis of the same results it appears that the efficiency of the ramjet energy conversion process has the potential of being fairly high.

REFERENCES

1. Siegel, Arnold E., ''Theory of High-Muzzle-Velocity Guns,'' appears in Interior Ballistics of Guns, H. Krier and M. Summerfield eds., vol. 66, Progress in Astronautics and Aeronautics Series, American Institute of Aeronautics and Astronautics, 1979, pp. 135-175.

2. Kolm, H. et al, ''Electromagnetic Propulsion Alternatives,'' AIAA Paper 79-1400, Fourth Princeton/AIAA Conference on Space Manufacturing Facilities, May 1979.

3. Snow, W.R. and G. K. O'Neill, ''Construction and Testing of the 2.5 m Mass Driver,'' AIAA Paper 79-2095, Princeton/AIAA/DGLR 14th Electric Propulsion Conf., Oct. 1979.

4. Jahn, R.G., Physics of Electric Propulsion, Chapter 6, 1968, McGraw Hill.

5. Hildebrand, R.B. ''Aerodynamic Fundamentals'', appears in Handbook of Astronautical Engineering, H. H. Koelle, ed., McGraw Hill, 1961, p. 5-24.

6. Kerslake, W.R., Private Communication of unpublished results, NASA Lewis Research Center, Oct. 1980.

7. Wilbur, P.J., ''Ion and Advanced Electric Thruster Research'' NASA CR-165253, Dec. 1980, p. 118.

8. Kemp, N.H. od R.G. Root, '' Analytical Study of laser supported Combustion waves in Hydrogen,'' NASA CR-135349, Aug. 1977.

National Aeronautics and Space Administration
Washington, DC 20546
Attn: RS/Mr. Dell Williams, III   1
       RTS-6/ Mr. Wayne Hudson   1
       RTS-6/ Mr. Jerome Mullin   1
       MT/ Mr. Ivan Bekey   1

National Aeronautics and Space Administration
Lewis Research Center
21000 Brookpark Road
Cleveland, OH 44135
Attn: Research Support Procurement Section
       Mr. G. Golinski, MS 500-306   1
       Technology Utilization Office, MS 3-19   1
       Report Control Office, MS 5-5   1
       Library, MS 60-3   2
       Mr. N. Musial, MS 500-113   1
       Dr. M. Goldstein, Chief Scientist, MS 5-3   1
       Mr. T. Cochran, M.S. 501-7   1
       Dr. F. Terdan, MS 501-7   1
       Mr. R. Finke, MS 77-4   1
       Mr. B. Banks, MS 11-4   1
       Mr. D. Byers, MS 501-7   1
       Mr. W. Kerslake, MS 501-7   20

National Aeronautics and Space Administration
Lyndon B. Johnson Space Center
Houston, TX 77058
Attn: Mr. Hu Davis   1

National Aeronautics and Space Administration
Marshall Space Flight Center
Huntsville, AL 35812
Attn: Mr. Robert Bechtel   1

Research and Technology Division
Wright-Patterson AFB, OH 45433
Attn: (ADTN) Mr. Everett Bailey   1

NASA Scientific and Technical
Information Facility
P. O. Box 8757
Baltimore, MD 21240
Attn: Accessioning Dept.   1

Copies

Case Western Reserve University
10900 Euclid Avenue
Cleveland, OH 44106
Attn: Dr. Eli Reshotko   1

DST 1
Ministry of Defence
Metropole Building
Northumberland Avenue
London, WC2 N5BL ENGLAND
Attn: Dr. D. G. Fearn   1

United Kingdom Atomic Energy Authority
Culham Laboratory
Abingdon, Berkshire
ENGLAND
Attn: Dr. P. J. Harbour   1
      Dr. M. F. A. Harison   1

National Aeronautics and Space Administration
Goddard Space Flight Center
Greenbelt, MD 20771
Attn: Mr. W. Isley, Code 734   1
      Mr. A. A. Vetman   1
      Dr. David H. Suddeth   1

COMSAT Laboratories
P. O. Box 115
Clarksburg, MD 20734
Attn: Mr. B. Free   1
      Mr. O. Revesz   1

Comsat Corporation
950 L'Enfant Plaza, SW
Washington, DC 20024
Attn: Mr. Sidney O. Metzger   1

Intelsat
490 L'Enfant Plaza, S.W.
Washington, DC 20024
Attn: Mr. Rolland Schreib   1

Rocket Propulsion Laboratory
Edwards AFB, CA 93523
Attn: LKDH/Mr. Walt Detjen   1
      LKDH/Dr. Robert Vondra   1

DFVLR - Institut fur Plasmadynamik
Technische Universitat Stuttgart
7 Stuttgart-Vaihingen
Allmandstr 124
West Germany
Attn: Dr. G. Krulle   1

Copies

Giessen University
1st Institute of Physics
Giessen, West Germany
Attn: Professor H. W. Loeb   1

Jet Propulsion Laboratory
4800 Oak Grove Drive
Pasadena, California 91102
Attn: Technical Library   1
       Mr. Eugene Pawlik   1
       Mr. James Graf   1
       Mr. Dennis Fitzgerald   1
       Dr. Graeme Aston   1

Electro-Optical Systems, Inc.
300 North Halstead
Pasadena, California 91107
Attn: Mr. E. James   1
       Mr. W. Ramsey   1

TRW Inc.
TRW Systems
One Space Park
Redondo Beach, California 90278
Attn: Mr. Sid Zafran   1

National Aeronautics and Space Administration
Ames Research Center
Moffett Field, California 94035
Attn: Technical Library   1

National Aeronautics and Space Administration
Langley Research Center
Langley Field Station
Hampton, Virginia 23365
Attn: Technical Library   1

Hughes Research Laboratories
3011 Malibu Canyon Road
Malibu, California 90265
Attn: Mr. J. H. Molitor   1
       Dr. R. L. Poeschel   1
       Dr. Jay Hyman   1
       Dr. J. R. Beattie   1
       Dr. W. S. Williamson   1
       Dr. H. J. King   1

Princeton University
Princeton, NJ 08540
Attn: Dean R. G. Jahn   1
       Dr. Arnold Kelly   1

Copies

Boeing Aerospace Co.
P. O. Box 3999
Seattle, Washington 98124
Attn: Mr. Donald Grim, M.S. 8K31   1

Lockheed Missiles and Space Co.
Sunnyvale, California 94088
Attn: Dr. William L. Owens
        Dept. 57-24

Electrotechnical Laboratory
1-1-4, Umezono, Sakura-Mura,
Niihari-Gun
Ibaraki, Japan
Attn: Dr. Katsuya Nakayama   1

Sandia Laboratories
Mail Code 4537
Albuquerque, NM 87115
Attn: Mr. Ralph R. Peters   1

Ion Tech   Inc.
P. O. Box 1388
1807 E. Mulberry
Fort Collins, Colorado 80522
Attn: Dr. Gerald C. Isaacson   1

EG & G Idaho
P. O. Box 1625
Idaho Falls, Idaho 83401
Attn: Dr. G. R. Longhurst, TSA-104   1

Michigan State University
East Lansing, MI 48824
Attn: Dr. J. Asmussen   1
        Dr. M. C. Hawley   1

The Aerospace Corporation
Space Sciences Lab.
P. O. Box 92957
Los Angeles, California 90009
Attn: Dr. Y. T. Chiu   1

The Takagi Research Laboratory
Department of Electronics
Kyoto University
Yoshidahonmachi Sakyo-ku Kyoto 606
JAPAN
Attn: Dr. Toshinori Takagi   1

Copies

Department of Aeronautics
Faculty of Engineering
University of Tokyo
7-3-1, Hongo, Bunkyo-ku
Tokyo, JAPAN
Attn: Prof. Itsuro Kimura   1

Prof. Tom Maul
P. O. Box 98182
Tsim Sha Tsui Post Office
Kowloon, Hong Kong
British Crown Colony   1

Mr. Susumu Masaki
Department of Electronics
Tokyo National Technical College
No. 1220-2
Kunugida-cha, Hachioji 193
Tokyo, JAPAN   1

Dr. Pradosh Ray
Tuskegee Institute
School of Engineering
Tuskegee Institute, Ala. 36088   1

Dr. John Barber
International Applied Physics Inc.
7546 McEwen Road
Dayton, Ohio 45459   1

Dr. Ron Hawke
Lawrence Livermore Laboratory
Livermore, California 94550   1

Dr. Richard A. Marshall
University of Texas
Taylor Hall 167
Austin, Texas 78712   1

Dr. V. V. Zhurin
Computing Center of the USSR
    Academy of Sciences
Vavilova 40
117333 Moscow, B-333
USSR   1

Dr. M. Krishnan
Dept. of Applied Physics
P. O. Box 2159
Yale Station
New Haven, Connecticut 06520   1

Copies

Dr. Ed Goldman
Physics International Co.
2700 Merced Street
San Leandro, CA   94577   1

Mr. An Shih-Ming
Vice Director of Electric Propulsion Laboratory
Space Science and Technology Center
Chinese Academy of Sciences
Beijing, China   1

Mr. Lee W. Parker
252 Lexington Road
Concord, Massachusetts   01742   1

Dr. Chris Olson
Dept. of Physics
University of Huntsville
Huntsville, AL   35899   1

Dr. Kevin Rudolph
M.S. M0482
Martin Marietta Aerospace
P. O. Box 179
Denver, Colorado   80201   1

Dr. Rolf Bühler
Institut für Raumfahrtantriebe
Universitat Stuttgart
7 Stuttgart 80
Pfaftenwaldring 31
West Germany   1

Internal Distribution:
Dr. H. R. Kaufman   3
Dr. R. S. Robinson   3

End of Document